Novel pre-interventional atrial flutter localization tool for the improvement of radiofrequency ablation efficacy

Muhammad Haziq Bin Kamarul Azman

UNIVERSITÉ CÔTE D'AZUR

ÉCOLE DOCTORALE
SCIENCES ET TECHNOLOGIES DE L'INFORMATION ET DE LA COMMUNICATION

UniKL
UNIVERSITI KUALA LUMPUR

THÈSE DE DOCTORAT

NOUVEL OUTIL DE LOCALISATION PRÉ-INTERVENTIONNELLE DU FLUTTER AURICULAIRE POUR L'AMÉLIORATION DE L'EFFICACITÉ DE L'ABLATION RADIOFRÉQUENCE

Muhammad Haziq BIN KAMARUL AZMAN

Laboratoire I3S

Présentée en vue de l'obtention du grade de docteur en Automatique, Traitement du Signal et des Images **d'**Université Côte d'Azur **et** Doctor of Philosophy (Electrical and Electronics Engineering) **d'**Universiti Kuala Lumpur

Dirigée par: Olivier MESTE / Kushsairy KADIR

Soutenue le: 16/12/2019

Devant le jury, composé de:

Leif SÖRNMO, Prof.
LU, Sweden

Raveendran PARAMESRAN, Prof.
UM, Malaysia

Kushsairy KADIR, Assoc. Prof.
UniKL, Malaysia

Olivier MESTE, Prof.
UCA/I3S, France

Azmi HASSAN, Prof.
UniKL, Malaysia

Mohd. Razif IDRIS, Prof.
UniKL, Malaysia

Asadullah Shah SYED, Prof.
IIUM, Malaysia

Norliza MOHD. NOOR, Assoc. Prof.
UTM, Malaysia

Liberté • Égalité • Fraternité
RÉPUBLIQUE FRANÇAISE

Novel Pre-Interventional Atrial Flutter Localization Tool for the Improvement of Radiofrequency Ablation Efficacy

Jury:

President of the Jury

Mohd. Razif Idris, Professor, Universiti Kuala Lumpur

Directors of the thesis

Olivier Meste, Professor, Laboratoire I3S/Université Côte d'Azur

Kushsairy Kadir, Associate Professor, Universiti Kuala Lumpur

Reviewers

Leif Sörnmo, Professor, Lund University

Raveendran Paramesran, Professor, Universiti Malaya

Examiners

Azmi Hassan, Professor, Universiti Kuala Lumpur

Asadullah Shah Syed, Professor, International Islamic University Malaysia

Norliza Mohd. Noor, Associate Professor, Universiti Teknologi Malaysia

For this little boy 

, and his beautiful mother.

Untuk Mak dan Ayah.

Acknowledgment

I would like to express my thanks to, first of all, Syafiq Kamarul Azman, my brother, for having submitted my documents for registration at Universiti Kuala Lumpur. Without his help, the events leading up to the production of this manuscript will probably never happen. And also, I promised to put his name first in this section. Thanks mate.

I express the highest of thanks to my supervisors, Prof. Olivier Meste, and Assoc. Prof. Kushsairy Kadir, for their guidance and advice throughout the formation. It has been a long journey with challenges from start to finish, but it was worth it.

I also thank Prof. Dr. Decebal Gabriel Laţcu, Prof. Dr. Nadir Saoudi, Dr. Sok-Sithikun Bun and the Cardiology Department of Centre Hospitalier Princesse Grace for having welcomed me warmly every time I visited. Their assistance was crucial to this research, and without their help the data collection process and result interpretation would have been difficult indeed. Also, I thank Dr. Ahmed Mostfa Wedn from Cairo University, who–at the time of data collection–was an attaché to the Centre Hospitalier.

I thank many friends who've helped lodge me when I was looking for PhD opportunities in Nice (Hariz, Din, Ikhwan, Asree), families who supported my struggles, and colleagues (Dien Hoa and Pedro Marinho) who never ceased to make my journey cheerful.

Table of Contents

List of Tables

List of Figures

List of Abbreviations

2D	2-Dimensional
3D	3-Dimensional
AA	Atrial Activity
Acc	Accuracy
AF	Atrial Fibrillation
AFL	Atrial Flutter
AP	Action Potential
ATP	Adenosine Triphosphate
AV	Atrioventricular
BSPM	Body Surface Potential Map
CCW	Counterclockwise
CV	Cross-Validation
CVD	Cardiovascular Disease
CS	Cuckoo Search
CSin	Coronary Sinus
CT	Crista Terminalis
CTI	Cavotricuspid Isthmus
CW	Clockwise
ECG	Electrocardiogram
EPS	Electrophysiologic Study
FO	Fossa Ovalis
GA	Genetic Algorithm
GLRT	Generalized Likelihood Ratio Test
IDT	Inverse Dower Transform
IVC	Inferior Vena Cava
L1GD	L_1 Gradient Descent
LAD	Least Absolute Deviation
LAO	Left Anterior Oblique

LIPV	Left Inferior Pulmonary Vein
LDA	Linear Discriminant Analysis
LOG	Logistic Regression
LOO	Leave-One-Out
LOOCV	Leave-One-Out Cross-Validation
LS	Least Squares
LSPV	Left Superior Pulmonary Vein
MLE	Maximum Likelihood Estimation
NSR	Normal Sinus Rhythm
PDF	Probability Density Function
PSO	Particle Swarm Optimization
RIPV	Right Inferior Pulmonary Vein
ROC	Receiver Operating Characteristic
RP	Recurrence Plot
RQA	Recurrence Quantification Analysis
RSPV	Right Superior Pulmonary Vein
SA	Sinoatrial
Se	Sensitivity
SNR	Signal-to-Noise Ratio
Sp	Specificity
SVC	Superior Vena Cava
SVD	Singular Value Decomposition
SVM	Support Vector Machine
URP	Unthresholded Recurrence Plot
VA	Ventricular Activity
VCG	Vectorcardiogram

Abstract

The prevalence of atrial flutter (AFL) is predicted to increase in the future. The pathology involves a rotating circuit in the atrium due to defective activation propagation. Radiofrequency catheter ablation is one of the most preferred treatment for its efficiency, but has low procedural efficacy due to necessity of crucial pre-operative information on AFL, for example the localization of AFL circuit (right or left atrium). This thesis shows how to localize AFL circuits using variability extracted from the ECG via a beat-to-beat approach. F waves are detected and segmented using generalized likelihood ratio test detectors that adapt to challenging conditions (wave overlaps, non-Gaussian noise, non-stationarity) by parametrization of the ratio. The best detector has satisfactory performance as tested with a dataset of more than 2900 F waves (cross-validated Acc = 0.93, $(\mathrm{Se}, \mathrm{Sp}) = (0.90, 0.93)$). 12-lead F waves are transformed into 3D vectorcardiographic loops using the Inverse Dower Transform. F loops are characterized by orientation and geometry parameters, with improvements in parameter estimation to correct for artificial variability from singular value decomposition. Parameter variability was quantified using higher-order statistics and serve as classification features. Linear classifier techniques were used to achieve good localization performance using a dataset of 56 recordings (31 right AFL, 25 left AFL; 100% training, best Acc = 0.93; cross-validated Acc = 0.88): better than the reference (same dataset; 100% training, best Acc = 0.63). Extracted relevant features show that variability in right and left AFL is different. However, it is posited that respiration combined with different anatomical location of the right and left atrium inside the chest is a possible confounding source of variability that allowed right-or-left localization. This matter was investigated by correcting respiratory motion from F waves and assessing change in variability. Improvement in motion parameter estimates was made to obtain physiologically-correct values. It was found that respiratory motion was not the source of discriminatory variability, and it was most likely produced by AFL circuits. Spatiotemporal variability of AFL was also explored using recurrence quantification analysis, and permits an insight to the pathology.

---

keywords: arrhythmia, atrial flutter, non-invasive localization, signal processing, detection theory, machine learning

Abstrak

Penyebaran debar atrium (DA) dijangka meningkat pada masa akan datang. DA melibatkan litar pengaktifan berpusing didalam atrium akibat kecacatan mekanisma penyebaran dedenyut. Ablasi kateter radiofrekuensi adalah rawatan pilihan yang berkesan, namun tidak cekap kerana memerlukan maklumat tentang DA pra-prosedur, seperti keletakan litar (atrium kanan atau kiri). Tesis ini menunjukkan bagaimana penyetempatan litar DA dilakukan dengan pendekatan denyut-ke-denyut bagi memperoleh maklumat tentang kestabilan litar dari EKG. Gelombang debar (GD) diperoleh dari EKG melalui ujian nisbah kebarangkalian umum yang mengambil kira penindihan gelombang, hingar bukan Gaussian dan ketidakstabilan. Pengesan terbaik menunjukkan prestasi memuaskan apabila diuji dengan set data mengandungi lebih dari 2900 GD (Acc = 0.93, (Se, Sp) = (0.90, 0.93) setelah pengesahan rentas). GD 12-saluran diubah menjadi gelung vektorkardiogram 3D menggunakan Transformasi Songsang Dower. Gelung D disifatkan dengan parameter orientasi dan geometri, dengan penambahbaikan dalam penganggaran nilai parameter untuk membetulkan keragaman palsu yang terhasil dari penguraian nilai singular. Kestabilan gelung ditaksir dengan statistik aras tinggi yang digunakan sebagai ciri untuk pengkelasan. Teknik pengklasifikasian linear digunakan untuk mencapai prestasi penyetempatan yang bagus pada 56 set rakaman (31 DA kanan, 25 DA kiri; 100% latihan, prestasi terbaik Acc = 0.93; setelah pengesahan rentas Acc = 0.88): lebih bagus dari metod rujukan (set data yang sama; 100% latihan, prestasi terbaik Acc = 0.63). Ciri-ciri berkesan terpilih menunjukkan bahawa DA kanan dan kiri mempunyai kestabilan litar yang berbeza. Walaubagaimanapun, pernafasan dan perbezaan lokasi atrium kanan dan kiri dalam dada dijangka menjadi penyebab perbezaan kestabilan litar. Perkara ini disiasat dengan menyingkirkan pergerakan pernafasan dari gelung D dan menilai perubahan dalam kestabilan litar. Penambahbaikan kepada metod penganggaran pergerakan dibuat untuk mendapatkan nilai yang munasabah. Penilaian menunjukkan bahawa gerakan pernafasan bukanlah sumber perbezaan kestabilan litar: kemungkinan besar ia terhasil oleh litar DA sendiri. Variasi spatiotemporal DA juga diterokai menggunakan teknik analisa pengulangan kuantitatif dan membuka sebuah sudutpandang terhadap DA.

---

kata kunci: aritmia, debar atrium, penyetempatan tak invasif, pemprosesan isyarat, teori pengesanan, pembelajaran mesin

Résumé de Thèse

La prévalence du flutter auriculaire (FLA) va augmenter dans le futur. La pathologie consiste en un circuit tournant dans l'oreillette à cause des défaits de conduction. L'ablation cathéter radiofréquence est l'un des traîtements effectifs, mais de basse efficacité dû à la nécessité aux informations sur le FLA avant la procédure, telle que la localisation du circuit (oreillette droite ou gauche). Cette thèse illustre comment localiser les circuits FLA avec la variabilité contenue dans l'ECG par une analyse battement-par-battement. Les ondes F sont détectées et segmentées à l'aide du test du rapport de vraisemblance generalisé qui s'adapte à la superposition de l'onde, au bruit non-Gaussien et aux non-stationarités, avec la meilleure performance sur une base de plus de 2900 ondes F très satisfaisante (Acc = 0.93, $(\mathrm{Se}, \mathrm{Sp}) = (0.90, 0.93)$ après validation croisée). Les ondes F 12-voies sont transformées en boucles vectorcardiographiques 3D par la transformée inverse de Dower. Les boucles F sont caractérisées par des paramètres d'orientation et de géométrie, avec amélioration dans l'estimation pour corriger la variabilité artificielle dû à la décomposition en valeurs singuliers. Des statistiques d'ordre supérieur quantifient la variabilité, et servent comme des features de classification. Des classificateurs linéaires ont été utilisés pour la localisation avec une bonne performance sur une base de 56 enregistrements (31 FLA droite, 25 FLA gauche ; 100% entraînement, meilleure Acc = 0.93 ; après validation croisée Acc = 0.88), ce qui est meilleure que la référence (même base de données ; 100% entraînement, meilleure Acc = 0.63). Les features pertinents montrent que les FLA droites et gauches presentent une variabilité différente. Cependant, il est supposé que la respiration avec le placement anatomique des oreillettes dans la poitrine constitue une source confondante de variabilité qui a permis la localisation. Cette hypothèse à été testée en corrigeant l'effet de la respiration et en analysant le changement de variabilité. Une amélioration de la méthode classique de l'estimation du mouvement respiratoire a été faite. Il a été montré que la respiration n'est pas la source de variabilité discriminante : elle provienne plus probablement du circuit FLA. La variabilité spatiotemporelle du FLA a aussi été exploré avec une méthode d'analyse quantitatif de récurrence, permettant une compréhension sur le FLA depuis des indices non-cliniques.

---

mots clés: arythmie, flutter auriculaire, localisation non-invasive, traitement du signal, théorie de détection, apprentissage

Chapter 1

Introduction

1.1 Introduction

Over the years, the society has learned how to diagnose many kinds of disease through thorough research and study. Our focus will be on the diseases of the heart (cardiopathy). Arguably the greatest invention in the history of cardiac medicine is the electrocardiograph, back in 1908. This machine has helped not only the diagnosis of many different heart diseases, but also allowed understanding of the functionality of the heart as a bioelectric device.

Progress in electrocardiography allowed us to discover atrial flutter (AFL), a disease belonging to the subclass of cardiopathy called cardiac arrhythmia. It affects the top compartment of the heart (the atrium), and consists of a quasi-periodic activation of this compartment, due to an abnormal circular depolarization. Further works over the years by researchers around the world has now led to a detailed understanding of its mechanism, its effects and, most importantly, its therapeutic countermeasures.

Evidenced by an impressively high success rate (in excess of 90%), radiofrequency catheter ablation has become a 'treatment of choice' for elected patients suffering from AFL, with a low rate of recurrence (below 10%). Its procedures are well-defined and now commonly adopted in hospitals around the world. In catheter ablation, a catheter is inserted into the heart via the blood vessel from a cut on the skin at a defined area. The objective of ablation is to (1) locate a critical point in the abnormal circuit, and (2) ablate it by heating it with high radiofrequency energy.

However, up to date, the challenge on using such technique lies in identifying AFL characteristics. Localizing circuits take up a majority of the time, compared to the ablation (usually >4 hours total time spent on localization vs. <15 minutes spent on ablation). One aspect of localization on which this work focuses is in the determination of the AFL chamber of origin (left or right atrium). This particular information is important to determine early on because it conditions the procedural cost (extra time and equipment) and difficulty (different procedure strategies).

1.2 Problem Statement

New technology has allowed the use of advanced electroanatomic mapping techniques, but these must be performed in an invasive setting i.e. during ablation operation, which defeats the purpose of pre-procedural localization. Non-invasive tools for AFL localization–much to the author's surprise–are not well-researched.

The most utilized tool for AFL localization is visual inspection by the clinicians. Despite this simplistic approach, it has shown great performance in determination of AFL localization. It has been discussed that the ECG presents stereotypical patterns strongly associated with a typical form of AFL (which is exclusively in the right atrium), whilst abnormal patterns can be associated with either right or left AFL. However, this is good when AFL exists as the sole cardiopathy: this is unfortunately not always true, and many case reports attest to this in the literature.

Studies in the field of biomedical engineering showed that it is possible to leverage the information contained within the electrocardiogram (ECG) in order to reliably predict therapy success, extract characteristics of certain pathologies and understand diseases from a different, non-clinical viewpoint. The common ground for these studies are the use of advanced signal processing techniques.

Medical findings as well as previous research on AFL do suggest different variability between right or left AFL. By using an appropriate approach, this variability can be extracted and used for classifying AFL localization. Thus, this thesis presents a novel approach in extracting variability from AFL ECG signals and using them to perform classification of right or left localization. Asides from that, many information could hopefully be obtained, and allow understanding of AFL with insights from non-clinical indices.

1.3 Research Objectives

The main objective of this research is to improve AFL ablation procedure efficacy, by introducing a pre-interventional decision-making tool. Given the nature of the problem at hand, which is right-or-left localization, binary classification methods fit well into this problem. As previously stated, localization should be performed in a non-invasive manner to be able to obtain significant efficacy gains. This implies in an implicit manner, that localization should be performed using non-invasive data. A few selection of data are available, but the one most pertinent to the problem is the ECG, which is the marker for electrical cardiac functionality.

Furthermore, it should also be noted that efficacy gain should also reflect optimized cost. Clinicians should be able to use such decision-making tool without e.g. the use of costly advanced equipment. This means that the tool should rely on standard clinical equipment readily available in the clinic. This means that the tool must rely on standard 12-lead ECG, which is the most common and readily available form of ECG available in the clinic. However, it is well known that the ECG captures not only the electrical activity of the heart, but also noise from many sources. Thus, a thorough processing chain must be developed to ensure proper extraction of information. This includes removing electrical as well as physiological sources of noise, and optimization of transform (in particular the Inverse Dower transform).

Robustness of the decision tools must be taken into account as well, to ensure that future samples may be localized as accurately as possible. However, the challenge in this research (as with most biomedical engineering research) is the small sample size of patients available for analysis, which does not help in building robustness. Therefore, machine learning techniques will be employed in order to combat this problem.

In addition to developing a classification algorithm for right-or-left localization, it is somewhat implied that both these classes are separable. The physiological understanding of AFL does suggest this separability, but it is also of interest to identify what kind of variables are different between these classes. Therefore, some of the work will pertain on capturing this (or these) discriminating variable(s).

To summarize, the list of research objectives are:

1. To develop a signal processing chain that properly extracts features from the 12-lead ECG
2. To develop a binary classifier using given dataset and features for localizing AFL circuits
3. To test the binary classifiers and obtain generalized performance scores
4. To extract relevant discriminating features from the list of features proposed
5. To obtain insights into AFL via non-clinical indices

1.4 Summary of Chapters

A summary of chapter contents is provided below. To render the reading experience more modular, necessary recalls will be made.

Chapter 2 provides a comprehensive basis of electrocardiophysiology in order to better understand the electrical functionality of the heart. From there, the basis of electrocardiography will be presented, considering aspects of acquisition as well as design of lead systems and its challenges. Clinical as well as electrophysiological aspects of cardiac arrhythmia and atrial flutter are also described. Finally, clinical therapies are detailed, with a particular attention to radiofrequency ablation therapy, in order to highlight the challenges of this procedure.

Chapter 3 presents a review of literature, that not only covers previous works related to atrial flutter, but also aims to further emphasize the difficulty in right-or-left localization. Prospective approaches that could be utilized to design a robust and novel classifier are discussed.

Chapter 4 is dedicated to detailing the methodological developments that were employed to achieve our goal. This includes novel methods for (i) wave detection based on statistical detection theory, (ii) wave correction for two prominent sources of distortion: respiratory motion and T wave overlap, and (iii) optimization of wave transformation. Two complementary characterization methods will be described: one focusing on a beat-to-beat approach applied to vectorcardiograms, and the other on a continuous-time recurrence quantification approach.

Chapter 5 consists of a summary of machine learning methodologies for classification, generalization of classifier performance and selection of relevant features, as well as its application on the processed dataset from Chapter 4.

Chapter 6 studies the effect of ECG distortion due to respiration, and employs methods from Chapter 4 to correct this distortion and boost classifier performance. Analysis of the results provides not only proof of increased performance, but also interesting physiological results.

Chapter 7 concludes on the items presented in this document. Perspectives are provided in this chapter, as well as a list of publications.

Chapter 2

Electrocardiophysiology and Arrhythmia

2.1 Introduction

In this chapter, a review of the pertinent literature is provided, dedicated to introducing the organ of study: the heart, as well as the basic concepts of electrophysiology and electrocardiology: the study of the heart's electrical activation, and how these bioelectric potentials are measured. In Section 2.2, a succinct description of the heart is provided, that aims to capture its structural and functional nature. Cardiac depolarization phenomenon and surface potential measurement techniques are discussed in Section 2.3. Finally, Section 2.4 provides a succinct description of arrhythmia, its mechanism and a description of AFL. Section 2.5 provides a brief description of catheter ablation.

The basis established in this chapter will be useful in understanding AFL as a pathology, but should also shed light onto how its electrocardiographic manifestation is produced, which will be of value in developing the methodologies for localization. Much of the material is referenced from the medical literature [5] as well as from the biomedical engineering literature [1].

2.2 Cardiac Anatomy and Physiology

The heart is one of the most critical organs found in essentially all living beings. Its size is roughly a little larger than an adult human fist, and is shaped like a cone (similar to a strawberry). Its primary role is to circulate blood by periodically creating a pressure gradient through pumping. This is done through the contraction of its muscular structure, triggered by periodic electrical activation. The circulation of blood allows the transport of oxygen, gases, ions and nutrients to the entire body.

The heart is located within the thoracic cavity: the space inside the chest. It is pointed at an angle, with the apex (tip of the heart) usually pointed towards the left and downwards. It is placed in between the two lungs that almost envelope it. Since it resides more towards the left, the left lung cavity (the left pleura) presents a notch that allows the heart to be accommodated. Towards the rear or posterior aspect of the heart, one can find the esophagus and vertebral column. Towards the lower or inferior aspect, one can find the diaphragm membrane. Figure 2.1 illustrates the heart within the thoracic

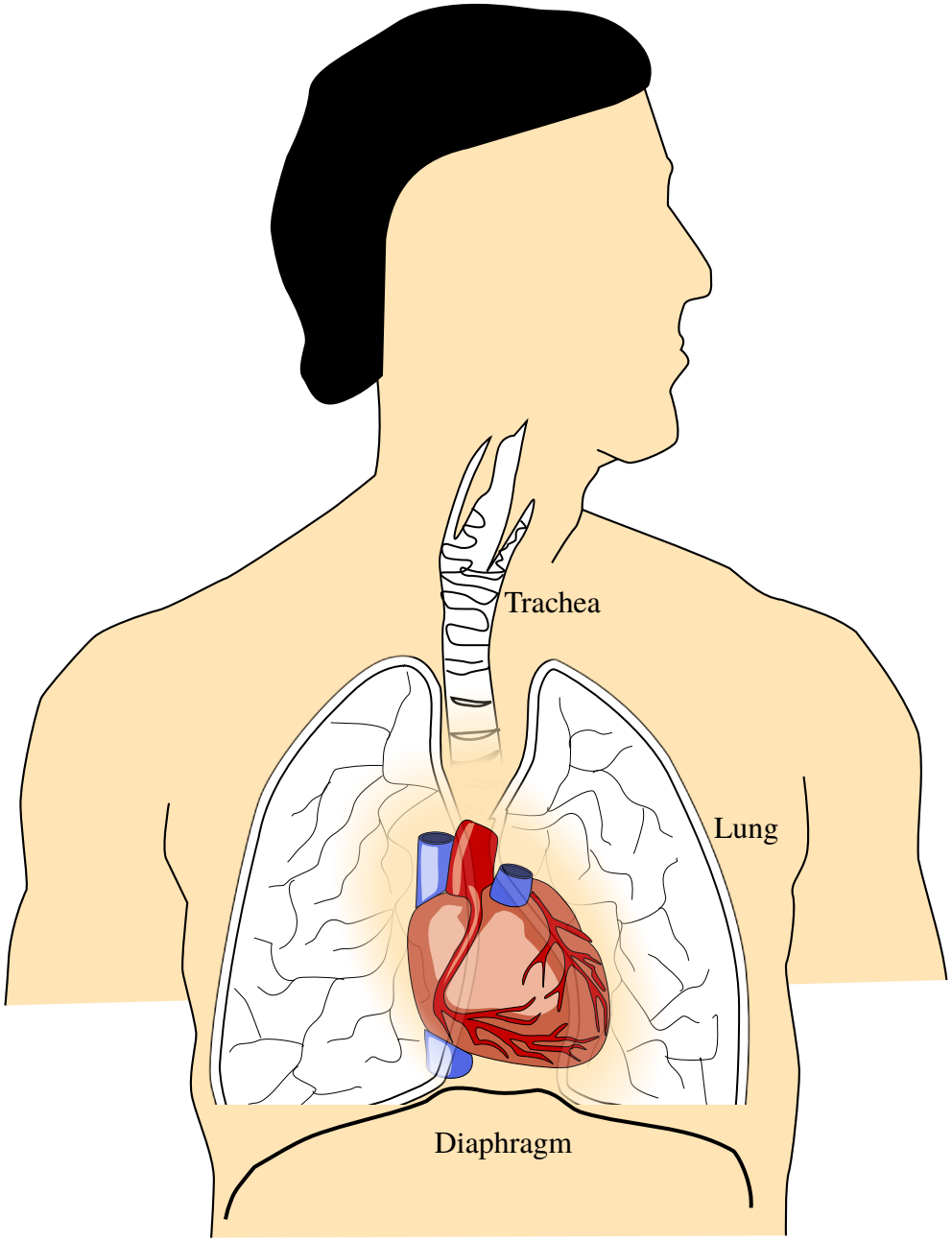

Figure 2.1: Illustration of heart location within the thorax.

cavity.

2.2.1 Muscular Structure

2.2.1.1 Heart Layers The heart is composed of several layers, as illustrated in Figure 2.2. The majority of its functional structure is contained within several initial sublayers of protective tissue known as the *pericardium*. They act as a stable container, and are anchored to other anatomical landmarks such as the ribcage, the vertebral

column and the diaphragm via loose connective tissues. This fixes the heart's location inside the cavity as well as its maximum volume, and helps it perform the pumping action.

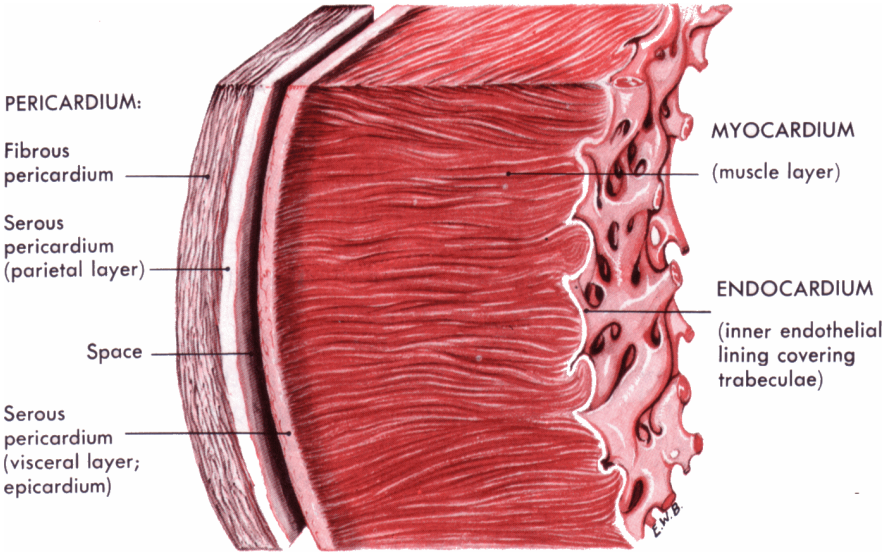

Figure 2.2: Illustration of heart layers [1].

The outer pericardial layer is fibrous in nature and continuous with the outer layers of the great blood vessels, whilst the inner layers are in the form of a serous double-layered sac. The parietal pericardium borders the fibrous pericardium, whilst the visceral pericardium borders the heart muscles, and is also termed the *epicardium*. Within the sac is pericardial fluid that acts as a lubricant and allows the heart to contract with minimal friction.

The *myocardium* is the term used to denote the middle and thickest layer of the heart. It is essentially an arrangement of fibre-like heart muscle cells called *cardiomyocytes* (or myocytes): a special type of muscle cell, which are attached to a fibrous structure called the cardiac skeleton. Cardiomyocytes are able to conduct electrical impulses thanks to a complex ion exchange system, and in addition, they respond to electrical stimuli by contracting. The skeleton provides support to the entire muscular structure in order to allow them to perform a contraction of the chambers.

The interior lining of the heart is termed the *endocardium*, and is made of smooth endothelial cells. The smoothness of the interior lining ensures good pumping efficiency, much similar to the smooth membrane of a diaphragm pump. On the other hand, there exists, especially in the bottom chambers, ridge-like features called *trabeculations*. This is useful during the relaxation phase of the heart (i.e. expanding after expulsion of

[1] http://stevegallik.org/sites/histologyolm.stevegallik.org/htmlpages/HOLM_Chapter09_Page02.html

blood), as it avoids the creation of a suction force that pulls blood backwards. Beneath this layer–referred to as the *subendocardium*–one can find veins and nerve endings of the impulse conduction system, as well as from the central nervous system.

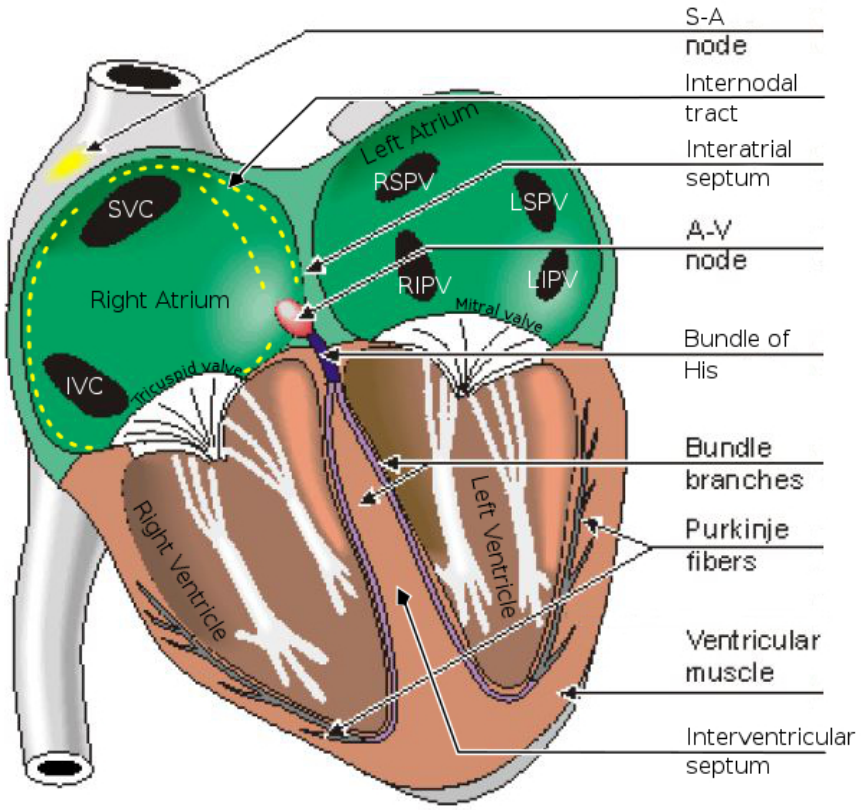

Figure 2.3: Illustration of heart chambers and structure. Edited from [1].

2.2.1.2 Heart Chambers The heart is divided into four chambers: the *right atrium* and *left atrium*, and the *right ventricle* and *left ventricle*. Figure 2.3 shows the general interior anatomy of the heart. The atria play a role of accumulating blood from various organs via the great vessels, whilst the ventricles are responsible for the distribution of blood via the aorta. The right atrium receives blood from the organs via the superior and inferior venae cavae (SVC and IVC), and the left atrium from the lungs via the right and left, superior and inferior pulmonary veins (RSPV, LSPV, RIPV, RSPV). The right ventricle distributes blood towards the lungs via the pulmonary artery, and the left ventricle towards the organs via the aorta.

Integral to the atrial structure and volume are *atrial appendages* (right and left). These are vestiges of the atria, located at the superior aspect of each atrium, that were functional during the early phases of heart development. Upon maturation, the appendages shrink and become non-functional. Despite that, they are not electrically inert and may

respond to electrical stimulus.

2.2.1.3 Borders of Heart Chambers Between the four chambers, there exists separation boundaries. Between right and left chambers, this boundary is in the form of a wall called the *septum*. It prevents oxygenated blood from mixing with deoxygenated blood. Between atria and ventricles, there are *atrioventricular orifices* (openings) regulated by *valves*: *tricuspid* (right side) and *mitral* (left side), that close during contraction and open outside of contraction. Valve leaflets are attached, on one end, to the cardiac skeleton, and on the other end to *papillary muscles* located inside the ventricles. During ventricular contraction, these muscles pull the leaflets close, and prevent blood from flowing in the reverse direction (i.e. back to the atria).

The *interatrial septum* is a two-layer wall, with each layer having a circular hole. In a mature heart, the hole centers are not aligned, hence the wall is opaque. The rim of the left septum is visible from the right atrium and forms a sort of flap (the *fossa ovalis*, FO) that remains closed due to interatrial pressure difference. During maturation however, the holes are slightly aligned such that a shunt (the *foramen ovale*) is realized from the right to left atrium. This is crucial for the fetal circulation as the lung is non-operational and oxygen supply comes from the mother, delivered straight into the right atrium. The *interventricular septum* is different: a large portion of the septum is a single thick wall. A small upper portion of it is in fact continuous with the interatrial septum, and is membraneous instead of muscular.

2.2.2 Impulse Conduction System and Innervation An equally important structure of the heart is the impulse conduction system that generates and distributes electrical activation around the heart structure. This system is made up of several special cardiac *pacemaker cells*, with a slightly different activation mechanism than normal cardiomyocytes. The outline of the system can be seen in Figure 2.3.

Normal myocytes do not trigger any electrical activation without itself being first activated. It sits at a resting state and awaits a stimulus. However pacemaker cells undergo spontaneous self-activation–usually referred to as *self-depolarization* or *automaticity*. Regions of the myocardium containing these cells are the ones responsible for generating periodic stimuli that drive the heart at a defined rate. Several notable ones are those between the CT and the superior vena cava: the *sinoatrial node* (SA node), and those nearby the coronary sinus orifice: the *atrioventricular node* (AV node). The SA node has an intrinsic self-depolarization rate of about 70 bpm (beats per minute) or roughly 1 activation every 860 ms, and the AV node has a slower rate of about 50 bpm.

Special rapid-conducting system of fibers can be found in the right atrial subendocardium, as well as within the ventricular septum and walls. These fibers are responsible for the fast conduction and distribution of electrical activation across the whole atrial and ventricular structure respectively. Fiber pathways from the SA node to the AV node are called *internodal tracts*. A branch of this tract splits at the superior level of the interatrial septum and continues toward the left atrium via the Bachmann's bundle.

Protruding from the AV node towards the apex of the heart is the thick fiber *bundle of His*. Traveling inside the septum, it then splits into two large bundles: the *right and left bundle branches*, each protruding their respective ventricles. A large trabeculation called the *moderator band* protrudes from the ventricular septum towards the lateral wall of the right ventricle, and carries a branch of the right bundle along with it. The bundle branches terminate into *Purkinje fibers* that distribute the impulse at the subendocardial level of the ventricles. These fibers also undergo spontaneous depolarization, but at a much slower rate than the SA or AV node (15-30 bpm). This ensures that in the case of AV node dysfunction, the ventricles can still be activated.

2.3 Generation and Measure of Cardiac Potential

To understand how the electrocardiogram (ECG) is generated and its measure possible, it is necessary to detail how the cardiac electric potential is generated from the collection of cardiomyocytes, and how it is affected by the organic mass present in the thorax. This is a subject particular to the study of bioelectrical volume source and volume conduction theory, and accounts for the fact that the source(s) and sink(s) of the bioelectric potential are not a single element with singular point-like properties, but a 3D volume with properties that are distributed across the volume.

2.3.1 Impulse Generation When a myocyte is presented with a *depolarizing stimulus*: a change in electrical potential such that the *transmembrane voltage* (voltage between the inside and outside of a cardiomyocyte) becomes less negative, gated ion channels become open and allow ions to flow into the cell. This process occurs in 5 phases:

Phase 0 *Rapid depolarization*: The stimulus raises the cellular transmembrane voltage above -70 mV. Rapid opening and inactivation of fast sodium channels is observed during this phase. The whole process takes a very short time ($\sim$ 1 ms).

Phase 1 *Slight repolarization*: Calcium and potassium ions are progressively taken

in and egressed respectively. Potassium outflow is slightly larger, resulting in a gradual decrease of the transmembrane potential V_m. This continues until the voltage reaches about 0 mV.

Phase 2 *Plateau*: Outward potassium flow is balanced by inward calcium flow, resulting in zero net transmembrane voltage for a prolonged period of time. Small amounts of calcium flowing into the cell trigger more release of calcium from inside the cell.

Phase 3 *Rapid repolarization*: Calcium channels begin to deactivate. Remaining ions of extracellular origins are removed via ion transporters and exchangers. Outflow of potassium continue until the transmembrane voltage returns to -90 mV. Sodium channels reactivate at around -60 mV, but is closed due to the negative transmembrane voltage.

Phase 4 *Rest*: The cell remains idle and awaits another stimulus.

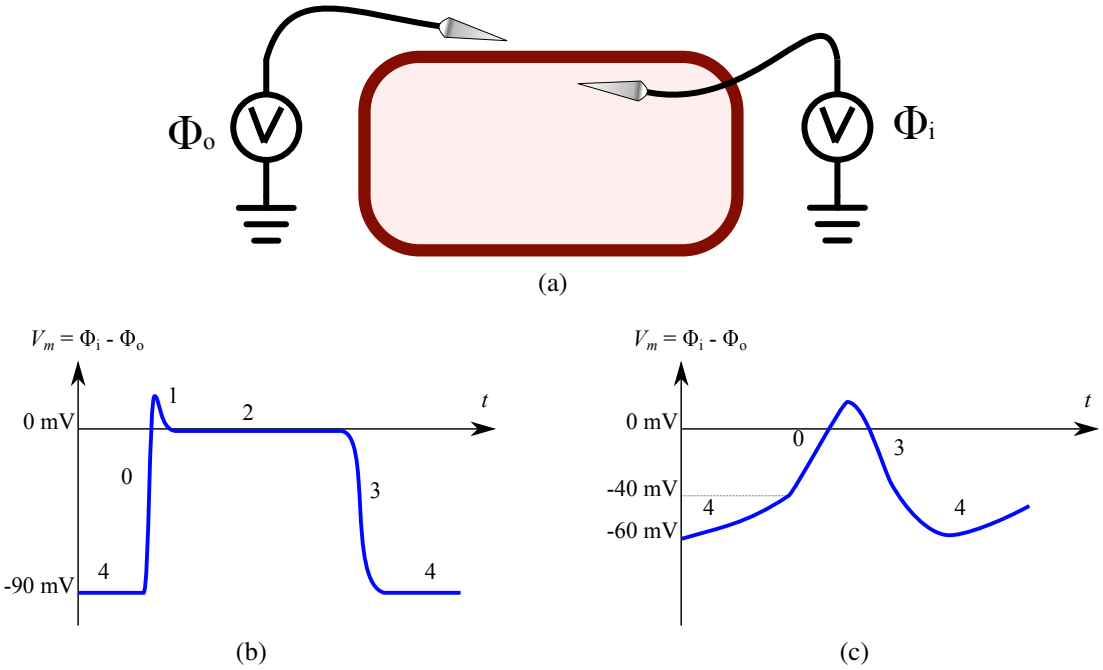

Figure 2.4: Measure of action potential: (a) Ideal picture of single-cell AP measure using needle electrodes; (b) and (c) AP profile for normal cardiomyocytes and pacemaker cells respectively.

The transmembrane voltage V_m can be measured using needle electrodes, as shown in Figure 2.4(a), and evolves during the 5 phases. When plotted against time gives the voltage profile of the cell, commonly termed the *action potential* (AP), shown in Figure 2.4(b). It is worthy to note that during Phase 2 (plateau) some important ion

channels remain closed to prevent early activation of the cell by unwanted stimulus. This makes the cell functionally inert to electrical activation: a property called *refractoriness*. The duration starting from the start of Phase 0 to the start of Phase 3 is termed the *refractory period*.

Pacemaker cells have a different depolarization profile than normal cardiac cells due to a more elevated resting potential (transmembrane voltage > -90 mV). This leads to a slow influx of sodium during phase 4, and as a consequence the transmembrane voltage is not steady, but has an upward slope. Mass depolarization occurs at a transmembrane voltage of about -40 mV. Depolarization relies only on calcium, thus phase 0 has a less steeper spike. Phases 1 and 2 do not occur in these cells. Figure 2.4(c) illustrates the AP profile of pacemaker cells.

2.3.1.1 Cardiac Activation Sequence The activation impulse is normally initiated by the SA node thanks to its automaticity. The activation travels along the internodal tract and depolarizes the right atrial musculature along the way. A part of the impulse is directed towards the left atrium via the Bachmann's bundle and causes left atrial depolarization. Both events happen in a very short time (<100 ms). At the level of the coronary sinus, the impulse activates the AV node. There is a remarkable delay lasting from 20 to 100 ms before the impulse is conducted through to the bundle of His and consequently to the bundle branches. This delay, due to the slow conduction speed in the AV node, allows sufficient time for blood from the atrium to pool inside the ventricles. Several branches of the bundle activate the papillary muscles which pull the valves close before the impulse finally activates the bulk of the ventricular musculature via Purkinjian fibers. Past this event, the heart contracts to expulse blood into the respective arteries. This stage of the activation sequence is commonly termed the *systole*. A brief period of inactivity can be observed due to refractoriness of the ventricular myocytes. The heart then proceeds to relax and expand: a stage called the *diastole*. The cycle repeats as long as the SA node generates an impulse. This is the normal cardiac activation sequence, and is commonly termed *normal sinus rhythm* (NSR).

2.3.2 Equivalent Cellular and Cardiac Dipole A depolarizing stimulus travels along the myocyte due to low resistance in the direction parallel to the cell (a property called *anisotropic conduction*). The traveling stimulus, commonly referred to as the *activation wavefront* causes a certain region of the cell to become positively charged, hence the cell develops a certain polarity. This is illustrated in Figure 2.5. The region of depolarization (generally a very thin layer of roughly 1 mm) can be modeled as a

bipolar layer termed the *double layer*. The cell then behaves as a double layer source or a cellular *dipole source*.

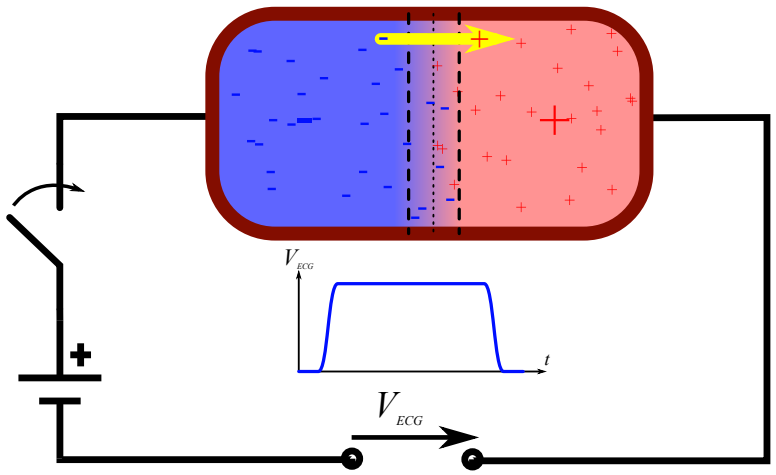

Figure 2.5: Hypothetical setup and measure of a single-cell double-layer field potential. The depolarization zone is contained within the two dashed lines. The dotted line in between indicates the surface of neutral charge.

In repolarization, the polarity of the double layer is essentially the inverse of depolarization because the wavefront moves in the reverse direction, hence for a fixed point of measure, repolarization produces a deflection in the inverse polarity than that of depolarization. Also of note, the repolarization region is generally larger than the depolarization region (reaching up to 100 mm).

In the light of the double layer source model, and the fact that the heart functions as a synchronous syncytium, the cardiac activation wavefront is commonly modeled as the superposition of all cellular dipoles. Cardiac activation then can be equated to a dipole source whose strength and direction results from the vector addition of the many (thousand) cellular dipoles, and varies with the cardiac activation sequence. This dipole is usually termed the *cardiac dipole*. Figure 2.6 illustrates the cardiac dipole viewed from the front of the body.

2.3.3 Lead Vectors and Image Space The simultaneous and progressive activation of cardiac fiber bundles generates an electric field whose potential can be measured using electrodes attached to the surface of the skin. Given the depolarization sequence, mass of fibers being activated and fiber orientation, the strength of the potential varies in time and may manifest greatly or poorly in one electrode. This variation in cardiac electric potential is the core interest of electrocardiography and has served as a significant tool for clinical diagnosis of cardiac pathologies since the beginning of the 20th century.

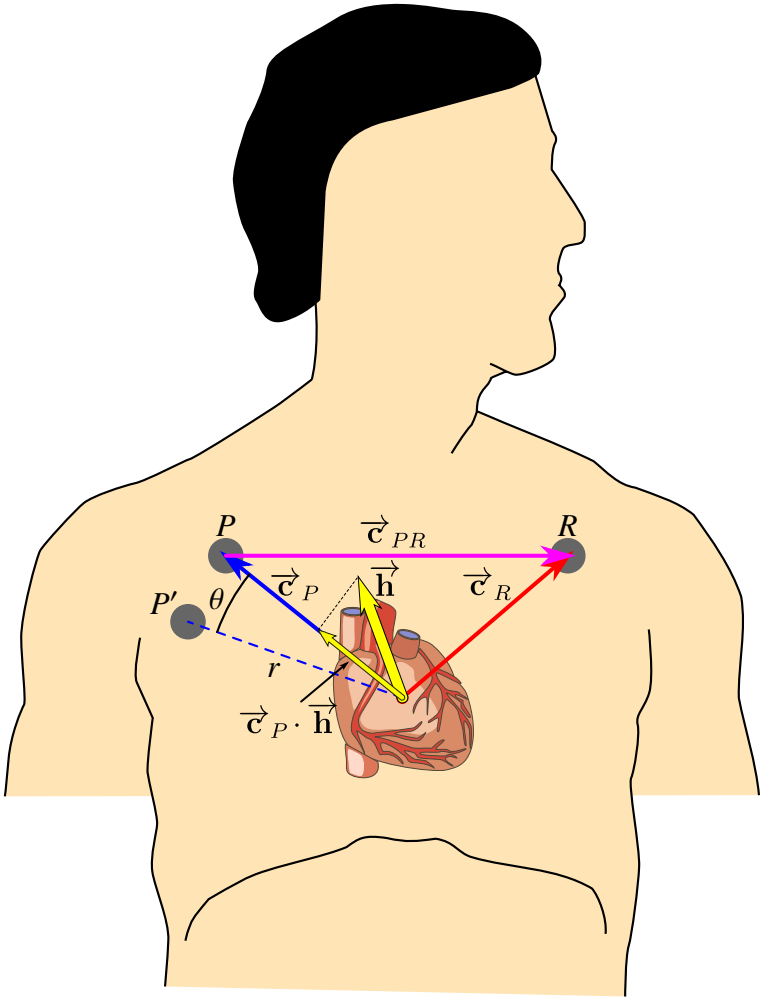

Figure 2.6: Illustration of the cardiac dipole and lead vectors.

Assume a point P located at a remote point from the resting heart (see Figure 2.6). An electrical field potential Φ_P can be observed at this point. Depending on the direction of the cardiac dipole with respect to P, the polarity of the observed voltage or *deflection* may be positive (if the dipole points toward P) or negative (if away from P). Assuming now that the origin is fixed to the dipole source origin, then if a point P' was located away from the dipole direction, then the amplitude drops by a factor related to the angle θ between the dipole direction and P', as well as the distance r of the point from the dipole origin.

The dipole source model allows a simple visualization of the cardiac activation as a fixed vector with varying orientation and length in time. This in turn allows a quite simple relation of the cardiac dipole with the electric potential at an arbitrary point. A particular application of this representation is when the point is situated at the boundary of a volume conductor (e.g. on the body surface). This is essentially the objective of electrocardiography.

Throughout this section, it is assumed that the point P has an associated vector $\overrightarrow{\mathbf{c}}_P$ in 3D space originating from a reference whose location is not currently specified. The length of the vector represents the potential observed at P when a 'unit activation' (i.e. dipole length of 1) is present at the cardiac dipole origin Q and points towards P, and is commonly known as the *lead vector*. The total electric potential Φ_P measured at this point in presence of cardiac activation is equivalent to the dot product of $\overrightarrow{\mathbf{c}}_P$ and the cardiac dipole $\overrightarrow{\mathbf{h}}$ ($\Phi_P = \overrightarrow{\mathbf{c}}_P \cdot \overrightarrow{\mathbf{h}}$).

Through application of vector algebra, it is easy to see that the voltage $V_{PR} = \Phi_R - \Phi_P$ between two points P and R can also be written as the dot product of a combined lead vector $\overrightarrow{\mathbf{c}}_{PR} = \overrightarrow{\mathbf{c}}_R - \overrightarrow{\mathbf{c}}_P$ and the cardiac dipole. The only difference is that each individual lead vectors were obtained from potential measures with respect to a reference, whereas $\overrightarrow{\mathbf{c}}_{PR}$ is the lead vector was obtained with respect to the two points.

In practice, the reference is a remote point far away from the source, where the electric potential due to it is zero. The measured potential at an arbitrary point P will then be considered a true point-measure of electric potential, and the associated lead vectors are termed *unipolar lead vectors*. Lead vectors resulting from the combination of unipolar leads are termed *bipolar lead vectors*.

An interesting observation can be made by noting that if one were to obtain the electric field potential of all points on the body surface considering a unit dipole source pointing to each point, it would be possible to obtain a surface directed normally by all possible lead vectors. This surface is known as the *image surface* [6]. An ideal example of image surface is shown in Figure 2.7 for the 12-lead ECG, assuming a spherical homogeneous conductor.

It is worth noting that the strength of the dipole source is inversely proportional to the conductance of the surrounding volume. Decreasing the conductance between the observation point and the volume source will reduce the lead vector strength: essentially scaling the lead vector length. In practical electrocardiography, this amounts to adding a resistor in series with the electrode to simulate a decrease in conductance. Through application of trigonometry, points inside and outside of the image surface can be reached. This is a practical application to the image surface, and allows the *synthesis of lead vectors* corresponding to (usually bipolar) measures of potential between points that do not physically map to the body surface.

2.3.4 12-Lead Electrocardiogram The standard 12-lead ECG is the de facto representation of clinical surface ECG recordings, following the standardization efforts of several clinical institutions over the years [7, 8]. The idealized model of the 12-lead

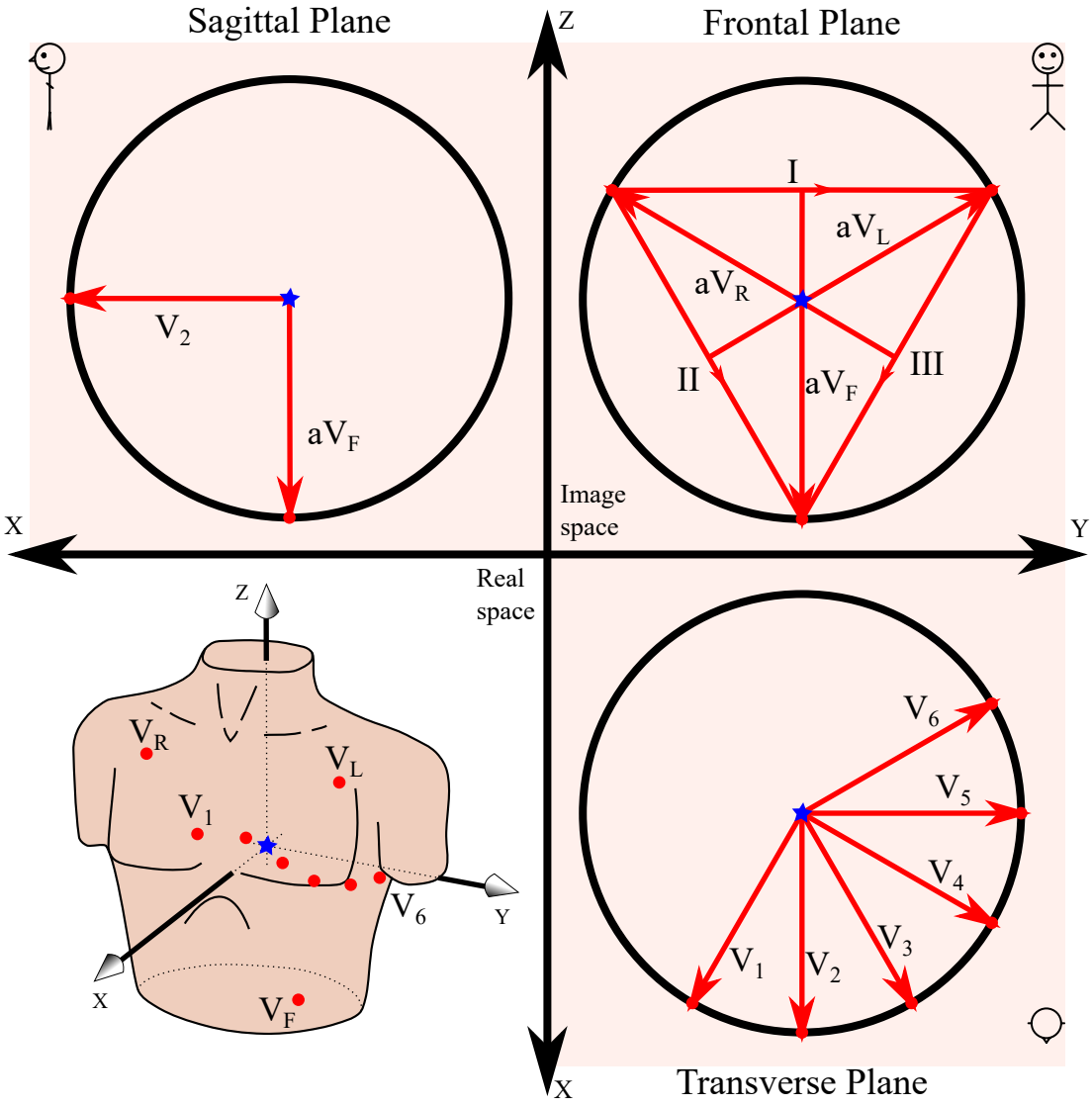

Figure 2.7: 12-lead ECG electrode placement on the torso (red dots), as well as an ideal representation of each associated lead vectors and the ideal image space. The blue star indicates Wilson's central terminal. The equilateral triangle in the frontal plane is known as the Einthoven triangle.

ECG can be shown to capture cardiac electrical activity at regularly spaced intervals over the whole heart geometry, despite only having leads that are mostly located on the front of the body. The schematic view of electrode placements is shown in Figure 2.7. Note that a reference electrode is required for voltage measure: this is usually placed at the right leg. Geometrically, it seems to the be the furthest limb from the heart.

The 12 leads of the standard ECG can be grouped into two: *limb leads* I, II, III, aV_R, aV_L and aV_F, and *precordial leads* V_1, V_2, V_3, V_4, V_5 and V_6. Leads **I**, **II** and **III**, called Einthoven leads, are obtained from 3 electrodes V_R, V_L and V_F placed on the torso. These leads are termed *bipolar leads* because they measure potentials between two points that are not located at 'infinity' where the electric field potential due to the cardiac activation is zero. In an idealized view, these 3 leads form the *Einthoven triangle*, as can be seen in Figure 2.7.

In order to perform a true point-measure of the electric potential, the measure must be made with respect to a reference located at 'infinity'. This reference can be constructed by connecting all 3 limb electrodes to a common point with a resistor. This point is commonly referred to as the Wilson central terminal [9]. By some omission of resistors, it is possible to construct the leads $\mathbf{aV_R}$, $\mathbf{aV_L}$ and $\mathbf{aV_F}$, called the augmented Goldberger leads. Because they are measured with respect to a point at 'infinity', they are termed *unipolar leads*.

To better observe the activity of the ventricles, the precordial leads $\mathbf{V_1}$, $\mathbf{V_2}$, $\mathbf{V_3}$, $\mathbf{V_4}$, $\mathbf{V_5}$ and $\mathbf{V_6}$ were introduced. These unipolar leads correspond to electrodes that observe the ventricles in the transverse axis.

In an ideal geometric view, the 12 leads spans the 3D space with vectors arranged in 60° intervals, as shown in Figure 2.7. From here, only 3 leads would be sufficient to describe the whole possible cardiac dipole configuration (possibly V_1 or V_2 as X, V_6 or I as Y, and aV_F as Z). But due to their proximity to the heart, the precordial leads are able to pick up other non-dipolar sources, and hence contain slightly more information than only that of the cardiac dipole. Limb leads are redundant since the same 3 points were used to derive the 6 leads, thus in theory only any 2 leads are truly independent. Thus, the ECG is regarded as containing only 8 independent leads, and 4 redundant leads. However in the clinic, all 12 leads are used.

2.3.5 Standard ECG Nomenclature Einthoven described the names of the different standard deflections observed on the ECG [10]. These have been found to be linked to the cardiac activation sequence, and so have become markers for non-invasive analysis

[2]https://en.wikipedia.org/wiki/Electrocardiography#/media/File:SinusRhythmLabels.svg

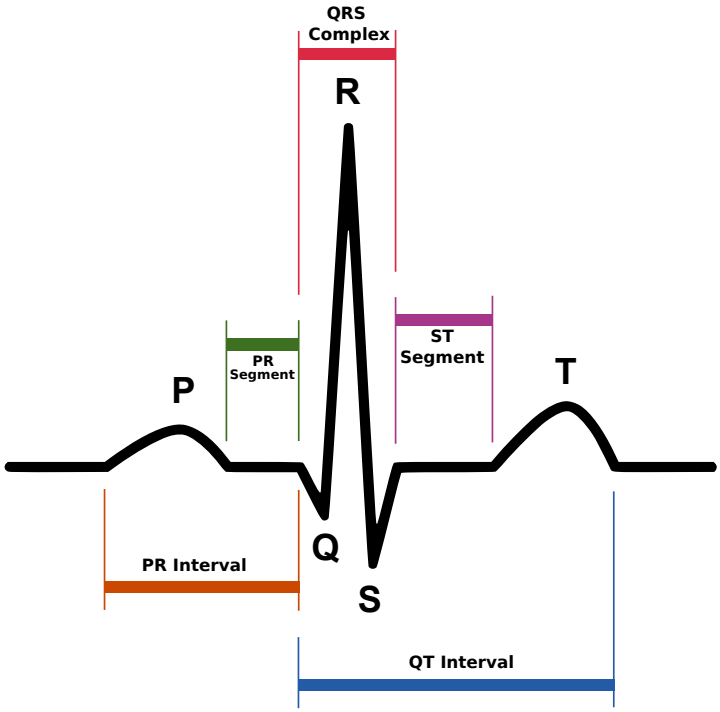

Figure 2.8: Standard ECG deflections and timings [2].

of cardiac activation. In particular, the following are most common:

P A (generally) low-amplitude deflection (< 500 µV) lasting about 250 ms, related to the activation of both atria. The deflection polarity can be positive (+) or negative (-)

Q A low-amplitude and very brief - deflection, related to the start of activation of the ventricles

R A large-amplitude + and relatively long-duration deflection (up to +1 mV), related to the mass activation of ventricular muscles

S A - deflection following R, related to the final stages of ventricular activation

T A large and generally long deflection related to the repolarization of the ventricles

Q, R and S waves are not commonly discussed as separate entities, but rather as a combination of successive events called the *QRS complex*. Between the T and P deflection or *waves*, there is no cardiac activation. This temporal region is usually termed the *isoelectric period*. The *isoelectric baseline*: the voltage during this period should theoretically be zero, but in practice fluctuations may be observed due to various reasons (respiration, body or electrode motion, etc.).

Several temporal landmarks can be described, and relate to the cardiac activation with equal importance as the waves. These are:

PR interval The duration beginning at the onset of the P wave until the onset of the Q wave, related to the duration of activation and repolarization of the atrium (generally between 120 to 200 ms)

PR segment The duration beginning at the end of the P wave until the onset of the Q wave, related to the conduction delay between atrial and ventricular activation

QT interval The duration beginning at the onset of the Q wave until the end of the T wave, related to the duration of activation and repolarization of the ventricle (roughly half the RR interval in NSR)

ST segment The relatively short time interval between the end of the S wave and the onset of the T wave. This period should present an isoelectric baseline, but may change in presence of heart disease

RR interval The duration between two R wave peaks (0.8 to 1 s during NSR). The inverse of this quantity is generally taken as the measure of the instantaneous heart rate

Figure 2.8 provides an example of an ECG recording with the deflections and temporal landmarks annotated. This ideal picture may change in practice, as it depends on the cardiac activation sequence which itself depends on a multitude of factors. In some cases or leads, some deflections may disappear completely, have irregular shapes or abnormal periods, and may appear twice. In any case, these are among the most common markers subject to analysis, and are what the clinicians use for non-invasive diagnosis of cardiac pathologies.

2.3.6 Frank's Vectorcardiogram It has been discussed that the heart activation can be equated to an associated cardiac dipole, which is a vector in 3D space. Quite naturally, one would also like to view this dipole in its 3D vector representation: hence the term *vectorcardiography*. A familiar example of vectorcardiogram is in fact the cardioid shape obtained by tracing the bipolar limb lead activations in the Einthoven triangle. (This was in fact the first ever vectorcardiogram (VCG), developed initially by Mann, then by Hollmann et al. [11, 12].)

The most common VCG is an orthogonal 3-lead system proposed by Frank in 1956 [2]. The 3 leads X, Y and Z are synthesized leads, obtained by the combination of several

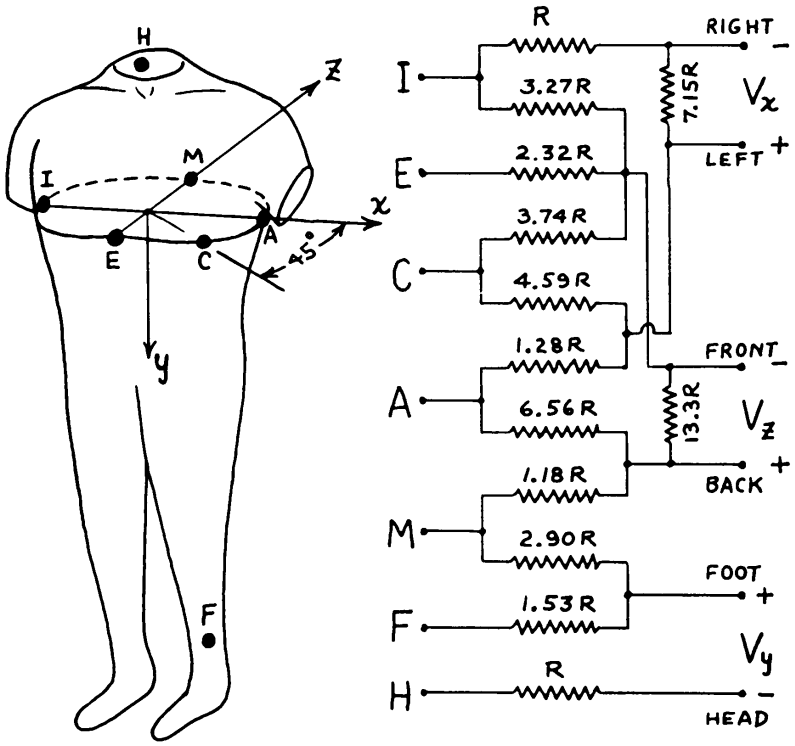

Figure 2.9: The original lead setup of the Frank VCG described in [2].

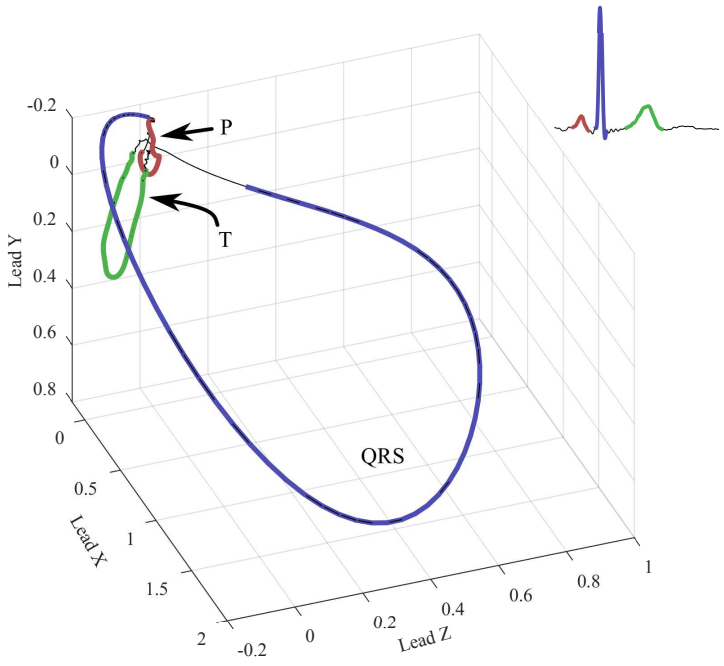

Figure 2.10: Representation of a single heartbeat as a 3D VCG. Recording obtained from `patient104/s0306lre` of the PTB database [3, 4].

lead vectors of a 7-unipolar electrode system set up at specific locations on the body (see Figure 2.9). Prior to this, he performed a quite laborious mapping of the image surface at 192 points on a torso-shaped tank filled with some kind of conducting fluid [13]. The resulting image surface (usually referred to as the Frank image surface) was then usable for synthesizing the 3 orthogonal leads X, Y and Z. Figure 2.10 illustrates an example VCG of one single heartbeat, which when plotted in 3D, resembles a set of loops.

Despite requiring less electrodes and a simpler and more intuitive representation and interpretation of the cardiac activation propagation, Frank's VCG (and other VCG systems) did not become a staple name in the clinic. One possible explanation for this would be the much earlier commercialization of the ECG in the clinical environment, beginning as early as 1908 (just before the publication of Einthoven's paper on the ECG).

2.3.7 Transformation of Lead Systems These 3 orthogonal Frank leads can be used to represent virtually any potential on the body surface by linear combination, yet they remain relatively less complex in terms of recording equipment. Motivated by this, Dower developed a method to recover the 12-lead ECG from recorded VCGs by synthesizing each 12 leads using Frank's image surface. The resulting coefficients can be arranged in matrix form and is usually termed the *Dower Transform* [14]:

$$\mathbf{A} = \begin{bmatrix} -0.515 & 0.157 & -0.917 \\ 0.044 & 0.164 & -1.387 \\ 0.882 & 0.098 & -1.277 \\ 1.213 & 0.127 & -0.601 \\ 1.125 & 0.127 & -0.086 \\ 0.831 & 0.076 & 0.230 \\ 0.632 & -0.235 & 0.059 \\ 0.235 & 1.066 & -0.132 \end{bmatrix} \tag{2.1}$$

It should be noted that technically, the 12-lead ECG derived from the Dower Transform is a synthesized lead that approximates the real 12-lead ECG. However, it was shown to be very similar to real recordings. Only 8 leads were considered in the following order: V_1 - V_6, I and II. It is acceptable to discard the remaining limb leads since they have been shown to be redundant.

In a similar fashion to what Dower has done, it is also possible to obtain the 3 orthogonal Frank leads from the 12-lead ECG. This performed by Edenbrandt and Pahlm to obtain

the *Inverse Dower Transform*. However, the transform coefficients were not sampled from Frank's image space, but rather calculated from the pseudo-inverse of the Dower Transform matrix ($\mathbf{T} = (\mathbf{A}^\intercal\mathbf{A})^{-1}\mathbf{A}^\intercal$) [15]:

$$\mathbf{T} = \begin{bmatrix} -0.172 & -0.074 & 0.122 & 0.231 & 0.239 & 0.194 & 0.156 & -0.010 \\ 0.054 & -0.019 & -0.106 & -0.022 & 0.041 & 0.048 & -0.227 & 0.887 \\ -0.229 & -0.310 & -0.246 & -0.063 & 0.055 & 0.108 & 0.022 & 0.102 \end{bmatrix} \tag{2.2}$$

2.3.8 Distortion in Surface Potential Measures An important factor to obtaining good interpretation of the ECG is to ensure that the factors that contribute to the distortion of the ECG are handled appropriately. Below are examples of the common distortion factors that can be observed in practical cases.

2.3.8.1 Physiologic Sources of Noise Throughout the previous discussion, it was always assumed that the torso is modeled as a homogeneous volume conductor. This would mean that the surface potentials are linearly related to the dipole source potential and the distance between them, and this linear relation should be invariant regardless of the location of measure on the body surface (i.e. conductance per unit volume is constant across the entire geometry).

Research has shown that the various organs and tissues located inside the thorax have greatly different conductivity, and may even change depending on body states (e.g. inhaling). The thorax (and by logical extension, the torso) is thus inhomogeneous. This is further worsened by non-linear propagation phenomena at the interface of different conductors (the Brody effect). At the end, a non-linear relation exists between volume source potentials and surface measured potentials. Furthermore, organs do not have a regular geometry, and hence the relationship is additionally varying over the body surface.

A common source of distortion on the ECG is caused by respiratory motion. Breathing causes a change in the shape of the thoracic cavity. The ribcage is shifted upwards and expands outwards due to the change in intrathoracic pressure. During inspiration, the lungs fill in with air and gaseous exchange occurs within the lung structure. The presence of gasses has the effect of increasing lung resistivity [16].

Electrode misplacement occurs when the placement of ECG electrodes do not match a predefined location. This is required to ensure perfect resemblance to a predefined lead system. This is arguably the most common source of distortion for many reasons.

Misplacement could be unintentional and is usually the case with operator error or placement of electrodes on surface with large amounts of fat. However, it could be intentional: an example is to avoid the breast in female patients.

In presence of these distortion effects, the lead vectors will be modified in some unknown way, departing from an ideal model. These distortions are inherited by the ECG recordings. It is important to compensate for these effects to avoid misrepresentation of the cardiac activation and ultimately misinterpretation. Device calibration is required and can be performed using a special equipment to partially address this issue. Unfortunately, it is not possible to completely compensate for these distortions due to their nonquantifiable nature.

The geometric change of the thorax varies the lead vector magnitudes and orientation. Reduction in lung conductivity incurs a decrease in lead vector magnitude. On the ECG, this was shown to result in almost 10% reduction in amplitude [17]. Orientation change is due to the ribcage movement which displaces the electrodes. A study of QRS and T angle changes during respiration showed a rotation of the orientation on all three XYZ axes [18]. A 3D representation of sequential QRS loops is shown in Figure 2.11. Shift in the cardiac dipole origin can also be observed due to the movement of the heart. However, it is difficult to quantify this on the ECG. In a similar fashion, electrode misplacement also causes the same effects.

Another physiologic source of noise is muscle tension and tremor. Tension is caused by voluntary or involuntary contraction of any muscle near to the electrodes. Tremor, on the other hand, is caused by involuntary rapid activation of the muscles and often causes trembling or convulsion. Although not properly coupled with the electrode interface, they are acquired as far field potentials, and increases the baseline noise level in the ECG.

2.3.8.2 Electrical Sources of Noise As with any signal acquisition chain, there is always additive noise which superposes itself onto the signal of interest. This noise occurs for many reasons: random movement of electrons and ions (thermal noise) within the acquisition chain, capture of far field potentials by the electrode wires, electronic amplifier and quantizer errors. Although each mentioned reason constitutes an independent component in their own self, they can generally be viewed as originating from a single source with a distribution profile. Generally, they are regarded as Gaussian distributed, but may deviate from a Gaussian profile when there are strong 'spiky' sources.

Motion artifact is another type of noise that is generated when the electrode wires are

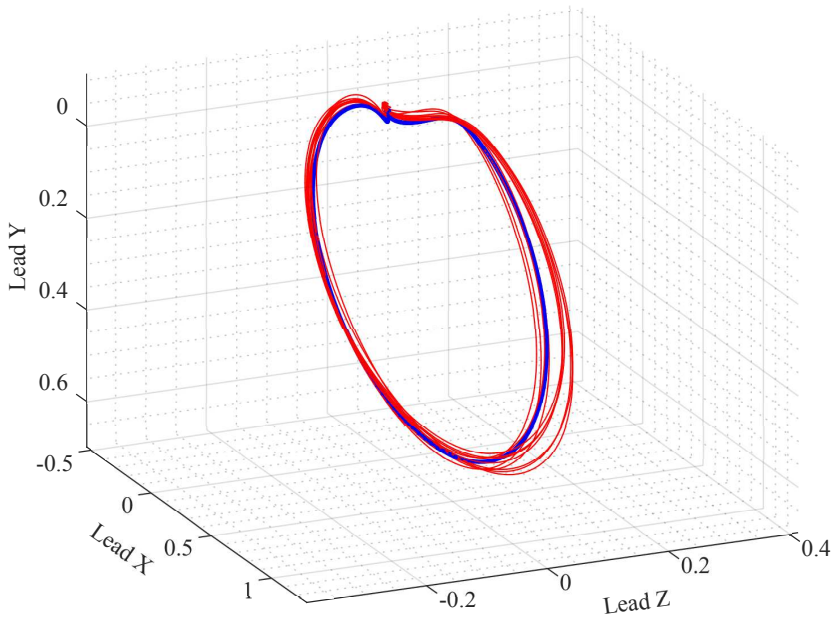

Figure 2.11: Effect of respiration on QRS VCG loops, segmented from recordings after filtering. Blue loop indicates the first QRS in a recording, and red loops are subsequent QRS. Note the shift in the apex in subsequent loops.

disturbed. The disturbance generates current via the piezoelectric effect and results in a voltage spike on the recording. Also, trembling due to muscle tremor would also cause this. These spikes are often wide and transient in nature, and is difficult to remove.

Baseline wander is a subtle change of the ECG baseline, caused by a non-constant voltage bias. This is usually a very slow and gradual process change.

2.4 Cardiac Arrhythmia

The prevalence of cardiovascular diseases (CVD) has been predicted to increase in the coming years. In 2016 alone, this accounted for almost 18 million deaths worldwide [19]. One particular cause of concern is the increase in the incidence of *cardiac arrhythmia*: the abnormal rhythm of the heart. This abnormality causes blood to be suboptimally delivered, hence leading to other pathologies such as stroke and heart failure.

In this thesis, we give focus on *atrial tachyarrhythmia* (abnormal rapid activation of the atrium), of which two are considered most common: atrial fibrillation (AF) and atrial flutter (AFL). In 2010 alone, it has been estimated that about 33.5 million people were affected with AF around the world [20], with more than 750000 hospitalization each year [21]. As for AFL, a study estimated that about 200000 new cases appear in

the US every year [22]. Atrial tachyarrhythmias are strongly associated with old age, and as life expectancy is expected to increase in the coming years, prevalence of this disorder is also expected to increase.

2.4.1 Mechanisms of Arrhythmia The abnormal activation is related to several mechanisms described below, but can be summarized as being caused by *alterations* in impulse conduction and/or impulse generation. A multitude of factors contribute to these, and some do not relate to cardiomyopathy (e.g. sympathovagal interference, drugs). Both these mechanisms usually give rise to *tachycardia*: the rapid activation of the heart.

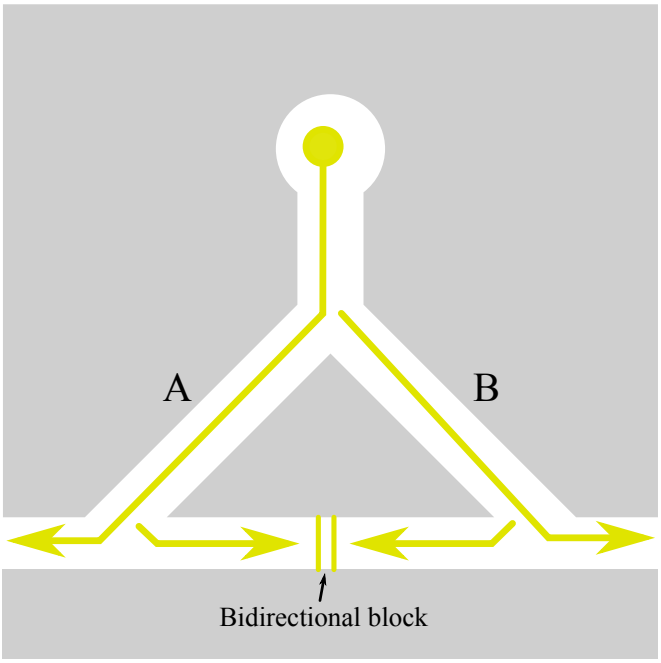

Figure 2.12: Mechanism of arrhythmia in a hypothetical structure: Normal conduction.

Impulse conduction in normal cardiomyocytes has a relatively fast velocity, and this property is generally true across the cardiac structure. An impulse should thus propagate at a uniform speed and cover the same distance regardless of the direction of propagation. This is illustrated in Figure 2.12, where the impulse originating from the natural focus (large yellow dot) travels down two paths A and B at the same speed and activate the same amount of cardiac tissue. Two impulses that collide with each other will produce a *bidirectional conduction block* (yellow parallel bars).

2.4.1.1 Reentry Some conditions may result in the reduction of conduction velocity: for example a reduction in ion current, increased gap-junction resistance and physical dislocation of the serial myocyte connection due to fibrosis [23]. These causes

themselves may arise from other cardiac pathologies or genetic mutations. The main consequence of this is the formation of *regions of slow conduction* that promotes the formation of *reentry pathways*, allowing the activation to circle around an obstacle. To illustrate how this can be achieved, Figure 2.13 shows a scenario of activation leading to reentrant depolarization.

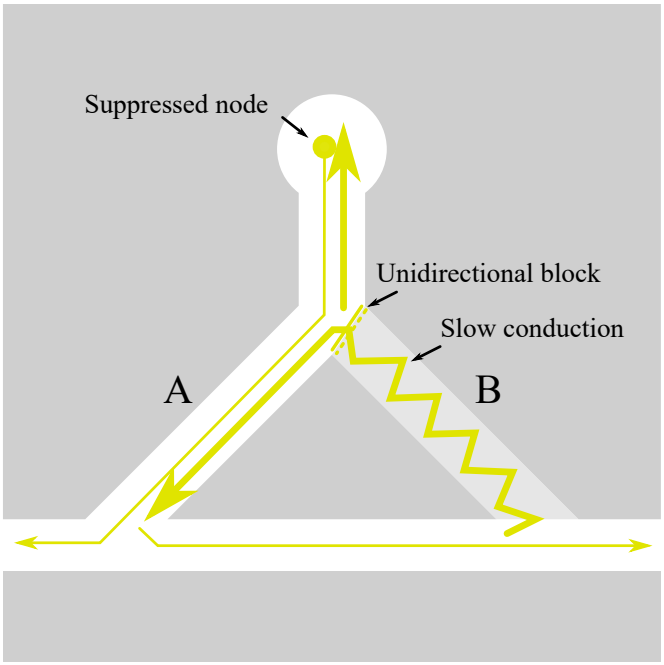

Figure 2.13: Mechanism of arrhythmia in a hypothetical structure: Reentry.

An incoming wavefront splits at a junction down two paths A and B. Conduction is normal down A but blocked at the entry of B. The successfully conducted impulse continues to depolarize the remaining tissue and encounters the exit of B in the reverse direction. This path presents a slow conduction with a total propagation time larger than the effective duration of cell activation. Upon successful conduction of the impulse in reverse along B, it proceeds to reactivate the repolarized tissues. The *reentry circuit* is established and continues as long as the conduction velocity in B is larger than the effective activation time, and the reentrant wavefront is not blocked.

From the above, two conditions are necessary for reentrant depolarization: (i) initial unidirectional block along a specific, well delineated path; and (ii) total propagation time along the reentry pathway larger than the effective duration of cell activation. It seems that condition (ii) may happen without the need of a slow conduction. As an example, consider A being a much shorter path than B. But in virtually all atrial tachyarrhythmia, B is either very small or of similar size to A. The former is particularly true for AFL, where the reentry pathway only covers a small percentage of the reentry circuit. Because of this, it is often termed an *isthmus*.

In general, reentrant depolarization presents a circuit with large diameters (e.g. accessory pathways linking the atrium and ventricle). A reentry with a large diameter circuit is commonly termed *macro-reentry*. However, circuits need not be of large diameters: as long as the conditions for reentry can occur, any size of circuit is possible. In some cases reentry can be confined to a small area resembling a dense point, commonly termed *micro-reentry*.

2.4.1.2 Ectopic Automaticity Pacemaker cells and special fibers of the impulse conduction system are endowed with automaticity, and the rest of the cardiac tissue are normal cardiomyocytes that do not spontaneously self-depolarize. However, cells that are injured due to e.g. ischemia or infarct can become continuously permeable to ions or 'leaky'. The consequence of this is that the resting potential becomes less negative and they undergo self-depolarization. When occurring in cells outside of the impulse conduction system, this is termed *ectopic automaticity* and gives rise to *ectopic pacemakers* or *ectopic foci* (singular form: focus).

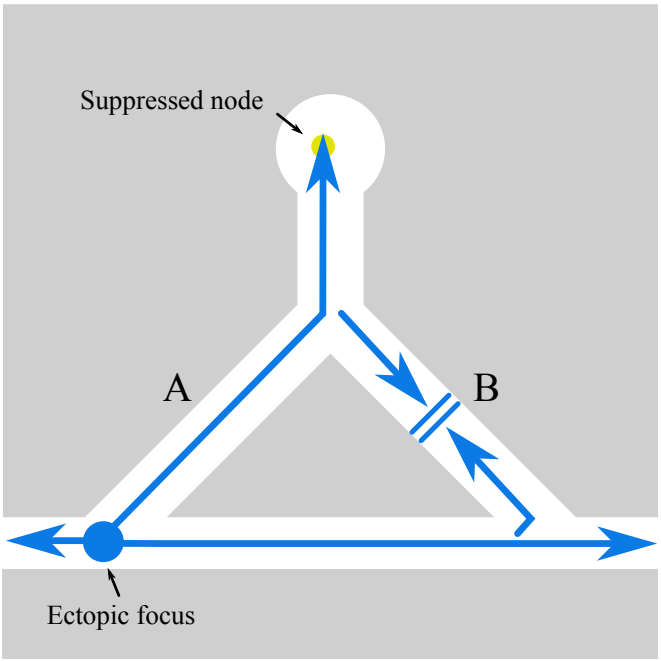

Figure 2.14: Mechanism of arrhythmia in a hypothetical structure: Ectopic focus.

An important relation to AFL (and also AF) is the rate at which it occurs. The *natural pacemaker* is the SA node, which has the highest intrinsic self-activation rate of all the elements within the impulse conduction system. Due to this property, the SA node *suppresses* any other pacemakers. However, if the natural activation rate is slower than any ectopic rates, then the natural pacemaker becomes suppressed instead. Figure 2.14 illustrates an example of ectopic activation (large blue dot) which suppresses

the dominant node. Note that the ectopic propagation (blue lines) are not similar to those in the normal case (yellow lines in previous figures).

Micro-reentry is sometimes mistaken for a focus, due to the size of the circuit. Although the mechanism is different, in cases where the circuits are small enough, they may be classified as a focus.

2.4.2 Atrial Flutter Atrial flutter (AFL) is (and had always been) a term derived from the observation of continuous undulations on the ECG without presence of isoelectric baseline. AFL causes a rapid atrial beat rate, usually with regular ventricular beat rate that is lower than or, in the worst case, equivalent to the atrial rate. With the knowledge of arrhythmia mechanism at hand, AFL is defined as the continuous 'sawtooth'-like undulation on the ECG, usually indicating an estimate period $\leqslant$ 250 ms (or estimate atrial beat rate of $\geqslant$ 240 bpm), although some AFL may have higher periods. The mechanism that causes this undulation could be a macro-reentry, micro-reentry or ectopic focus. In general, only a single source is ever present and in some occasions, more than one coexists, usually with good amount of overlap between the sources. The *F wave*–the common term used for describing the atrial deflection–has generally one single pattern and remains stable over the duration of arrhythmia. For this reason, AFL can be regarded as a *monomorphic* arrhythmia. AF, on the contrary, is comprised of multiple sources that produce multiple deflections on the ECG, hence they can be termed as *polymorphic* arrhythmia.

By this definition, AFL encompasses two subclasses of arrhythmia: *focal atrial tachycardia* and *macro-reentrant atrial tachycardia*. The inclusion of focal tachycardia can be considered a controversy, and in addition the literature exclusively discusses AFL with a reentry setting. However in practice, the mechanism produces a compliant ECG criteria, and this presents the reason for its inclusion.

Typical AFL is a macro-reentrant tachycardia exclusively located in the right atrium. The circuit rotates around many well-defined anatomical landmarks, as shown in Figure 2.15(a). A standard description would begin at the area of the coronary sinus (CSin), just slightly posterior to the AV node. From the CSin, the circuit goes up the septum and towards the SVC. There, it encounters the fibers of the crista terminalis and proceeds inferiorly down the right lateral wall via the many pectinate musculatures, before arriving at the circumferential bundles near the tricuspid orifice. In this region, bordered by the tricuspid ring (a part of the fibrous skeleton) and Eustachian ridges (vestiges of a valve useful during cardiac maturation) is the *cavo-tricuspid isthmus* (CTI) that presents a significantly slow conduction velocity. Upon exit of the isthmus,

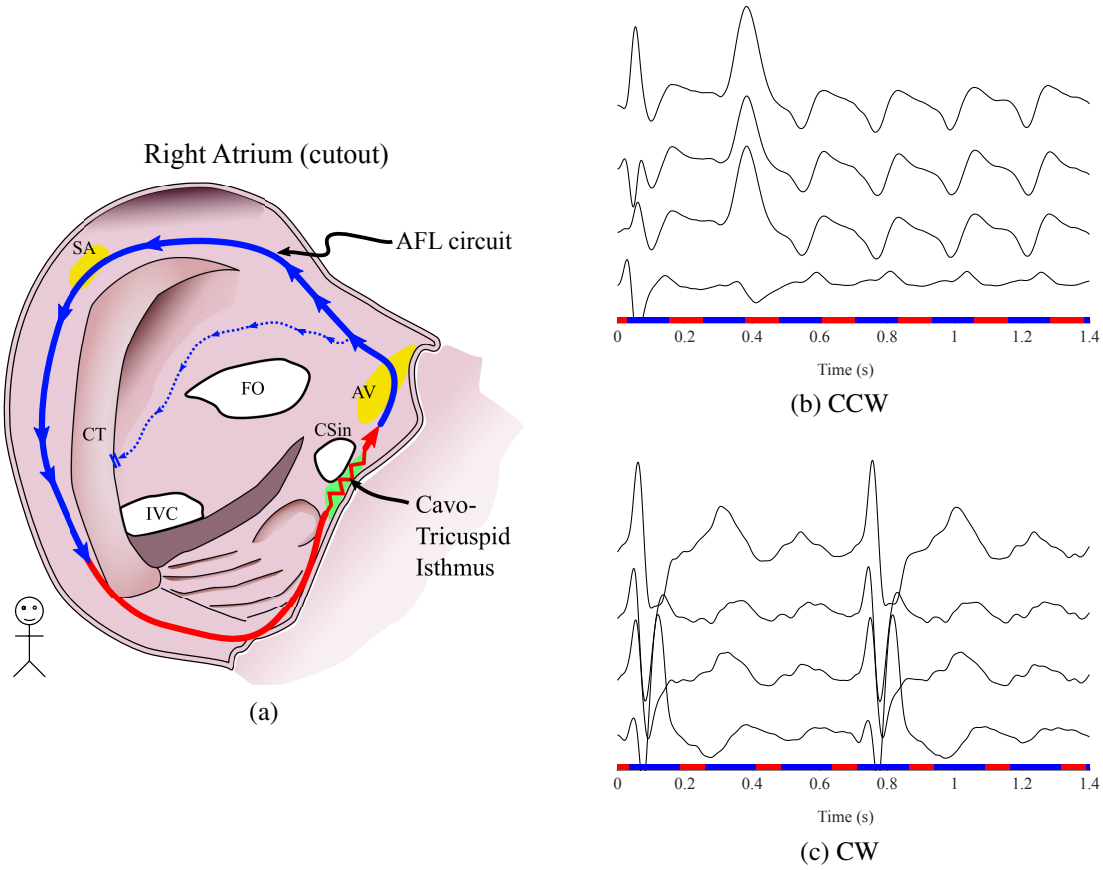

Figure 2.15: Mechanism of typical AFL. (a) Typical CCW AFL circuit, turning around specific anatomic landmarks; (b) and (c) Resulting ECG in leads II, III, aV_F and V_1 (top to bottom) for CCW and CW AFL respectively. Colorbars below the recordings indicate, in time, the current location of the wavefront in the circuit.

the circuit arrives at the area near the CSin, where it completes a closed loop. The left atrium is passively activated via the musculature of the CSin. It should be noted that when viewed from the frontal plane (with the observer facing the patient), the circuit turns around in a counterclockwise direction. For this reason, the AFL is also termed a typical counterclockwise (CCW) AFL.

Assuming no structural disease is present that could alter the impulse conduction path, the ECG waveform resembles a very marked sawtooth (see Figure 2.15(b)), with each tooth referring to one cycle of right and left atrial activation. This is essentially a P wave, but during arrhythmia it is commonly referred to as an *F wave*. Particular to typical AFL, the sharp deflection of the F wave, corresponding to massive depolarization of the atrial mass, has a defined polarity in certain leads. In leads II, III and aV_F, it has a negative polarity (i.e. deflection points towards negative values) and in lead V_1 it has a positive polarity. This is the most common ECG descriptor for typical CCW AFL.

It is also possible for the circuit to turn in the opposite direction (i.e. in a clockwise

direction). The pathway remains the same, but the ECG descriptors are usually inverted in polarity (see Figure 2.15(c)). This type of AFL is termed typical clockwise (CW) AFL. Typical CW AFL represents around 10-30% of all typical AFL cases [24].

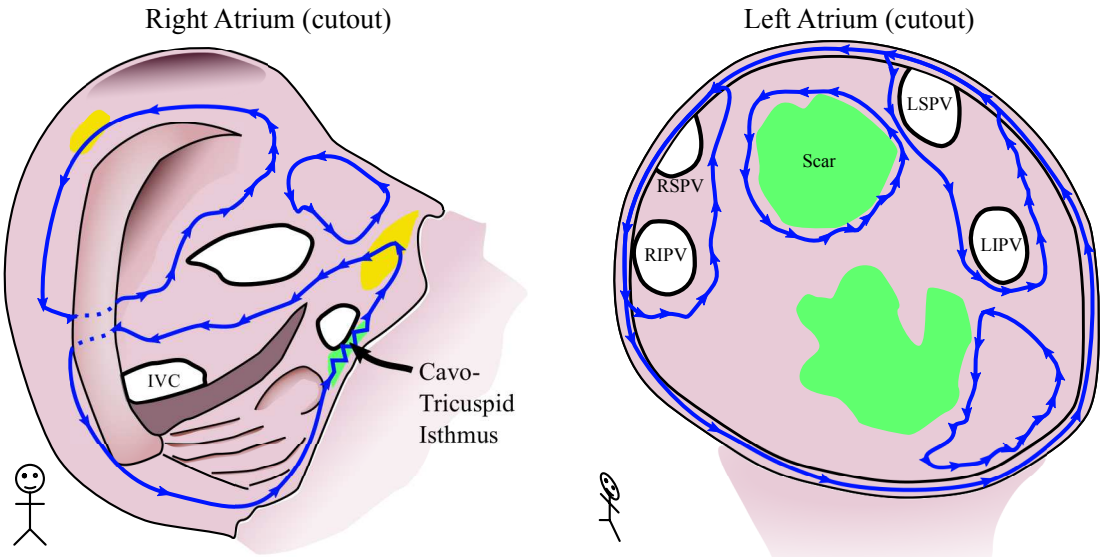

Figure 2.16: Examples of atypical flutter circuit in the right and left atrium. Dotted lines indicate CT breakthrough: abnormally fast conduction in the transverse direction to the cardiac fibers.

By definition, all other AFL that do not fit the description of typical flutter are *atypical AFL*. There have been many descriptions of atypical AFL circuits found in the literature, some with well-defined ECG manifestations. Below is a list of the most common atypical circuits derived from the literature [24–27]. Figure 2.16 provides a visual representation of some circuits.

- Lower loop reentry: Circuit turning around the inferior vena cava. Because of its dependence on the CTI (which also acts as its isthmus), lower loop reentry and typical AFL are referred to as *CTI-dependent AFL*. ECG patterns are mostly similar to that of typical AFL, due to the very similar circuits, but lead V_1 may change polarity when CT breakthrough occurs too high (near the SVC)

- Upper loop reentry: Circuit turning around the superior vena cava, with a significant portion of the circuit travelling down the septum towards the CT. A potential isthmus can be located between the beginning of the CT and the SVC. It can turn in both CW and CCW direction, but common descriptions are of a CW direction. Reports showed consistent ECG patterns to typical flutter. Lead I is typically low-voltage [28]

- Perimitral flutter: Circuit turning around the mitral valve, and usually involves

regions of functional block due to fibrosis or poor conduction located on the walls. The rotation can be CW or CCW direction. CCW perimitral flutter presents positive deflections in precordial and limb leads, except for leads I and aV_L where the activation is negative. The inverse happens during CW rotation. Some leads have been reported to be of low voltage (II, III, aV_F)

- Periveinous flutter: Circuit turning around the pulmonary veins. It can turn around a single pair of veins or both. Most of the time, the circuit involves a large area of functional or fixed block [29]. ECG criteria are poorly described

- Wall-related flutter: Wall flutters are macro-reentries confined to a region on the atrial walls. Common locations include the right and left lateral wall, the septum and the left posterior wall. Often, these flutters turn around a central obstacle comprised of lesions, scars or zones with no conduction. In some cases, the obstacle may be a prolonged or continuously refractory tissue. In the left atrium, wall flutters may also involve the 'atrial roof' passing between the right and left pulmonary veins. ECG criteria depends on the location of the scar

It should also be mentioned that focal origins are also classified as atypical flutters due to non-compliance with typical AFL criteria. Many potential locations of ectopic focus have been identified and pertain mostly to the CT, CSin orifice, right septum and pulmonary vein orifices [30]. ECG patterns depend strongly on the location of the ectopic focus.

2.4.3 Junctional Regulation of Rhythm Very fast activation of the cardiomyocytes have been shown to cause *atrial remodeling*: a combination of anatomic and electrophysiologic changes that cause cardiomyocytes to become more susceptible to arrhythmia [31]. Rapid activation of the ventricles would then promote arrhythmia in these chambers and would eventually lead to ventricular arrhythmia: a condition with higher risks than atrial arrhythmia.

In this situation, the role of the AV node becomes very clear. The delayed conduction allows rapid ectopic beats to be blocked. Therefore, despite the rapid atrial rate, the ventricular rate remains relatively low. In AFL, it is possible to 'count' the number of AFL cycles finished before the triggering of the ventricular beat. This is usually expressed in the form of a ratio termed the *AV block ratio*. In Figure 2.15(b), the ECG presents a 5:1 block ratio, whilst in Figure 2.15(c), it presents a 2:1 block ratio.

2.5 Catheter Ablation

Pathologic activations often present a risk of developing other medical complications. In the case of AFL and AF, the rapid activation of the atrium presents a risk of elevated heart rate. High ventricular rates may cause ventricular myocardial remodeling and predisposes them to arrhythmia, potentially leading to more life-threatening conditions. Blood stagnation may also occur due to reduced pumping efficiency and could potentially cause the development of embolism in the cerebrovascular system, leading effectively to stroke.

The primary goal of treatment would be to stop the pathologic activation and convert the patient back to sinus rhythm. A selection of therapies exists, with relatively good rates of success for selected patients. A common and trending treatment for both AF and AFL is *catheter ablation of cardiac tissues*.

The therapy consists of introducing special guided wires called *catheters* into the heart chambers via access veins. These wires have pairs of electrodes attached to their tips and allow the sensing of potential differences at a localized portion of the endocardium. The electrode spacing determines the spatial resolution of the measured local potential. Figure 2.17 illustrates the catheter locations within the right atrium. There are typically 3 catheters introduced at a time:

1. CSin catheter: typically a decapolar (5 electrode pair) catheter that is lodged inside the coronary sinus. It records the intracardiac propagation of activation and is used to estimate the tachycardia cycle length as well as to determine the right or left origin of the circuit

2. Mapping catheter: a multipolar catheter used to map endocardial potentials. This is used to visualize the physical depolarization sequence and is essential for exactly locating key ablation areas

3. Ablation catheter: a quadripolar catheter used to ablate cardiac tissue

Catheter ablation has been regarded as a very effective treatment for AF and AFL. *Radiofrequency catheter ablation* employs high-frequency electric current to generate heat (around 70°C for ablation, and has a very high success rate (>90%) and a relatively low recurrence rate (<10%) for AFL [32]. Another flavor of ablation: *cryoablation*, uses extremely cold temperatures (<-60°C) delivered using a gas cooling system and a cryoballoon instead of a traditional wire-style catheter. It has a comparable success rate as radiofrequency ablation [33]. However, cryoablation avoids the issue of myocardial

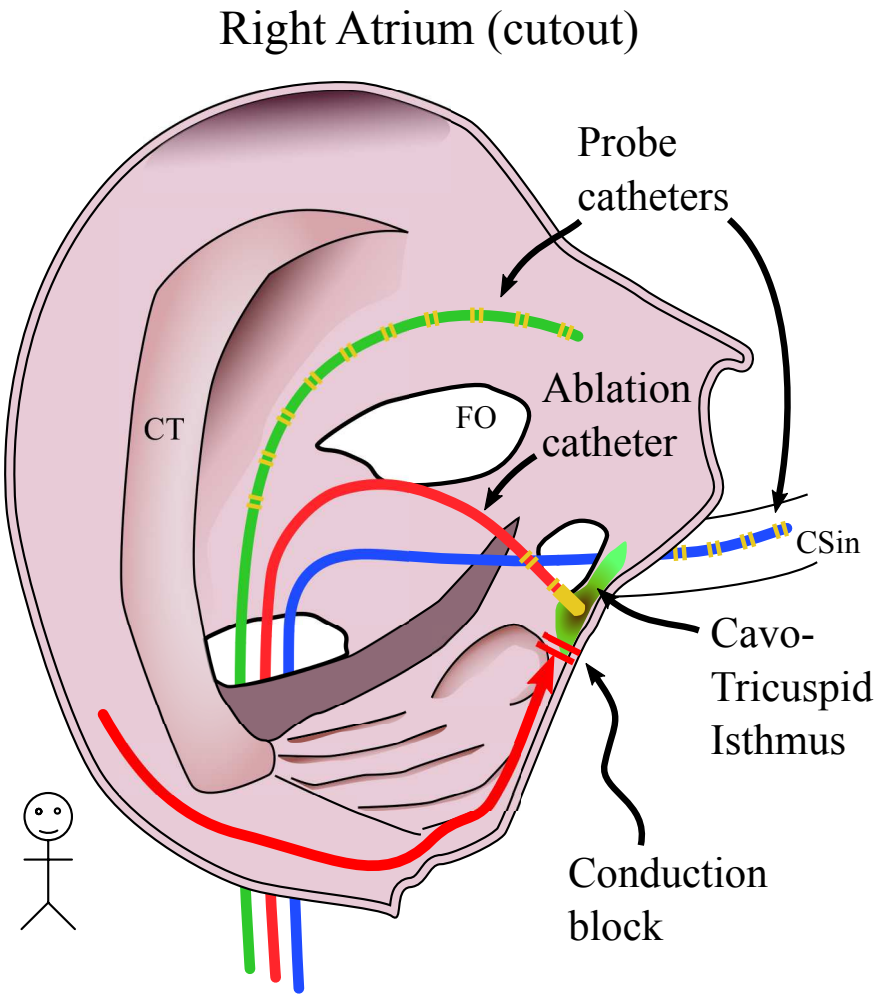

Figure 2.17: Cardiac ablation procedure using duodecapolar probe catheter for mapping.

perforation often associated with radiofrequency ablation, and is currently becoming popular.

2.5.1 Ablation Procedure A description of the ablation procedure is given here. The reason for a focus on this therapy is that the main goals of the research described in this document pertains to the improvement of the efficacy of the ablation procedure. Therefore, a good understanding of the procedure as well as its challenges may clarify the problematics associated with this work.

Catheter ablation is an elective procedure. This means that before an ablation procedure, patients are thoroughly assessed for adequacy to avoid complications. Often, antiarrhythmic drug therapies are stopped for at least five drug half-lives to ensure that the arrhythmia is not masked by pharmacologic effects. Anticoagulant intake is continued or prescribed to prevent development of blood clots. This preparation stage

usually begins about a month before the operation.

If arrhythmia is present during the preparatory stage, ECG traces may be obtained in order to assess the possible mechanism and other useful information. For AFL, the particular objective of interest is to determine typical or atypical mechanism. In the case of the latter, the 12-lead ECG may be further analyzed to determine the location of the reentry or focus. This is highly dependent on the clinician's skill in evaluating the ECG.

After proper preparation and adequate candidacy criteria, the patient may be elected for ablation. Prior to the main procedure, the patient is prepared and local or general anesthesia is applied. On suspicion or knowledge of prior arrhythmic episodes, a trans-esophagal echocardiography may be performed to rule out the presence of blood clots, especially in the left atrium. Once confirmed of absence, the ablation procedure is initiated.

Often, the patient's cardiac geometry is reconstructed using X-ray computed tomography provided by a mobile X-ray unit attached to the operating platform. This helps the clinicians visualize the endocardial geometry. Then, the catheter is inserted. Typical areas of insertion is the groin (to join the femoral vein), arm (to join the subclavian vein) or the neck (to join the jugular vein). The catheter is advanced towards the heart and ends up in the right atrium.

The first catheter to be introduced is the CSin catheter, which is lodged inside the CSin to establish a voltage and timing reference of the endocardium. Mapping and ablation catheters are introduced into the heart afterwards. These catheters are tracked using a magnetic localization system. A dedicated software is used to display the endocardial geometry as well as the real-time location of the catheter inside it.

Among the first steps of the procedure is to localize the chamber of origin (right or left atrium). From the intracardiac recordings of the CSin catheter, clinicians can determine this property. Analysis of the propagating impulse within the CSin shows that for right atrium origin, the impulse propagates from the electrodes at the stem towards those at the tip (proximal to distal propagation), whereas left atrium origin the pattern is reversed (distal to proximal propagation). Pacing maneuvers are also performed to provide additional evidence for localization.

In some cases, the arrhythmia may be absent during the operation. Rapid pacing or introduction of proarrhythmic drug (isoproterenol) may induce the arrhythmia. Note that if there is a strong suspicion of typical AFL, then the ablation can be performed even without the arrhythmia being induced, as the target isthmus is always the CTI.

If a left atrium origin has been determined, an access port must be made via the interatrial septum. An uncommon but beneficial situation is the existence of a patent foramen ovale that allows free access to the left atrium without the need for any surgery. Usually, a transseptal puncture has to be performed. This is achieved by using a sheath and needle. In cases where these equipment are unable to perform a puncture, an electric scalpel may be employed.

It should be noted that the puncturing equipment is not introduced if a right atrium origin is suspected. If left localization was not known beforehand, the puncturing equipment would also be absent. Only on validation of left origin would the equipment be introduced for puncture. This without doubt requires additional time.

Once inside the target chambers, an *electrophysiologic study* of the chamber is performed to precisely identify the arrhythmia mechanism and crucial ablation regions. Common techniques for this are cardiac pacing using catheters to determine inclusion or exclusion of a region of atrial tissue, as well as endocardial potential mapping to obtain a map of the voltage distribution across the interior anatomy. From these maneuvers, the mechanism may be identified along with crucial ablation targets such as the ectopic focus or the critical isthmus.

The ablation catheter is placed on the target, taking into account the pressure applied onto the target site. Ablation then occurs when radiofrequency energy or cryo-coolant is introduced. Usually, a specific energy or temperature is maintained over several seconds in order to achieve a proper lesion. Once complete, pacing tests are performed, usually to verify the existence of a fixed block. Some isthmus are wide, and require a linear lesion to establish a complete line of block. These are usually performed by multiple point-to-point ablation with some spacing in between each ablation point.

Both mapping and ablation continue until conversion to sinus rhythm. In some cases, other arrhythmia may occur during the operation, as a result of ablation, pacing or even catheter contact. Some arrhythmia may persist and do not terminate despite multiple efforts. In such a case, the operation may be aborted.

Catheter ablation operation generally lasts from 2 to 4 hours. In some complicated cases, it may last up to 8 or 9 hours. Operations are usually stopped due to prolonged duration or excessive patient intolerance to ablation (which they can feel). In the case where the arrhythmia persists, other therapy options may be considered to stabilize the heart rate.

2.6 Conclusion

In this chapter, a brief description has been provided of the heart, its functionality, how electrocardiographic measures are made, its inherent distortion factors as well as a review of AFL mechanism and the ablation operation. Important observations that should be made in this chapter are (1) the human physioanatomy contributes to the distortion of the ECG, which will have an effect on ECG interpretation; (2) AFL involves an abnormal activation that has a different activation sequence, that depends on the mechanism and location in the atrium; and (3) catheter ablation operations suffer inefficacy due to the lack of prior information available on AFL. These observations will be central to the coming chapters, and will help build the argument for the selection of some methods.

Chapter 3

Review of Techniques for AFL Localization

3.1 Introduction

As illustrated in the previous chapter, catheter ablation therapy is a well-defined treatment with a clear endpoint: prevent further ectopic activation of the heart by establishing a fixed block through ablation of cardiac tissue. Although currently a frontline therapy for cardiac arrhythmia in general, and specifically for AFL due to its high success rate, ablation procedures are more often than not complex and time-consuming.

The complexity arises from lack of knowledge on AFL properties beforehand. The ablation procedure described in Section 2.5 illustrates the explorative nature of the procedure, and it is clear that prior knowledge would improve procedural efficacy by allowing earlier access to critical information, thus reducing procedural time as well as overall cost of ablation.

One focus of this research is on the *right-or-left localization* of AFL. Indeed, early determination of this property would help clinicians better prepare the operation in terms of the necessity of introducing the trans-septal puncture equipment for left atrium access. Furthermore, this must be done in a non-invasive setup as there is little gain in determining localization after introduction of catheters. Therefore, the challenge is to perform localization from non-invasive data. The selected non-invasive data in this research is the *12-lead ECG*, which is adequate in theory as it conveys information on cardiac activation.

In this chapter, a review of localization techniques will be presented. Section 3.2 details the current standard procedure for AFL localization conventionally performed in the clinic. In Section 3.3, a prospective discussion of non-conventional methods is presented. In both sections, the aim is to introduce localization techniques, but attention should be given as well to the underlying assumptions, which will be incorporated into this research.

3.2 Conventional Techniques

3.2.1 Non-Invasive Technique The common method of prediction, used by practically all clinicians, is *visual inspection of the F wave morphology* on the standard 12-lead ECG recording. The polarity and the wave amplitude are the two most utilized criteria, and are commonly examined on a subset of leads. The most well-documented indicators are that of typical AFL, which is exclusively located in the right atrium (see Section 2.4). Therefore, one of the simplest starting points in AFL localization consists in determining whether the ECG indicates a typical or atypical AFL.

A retrospective study on ECG patterns and predictivity of AFL category (typical or atypical) has been done [34]. The selection of patients was strict: no patients had undergone previous ablation for any arrhythmia, nor did they have any previous surgery. This study showed that typical AFL ECG patterns predicted typical AFL with 83% rate of correct prediction (sensitivity, Se), and 75% rate of correct rejection of atypical AFL (specificity, Sp). The association between ECG morphology and AFL mechanism is shown to be very strong by observation.

In practice, clinicians achieve similar performance to this. A study involving a large number of clinicians ($n = 689$) from novice to expert skill rank showed that typical AFL can be correctly diagnosed–on average–by $> 85\%$ of clinicians from all ranks, with cardiology experts having correct diagnosis $\geqslant 90\%$ on average [35].

When the ECG morphology is atypical (i.e. not representing typical AFL ECG), the situation becomes challenging. It was found that 25% of atypical ECG recordings are associated with left AFL [34]. In terms of numbers, this was 15 recordings; the total number of left AFL in that study was 18. This shows that left AFL is well-associated with atypical ECG patterns. But unfortunately, atypical ECG recordings are also well associated with atypical right AFL (21 out of 30 atypical right AFL have atypical ECGs).

A comprehensive report on using the ECG for right or left localization suggested the analysis of lead V_1 polarity and voltage profile [36]. From a comparison of several different types of AFL, it was suggested that an initial negative or isoelectric component followed by a sharp positive deflection was suggestive of right AFL. Additionally, deep negative deflections are also suggestive of right localization. A broad and upright F wave is suggestive of left AFL.

In passing, it is notable that amplitude and polarity criteria are the most used in conventional setting. F wave duration or F-F interval (akin to the cycle length), however,

are rarely if not ever studied.

3.2.1.1 Limitations and Pitfalls Visual inspection is quick and convenient in a clinical setting. Nevertheless it is not robust, because visual inspection does not account for the bioelectrophysiological effects governing the genesis of the ECG. The biggest factors of morphological change are the alteration in the activation sequence as well as atrial mass under depolarization. Ablation lesions or structural heart disease are the two common causes of ECG morphological change as their side effects are exactly that, and unfortunately are commonly found with cases of AFL (due to prior ablation therapies).

In addition, circuit direction also affects the morphology, making it difficult to distinguish between right and left AFL. In some cases, the two categories may mimic each other, especially in the presence of heart disease or abnormalities. This would essentially render the localization problem a random guess. Furthermore, these abnormalities may be difficult to diagnose from the ECG (e.g. [37]).

The cost of wrong localization would depend on the actual localization of the AFL circuit. A false left localization does not entrain much loss since the catheter has to be introduced in the right atrium anyway. The same cannot be said for a false right localization, where a puncturing equipment is needed and may not be installed at the beginning of the procedure. To the author's knowledge, there isn't any previously published paper with an objective comparison of this exact cost. However, one study did highlight the cost-saving (in the order of $\$1,300$) and quality-of-life gain from correct diagnosis of tachycardia [38].

3.2.2 Invasive Technique Besides inspecting the ECG, AFL localization can be performed by analyzing the depolarization pattern within the coronary sinus (CSin, refer to Section 2.4 for detail). This is typically done using the CSin catheter which is lodged inside this vein at the beginning of the electrophysiologic study (EPS). This is an important step in the ablation procedure, not only because of its ability to localize AFL origin, but to also provide information on the actual physical form of the circuit. In addition, the CSin catheter serves as a reference for the positioning of other catheters.

Depolarization originating from the right atrium will typically have a proximal-to-distal propagation, illustrated by the movement of the activation wavefront from electrodes furthest from the tip to electrodes at the catheter tip. In the reverse direction i.e. distal-to-proximal, this is suggestive of left atrium origin. However, it has been observed in some cases that the direction of propagation does not determine right-or-left atrial

origin. This can be observed in focal AFL originating near the left septal wall, where the CSin propagation pattern suggests right atrial origin.

EPS allows direct access to the actual AFL circuit, and this is useful in probing the actual location of the circuit. This renders is useful as a 'gold standard' source of information regarding e.g. AFL circuit localization. However, it should be kept in mind that the non-invasive nature of the technique incurs a high cost due to the necessity of intervention, hence it is not the 'first-in-line' procedure for AFL localization. Typically, the clinicians would analyze the ECG first to obtain an estimate localization, and then verify this with the result of EPS.

3.3 Non-Conventional Techniques

By appropriately leveraging electrophysiological knowledge, it is possible to extract characteristics and information from the surface ECG recordings, which cannot be obtained by visual inspection. This can fortunately be done by applying advanced signal and data processing techniques.

In this section, a review of the state of the art is presented. However, it should be mentioned that most of these techniques are not explicitly targeted at localizing AFL origin, but consists of studies on the pathology with diverse aims. Two studies focus on AF, but have similar methodologies to those focusing on AFL. Nevertheless, the conclusions brought about from these studies are useful in shaping our approach. To the author's knowledge, only one paper has proposed a direct method for non-invasive AFL localization [39]. Table 3.1 provides a tabular summary of the existing studies pertaining to the analysis of AFL as well as AF.

Table 3.1: Previous Studies on AF and AFL

	Reference	Year	Study objective
(1)	Narayan et al.	2003	Characterization of spatial and temporal variability of organized AF, atypical and typical AFL
(2)	Ng et al.	2003	Analysis of the orientation of loop plane in typical AFL
(3)	Kao et al.	2004	Classification of typical & atypical AFL and AF using delay-embedding approach
(4)	Kahn et al.	2007	Localization of right or left AFL using a spatiotemporal coherence approach
(5)	Richter et al.	2008	Analysis of AF using VCG loop orientation and geometry parameters
(6)	Castells et al.	2011	Characterization of typical and atypical AFL using VCG spatial parameters
(7)	Meste et al.	2016	Characterization of persistent AF using recurrence quantification analysis

3.3.1 Spatiotemporal Coherence Approach The earliest mentioned work pertaining to non-invasive AFL classification was in 2003, performed by the team of Narayan et al. [40]. Their focus was on the characterization of spatial and temporal variability in the atrial activity during AF, atypical and typical AFL. Their hypothesis was that atrial activity is regular in typical AFL, and becomes progressively more irregular in atypical AFL and in AF.

Their main contribution was the analysis of AFL correlation series, defined as the Pearson correlation r of a template F wave S (duration of 120 to 200 ms) with a similar-sized sliding window X on the whole ECG of 10 second duration:

$$r(S,X,j) = \frac{N(\sum_{i=j}^{j+N-1} S_{i-j}X_i) - \sum_{i=j}^{j+N-1} S_{i-j} \sum_{i=j}^{j+N-1} X_i}{\sqrt{[N\sum_{i=j}^{j+N-1} S_{i-j}^2 - (\sum_{i=j}^{j+N-1} S_{i-j})^2][N\sum_{i=j}^{j+N-1} X_i^2 - (\sum_{i=j}^{j+N-1} X_i)^2]}} \tag{3.1}$$

Correlation aims to quantify the association between two sets of observations or data. When two sets of data agree–in the statistical sense–with each other, then this would produce a large correlation coefficient. Typically, the coefficient is normalized to obtain values within a limited interval (typically $[-1;\ 1]$).

This was done for 3 leads (V_5, aV_F and V_1) which represent a pseudo-orthogonal 3D space. Due to F wave similarity from cycle to cycle, the correlation becomes high ($\simeq 1$)

when subsequent F waves appear in the window. The correlation series resembles a pseudo-cosinusoid function. When visualized in 3D space using each time point in the 3 leads to form a vector, the correlation series resembles a loop.

Several markers were explored, based on thresholding of the loop trajectory (i.e. the loop must pass a certain point in 3D) and spectral analysis of the correlation series. In a much later publication, they defined a marker for atrial activity regularity: the spatiotemporal coherence, which is the Pearson correlation of pairs of correlation series [39]:

$$R_{XY} = r(r_{V_1}, r_{aV_F}) \tag{3.2}$$

Note that the correlation averages over the entire signal length. This marker was used to classify between right and left AFL. The results of their experiment showed that right AFL was more coherent than left AFL when evaluating correlation series of V_5 and aV_F ((Se,Sp)=(0.84,0.75) for a total of 66 patients, 8 with left AFL). This was in line with their hypothesis of progressive irregularity from typical AFL to atypical AFL, but also showed that right and left AFL have different atrial activity regularity.

3.3.2 Vectorcardiographic Loop Approach In 2003, the team of Ng et al. performed a study on characterization of typical AFL [41], with a focus on VCG loop orientation. Their intent was to evaluate whether the if typical AFL VCG loops have the same orientation as the physical AFL circuit, whose azimuth is rotated by -45° (i.e. 45° to the left). This is commonly referred to as the left anterior oblique (LAO) view. Among their main contribution was the use of the Karhunen-Loève transform–which is equivalent to a singular value decomposition (SVD)–to obtain orthogonal vectors that span the F loop in 3D space.

SVD aims to provide a complete representation of an observation in a basis spanned by orthogonal, singular vectors $\mathbf{V} = [\mathbf{v}_1\ \mathbf{v}_2\ \mathbf{v}_3]$. These vectors indicate, in the original basis, the directions corresponding to the highest variances. They have associated singular values $\mathbf{\Lambda} = \text{diag}(\lambda_1, \lambda_2, \lambda_3),\ \lambda_1 > \lambda_2 > \lambda_3$ that rank the directions from the highest variance to the lowest (possibly zero) variance.

The 3rd singular vector issued from the transform, which is essentially the normal to the loop 'plane' was used to determine loop orientation parameters, which are the azimuth and elevation. The result of their experiment, performed on a single-cycle signal-averaged F loop showed that typical AFL has a mean azimuth of -50±46°. This illustrates a certain directionality of the orientation, which reflects in a way, the sequence of atrial activation. However, they did not correlate this geometrically with

a geometric model of the heart. No further analysis on atypical or left AFL has been performed in the study or after that, to the author's knowledge.

In another line of work, the team of Richter et al. performed the same analysis on each individual cycle of AF (i.e. a *beat-to-beat* analysis) [42]. They introduced two additional loop parameters, both of which capture geometric properties of the loop: the loop flatness and the loop shape, obtained from the singular values of the transform. Although their focus was on AF, the main findings suggested that AF loops have more defined shape with increasing AF frequency, which is known to be associated with increase in AF complexity. This suggests a relation between activation propagation dynamics and arrhythmia complexity.

Loop orientation, given in terms of azimuth ϕ_{AZ} and elevation ϕ_{EL} was calculated from the normal vector $\mathbf{v}_3$ by finding the angle of the vector's component with planes XY and XZ respectively.

$$\phi_{AZ} = \arctan(\frac{v_{3z}}{v_{3x}}) \tag{3.3}$$

$$\phi_{EL} = \left|\arctan(\frac{v_{3y}}{\sqrt{v_{3x}^2 + v_{3z}^2}})\right| \tag{3.4}$$

Loop geometry, given in terms of planarity ψ_{PL} (flatness of the loop) and plane geometry (the shape of the loop) ψ_{PG} was calculated using the singular values.

$$\psi_{PL} = 1 - \frac{\lambda_3}{\sum_{i=1}^{3} \lambda_i} \tag{3.5}$$

$$\psi_{PG} = \frac{\lambda_2}{\lambda_1} \tag{3.6}$$

In a different direction than the previous two research, the team of Castells et al. analyzed the spatial variability of VCG loops by quantifying the variability in loop trajectory [43]. Several descriptive markers are proposed for this. They performed two types of analysis to compare the trajectories of the averaged loop of typical and atypical patients (interpatient analysis), and to compare the trajectories of each loop with respect to a leave-one-out averaged loop in a single patient (intrapatient analysis). Of particular interest, the result of intrapatient analysis showed significant differences between the variability of typical and atypical AFL: typical AFL has a more regular mean trajectory with little variations from beat to beat, whilst the inverse occurs for atypical AFL.

3.3.3 State-Space Analysis Approach A single instance of work by the team of Kao et al. utilized non-linear methods to characterize the atrial activity of AF and AFL using lead V_1 only [44]. The quasi-periodic atrial activity (AA) during these arrhythmia can be interpreted as a trajectory map of an oscillating system, characterizable by a *state vector*. The trajectory may be described as a random process with varying degrees of stability, with AFL being the most stable. The team used a delay-embedded representation of the signal in order to obtain a state vector in high dimension.

Delay embedding, introduced by Takens [45], essentially constructs a high-dimensional state vector from several delayed observations $\mathbf{x}(t) = [x(t)\, x(t-\tau)\, \cdots\, x(t-(K-1)\tau)]$, with τ the delay variable, and K the embedding dimension. The classic technique employed only 1-dimensional observation (i.e. one single lead). Some contemporary techniques do not perform delay embedding (i.e. $K = 0$), but extends the observation to L dimensions instead of 1. This is not a 'true' delay embedding, but has some usefulness in trajectory analysis.

Several parameters were used to characterize the complexity of the state vector trajectory, and were used as features for classification with a back-propagated neural network. The authors hinted at varying trajectory complexities, with typical AFL being the least complex, but little information was provided on the difference between typical and atypical AFL.

A different work by the team of Meste et al. focused on the characterization of AF using *recurrence quantification analysis* (RQA) that analyzes *recurrence plots* (RP): a 2D graph that captures any recurrent behavior in a process, in order to predict persistent AF patients who would have recurring episodes after therapy [46]. Delay-embedding was not performed, but instead they considered each time point of a 164-lead ECG as a high-dimensional state vector instead. This is equivalent to observing the trajectory of the cardiac dipole in L-space, with L the number of ECG leads.

Recurrence quantification analysis (RQA) is a non-linear technique that aims to quantify the properties of a dynamic, often oscillatory system by comparison of the state vector $\mathbf{x}(t)$ of dimension K at one instant with another delayed instant in time $\mathbf{x}(t-\tau)$, with τ a delay variable. Note that this is slightly different than delay-embedding: the dimension K in RQA usually denotes e.g. multiple leads instead of K delayed samples. In essence, no delay-embedding is performed.

The comparison allows one to obtain a *recurrence plot* (RP): a 2-dimensional graphical plot representing similarity measures of two different states [47]. The classic similarity is calculated by:

$$R(t_1, t_2) = H(\varepsilon - \|\mathbf{x}(t_1) - \mathbf{x}(t_2)\|) \tag{3.7}$$

with $H(\cdot)$ the Heaviside step function and ε a constant error term. Hence, the classical recurrence value is binary (1 or 0). This indicates a measure of state similarity within a hard fixed radius ε. In practice, and especially in digital signal processing, it is useful to quantize the continuous time by replacing it with sample indices. In other words, $t \rightarrow n\mathrm{T}$, with T the sampling interval. The recurrence can now be defined as

$$R(i, j) = H(\varepsilon - \|\mathbf{x}(i\mathrm{T}) - \mathbf{x}(j\mathrm{T})\|) \tag{3.8}$$

and can be represented as a 2D matrix $\mathbf{R}$ whose entries at the index pair $(i, j), i \leq j$ corresponds to the above measured recurrence. It is remarkable that when $i = j$, there exists perfect recurrence, thus its value is always equal to 1. The entries on the main diagonal of $\mathbf{R}$ is always equal to 1 by this definition. In addition, $R(j, i) = R(i, j)$ since it is equivalent to swapping the vectors.

The step function can be generalized to other strictly monotonous measurement functions with bounded outputs to have graded recurrence values (or a soft radius). Plots derived from graded measures are not true recurrence plots, but are termed unthresholded recurrence plots (URP) [48]. One such function used by the team of Meste et al. is the normalized dot product:

$$D(i, j) = \frac{\mathbf{x}(i)^{\intercal}\mathbf{x}(j)}{\|\mathbf{x}(i)\|_2\|\mathbf{x}(j)\|_2} \tag{3.9}$$

This function is related to the cosine of the angle between the two vectors. One may recall that $\cos(\phi_{u,v}) = \overrightarrow{u} \cdot \overrightarrow{v} \| \overrightarrow{u} \| \| \overrightarrow{v} \|$. By this consideration, a more intuitive description of this function can be obtained. When the two vectors are colinear, D will have a value of 1; when perpendicular, the value will be 0; when anticolinear, the value will be -1.

Further processing of the RP allowed them to obtain instantaneous autocorrelation functions that present different profiles for the two patient groups. In addition, subsequent works allowed the team to provide a descriptive mathematical model of AF [49].

3.4 Discussion & Conclusion

It has been discussed in Section 3.2 that the ECG presents stereotypical patterns strongly associated with typical (right) AFL, whilst abnormal patterns can be associated with either right or left AFL. However, presence of structural heart disease or previous ablation lesions may make it difficult to determine right or left atrium origin.

Application of advanced signal and data processing techniques were able to extract information from the ECG which cannot be done using visual inspection, as mentioned in Section 3.3. In these studies, atypical AFL was always shown to be more variable than typical AFL, as concluded by studies (1), (3), (4) and (6) from Table 3.1. It is posited then that right and left AFL should also demonstrate different variability, with the right being less variable than the left.

This can be explained in part by the electrophysiology of the atrial anatomy. The anatomy of the right atrium presents fixed, well-defined conduction blocks. The relatively large crista terminalis (CT) fibre bundle acts as a sort of waveguide, in addition to the non-conductive anatomies located between the ring of the tricuspid valve and the inferior vena cava (IVC) (see Section 2.4 for illustrations). This should cause propagation to be well-directed, hence obtaining a very similar activation sequence from cycle to cycle in right AFL.

In the left atrium, no similar anatomic structures exist that could direct the propagation. The orifices of the pulmonary veins may be seen as an equivalent structure, although it does not cover the majority of the left atrial endocardial surface area. Furthermore, there have been evidences of functional blocks across large portions of the atrial musculature due to cellular fibrosis [27, 29, 50], whose size and property may vary in time and according to various factors.

The spatiotemporal coherence approach in [39] showed a possibility of exploiting this difference in variability for right-or-left AFL localization. However, the Pearson correlation of two series essentially averages over time. The downside of this is not exploiting information regarding variability that may be observed from one beat to the next. On the other hand, the beat-to-beat approach employed by [42] and [43] allowed full use of the present variability, since it captures the variability of each cycle.

Furthermore, AFL is a quasi-periodic (and hence recurrent) process. RQA is a promising method that allows the capture of this evolution. This allows a more continuous assessment of propagation variability as opposed to a beat-to-beat approach. However, it should be regarded as a complimentary approach, and not a competing one.

To conclude this chapter, it has been assumed that due to the different electrophysiological anatomy of the right and left atrium, propagation variability should be different. This variability is different from cycle to cycle, and can be observed within the duration of each F wave. It is then proposed here an approach of beat-to-beat analysis of F waves in order to obtain this variability. To supplement this first approach, and take into account the recurrent nature of AFL, it is also proposed a recurrence quantification analysis of the atrial activity.

Chapter 4

Signal Processing Methodology for AFL Variability Extraction

4.1 Introduction

In previous chapters, the need to develop non-invasive methods for AFL localization to improve efficacy of radiofrequency ablation procedure was established. An assumption of differing circuit variability was made in regards to the different elements that contribute to this phenomenon (structuredness of right atrium, abundance of fibrosis in left atrium, etc.). Relying solely on non-invasive measures such as the 12-lead ECG, it is important to ensure that the information of interest is reliably extracted. Alas, clinical 12-lead ECG is subject to many sources of noise that make this difficult. This chapter will thus present the methodology employed to firstly condition the data and secondly to characterize the observation and to extract AFL variability features.

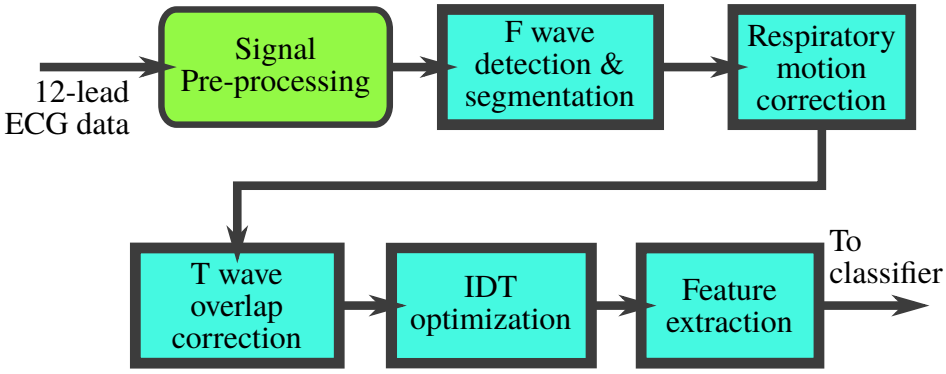

Figure 4.1: Schematic of the processing methodology. Thick blue boxes are novel contributions from this thesis.

A flowchart summary of the processing pipeline is shown in Figure 4.1. The 12-lead ECG signal is firstly pre-processed to remove variability external to the electrocardiological records (noise, power line interference) (Section 4.2). Then, F waves are detected and segmented using novel statistically rigorous detectors based on generalized likelihood ratio test (Section 4.3). Next, respiratory motion variability is removed from F waves using an original approach with improvement in classical motion parameter estimation (Section 4.4). Afterwards, T wave overlaps are corrected from F

waves by modeling the T wave spline using polynomials and subtracting them (Section 4.5). Additionally, an optimized Inverse Dower Transform–obtained using an original method–is applied, that accounts for the complexity of the bioconductive volume (Section 4.6). Finally two methods for characterizing F waves and for extracting variability features are utilized to obtain variability features (Section 4.7). A description of the dataset used in this research is given towards the end of this chapter (Section 4.8). All computational processes were implemented on MATLAB (MathWorks, USA).

It is useful to define some standard conventions concerning mathematical notations, which are used abundantly in this section. Italicized letters x or X refer to scalars. Lowercase boldface letters $\mathbf{x}$ refer to a column vector, and $\mathbf{x}^\top$ its transpose. Uppercase boldface letters $\mathbf{X}$ refer to a matrix. Sizes are described in the text, according to the context of discussion.

4.2 Signal Pre-processing

Prior to any data processing activities, it is often necessary to remove or reduce effects of unwanted noise. Not only does this serve to improve signal-to-noise ratio in parameter estimation, but it is imperative to remove all sources of noise that may introduce variability in the observation. This variability coexists with the one produced by AFL circuits, and must be removed or risk a confusion of variability sources.

Considering all the identified sources of noise discussed at the end of Section 2.3, the following filtering procedure was employed: 12-lead ECG signals were filtered at a very narrow band centered around 50 Hz using a notch filter to reduce electrical mains noise influence. Then, the signals were band-pass filtered using cascaded high-pass and low-pass filters at cutoff frequencies of $(f_{\text{lo}}, f_{\text{hi}}) = (0.5, 70)$ Hz. This attenuates out-of-band noise including most of the baseline wander components (< 0.5 Hz). The low-pass cutoff of 70 Hz attenuates high-frequency noise. The filters are Chebyshev type II IIR filters applied in a forward-backward fashion, and ensure that a steep roll-off can be achieved whilst preserving signal integrity.

Several recordings present motion artifacts that were large and cannot be filtered. These artifacts, although brief, affect certain algorithms like those for QRS detection. They were manually removed by clipping their amplitude to a level much lower than the surrounding R peak.

4.3 F Wave Detection and Segmentation

In this study, we rely on the information present inside the portion of the ECG related to the atrial activation. The ventricular activity (VA) is thus regarded as a source of noise, and must be removed in order to access the signal of interest. This is a common step in analyses of this sort, and has particularly been developed in the cardiac signal processing domain for extraction of AF atrial activity (AA).

Among the most common techniques used nowadays are related to decomposing the ECG into each individual activities: a technique commonly known as *source separation*. It may be done blindly (i.e. without any knowledge of the signal properties) [51] or accounting for some available information (e.g. quasi-periodicity [52]). The technique treats the two activities (as well as others) as signals derived from independent sources. This independence is leveraged in the algorithms which are mainly based on matrix factorization and derivation of principal components, with a post-processing step for source identification to retrieve the AA.

Another line of extraction focuses on estimating the best VA template, and assumes that it does not change substantially and has a compact temporal support [53]. The AA is regarded as random noise whose influence can be minimized by averaging of multiple VA patterns. The averaged template can then be used to subtract the VA from the ECG, leaving behind the AA. This technique is known as the *averaged beat subtraction*. A more statistical approach also exists, and directly estimates the AA overlapped within the QRS complex, using a Bayesian framework [54].

These works pertain mostly to AF, and benefits from the independence of AF AA signals from VA signals. However, in AFL, the activation is more stable. This in turn causes the VA to be highly synchronized with AA signals since the activation at the AV node should be more regular than during AF. The averaged beat subtraction method cannot reliably average out the residual AFL signal because of this. Furthermore, this essentially increases dependence of VA on AA, invalidating the assumptions in source separation methods. Linear filtering does not work because the spectral components of AFL AA overlap significantly with VA components.

There are several methods that exploit the quasi-periodicity of AA in AFL for gap-filling between the QT intervals [55, 56]. They essentially interpolate areas of missing data using the signal spectrum in order to obtain an estimate waveform. However, estimation of F waves from the spectrum is essentially artificial, and does not replicate the variability of the waves at the locally interpolated segments.

In a different view, the general pattern of AA remains similar during AFL, owing to the single circular activation of the atrium. This makes detection methods suitable for use. A single reference may be used to retrieve all other occurrences. Detection models can be modified to include additional effects that are more befitting to the observation. Because the key information is present only within the F waves, it is not necessary to extract the totality of the signal, but only segments containing F waves. Thus, in this section, we focus on the *detection and segmentation of F waves* as an alternative to whole-signal extraction.

A plethora of algorithms for ECG waves detection (P, QRS and T waves) can be found in the literature, dating back to as early as the late 80s. A majority of these algorithms employ some sort of transformation of the ECG in order to exaggerate components related to the wave of interest, or attenuate components not related to the wave of interest. This is commonly coupled with a search window–typically around an R peak–whose length is determined by physiological knowledge of standard interval values and wave duration. However, almost all these cases deal only with ECG recordings during sinus rhythm. Few methods focus on the detection of atrial waves in arrhythmic contexts; even less in the reentrant variants.

A prospective technique that aligns with many of the considered opportunities in F wave detection is the generalized likelihood ratio tests (GLRT): a technique that employs statistical modeling of the signal in order to robustify the detection. In this section, the development of several GLRT detectors, accounting for several different signal and noise models will be performed.

4.3.1 Basics of Likelihood-Ratio Tests The basis of GLRT detectors come from the theory of statistical detection [57]. To summarize, the detection problem consists in deciding whether a given *sequence* $\mathbf{s}$: $s[n], n \in [0; N-1]$ exists or not in an *observation* $\mathbf{x}$, typically modeled as a linear combination of signal and *noise* $\mathbf{w}$. The noise is considered a random variable distributed according to a specific law (Gaussian, Laplacian, etc.) with certain parameters that need not be known.

The sequence $\mathbf{s}$ may or may not be present in the observation. The aim in statistical detection is to quantify the probability of which of the two cases (formally referred to as *hypotheses*) are correct. We therefore formulate the problem as deciding between two hypotheses (a null hypothesis $\mathcal{H}_0$ and an alternative hypothesis $\mathcal{H}_1$):

$$\mathcal{H}_0 : \mathbf{x} = \mathbf{w} \tag{4.1}$$

$$\mathcal{H}_1 : \mathbf{x} = \mathbf{s} + \mathbf{w} \tag{4.2}$$

This problem is also referred to as *binary hypothesis testing*. It is obvious that by the incorporation of a random variable in the model, the resulting observation becomes random as well, and has an associated *probability density function* (PDF) $p(\mathbf{x}; \mathcal{H}, \boldsymbol{\theta})$, parameterized by the hypothesis in consideration and some *model parameters* $\boldsymbol{\theta}$.

If the PDFs of the two hypotheses are sufficiently distinct (zero overlap in PDFs for the given range of values of $\mathbf{x}$) due to very different signal properties such as e.g. bias value, frequency, etc. then it should be simple, if not obvious to decide on the correct hypothesis through some manipulations on the observation. However, this is very idealistic.

In practice, the signal of interest is embedded in possibly large-amplitude noise which deteriorates the signal-to-noise ratio (SNR), and undergoes distortions like attenuation, Doppler shifts and modulation. This makes the decision more challenging, as the alternative hypothesis $\mathcal{H}_1$ becomes very similar to the null hypothesis $\mathcal{H}_0$. In this case, the overlap induces a probability of performing an error in decision. A tradeoff needs to be made between the *probability of detection* ($P_D = \mathbb{P}\{\text{Decide } \mathcal{H}_1 \text{ when } \mathcal{H}_1 \text{ is true}\}$) and the *probability of false alarm* ($P_{FA} = \mathbb{P}\{\text{Decide } \mathcal{H}_1 \text{ when } \mathcal{H}_0 \text{ is true}\}$) given an observed value $\mathbf{x}$.

The role of the detector can be seen, from a different point of view, as a map from an observed sequence of data values to a binary decision space. A space $R^1 \subset \mathbb{R}^N$ denotes the region of data values that map to a positive decision space. For simplicity of illustration, assume $N = 1$, $\mathbf{s} = s[0] = A \approx 0.23$, and $\mathbf{w} = w[0]$ follows the univariate Gaussian distribution. Then the PDFs of an observation $x[0] = s[0] + w[0]$ under each hypothesis resembles that of Figure 4.2. The region R^1 is separated by γ, as shown. P_D and P_{FA} are shown accordingly. The *threshold* γ trades off P_D and P_{FA}. Lowering the threshold enlarges R^1 and maps more data values into the positive decision space. Observations conforming to (4.2) have higher probability of mapping into R^1, hence increasing P_D, but so will those conforming to (4.1), hence also increasing P_{FA}.

The Neyman-Pearson theorem, which is central in the statistical detection theory, provides a way to determine the best R^1 such that P_D is maximized for a given, fixed P_{FA}. This is achieved by maximizing the objective $F = P_D + \lambda(P_{FA} - \alpha)$, with α a fixed probability of false alarm. A crucial result can be obtained:

$$T(\mathbf{x}) = \frac{p(\mathbf{x}; \mathcal{H}_1, \boldsymbol{\theta}_1)}{p(\mathbf{x}; \mathcal{H}_0, \boldsymbol{\theta}_0)} = \frac{p_{\mathcal{H}_1}}{p_{\mathcal{H}_0}} \underset{\mathcal{H}_0}{\overset{\mathcal{H}_1}{\gtrless}} \gamma \tag{4.3}$$

Interpretation of this is rather simple: if a sequence has a ratio of likelihoods greater than γ (the boundary of the decision space), then it is probably a signal present, else it

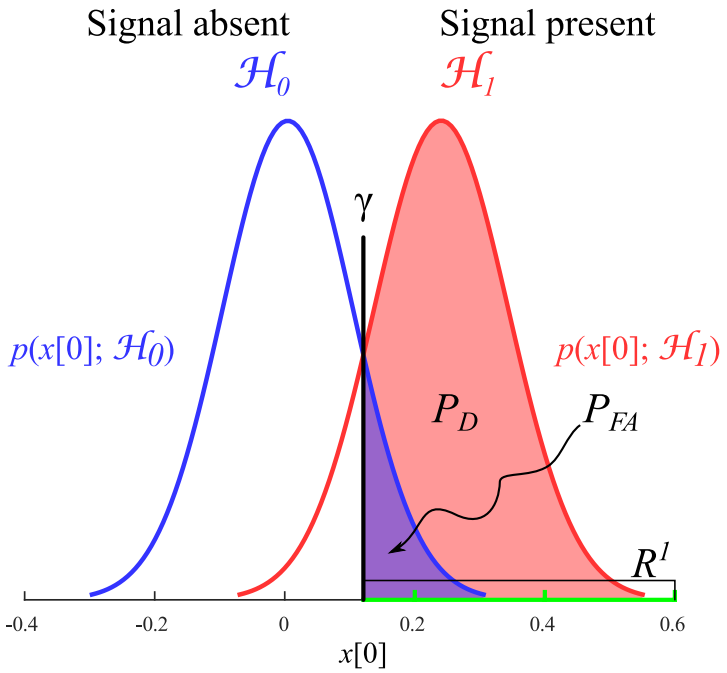

Figure 4.2: Illustration of hypothetical Gaussian normal PDFs under different hypotheses. γ represents the threshold of decision. The region R^1 is highlighted in green.

is a signal absent. The expression of the *likelihood ratio test* $T(\mathbf{x})$ can be developed to obtain an implementable and practical detector. In the case where the parameter $\boldsymbol{\theta}$ is unknown, it needs to be estimated to arrive at an implementable detector. The test in this case is called a *generalized likelihood ratio test* (GLRT).

4.3.2 Signal Models In order to find a proper GLRT for the AA detection problem, a *signal model* must be formulated. As was discussed previously, one particularly useful information is the regular and periodic nature of F waves. This provides some ease, as the model complexity can be limited instead of requiring e.g. spline estimation of the F wave to obtain a general representation [58]. We assume that a template F wave is available. This wave should be selected according to its distance with respect to a QRS complex. A single F wave that is far from the preceding QRS complex and just before the succeeding one, in order to isolate ventricular activity as much as possible, was manually selected for all patients. Note that this selection criteria implies that the AV block ratio be sufficiently large. We consider block ratios of 3:1 and higher, although this is not an exclusive criteria. With careful consideration, several signals with a block ratio of 2:1 were also used, provided that the VA components are sufficiently distinct.

4.3.2.1 Basic Model The most basic signal model that is considered is

$$\mathbf{x} = A\mathbf{s} + \mathbf{w} \tag{4.4}$$

where again, $\mathbf{x}$ is the observation, $\mathbf{s}$ the target sequence, $\mathbf{w}$ the observation noise, and A is a *known* scale value. A generalization of this model can be obtained when A is assumed to be unknown.

$$\mathbf{x} = A\mathbf{s} + \mathbf{w}, \quad A \text{ unknown} \tag{4.5}$$

This takes into account some amplitude modulation that may affect the observation from beat to beat, such as electrode impedance change due to improper contact or body movement, and amplifier gain errors. Note that if A is considered unity (i.e. no modulation), then (4.5) becomes (4.4).

The signal models above constitute the alternative hypothesis $\mathcal{H}_1$. Their corresponding null hypothesis $\mathcal{H}_0$ is

$$\mathbf{x} = \mathbf{w} \tag{4.6}$$

4.3.2.2 Detection Under T Wave Overlap The previous signal models should be sufficient for detection in conditions where there is only AA present in the signal. However, on the ECG, there are VA that coexist with AA. This causes overlaps of VA on top of AA, hence several F waves may be 'masked' by VA. It thus makes the previous signal models insufficient for detection when there is significant overlap, which typically occurs during very fast atrial rates and low AV block ratio.

Fortunately, the contributions of the VA can be modeled. This is possible due to the assumption of F wave regularity. Any F wave has a similar morphology to the template F wave. The overlapped F wave could be seen as equal to the template F wave with an additional low-frequency spline, representing a portion of the VA. This portion of VA can modeled mathematically by a basis of independent functions. In this research, we consider the *polynomial basis* for modeling of overlap components. The signal model can be written then as:

$$\begin{aligned}
\mathbf{s}_o &= \mathbf{s} + \sum_{k=0}^{K} b_k \mathbf{h}^k = \mathbf{s} + \mathbf{H}\mathbf{b} \\
\mathbf{h}^k &= \begin{bmatrix} 0^k & 1^k & 2^k & \cdots & (N-1)^k \end{bmatrix}^\intercal \\
\mathbf{H} &= \begin{bmatrix} \mathbf{h}^0 & \mathbf{h}^1 & \mathbf{h}^2 & \cdots & \mathbf{h}^K \end{bmatrix} \\
\mathbf{b} &= \begin{bmatrix} b_0 & b_1 & b_2 & \cdots & b_K \end{bmatrix}^\intercal
\end{aligned} \tag{4.7}$$

where $\mathbf{s}_o$ denotes the target sequence superposed by a polynomial spline $\mathbf{Hb}$, $\mathbf{H} \in \mathbb{R}^{N \times K}$ being the polynomial basis and $\mathbf{b} \in \mathbb{R}^K$ the weights of each component.

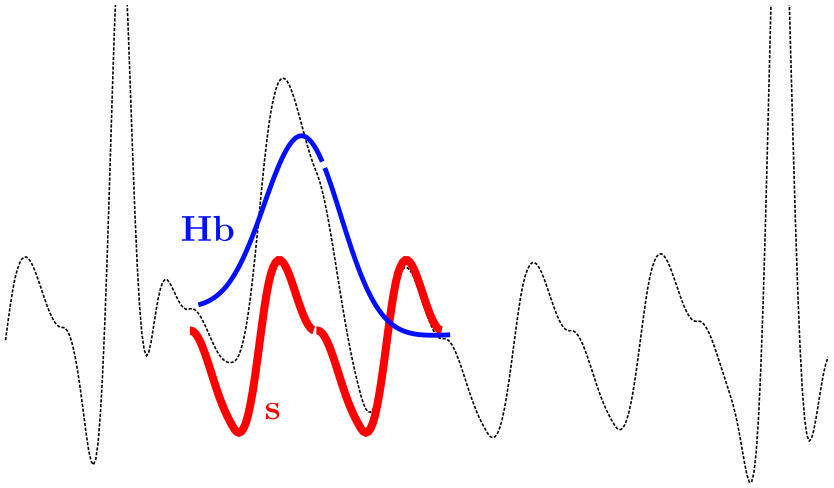

Figure 4.3: Illustration of the T wave overlap in ECG with AFL. Black dotted lines represent an ECG recording. Blue lines represent the overlapping VA spline, and thick red lines represent the actual AA at the duration of observation.

Illustration of this overlap is given in Figure 4.3. Note that the overlapping component is different for each F wave, and depends on the local contribution of the VA. It is expected that when overlap is taken into account in the signal model, and proper estimation of parameters is performed, the result would be better detection performance as compared to models without account of overlaps. Thus, two more signal models are proposed:

$$\mathbf{x} = A\mathbf{s} + \mathbf{Hb} + \mathbf{w} \tag{4.8}$$

$$\mathbf{x} = A\mathbf{s} + \mathbf{Hb} + \mathbf{w}, \quad A \text{ unknown} \tag{4.9}$$

The signal models above constitute the alternative hypothesis $\mathcal{H}_1$. Their corresponding null hypothesis $\mathcal{H}_0$ is

$$\mathbf{x} = \mathbf{Hb} + \mathbf{w} \tag{4.10}$$

The complexity of the polynomial basis plays a role in obtaining a good estimate of overlap components: the higher the polynomial order, the better. However, this would lead to overfitting on the observation as the basis obtains more degrees of freedom. Furthermore, polynomial basis is known to suffer from increasing estimation error at the 'edges' of the observation with increasing degrees of freedom, due to spurious splines, attributed to the equidistancing of the sample points (Runge's phenomenon) [59]. In general, the maximum polynomial degree K should be kept low (e.g. below 4), and are

rarely used above 5.

By including the template wave in (4.8) and (4.9), there exists a possibility of ill-posedness. This is because $\mathbf{s}$ might not be orthogonal to the polynomial basis i.e. $\mathbf{s} = \mathbf{H}\mathbf{b}_s + \boldsymbol{\epsilon}$, where $\mathbf{b}_s$ are the model coefficients that approximate $\mathbf{s}$, and $\boldsymbol{\epsilon}$ the systemic error in approximation. This may be ignored if $\|\boldsymbol{\epsilon}\|_2$ is relatively large, or in other words, if the polynomial degree is kept relatively low (and hence $\mathbf{s}$ is pseudo-orthogonal to the basis). To the author's knowledge, there isn't any method of determining K such that the problem remains well-conditioned. K is thus empirically set to 3. This is deemed appropriate as it adds slightly more complexity than a standard 2nd order polynomial, but is relatively low-order such that it does not overfit the data, or cause spurious estimate or rank-deficiency.

4.3.3 Practical Derivation of Detectors Many statistical estimation frameworks rely on the knowledge of the distribution of the signal model. In the case of GLRTs, knowledge of this distribution up to a certain extent is crucial in order to derive a closed-form expression of the tests. It is well known that the Gaussian distribution is widely considered in many estimation problems, one of the reason being the inherent simplicity (and tractability) of the mathematical development of estimators under this assumption.

An observation $\mathbf{w}$ distributed according to the Gaussian law $\mathcal{N}(\boldsymbol{\mu}, \mathbf{C}_w)$ with the location vector $\boldsymbol{\mu}$ and covariance matrix $\mathbf{C}_w$ has the following PDF:

$$p(\mathbf{w}; \boldsymbol{\mu}, \mathbf{C}_w) = \frac{1}{(2\pi)^{\frac{N}{2}} |\mathbf{C}_w|^{\frac{1}{2}}} e^{-\frac{1}{2}(\mathbf{w}-\boldsymbol{\mu})^\intercal \mathbf{C}_w^{-1} (\mathbf{w}-\boldsymbol{\mu})}$$

We assume that the noise samples $\mathbf{w}$ are independent and identically distributed (i.i.d.). This simplifies the estimation procedure as the covariance matrix $\mathbf{C}_w$ reduces to $\sigma_w^2 \mathbf{I}$ where $\mathbf{I} \in \mathbb{R}^{N \times N}$ is the identity matrix and σ_w^2 the sample variance. The PDF thus reduces to:

$$p(\mathbf{w}; \boldsymbol{\mu}, \sigma_w^2) = \frac{1}{(2\pi\sigma_w^2)^{\frac{N}{2}}} e^{-\frac{1}{2\sigma_w^2}(\mathbf{w}-\boldsymbol{\mu})^\intercal (\mathbf{w}-\boldsymbol{\mu})} \tag{4.11}$$

It has been mentioned in Section 2.3 that outlier-prone noise such as muscle artifacts and ectopic beats are more pronounced in ECG recordings. This constitutes a more heavy-tailed noise distribution than Gaussian. Typically, we can consider the Laplacian distribution as a distribution of choice to model this effect. A noise $\mathbf{w}$ distributed according to the Laplace law Laplace$(\boldsymbol{\mu}, \sigma_w^2)$ with the location vector $\boldsymbol{\mu}$ and variance

σ_w^2 and under the same i.i.d. assumption has the following PDF:

$$p(\mathbf{w}; \boldsymbol{\mu}, \sigma_w^2) = \frac{1}{(2\sigma_w^2)^{\frac{N}{2}}} e^{-\sqrt{\frac{2}{\sigma_w^2}} \sum_{n=0}^{N} |(w[n]-\mu[n])|} \tag{4.12}$$

The expression in (4.12) is the multivariate version of the form derived in [57] and [60]. It is known that the multivariate Laplace PDF was described differently using a much more complex, multi-parametered model [61]. However, a simpler model has been employed in this research under the assumption of sample independence, as the complex model may be difficult to manipulate. Results discussed in later sections show that it is indeed adequate.

As an illustration, the next section describes an example workout of a detector (detector T_1 from Table 4.1).

4.3.3.1 Derivation of Detector: Example of Model (4.4) To obtain a practical detector, the Neyman-Pearson theorem in (4.3) has to be developed according to the assumptions on the parameters. An example is provided below. Assume an observation $\mathbf{x}$ embedded in Gaussian noise of mean $\boldsymbol{\mu}_\mathbf{x}$. Substituting the PDF expressions accordingly and simplifying, we have:

$$\frac{p_{\mathcal{H}_1}}{p_{\mathcal{H}_0}} = T(\mathbf{x}) = \left(\frac{\sigma_0^2}{\sigma_1^2}\right)^N e^{-\frac{1}{2}\left(\frac{1}{\sigma_1^2}\|\mathbf{x}_1-\boldsymbol{\mu}_1\|_2^2 - \frac{1}{\sigma_0^2}\|\mathbf{x}_0-\boldsymbol{\mu}_0\|_2^2\right)} \tag{4.13}$$

The test statistics expression can be developed according to the selected model. For the purpose of demonstration, assume the model in (4.5) is selected. $\mathbf{x} = A\mathbf{s} + \mathbf{w}$ with $\mathbf{w}$ a zero-centered vector Gaussian noise. The expression above becomes:

$$\begin{aligned} T(\mathbf{x}) &= \left(\frac{\sigma_0^2}{\sigma_1^2}\right)^N e^{-\frac{1}{2}\left(\frac{1}{\sigma_1^2}\|\mathbf{x}-A\mathbf{s}\|_2^2 - \frac{1}{\sigma_0^2}\|\mathbf{x}\|_2^2\right)} \\ &= \left(\frac{\sigma_0^2}{\sigma_1^2}\right)^N e^{-\frac{1}{2}\left(\frac{1}{\sigma_1^2}(\mathbf{x}-A\mathbf{s})^\intercal(\mathbf{x}-A\mathbf{s}) - \frac{1}{\sigma_0^2}\mathbf{x}^\intercal\mathbf{x}\right)} \end{aligned}$$

It is further assumed, for the simplicity of demonstration, that the variances $\sigma_\mathbf{w}^2$ are known and equal under both hypotheses. This essentially means that we consider a stationary noise on the observed data, and that the F wave amplitude is constant across

any subsequent observation. The simplified likelihood ratio is:

$$T(\mathbf{x}) = e^{\frac{1}{2\sigma_w^2}(2A\mathbf{x}^\intercal\mathbf{s} - A^2\mathbf{s}^\intercal\mathbf{s})} > \gamma$$

In order to arrive to a more convenient form, we obtain the log-likelihood ratio by applying a natural logarithm on both sides:

$$\begin{aligned}\ln T(\mathbf{x}) = T'(\mathbf{x}) &= \ln\ e^{\frac{1}{2\sigma_w^2}(2A\mathbf{x}^\intercal\mathbf{s} - A^2\mathbf{s}^\intercal\mathbf{s})} \\ &= \frac{1}{2\sigma_w^2}\left(2A\mathbf{x}^\intercal\mathbf{s} - A^2\mathbf{s}^\intercal\mathbf{s}\right) > \gamma' = \ln\gamma\end{aligned}$$

We observe that all the quantities of the left-hand side are known. The final form of the detector is obtained by applying the following transform:

$$A^{-1}2\sigma_w^2 T'(\mathbf{x}) + \frac{A}{2}\mathbf{s}^\intercal\mathbf{s} = T''(\mathbf{x}) = \mathbf{x}^\intercal\mathbf{s} > \gamma'' = A^{-1}2\sigma_w^2\gamma' + \frac{A}{2}\mathbf{s}^\intercal\mathbf{s} \tag{4.14}$$

This particular detector is known as the *replica-correlator*, or *matched filter* [57].

When a more heavy-tailed noise distribution is considered such as the Laplacian distribution, the PDF expression changes. Note that instead of the transposed matrix multiplication, a sum of absolute values is found instead. The simplified likelihood ratio, with the same considered case concerning parameter values, is written as follows:

$$\begin{aligned}\frac{p_{\mathcal{H}_1}}{p_{\mathcal{H}_0}} = T(\mathbf{x}) &= \left(\frac{\sigma_0^2}{\sigma_1^2}\right)^{\frac{N}{2}} e^{-\left(\sum_{n=0}^{N-1}\sqrt{\frac{2}{\sigma_1^2}}|x_1[n]| - \sqrt{\frac{2}{\sigma_0^2}}|x_0[n]|\right)} \\ &= e^{-\sqrt{\frac{2}{\sigma_w^2}}\left(\sum_{n=0}^{N-1}|x[n]_1| - |x_0[n]|\right)} \\ &= e^{-\sqrt{\frac{2}{\sigma_w^2}}\left(\sum_{n=0}^{N-1}|x[n] - As[n]| - |x[n]|\right)} > \gamma\end{aligned}$$

In order to arrive to a more convenient form, we obtain the log-likelihood ratio:

$$\frac{\sigma_w^2}{2}\ln T(\mathbf{x}) = T'(\mathbf{x}) = \sum_{n=0}^{N-1}|x[n]| - |x[n] - As[n]| > \gamma' = \frac{\sigma_w^2}{2}\ln\gamma \tag{4.15}$$

The expression can be made symmetric by considering $y[n] = x[n] - \frac{A}{2}s[n]$, hence the two summands become $\left|y[n] + \frac{A}{2}s[n]\right|$ and $\left|y[n] - \frac{A}{2}s[n]\right|$, which are the difference of absolute deviations of $y[n]$ about $s[n]$. This does not change the detector properties.

4.3.4 Model Parameter Estimation The development of detectors depend on the considered model and its parameters, which condition the PDF under each hypothesis. In this research, the considered the parameters are the scale factor of the sequence A, the sample noise variance σ_w^2 and the T wave polynomial wights $\mathbf{b}$. These can be assumed to be a known, fixed value. However, they can be assumed unknown, and so must be estimated from the data itself, or from an auxiliary data (the so-called *estimate-and-plug approach*).

Typically, the parameter estimation is done using a *maximum likelihood estimation* approach (MLE) [62]: an asymptotically optimal (i.e. approaches optimum performance only with large amounts of data) but tractable procedure consisting of estimating the parameters with the goal of maximizing the value of the PDF. This is seen in a probabilistic sense as obtaining a parameter estimate that is most likely to occur (i.e. estimate a parameter $\boldsymbol{\theta}$ such that $p(\mathbf{x};\boldsymbol{\theta})$ is maximum). To perform such an estimation, it is customary to work with the derivative of the log-likelihood function $\partial \ln p(\mathbf{x};\boldsymbol{\theta})/\partial\boldsymbol{\theta}$, and evaluating it at 0. This reflects an estimation done at the inflection point of the PDF, now viewed as a likelihood function. Observing the expressions in (4.11) and (4.12), the terms in the exponentials, which are the subject of optimization in MLE, are essentially the L_2- and L_1-norm of a zero-centered variable.

4.3.4.1 Least-square estimation It is known that the setup in the L_2 case is treated as the *least squares* (LS) estimation problem. LS is a classical estimation procedure that is simple to perform. Coupled with the MLE objective (i.e. evaluating $\partial \ln p(\mathbf{x};\boldsymbol{\theta}) = 0$), this allows a simple solution to the LS problem. LS is a popular estimation technique due to the fact that on observations that are distributed according to Gaussian normal, the estimate is equivalent to the MLE, hence it is asymptotically optimal.

Another area that focuses on solving LS problems is optimization. The goal here is to estimate the parameter $\boldsymbol{\theta}$ that allows a minimization or maximization of a certain goal function $J = \|\mathbf{x} - \mathbf{H}\boldsymbol{\theta}\|_2$. The optimal solution is found commonly using:

1. the closed-form *normal equations*, or
2. computational methods where the feasible parameter space is explored

Solution 1) arises from evaluating $\partial J/\partial\boldsymbol{\theta} = 0$. Note that the expression develops to:

$$\begin{aligned} &\frac{\partial}{\partial\boldsymbol{\theta}}(\mathbf{x}^\top\mathbf{x} + \boldsymbol{\theta}^\top\mathbf{H}^\top\mathbf{H}\theta - 2\mathbf{x}^\top\mathbf{H}\boldsymbol{\theta}) = 0 \\ \Leftrightarrow &2\mathbf{H}^\top\mathbf{H}\boldsymbol{\theta} - 2\mathbf{H}^\top\mathbf{x} = 0 \end{aligned}$$

$$\Rightarrow \hat{\boldsymbol{\theta}} = (\mathbf{H}^\intercal \mathbf{H})^{-1} \mathbf{H}^\intercal \mathbf{x} = \mathbf{H}^\dagger \mathbf{x}$$

When resubstituting the solution back into J, the expression becomes $\|\mathbf{x} - \mathbf{H}\mathbf{H}^\dagger \mathbf{x}\|_2 = \|\mathbf{x} - \mathbf{P}_H \mathbf{x}\|_2$, or essentially the norm of the difference between the observation and the projection of itself onto the subspace spanned by $\mathbf{H}$ via the projector matrix $\mathbf{P}_H$. The expression can be further simplified by $\|(\mathbf{I} - \mathbf{P}_H)\mathbf{x}\|_2 = \|\mathbf{P}_H^\perp \mathbf{x}\|_2$, where the matrix $\mathbf{P}_H^\perp$ is the orthogonal projector matrix of $\mathbf{H}$.

Computational methods include the *gradient descent* method that performs an iterative minimization of J according to a controlled update:

$$\boldsymbol{\theta}^{(k+1)} = \boldsymbol{\theta}^{(k)} - \alpha \frac{\partial J(\boldsymbol{\theta}^{(k)})}{\partial \boldsymbol{\theta}}$$

with the superscript (k) denoting the k-th iteration, and α an update weight.

The latter is sometimes preferred when the number of independent basis is large. Using normal equations, the matrix operations have a complexity of $O(NM^2 + M^3)$ and can become expensive to calculate in a large M setting.

4.3.4.2 Least-absolute deviation estimation In the case of L_1, the problem is referred to as *least absolute deviation* (LAD) estimation problem. Unlike the LS problem, the LAD problem does not have a direct closed-form solution due to the use of the non-analytic absolute value function $|\cdot|$. They are exclusively solved using computational methods [63, 64]. In LAD, the goal surface is shaped like a polyhedron, with flat faces and edges (Figure 4.4). Analysis and demonstration showed that the LAD problem is a convex optimization problem [65] with possibly infinitely many solutions, depending on the problem. LAD estimation is equivalent to the MLE under Laplacian noise.

In general, two methods exist to solve this problem: descent algorithms which attempt to move on the edges and vertices in order to descend to the location of lowest goal [65–67], and simplex methods, which treat the problem as a series of linear programs with constraints, and attempt to solve them via a sequence of pivot operations [68].

In this research, the method of steepest descent was used to solve the LAD problem [65], termed here as the L_1 gradient descent (L1GD). The method can be resumed as follows. Let an initial solution be $\mathbf{b}^{(i)} \in \mathbb{R}^K$, and the fitting problem attempts to minimize $\|\mathbf{H}\mathbf{b} - \mathbf{x}\|_1$:

1. Calculate the gradient $\mathbf{g} = -\operatorname{sgn} \mathbf{v}^\intercal \mathbf{H}$ with $v[n] = \mathbf{H}(n)\mathbf{b}^{(i)} - x[n]$. The function sgn returns the sign of an element (1 or -1) and is applied element-wise. $\mathbf{H}(n)$

denotes the n-th row of $\mathbf{H}$

2. Calculate the projection $\mathbf{w} = \mathbf{X}\mathbf{g}^\intercal$ and residuals $\mathbf{z} = \mathbf{x} - \mathbf{H}\mathbf{b}^{(i)}$

3. Calculate the learning parameter $t = z_{k^*}/w_{k^*}$ where k^* is the index at which $\sum_{k=1}^{K} |w_k| = \frac{1}{2}\sum_{k=1}^{K} |w_k|$

4. Compute the next point $\mathbf{b}^{(i+1)} = \mathbf{b}^{(i)} + t\mathbf{g}$

5. If any $v[n] = 0$, test the condition to stop, else determine the best direction of the gradient by flipping the sign of that $v[n]$ (by multiplying with 1 or -1) and removing the contribution of the gradient of these points

The stopping condition is rather complicated, involving an algebraic analysis of the minimum point, which in theory should not have a gradient. To summarize, the algorithm tests the stopping condition when the gradient evaluation in Step 5 does not return a valid gradient.

An example iteration of this algorithm can be seen in Figure 4.4 for synthetic data. The objective is $\min_{\mathbf{a}} \|\mathbf{x}-\mathbf{H}\mathbf{a}\|_1$ with $\mathbf{x} = \mathbf{H}\mathbf{a}^*+\mathbf{w} \in \mathbb{R}^4$ an observation embedded in Laplacian noise $\mathbf{w}$ with $\sigma_w^2 = 1.4$, $\mathbf{H} = [\mathbb{1}\ \mathbf{n}]$ with $\mathbb{1}$ the vector of all ones, $\mathbf{n} = [-1\ -\frac{1}{3}\ \frac{1}{3}\ 1]^\intercal$ and $\mathbf{a} = [A_1\ A_2]^\intercal$. The true value of the weights $\mathbf{a}^*$ are $A_1^* = 1.5$ and $A_2^* = 2.5$ and their position in the parameter space is marked by a black crosshair in Figure 4.4(a) and Figure 4.4(b).

Starting at the point $\mathbf{a}^{(i)} = [-6\ 10]^\intercal$, the algorithm iterates until convergence. For comparative purposes, Figure 4.4(a) displays the cost surface calculated using the L_2 norm, whereas Figure 4.4(b) uses the L_1 norm. In implementing this algorithm for use with the Laplacian detectors, the initial point is taken as the LS solution of the equation. This is a good technique to achieve faster convergence since it could be that the minima under L_1 and L_2 are not far.

4.3.4.3 Practicalities on Parameter Estimation We consider the following cases of estimation:

1. Constant F wave morphology, stationary noise:
   no parameters are estimated

2. Modulated F wave morphology, stationary noise:
   only A is estimated for both $\mathcal{H}_0$ and $\mathcal{H}_1$

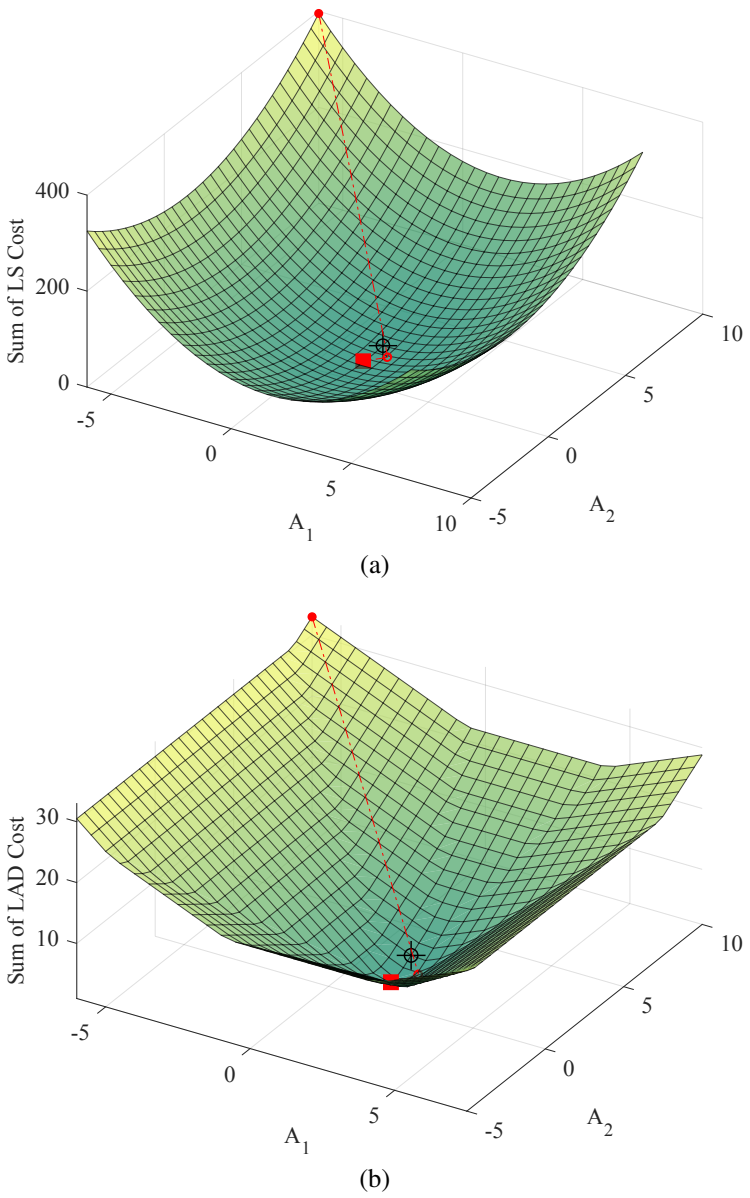

Figure 4.4: Illustration of the L_2 and L_1 goal surface. The red line and dots show the L1GD path and goal value at each iteration. The red square indicates the minimum found by L1GD.

3. Constant F wave morphology, non-stationary noise:
   only σ_w^2 is estimated for both $\mathcal{H}_0$ and $\mathcal{H}_1$

4. Modulated F wave morphology, non-stationary noise:
   both A and σ_w^2 are estimated for both $\mathcal{H}_0$ and $\mathcal{H}_1$

When the estimation of the scale A or the variance σ_w^2 is ignored (i.e. assumed constant), they will be set equal to 1. Some information for the estimation of the noise variance can be found in Appendix A. All four cases above are also considered under account of VA overlap. In those cases, the parameters of the T wave spline $\mathbf{b}$ will also be estimated

for both $\mathcal{H}_0$ and $\mathcal{H}_1$.

Note that in the discussion so far, the model of observation for only aims at determining the presence or absence of a target sequence $\mathbf{s}$ that is completely captured within the length of the observation $\mathbf{x}$. Often times, this sequence may be subject to a delay n_0 such that:

$$\mathcal{H}_0 : \tilde{\mathbf{x}} = \tilde{\mathbf{w}} \tag{4.16}$$

$$\mathcal{H}_1 : \tilde{\mathbf{x}}(n_0) = \tilde{\mathbf{s}}(n_0) + \tilde{\mathbf{w}} \tag{4.17}$$

where the tilde indicates addition of M samples, and

$$\tilde{\mathbf{s}}(n_0) = \begin{cases} \tilde{s}[n] = s[n - n_0] & n \in [n_0; n_0 + N - 1] \\ 0 & \text{otherwise} \end{cases}$$

This means that the template is located within a large observation window at a certain delay. In addition to requiring the estimation of model parameters, the optimal delay must be estimated as well. This is achieved through a test of all possible values of n_0, which can be typically viewed as a sliding window of length N across the entire recording. The selection of the best n_0 can be performed as follows.

Consider $0 < m < n_0 < N - 1$, and the matched filter detector T_1 for simplicity. The sliding window can be written as:

$$T_1(\mathbf{x}) = \sum_{n=m}^{m+N-1} \tilde{x}[n] s[n - m]$$

Under $\mathcal{H}_1$, the detector expression can be split into

$$T_1(\mathbf{x}) = \begin{cases} \sum_{n=m}^{n_0-1} \tilde{s}[n] s[n - m] & = S_1 \\ \sum_{n=n_0}^{m+N-1} \tilde{s}[n] s[n - m] & = S_2 \end{cases}$$

with the noise term neglected. It is clear that if $m \neq n_0$, then the first sum occurs within the instants before apparition of the template signal. Therefore, S_1 should theoretically equal to zero. S_2 corresponds to the correlation of a misaligned signal with its template. As m approaches n_0, S_2 becomes larger due to reduction of the misalignment error. When $m = n_0$, S_1 can be neglected, and S_2 equals $\mathbf{s}^\intercal \mathbf{s} = \varepsilon_s$. When $m > n_0$, misalignment occurs again, hence the value of the non-zero sum decreases.

Hence, the estimator of n_0 is:

$$\hat{n}_0 = \arg\max_{n_0} \; T(\tilde{\mathbf{x}}(n_0)) \tag{4.18}$$

In other words, the maximum or peak of the test output indicates the time instant where the signal is aligned with the template. An example can be seen in Figure 4.5, where the test value presents peaking at the location of F waves.

4.3.5 Summary of Detector Expressions Table 4.1 summarizes the various detectors that were used, considering all estimation cases, and under different noise distributions. The complete workout of detector expressions is not provided; a partial workout is provided in Appendix A. An example output of the detector is given in Figure 4.5.

Table 4.1: GLRT expressions

	Estimate?			$\mathbf{x} \sim \mathcal{N}$	$\mathbf{x} \sim$ Laplace
	A	σ_w^2	$\mathbf{b}$		
(1)				$T_1(\mathbf{x}) = \mathbf{x}^\intercal \mathbf{s}$	$T_9(\mathbf{x}) = \sum_{n=0}^{N-1} \operatorname{sgn}(x[n]) s[n]$
(2)	✓			$T_2(\mathbf{x}) = \mathbf{x}^\intercal \mathbf{P}_s \mathbf{x}$	$T_{10}(\mathbf{x}) = \sum_{n=0}^{N-1} \lvert x[n] \rvert - \lvert x[n] - \hat{A} s[n] \rvert$
(3)		✓		$T_3(\mathbf{x}) = \dfrac{\mathbf{x}^\intercal \mathbf{s} - \frac{A}{2} \mathbf{s}^\intercal \mathbf{s}}{(\mathbf{x} - A\mathbf{s})^\intercal (\mathbf{x} - A\mathbf{s})}$	$T_{11}(\mathbf{x}) = \sum_{n=0}^{N-1} \dfrac{\lvert x[n] \rvert}{\lvert x[n] - A s[n] \rvert}$
(4)	✓	✓		$T_4(\mathbf{x}) = (N-1) \dfrac{\mathbf{x}^\intercal \mathbf{P}_s \mathbf{x}}{\mathbf{x}^\intercal \mathbf{P}_s^\perp \mathbf{x}}$	$T_{12}(\mathbf{x}) = \sum_{n=0}^{N-1} \dfrac{\lvert x[n] \rvert}{\lvert x[n] - \hat{A} s[n] \rvert}$
(5)			✓	$T_5(\mathbf{x}) = \mathbf{x}^\intercal \mathbf{P}_H^\perp \mathbf{s}$	$T_{13}(\mathbf{x}) = \sum_{n=0}^{N-1} \lvert x[n] - \hat{t}_0[n] \rvert - \lvert x[n] - A s[n] - \hat{t}_1[n] \rvert$
(6)	✓		✓	$T_6(\mathbf{x}) = (\mathbf{x}^\intercal \mathbf{P}_H^\perp \mathbf{s})(\mathbf{s}^\intercal \mathbf{P}_H^\perp \mathbf{s})^{-1} (\mathbf{x}^\intercal \mathbf{P}_H^\perp \mathbf{s})$	$T_{14}(\mathbf{x}) = \sum_{n=0}^{N-1} \lvert x[n] - \hat{t}_0[n] \rvert - \lvert x[n] - \hat{A} s[n] - \hat{t}_1[n] \rvert$
(7)		✓	✓	$T_7(\mathbf{x}) = \dfrac{\mathbf{x}^\intercal \mathbf{P}_H^\perp \mathbf{s} - \frac{A}{2} \mathbf{s}^\intercal \mathbf{P}_H^\perp \mathbf{s}}{(\mathbf{x} - A\mathbf{s})^\intercal \mathbf{P}_H^\perp (\mathbf{x} - A\mathbf{s})}$	$T_{15}(\mathbf{x}) = \sum_{n=0}^{N-1} \dfrac{\lvert x[n] - \hat{t}_0[n] \rvert}{\lvert x[n] - A s[n] - \hat{t}_1[n] \rvert}$
(8)	✓	✓	✓	$T_8(\mathbf{x}) = \dfrac{(\mathbf{x}^\intercal \mathbf{P}_H^\perp \mathbf{s})(\mathbf{s}^\intercal \mathbf{P}_H^\perp \mathbf{s})^{-1} (\mathbf{x}^\intercal \mathbf{P}_H^\perp \mathbf{s})}{(\mathbf{x}^\intercal \mathbf{P}_H^\perp \mathbf{x}) - (\mathbf{x}^\intercal \mathbf{P}_H^\perp \mathbf{s})(\mathbf{s}^\intercal \mathbf{P}_H^\perp \mathbf{s})^{-1} (\mathbf{x}^\intercal \mathbf{P}_H^\perp \mathbf{s})}$	$T_{16}(\mathbf{x}) = \sum_{n=0}^{N-1} \dfrac{\lvert x[n] - \hat{t}_0[n] \rvert}{\lvert x[n] - \hat{A} s[n] - \hat{t}_1[n] \rvert}$

$\hat{A}$ is the MLE estimate using L1GD in Laplace; $\mathbf{P}_s$ and $\mathbf{P}_s^\perp$ are the projector and orthogonal projector of $\mathbf{s}$ respectively; $\mathbf{P}_H^\perp$ is the orthogonal projector of $\mathbf{H}$; $\hat{\mathbf{t}}_n = \mathbf{H}\hat{\mathbf{b}}_{\mathcal{H}_n}$; sgn is the sign function

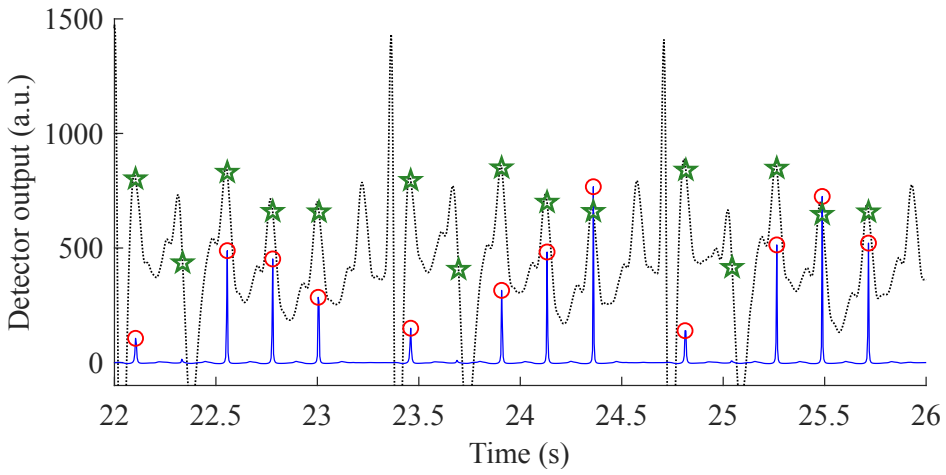

Figure 4.5: Example of T_7 GLRT detector output in the multilead setup (blue line). Red circles indicate the peaks of test value where $\hat{n}_0^{(i)}$ for the i-th F wave is found. The reference annotation is given by green stars. Lead V_1 is shown for comparison (black dotted line).

4.3.6 Multilead Extension Most detectors that are found in the literature use only single-lead recordings. This may be preferred in ambulatory monitoring setting and usually eases the algorithm to perform online, real-time detection due to the small data volume. Offline detection, however, is not limited by these constraints, and may benefit from the spatial richness of the data in performing detection. Therefore, a multilead strategy for the given detectors of Table 4.1 was also considered. The rationale for this is that integrating more leads should theoretically increase information content, and give better detection.

To obtain multilead expressions of each detector, some information is required on the covariant relation between leads. This would introduce a spatial covariance into the model. If the matrix observation $\mathbf{W} \in \mathbb{R}^{N\times M}$ composing N samples sorted in rows, of M leads sorted in columns is vectorized by stacking the matrix columns to form a tall vector $\text{vec}(\mathbf{W}) \in \mathbb{R}^{NM}$, then the multivariate PDF (assume Gaussian noise) can be written as:

$$p(\text{vec}(\mathbf{W}); \text{vec}(\mathbf{M}), \mathbf{C}_{WM}) = \frac{1}{(2\pi)^{\frac{NM}{2}} |\mathbf{C}_w|^{\frac{1}{2}}} e^{-\frac{1}{2}(\text{vec}(\mathbf{W})-\text{vec}(\mathbf{M}))^\intercal \mathbf{C}_{WM}^{-1} (\text{vec}(\mathbf{W})-\text{vec}(\mathbf{M}))}$$

where $\mathbf{M}$ indicates the matrix of the means of each lead and $\mathbf{C}_{WM}$ the covariance matrix of the vectorized observations.

The covariance matrix determines the properties of the relation between each time sample and each lead. In this research, this covariance is simplified by considering it to be a scaled identity $\mathbf{C}_{WM} = \sigma_w^2 \mathbf{I}$. This is essentially assuming a multichannel noise.

With this simplification, the Laplacian PDF can also be defined.

The assumption of no covariance between leads essentially makes them independent of each other. What this allows is to write the PDF as a follows:

$$\begin{aligned} p(\text{vec}(\mathbf{W}); \text{vec}(\mathbf{M}), \sigma_w^2) &= \frac{1}{(2\pi\sigma_w^2)^{\frac{NM}{2}}} e^{-\frac{1}{2\sigma_w^2}(\text{vec}(\mathbf{W})-\text{vec}(\mathbf{M}))^\intercal(\text{vec}(\mathbf{W})-\text{vec}(\mathbf{M}))} \\ &= \frac{1}{(2\pi\sigma_w^2)^{\frac{NM}{2}}} e^{-\frac{1}{2\sigma_w^2}\sum_{m=1}^{M}(\mathbf{w}_m-\boldsymbol{\mu}_m)^\intercal(\mathbf{w}_m-\boldsymbol{\mu}_m)} \\ &= \prod_{m=1}^{M}\left(\frac{1}{(2\pi\sigma_w^2)^{\frac{N}{2}}} e^{-\frac{1}{2\sigma_w^2}(\mathbf{w}_m-\boldsymbol{\mu}_m)^\intercal(\mathbf{w}_m-\boldsymbol{\mu}_m)}\right) \\ &= \prod_{m=1}^{M} p(\mathbf{w}_m; \boldsymbol{\mu}_m, \sigma_w^2) \end{aligned}$$

Following this result, the Neyman-Person theorem from (4.3) can be written then as:

$$T(\mathbf{x}) = \prod_{m=1}^{M} \frac{p(\mathbf{x}_m; \mathcal{H}_1, \boldsymbol{\theta}_1)}{p(\mathbf{x}_m; \mathcal{H}_0, \boldsymbol{\theta}_0)} \underset{\mathcal{H}_0}{\overset{\mathcal{H}_1}{\gtrless}} \gamma \tag{4.19}$$

where m denotes the lead number. This essentially means that the likelihood ratio of a multilead observation reduces to a product of likelihood ratios of all available leads. In practice, the product may become a sum when a logarithm is applied to obtain the final detector expression. Information on this can be found in Appendix A.

It is important to note here that the assumption of a scaled identity matrix for the covariance $\mathbf{C}_{WM}$ is necessary to obtain multilead detectors under Laplacian noise. As was mentioned earlier, the multivariate Laplacian distribution has a complex form [61], and does not allow an easy (or possibly even tractable) manipulation of the expression.

4.3.7 Detector Parameter Selection

4.3.7.1 Threshold Selection The test expressions as described above form a part of the detector, on one hand. On the other hand, the threshold value is equally important for a detector to function at a determined level of performance. The determination of a threshold value is however an open question: a detection objective will condition the threshold value to be taken, fixing as a result the detection performance. One aim in developing these detectors is automatic detection of F waves, meaning that an optimum threshold γ_{opt} should be found such that P_D is optimized, whilst keeping a reasonable P_{FA}.

The determination of this threshold, as well as its corresponding P_D and P_{FA} can be made analytically. This will require knowledge of the *test PDF*: something which is not readily available and may be difficult to derive, especially when a relatively complex model is considered. Furthermore, it is difficult in the case of Laplacian detectors due to non-trivial expressions of random variable algebra. Therefore, the threshold determination problem is posed differently.

It has been mentioned that $T(\mathbf{x})$ performs a map $T : \mathbb{R}^N \mapsto \mathbb{R} = R^0 \cup R^1$ (R^0 is the negative decision space). It is possible to view this problem as a binary classification problem. Detected F waves will appear as high-valued maxima in the test values, which is on average different than noise. Local maxima corresponding to false detections may appear, but their values should be significantly smaller than those of the F waves.

Therefore, γ_{opt} should be found such that the separation between the two classes–measurable by the accuracy–is optimized. This opens the problem to the use of methods from machine learning. Cross-validation (CV) is one example of such a method, and is detailed in Chapter 6. CV allows finding of a separation point that is not overly dependent on the data.

4.3.7.2 Single-Lead Selection Strategy F wave manifestation quality is different in each lead, due to the position of the different electrodes with regards to the reentrant circuit as well as bioelectric conductivity in the direction of the lead vectors. This translates to varying levels of SNR in each lead. Detector performance is impacted by this, but it is difficult to evaluate SNR in AFL due to the absence of an isoelectric baseline for lead selection. In addition, VA magnitude is different in each lead, hence it makes little sense in selecting an arbitrary lead. Two strategies for this are considered, based on the highest ratio between the energy of the template F wave to its corresponding 1) T wave (F-to-T selection criterion) and 2) QRS complex (F-to-QRS selection criterion).

4.3.7.3 Test Setup To select the best threshold, as well as to assess the best lead selection strategy, a CV approach is considered. From the 56 recordings that were obtained from the data acquisition process (see Section 4.8), 25 recordings were manually processed. These recordings were downsampled to 250 Hz to reduce the number of points.

First, a template F wave $\mathbf{s}$ is delineated manually on all 25 recordings. In AFL with high AV block ratio (3:1 and above), it is possible to obtain this easily. Alternatively, intermittent long RR intervals due to abnormal AV conduction behavior may provide a section with non-overlapped F waves. The template wave is segmented approximately

from the onset of the wave until the end.

Then, a least-square criteria $J = \|\mathbf{x} - \mathbf{s} - \mathbf{Hb}\|_2$ is calculated within a sliding window across the whole signal. The polynomial basis (order 3) allows the capture of waves within the VA overlap. From the minima of J, the waves are delineated by hand at a fixed length, equal to that of the template wave. The criteria serves as a guide to selecting the waves, and in some cases, manual correction is made. In total, there were 2930 delineated F waves.

The detectors in Table 4.1 were then used to calculate the GLRT output on all 25 recordings. Then, all maxima or peaks from the output are obtained using a peak finding algorithm. It is remarkable that the QRS complex presents a challenge for detection, as the SNR is too poor within this duration. Therefore, from the GLRT output, points inside the QRS duration were removed. Labels were assigned to each detected peak to determine whether if it was a true detection, or a false alarm. This is determined by evaluating the timing error with respect to the nearest known manual annotation. The largest peak within range of 25 ms counts as a true detection.

Cross-validation was then performed on the set of all obtained peaks of each detector. For each recording, all peaks were normalized by the range of value, given as the difference between the max peak and min peak. This ensures that the points of all recording have similar range of values, hence comparable to each other despite the difference in SNR among the recordings. The threshold value is defined as the percentile of the value of the peaks, varying between 0 (i.e. the minimum peak value) until 100 (i.e. the maximum peak value) in steps of 1. The modified leave-one-out CV routine in Section 5.2 is performed. To remove bias in the learning, at each CV iteration, all the peaks of the recording used as the test set is not included in the training set.

4.3.8 Results and Discussions Figure 4.6 and Figure 4.7 summarizes the cross-validated performance of all 8 detectors on the subset of 25 AFL recordings. F-to-T selection refers to the criterion of selecting the lead with the largest ratio of F wave energy to T wave energy, and F-to-QRS selection refers to the criterion of selecting the lead with the largest ratio of F wave energy to QRS complex energy. M-Lead represents the multilead setup. It can be seen that the majority of the detectors don't have good performances, as evidenced by values of accuracy and AUC below 0.75 in general. However, in Gaussian detectors (T_1 - T_8), it can be seen that performance is significantly higher when considering estimation of the noise variance (T_3,T_4,T_7,T_8) since the performance figures are generally above 0.75. This suggests that the detection

problem in this case presents non-stationary noise profile, which is properly handled by detectors that estimate the noise variance. Laplacian detectors are however more homogeneous across the whole range of model. It could be that the assumption of heavy-tailed noise is also suitable to a certain extent, therefore these detectors are able to compensate for it. However, estimating noise variance did not show increased performance in these detectors.

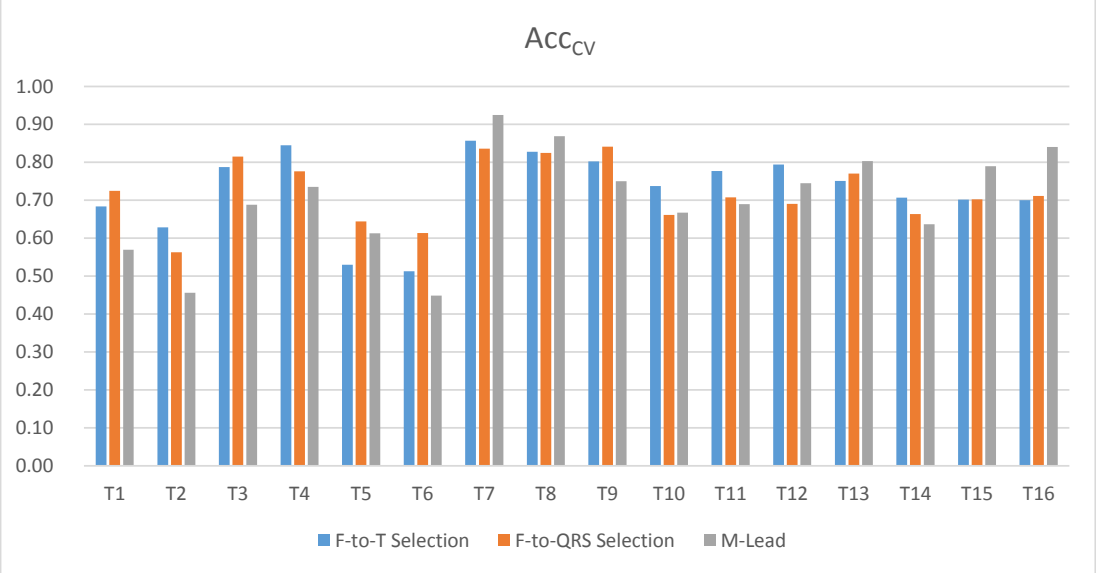

Figure 4.6: Summary chart of the LOOCV accuracy at the optimal point for all detectors.

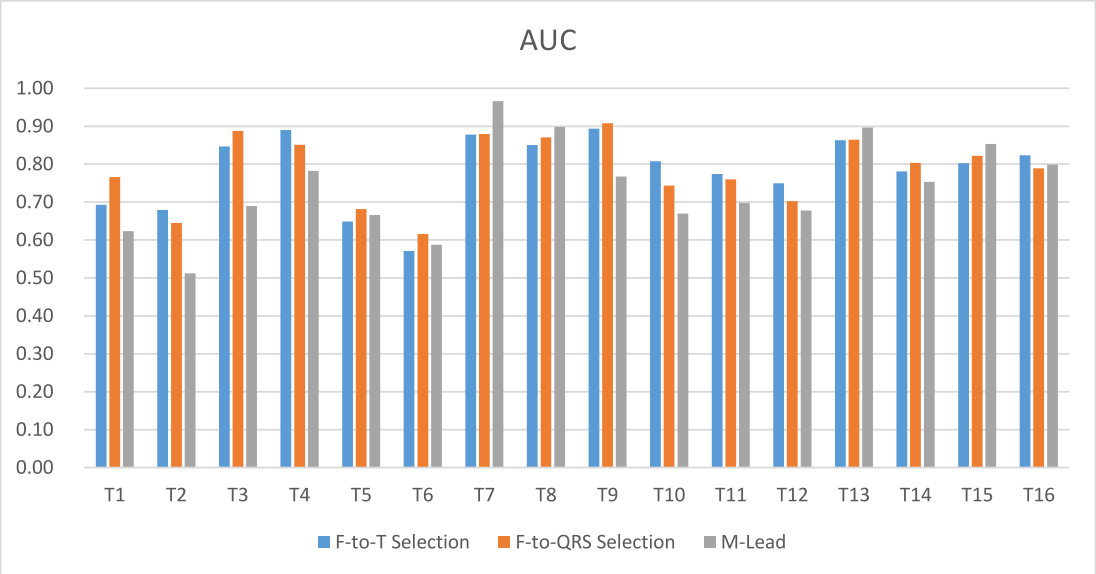

Figure 4.7: Summary chart of the LOOCV AUC for all detectors.

The pseudo-ROC curves for all detectors can be found in Figure 4.8, Figure 4.9 and Figure 4.10 for single leads (F-to-T strategy and F-to-QRS stategy) and multilead

models respectively. In detectors T_1, T_2, T_5 and T_6 a severe deterioration is observed. During cross-validation, it had been observed that the peaks in several recordings caused the procedure to fail by persistently misclassifying peaks and produce 0 probability of detection, but full probability of false alarm. One possible explanation of this problem is that the set of peaks are not independent and well-distributed draws of the test distribution, hence when a certain set is removed and given the right γ, the calculation of probabilities are biased. There is no easy way to correct this, therefore the values of γ for which this happens is omitted. The pseudo-ROC curves can be seen to contain missing portions which are represented by a straight line. This may have diminished the measure of performance. Nevertheless, according to the available portions of pseudo-ROC curves, these four detectors do not have a very great performance. Interestingly, this does not happen with Laplacian detectors under the same assumption, and they also exhibit better performance. It can be suggested that the heavy-tail assumption is better for detectors that do not estimate the noise variance, as is said earlier.

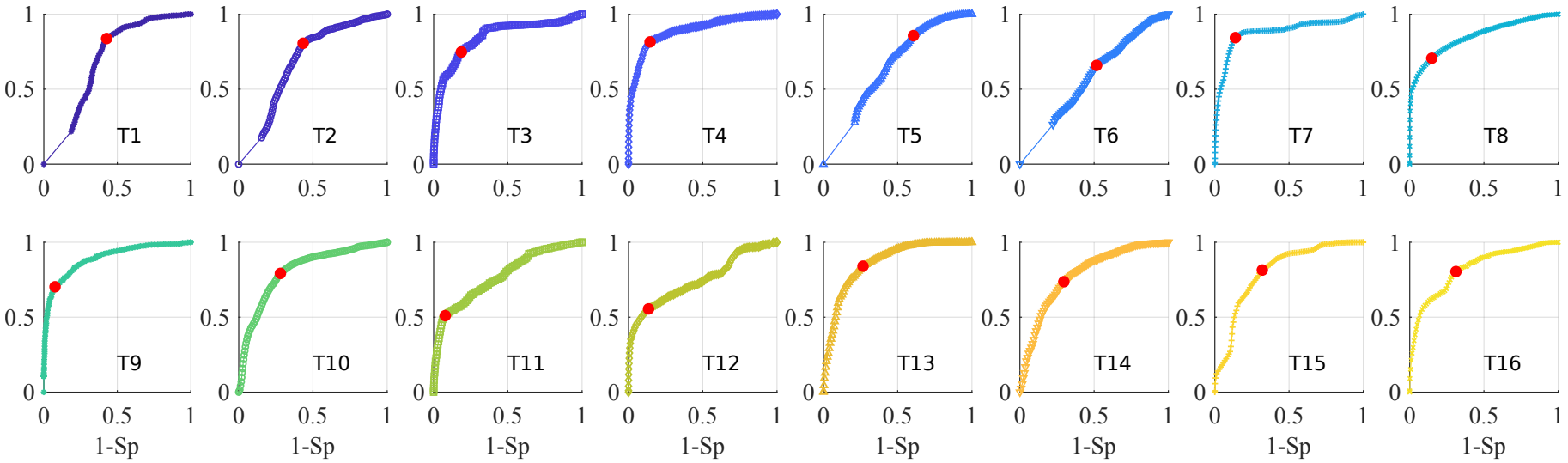

Figure 4.8: Pseudo-ROC curves for single lead GLRT using the F-to-T selection criterion. Red dots indicate the optimal point determined by the maximum of Youden's J criterion.

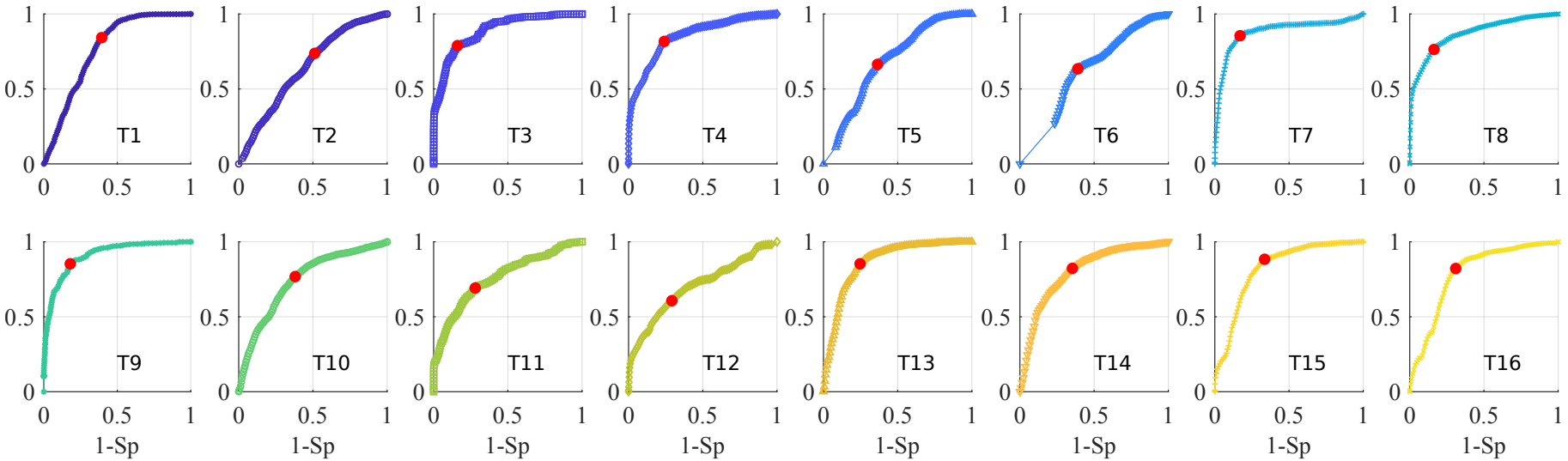

Figure 4.9: Pseudo-ROC curves for single lead GLRT using the F-to-QRS selection criterion. Red dots indicate the optimal point determined by the maximum of Youden's J criterion.

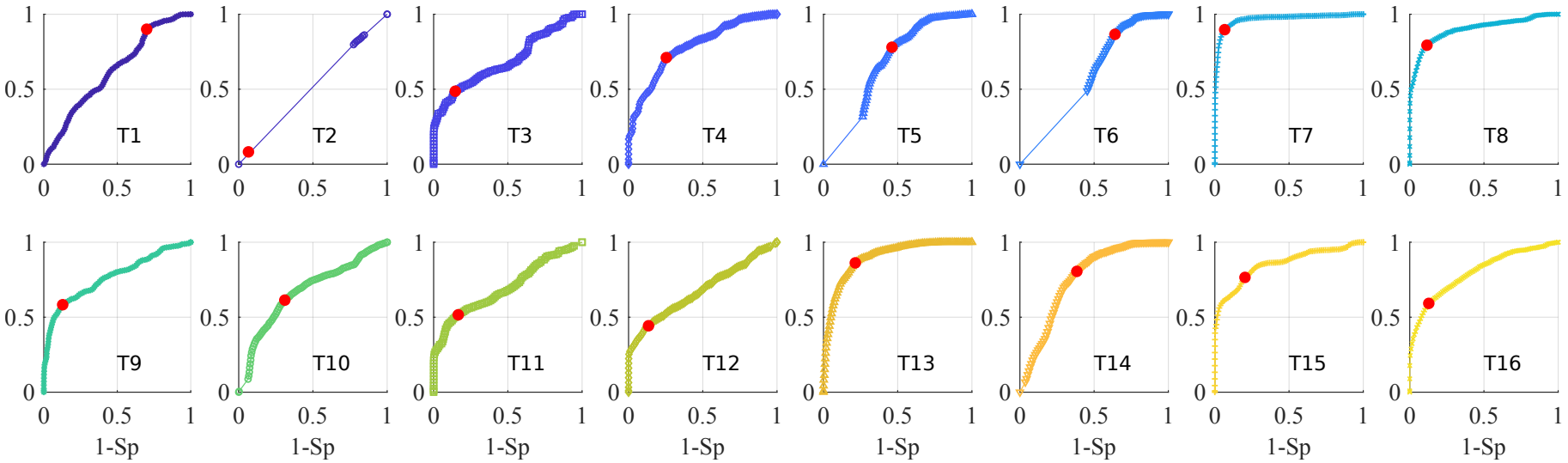

Figure 4.10: Pseudo-ROC curves for multilead GLRT. Red dots indicate the optimal point determined by the maximum of Youden's J criterion.

It is observed that using F-to-T criterion did not give better performance in general, compared to F-to-QRS criterion in selecting the lead of choice for single-lead detectors. Inspecting the F-to-QRS energy ratios in the lead selected using F-to-T criterion showed very similar ratio values to the lead selected using F-to-QRS criterion (median absolute relative difference 1.13%). The same can be said when doing the opposite (median absolute relative difference 0.78%). It can be concluded that either criteria can be used to select the best lead. By examining which leads are selected, it was found that a preference for limb leads is remarked (60% and 72% of the recording for F-to-T and F-to-QRS, respectively). It could be that because the precordial leads are closer to the ventricles, the QRS and T magnitudes are generally higher, therefore the selection avoids these leads rather than preferring limb leads.

Inspection of the AUC chart (Figure 4.7) and pseudo-ROC curves (Figure 4.8, Figure 4.9 and Figure 4.10) shows some promising detectors in both single-lead and multilead configuration. In particular, detector T_7 in multilead configuration achieved the highest accuracy as well as AUC ($\text{Acc}_{\text{CV}} = 0.93$, AUC = 0.97). Example of its output is shown in Figure 4.5. The automatic detection threshold is found to be $\gamma_{\text{opt}} = 24.0 \cdot 10^{-3}$, selected by finding the maximum point of Youden's J statistic $\text{J}_{\text{CV}}(\gamma) = \text{Se}_{\text{CV}}(\gamma) + \text{Sp}_{\text{CV}}(\gamma) - 1$ (refer to Section 5.2 for information on performance indices). Furthermore, it was among the top scorers in a single-lead configuration, with the best accuracy using F-to-T selection criterion ($\text{Acc}_{\text{CV}} = 0.86$, AUC = 0.88). This illustrates that a multilead approach is able to supplement the detector performance. In terms of timing accuracy, it was reported to have an error of $0.28 \pm 1.30\, ms$: a rather good performance. A second-best detector is T_9, which performs better in single-lead using the F-to-QRS criterion, with a $\gamma_{\text{opt}} = 0.66$ ($\text{Acc}_{\text{CV}} = 0.84$, AUC = 0.91, timing accuracy 0.29 ± 4.05 ms).

4.3.9 Application on Experimental Dataset The two best detectors presented above were used to detect F waves on the remaining recordings in the dataset described in Section 4.8. Manual inspection was performed to remove any false detection. The best-aligned output among the two detectors was selected to ensure that the set of F waves are temporally aligned for further processing. The result of this step is the obtention of segmented F waves, representing the atrial activity. The number of waves obtained was 64 ± 48, given as the mean and standard deviation.

It is important to note that some of these detected F waves are overlapped with VA. Therefore, it is important to separate them from those which are not overlapped, as their treatment should be different. Therefore, two sets of F wave are introduced: the set of pure, non-overlapped waves $\mathcal{F}_{\text{p}}$, and the set of overlapped waves $\mathcal{F}_{\text{o}}$. Throughout

the chapter, many references will be made to these notation, in order to identify them accordingly. Later chapters will also refer to these notations for identifying sets and associated treatments.

It is notable that the effects of respiration, as discussed in Section 4.4 also affect the F waves. Despite this, these effects are not integrated into any of the signal models of the detector. It could be hypothesized that by correcting these effects, the detection performance may increase. However, the results of Section 4.4 show that the F wave morphology is minimally affected by respiration, hence it should, in theory, not affect detection much. This is a strong counterargument to the aforementioned hypothesis.

In passing, it is worth to note that the methodology of detector development detailed here is not restricted to only obtain a high-performance F wave detector, but can also be generalized to the detection of any repetitive physiological sequence with a constant or quasi-constant form. In particular, by accounting for a low-frequency spline, the signal model in (4.8) and (4.9) can be used to perform e.g. QRS detection under large baseline wander and noise.

4.4 Respiratory Motion Correction

Respiratory motion has been shown to induce morphological changes in the ECG. This is caused by physiological and geometrical changes of the thorax, thus affecting bioelectric conductance and lead position relative to the heart. It is evident that this constitutes a (rather prominent) source of variability, which should be removed. It is worthy to mention that the changes brought about by respiration cannot be completely removed by linear filtering.

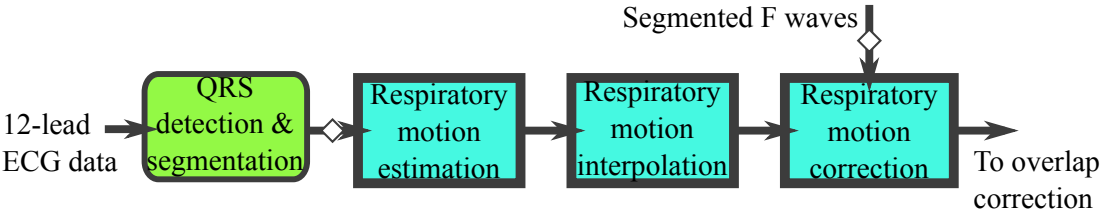

Figure 4.11: Schematic of the respiratory motion correction procedure on F waves. Arrows with diamonds indicate application of IDT. Thick blue boxes indicate novel approaches employed in this thesis.

A summary of the methodology in this section can be found in Figure 4.11. The blue, thick-edged boxes correspond to novel approaches used to correct the effects of respiratory motion from the F wave observations, thus removing the variability associated with the phenomenon. Note that the results in this section are obtained from the analysis of motion correction on the set $\mathcal{F}_{\mathrm{p}}$ only.

4.4.1 Estimation of Respiratory Motion ECG-derived respiratory motion estimation is a well-researched area of cardiac signal processing. Many techniques exist in the literature: the earliest works were done by Moody et al. and Pinciroli et al. [69, 70]. Both of them analyzed the change in the cardiac electrical axis, obtained from 2D vectorcardiographic loops using 2 different leads. The resulting estimated motion is very close to direct measures of respiratory motion using e.g. pneumatic transducer.

The concept of changes in the Frank's VCG during respiration was later studied in [71], where a nice set of respiratory motion parameter estimators was presented. The motion parameters directly reflect the effect of respiration on the VCG and particularly for QRS complexes, it reflects changes affecting the QRS loops in the XYZ space (see Figure 2.11).

The effects of respiratory motion on the VCG loops were assumed to be a scaling of the loop (i.e. increase or decrease in loop size), attributed to the change in impedance, and a rotation of the loop, attributed to the movement of the electrodes. Mathematically,

these effects are written as:

$$\mathbf{X} = \alpha\mathbf{S}\mathbf{Q} \tag{4.20}$$

where $\mathbf{S} \in \mathbb{R}^{N\times 3}$ represents a reference loop, α the loop scaling factor, $\mathbf{Q} \in \mathbb{R}^{3\times 3}$ the loop rotation factor. This formulation is called (although not explicitly) the primal formulation, and illustrates the respiratory motion effect on a reference loop to produce a subsequent loop $\mathbf{X}$. An equivalent formulation can be written as:

$$\mathbf{S} = \beta\mathbf{X}\mathbf{R} \tag{4.21}$$

where $\beta = \alpha^{-1}$ and $\mathbf{R} = \mathbf{Q}^\intercal$. This alternative form was referred to as the dual formulation and illustrates the reference as being the result of the correction of the effects of respiratory motion. The estimated parameter values should then reflect the amount by which one should correct the observation.

The estimators of β and $\mathbf{R}$ were obtained by assuming that the observation model was embedded in a multichannel white Gaussian noise (i.e. $\mathbf{S} = \beta\mathbf{X}\mathbf{R} + \mathbf{W}$). Using a MLE framework, the parameter estimates are the minimizers of the least-square error $J = \|\beta\mathbf{X}\mathbf{R} - \mathbf{S}\|_F^2$. This particular problem is known as the (extended) orthogonal Procrustes problem[1], which aims to find the best parameters $\hat{\beta}$ and $\hat{\mathbf{R}}$ that maps $\mathbf{X}$ to $\mathbf{S}$. There are many ways to solve this problem: one through the use of singular value decomposition (SVD) pioneered by Schönemann [72], and one through the use of quaternion rotations, developed by Horn et al. [73]. This research focuses on the SVD method.

SVD aims to provide a complete representation of an observation in a basis spanned by orthogonal, singular vectors $\mathbf{V} = [\mathbf{v}_1\ \mathbf{v}_2\ \mathbf{v}_3]$. These vectors indicate, in the original basis, the directions corresponding to the highest variances. They have associated singular values $\mathbf{\Lambda} = \mathrm{diag}(\lambda_1, \lambda_2, \lambda_3),\ \lambda_1 > \lambda_2 > \lambda_3$ that rank the directions from the highest variance to the lowest (possibly zero) variance. The mathematical operator diag indicates the arranging of the scalar values into the diagonals of a square matrix, and all other entries are set to 0.

Note that:

$$J = \mathrm{tr}(\mathbf{S}^\intercal\mathbf{S}) + \beta^2\,\mathrm{tr}(\mathbf{R}^\intercal\mathbf{X}^\intercal\mathbf{X}\mathbf{R}) - 2\beta\,\mathrm{tr}(\mathbf{R}^\intercal\mathbf{X}^\intercal\mathbf{S})$$

The middle term is equivalent to $\mathrm{tr}(\mathbf{X}^\intercal\mathbf{X})$, hence the only term with dependence on

[1]Procrustes was a Greek mythological persona who lived between Athens and Eleusis, a town northwest of Athens. He was a blacksmith who had an iron bed, and everytime a traveller would come by, he would invite them to sleep on the bed. If they did not fit on the bed, then he would amputate them to either stretch them out or fit them into the bed frame. He was eventually 'fitted' into his own bed by Theseus.

$\mathbf{R}$ is the third. Performing SVD, $\mathbf{X}^\intercal\mathbf{S} = \mathbf{U}\mathbf{\Lambda}\mathbf{V}^\intercal$. It is suggestive then that by setting $\mathbf{R} = \mathbf{X}^\intercal\mathbf{S}$ the third term becomes the aggregate of the squared matrix spectrum $\text{tr}(\mathbf{\Lambda}^2)$, and J is minimized, but this violates the orthogonality of $\mathbf{R}$. Hence, to fulfill this constraint, $\hat{\mathbf{R}} = \mathbf{U}\mathbf{V}^\intercal$. Using this result, and evaluating the partial derivative of J with respect to β allows us to obtain $\hat{\beta} = \text{tr}(\hat{\mathbf{R}}^\intercal\mathbf{X}^\intercal\mathbf{S})/\text{tr}(\mathbf{X}^\intercal\mathbf{X}) = \text{tr}(\mathbf{\Lambda})/\text{tr}(\mathbf{X}^\intercal\mathbf{X})$.

To summarize, the parameter estimates are given by:

$$\mathbf{X}^\intercal\mathbf{S} = \mathbf{U}\mathbf{\Lambda}\mathbf{V}^\intercal$$

$$\hat{\mathbf{R}} = \mathbf{U}\mathbf{V}^\intercal \tag{4.22}$$

$$\hat{\beta} = \frac{\text{tr}(\mathbf{\Lambda})}{\text{tr}(\mathbf{X}^\intercal\mathbf{X})} \tag{4.23}$$

The rotation factor $\mathbf{R}$ can be decomposed into 3 submatrices $\mathbf{R} = \mathbf{R}_X\mathbf{R}_Y\mathbf{R}_Z$, each one a standard 3×3 rotation matrix describing a rotation about the associated axis. By working out the expression of the multiplication, the matrix $\mathbf{R}$ has the form:

$$\mathbf{R} = \begin{bmatrix} * & \cos\phi_Y \sin\phi_Z & \sin\phi_Y \\ * & * & \sin\phi_X \cos\phi_Y \\ * & * & * \end{bmatrix}$$

with the asterisk denoting irrelevant entries. Three rotation angles ϕ_X, ϕ_Y, ϕ_Z: one for each axis, can be obtained:

$$\phi_X = \arcsin\left(\frac{r_{2,3}}{\cos(\phi_Y)}\right)$$

$$\phi_Y = \arcsin(r_{1,3})$$

$$\phi_Z = \arcsin\left(\frac{r_{1,2}}{\cos(\phi_Y)}\right)$$

with $r_{i,j}$ denoting the entry at the i-th row and j-th column of the matrix $\mathbf{R}$.

4.4.2 Correcting the Rotation Matrix It is remarkable that (4.22) relies on the singular vectors $\mathbf{V}$. This subspace spans the directions of maximum variance, with each direction orthogonal to each other. Although orthogonality is a specified constraint, orientation is not. Hence, the vectors are free to assume a direction or one opposite to it.

Given a certain combination of ambiguity in the direction (which is in essence an ambiguity in sign), the product $\mathbf{U}\mathbf{V}^\intercal$ may produce not a rotation, but a *reflection*. A reflection matrix $\mathbf{R}_r$ does minimize the criterion J, but does not represent a strict

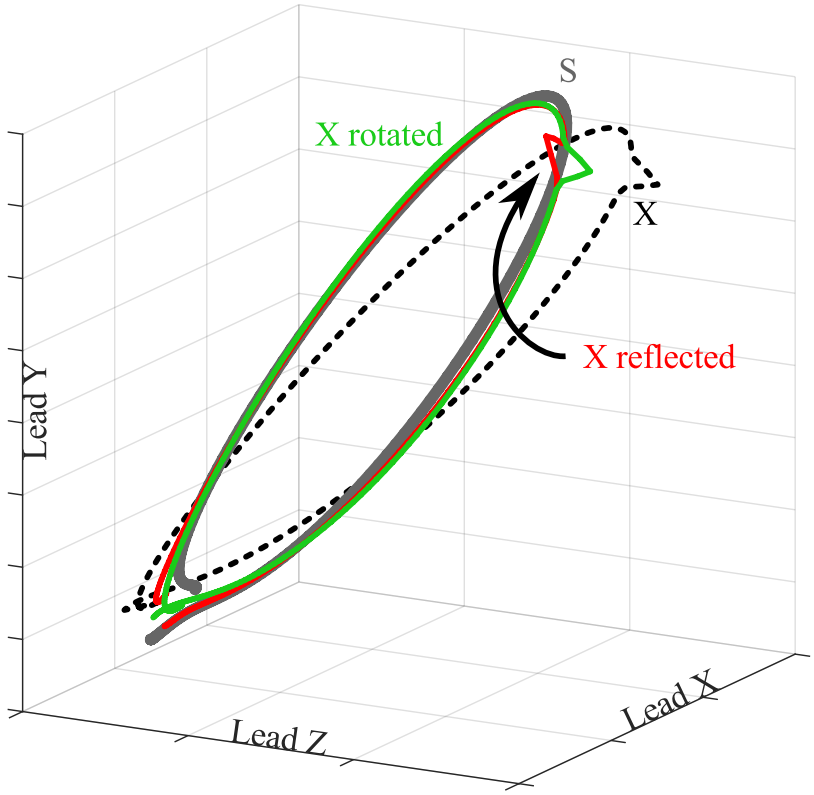

Figure 4.12: Illustration of rotation degeneracy on QRS loops, where **R** performs a reflection. The thick grey loop **S** represents the reference, with the black loop (broken lines) an observation to be synchronized. The red and green loops result from application of (4.21) when **R** is a reflection matrix and strict rotation matrix respectively. Noise spike was added before performing the transform, for clarity. Notice the opposing orientation during reflection.

rotation. This is caused in theory by degeneracy in the data, such that two set of points become coplanar (residing on the same plane) but not collinear (does not reside on the same line) [74]. This is impossible in real life, yet they signaled this issue in their publication. Furthermore, it was also observed in our dataset during estimation of parameters, illustrated by Figure 4.12, where an observed loop (dashed black line) is synchronized to a reference (thick line). The transform calculated from the vectors issued by `svd` in MATLAB gives a reflection (red line). It is never clear why such a case could appear, but it is assumed to be due to the computation of the SVD itself.

The effect of this on respiratory motion parameter estimation is the obtention of spurious angle values. This effect is illustrated in 4.13, where the red dashed line is the motion parameter estimate issued from the reflection matrix. Some values were significantly large ($> 80°$) and is clearly an outlier with respect to the mean value of the series, which was significantly below the outlier ($< 10°$). This constitutes an impossibility in terms of physiological values of rotation and therefore must be rectified, or risk a form of

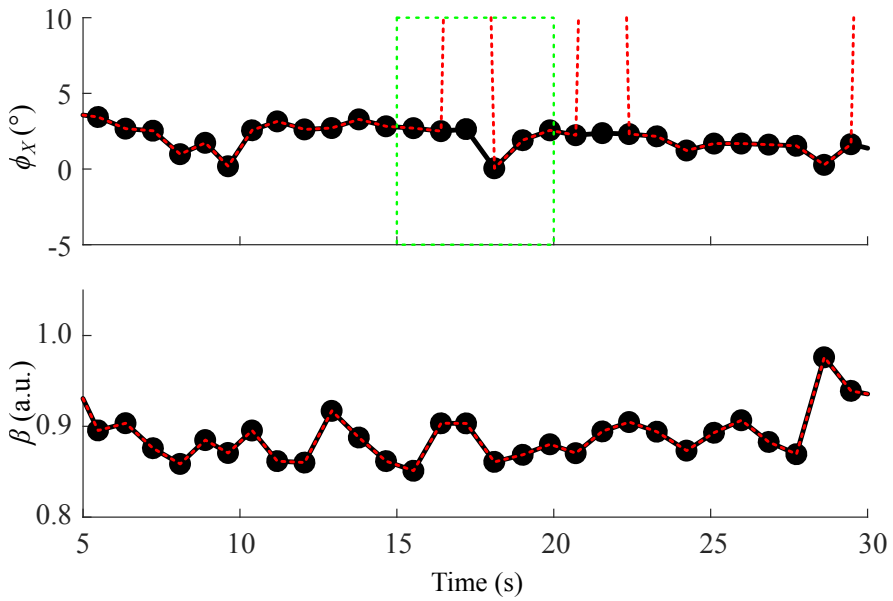

Figure 4.13: Effect of the reflection matrix on the motion parameter estimate. Only ϕ_X and β are shown for conciseness. Red broken lines represent the uncorrected parameter estimate. Note the spikes between seconds 15 and 25 in ϕ_X (peak value around 80°). Corrected parameter estimate (black line with dots) is more continuous and correct. Note that the series is discrete: the lines serve only as visual support.

variability that may enter into the correction procedure due to wrong parameter values. However, scale parameters do not suffer this problem, as seen in the illustration.

4.4.2.1 Subspace Alignment Approach for Correcting R It is fortunately possible to correct this effect by introducing several constraints to the estimation procedure. The subspace directions $\mathbf{V}$ should be consistent for all loops of a given recording. This can be obtained by aligning all subspaces to a reference subspace, which is the one obtained from the reference loop $\mathbf{S} = \mathbf{X}_R$. To do this, the SVD was calculated using a different algorithm. In the following, $\mathbf{s}$ is used in notation, but does not refer to the reference loop of the previous section.

SVD can be viewed as essentially an estimation of an unknown vector $\mathbf{s}$ weighted by $\mathbf{a}$, derived from a set of observations $\mathbf{Z} = [\mathbf{z}_1\ \mathbf{z}_2\ \cdots \mathbf{z}_K]$, embedded in Gaussian noise. The objective is to minimize $\|\mathbf{Z} - \mathbf{s}\mathbf{a}^\top\|_F$. This is in line with the notion of SVD finding the optimal subspace onto which the projection of the data minimizes the least-square error. Applying LS estimation, we obtain $\hat{\mathbf{a}} = \mathbf{Z}^\top\mathbf{s}/\mathbf{s}^\top\mathbf{s}$ and $\hat{\mathbf{s}} = \mathbf{Z}\mathbf{a}/\mathbf{a}^\top\mathbf{a}$. Note that $\hat{\mathbf{s}}$ is essentially a weighted average of the observations.

It is shown in Appendix B that the objective is minimized when $\hat{\mathbf{a}} = \mathbf{v}$, the eigenvector associated with the largest eigenvalue of $\mathbf{Z}^\top\mathbf{Z}$; and $\hat{\mathbf{s}} = \mathbf{Z}\mathbf{v}$, the projection of the observations onto $\mathbf{v}$. It is easy to show that the eigenvectors of $\mathbf{Z}^\top\mathbf{Z}$ are the singular

vectors $\mathbf{V}$ of $\mathbf{Z}$. Let $\mathbf{Z} = \mathbf{U}\boldsymbol{\Lambda}\mathbf{V}^\intercal$, then $\mathbf{Z}^\intercal\mathbf{Z} = \mathbf{V}\boldsymbol{\Lambda}^\intercal\mathbf{U}^\intercal\mathbf{U}\boldsymbol{\Lambda}\mathbf{V}^\intercal = \mathbf{V}\boldsymbol{\Lambda}^2\mathbf{V}^\intercal$, which is in the form of an eigendecomposition $\mathbf{WDW}^\intercal$, with $\mathbf{D} = \boldsymbol{\Lambda}^2$.

The residual $\mathbf{Z}_{\text{res}} = \mathbf{Z} - \hat{\mathbf{s}}\hat{\mathbf{a}}^\intercal$ is orthogonal to the first singular vector, due to the use of the least-square criterion. If the same procedure was applied onto the residual, we obtain the singular vector associated with the second largest singular value of $\mathbf{Z}^\intercal\mathbf{Z}$. In theory, it is possible to continue the procedure up to K iterations; the residuals should be zeros at the last iteration. It is worth to note that stopping the procedure after $J < K$ iterations, one obtains a truncated or reduced-rank decomposition of $\mathbf{Z}$.

At the end of the decomposition, the singular values $\boldsymbol{\Lambda}$ are obtained by calculating $(\hat{\mathbf{S}}^\intercal\hat{\mathbf{S}})^{\frac{1}{2}}$. This follows the observation that at iteration k, $\hat{\mathbf{s}}_k = \mathbf{Z}\mathbf{v}_k = \lambda_k\mathbf{v}_k$ due to the eigenvector invariance property, hence at the end of the iteration, $\hat{\mathbf{S}} = [\hat{\mathbf{s}}_1 \cdots \hat{\mathbf{s}}_K] = [\lambda_1\mathbf{v}_1 \cdots \lambda_K\mathbf{v}_K] = \mathbf{V}\boldsymbol{\Lambda}$. The matrix $\mathbf{U}$ can finally be estimated by $\mathbf{U} = \hat{\mathbf{S}}\boldsymbol{\Lambda}^{-1}$. Note that $\mathbf{Z}\mathbf{v}_k = \mathbf{U}\boldsymbol{\Lambda}\mathbf{V}^\intercal\mathbf{v}_k = \lambda_k\mathbf{u}_k$, hence $\hat{\mathbf{S}} = [\lambda_1\mathbf{u}_1 \cdots \lambda_K\mathbf{u}_K] = \mathbf{U}\boldsymbol{\Lambda}$.

In practice, the parameters $\mathbf{s}$ and $\mathbf{a}$ may be resolved using a classic eigendecomposition algorithm. Alas, this does not allow the previously mentioned constraint to be included. Instead, the estimators mentioned above were used. Although they are non-linear due to their interdependence, it can be solved using an iterative, alternating approach where one parameter is estimated at a time and its result is used to estimate the other, and continuing until a criterion is satisfied. The advantage of this setup is the ability to begin at a specified initial value. In particular, the initial values were given as the subspaces $\hat{\mathbf{A}}_{\text{init}} = \mathbf{V}_R$ associated with the reference loop (which can be calculated using any algorithm) for all 3 singular vectors. This ensures that the solution converges to the local minimum close to the initial value, hence aligning the subspaces. The procedure

is illustrated by Algorithm 1.

Data: $\mathbf{X}_R$: Reference QRS loop, $\mathbf{X}$: Current QRS loop

Get $\mathbf{V}_R$ from $\mathbf{X}_R$ by any SVD algorithm $\mathbf{Z} = \mathbf{X}^\top \mathbf{S}$

for $k \leftarrow 1$ **to** K **do**

  repeat

    Initialize $\mathbf{a}_{\text{init}} = \mathbf{v}_{kR}$

    Estimate alternatingly $\mathbf{s}$ and $\mathbf{a}$ from $\mathbf{Z}$, with:

$$\hat{\mathbf{s}} = \frac{\mathbf{Z}\mathbf{a}}{\mathbf{a}^\top \mathbf{a}}$$

$$\hat{\mathbf{a}} = \frac{\mathbf{Z}^\top \mathbf{s}}{\mathbf{s}^\top \mathbf{s}}$$

    Normalize $\hat{\mathbf{a}}$ to impose unit length

  until $\|\mathbf{Z} - \hat{\mathbf{s}}\hat{\mathbf{a}}^\top\|_F < tolerance$

  $\mathbf{Z} \leftarrow \mathbf{Z} - \hat{\mathbf{s}}\hat{\mathbf{a}}^\top$

end

$\mathbf{V} = [\hat{\mathbf{a}}_1 \cdots \hat{\mathbf{a}}_K]$

$\hat{\mathbf{S}} = [\hat{\mathbf{s}}_1 \cdots \hat{\mathbf{s}}_K]$

$\hat{\mathbf{\Lambda}} = (\hat{\mathbf{S}}^\top \hat{\mathbf{S}})^{\frac{1}{2}}$

$\hat{\mathbf{U}} = \hat{\mathbf{S}}\hat{\mathbf{\Lambda}}^{-1}$

Algorithm 1: Rotation matrix correction procedure via subspace alignment.

4.4.2.2 Constrained Estimation Approach for Correcting R The estimator of $\mathbf{R}$ can be constrained to produce only a rotation matrix. It is possible to assess the matrix $\mathbf{R}$ for possible reflection by calculating its determinant $\det(\mathbf{R})$. If equal to -1, then the transformation performed is a reflection. A strict rotation has a determinant equal to 1. This information is useful in modifying the estimator of $\mathbf{R}$ as it presents a clear criterion to obtain a rotation.

In [75], a constrained estimator was formulated. The criterion J was modified to include two Lagrangian multiplier terms $\mathbf{L}$ and g, as well as constraint terms to form a new objective $J' = J + \text{tr}(\mathbf{L}(\mathbf{R}^\top \mathbf{R} - \mathbf{I})) + g(\det(\mathbf{R}) - 1)$. The second term restricts the (arbitrary) matrix $\mathbf{R}$ to fulfill orthogonality, and the third term restricts it to strictly perform a rotation. By developing the solution, the following restricted estimator was obtained:

$$\hat{\mathbf{R}} = \mathbf{U}\mathbf{J}\mathbf{V}^\top \tag{4.24}$$

$$\mathbf{J} = \begin{cases} \text{diag}(1, 1, \quad 1) & \text{if } \det(\mathbf{U})\det(\mathbf{V}) = \quad 1 \\ \text{diag}(1, 1, -1) & \text{if } \det(\mathbf{U})\det(\mathbf{V}) = -1 \end{cases}$$

Both procedures were tested. It was found that the first approach of subspace alignment fails in some cases to correct the rotation matrix, despite being aligned to a reference subspace. One explanation to this issue is that some singular vectors, when aligned, may not be located at a local optimum. The iterative minimization may be able to locate a more optimal solution, which produces the opposing vector. However, the constrained estimation approach consistently produces a rotation matrix. Therefore, the latter approach was adopted. A corrected rotation matrix produces physiologically correct rotation values, and is illustrated in Figure 4.13 (black dots) where the corrected value is more sensible, and a good continuity between the previous and next values in the series is achieved.

4.4.3 Estimating Respiratory Motion at F Wave Instants Respiratory motion parameters have classically been estimated in the duration of the QRS complex. One of the reasons for this is due to the high amplitude of electrical activation of the ventricles, and that it also maintains a regular shape from beat to beat thanks to a very well-defined and stable activation pathway following the fiber bundles onto specific sites of the ventricle. The changes brought about by respiratory motion is thus more clearly observed.

At each occurrence of a QRS complex, respiratory motion parameters can be estimated. This is somewhat reminiscent of sampling at uneven intervals: the interval here referring to the one between two pair of QRS complexes. An interesting observation here is that during AFL, the heart rate tends to be elevated due to the rapid activation of the atrium (in the range of 1 to 2 Hz). Furthermore, respiratory motion tends to be very slow (band-limited frequency contents well below 0.5 Hz). In the context of sampling, the heart rate is well above the Nyquist rate of respiratory motion, hence the estimates are discrete samples that reliably captures the whole information regarding the motion. Given these samples, this allows us to interpolate the respiratory motion parameter values within the interval of two QRS complexes and access the respiratory motion parameter values that are located within the duration of the F waves and can then be used for correcting respiratory motion effects on the F loop.

Using this setup, the following procedure was performed to correct respiratory motion from F waves of all recordings:

1. QRS complexes were detected using Pan-Tompkins algorithm [76], transformed into VCG loops and temporally synchronized

2. The reference loop $\mathbf{X}_R$ was selected as the loop that minimizes the mean error

$$\bar{J}_k = \frac{1}{M} \sum_{m=1}^{M} J_m$$

with J_m the least-square error for the alignment of loop $\mathbf{X}_m$ with the reference $\mathbf{X}_R = \mathbf{X}_k$, according to (4.21)

3. Respiratory motion parameters $[\beta\ \phi_X\ \phi_Y\ \phi_Z]$ were correctly estimated for each QRS loops with respect to the reference

4. Parameter values were then interpolated using piecewise cubic Hermite polynomials with continuity of the first derivative, to ensure no overshoots due to oscillations occur

5. At each instant of available F waves, respiratory motion parameter values were sampled

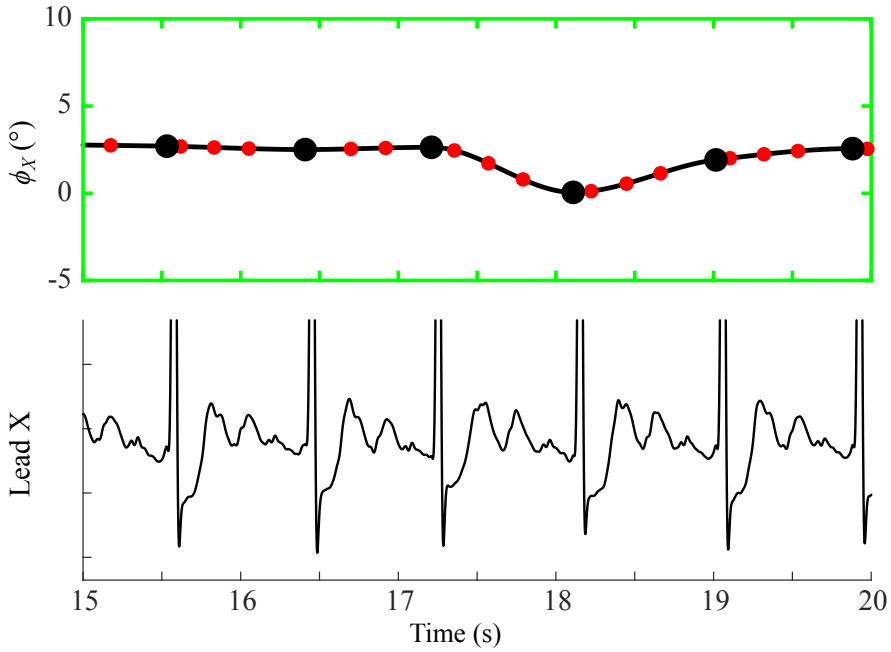

Figure 4.14: Interpolation of respiratory motion to obtain parameter values at F wave instants. This graph is a zoom-in of a portion of Figure 4.13 (inside the green dash-edged box). Black dots represent the estimated samples at QRS complexes, and red diamonds at F wave instants. Lead X VCG is shown for comparison. Note that the VCG has not been corrected for respiratory motion.

Following the procedure described previously, correct angle estimates at each QRS instants were interpolated, and the values sampled at each F wave instants were used to calculate individual $\hat{\beta}$ and $\hat{\mathbf{R}}$ for each wave (see Figure 4.14). The estimated motion

parameters were then used to correct each f waves as in (4.21). At the end, corrected F loops free from the effects of respiratory motion are obtained. In terms of set notation, respiratory motion corrected wave sets contain the superscript $\mathcal{F}^{\mathrm{r}}$.

To quantify the effect of respiratory motion correction on the F wave morphological variability, two indices are used. The first index is the parameter D described in [43], suitable for capturing local variations in F wave morphology across several leads, but also the global shape of the wave (spatial variability).

$$D = \frac{1}{N}\sum_{n=0}^{N-1}\frac{\sqrt{(\mathbf{X}(n)-\mathbf{S}(n))(\mathbf{X}(n)-\mathbf{S}(n))^{\mathsf{T}}}}{\|\mathbf{S}(n)\|_2} \tag{4.25}$$

where $\mathbf{X}(n)$ refers to the n-th row of $\mathbf{X}$. Calculating it requires a reference wave for comparison. It is suggestive to take the template F wave $\mathbf{S}$ as this reference, however this would induce a bias due to comparison with an arbitrary wave. A leave-one-out approach is adopted instead:

1. Wave $\mathbf{X}_k$ is left out
2. A mean reference wave $\overline{\mathbf{S}}_k$ is calculated from waves $[1, \cdots, k-1,\ k+1, \cdots K]$
3. Calculate $D(\mathbf{X}_k, \overline{\mathbf{S}}_k)$
4. Iterate for all waves

Finally, the mean $\overline{D}$ is calculated across the K values. The procedure ensures that the comparison is not biased by a single arbitrary reference.

The second index aims to quantify changes in individual XYZ leads. This is done by calculating for each lead, the standard deviation $\sigma[n]$ of all observation at each sample point n (i.e. $\sqrt{\mathrm{Var}(x_1[n], \cdots,\ x_K[n])}$). The mean of $\sigma[n]$ over the sample points, $\overline{\sigma}$, can then be obtained for each lead. This is similar to the approach adopted in [71], but without removing the additive noise variance (which should be estimated from the segments before and after the F wave). It would be difficult to obtain such an estimate due to the perpetuity of AA. However, it is assumed that proper filtering has minimized its effect.

All F waves were centered and normalized before the two proposed indices were calculated for all recordings, considering the case before and after respiratory motion correction.

4.4.4 Results and Conclusion A box-and-whiskers comparison is provided in Figure 4.15 and shows the difference between before and after correction. As can be seen, the differences are very close to zero, but mostly negative. Spatial variability is mostly negative (median value -4.70×10^{-3}, $p < 0.01$, Wilcoxon signed rank test), suggesting that correcting F waves adds variability into them. Inspection of the individual lead variability shows that Lead Z is mostly affected (median value -0.02×10^{-3}, $p < 0.01$, Wilcoxon signed rank test), but not other leads. This suggests that respiratory motion correction has the most impact on Lead Z.

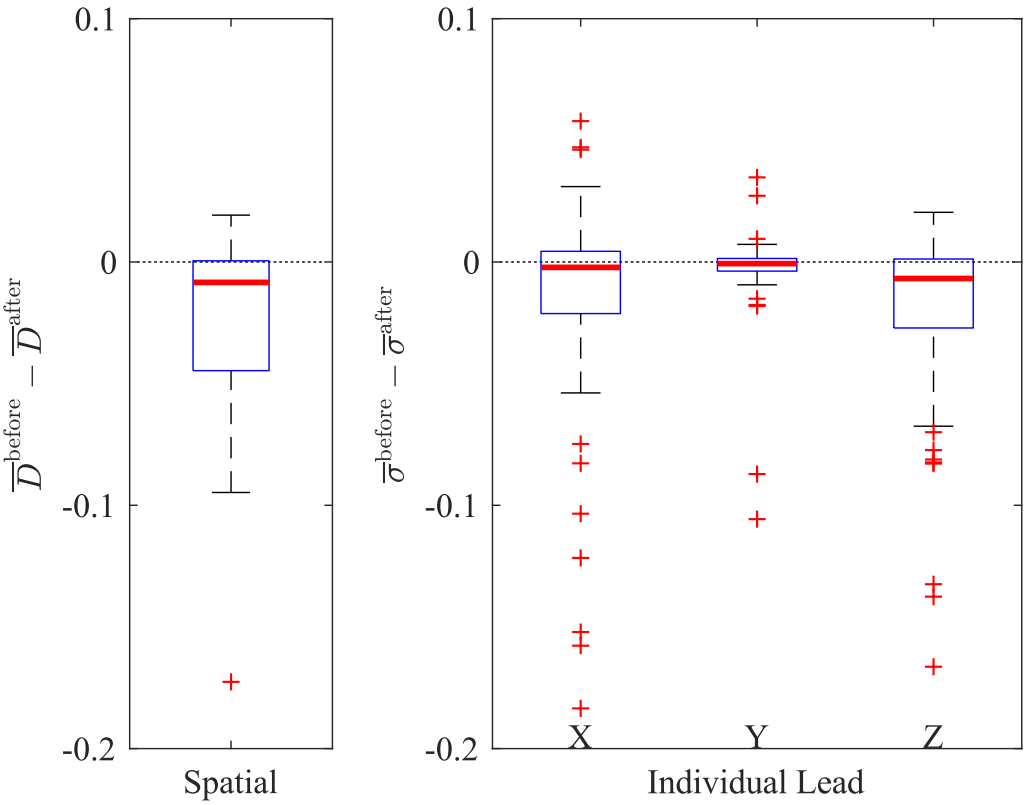

Figure 4.15: Box-and-whisker analysis of F wave morphology changes due to respiratory motion correction (set $\mathcal{F}_{\text{p}}$ only). Left figure shows the spatial variability, measured as the mean of the parameter D from a LOO evaluation (see text). Right figure shows individual lead variability, measured as the mean of the area under the curve $\sigma[n]$. Dashed line indicates the zero line.

Although the discussion seemingly leads to a conclusion that respiratory motion correction adds variability into F waves, the results should be interpreted carefully, as the changes are very small in magnitude. A more appropriate conclusion would be that respiratory motion affects the F waves slightly. It has been highlighted in previous studies that respiration does have an effect on the ECG, but only slightly [17, 77]. A second tentative conclusion would be to say that respiratory motion correction should not be performed. It should be kept in mind that this source of variability still exists on

the ECG (as evidenced by the QRS loop changes), and should be removed for proper assessment of AA variability.

4.5 Wave Overlap Correction

The issue of T wave overlap has been highlighted in Section 4.3. Although at this stage F waves have been segmented, a part of these waves suffer T wave overlap. This overlap significantly deforms the F wave morphology, and can essentially be viewed as a form of variability that superposes itself onto that of the AFL circuit. Therefore, in line with the goals of data conditioning, this variability must be removed.

4.5.1 Setup of Correction Scheme Overlapped waves are by definition, F waves located within the QT interval, or with partial overlap with the QT interval. However, it is remarkable that the QRS complex has very large deflection components. Compared to the (low-amplitude) F waves, this makes it rather impossible to recover any waves within this duration due to poor SNR. Hence, waves that are overlapped within the QRS are discarded. Only F waves located within the segment beginning at the end of the S wave until the end of the T wave were considered. Determination of the T wave end is a formidable task for any algorithm due to this overlap, hence it is performed manually, considering the normal durations of ventricular repolarization.

The overlap removal problem can be viewed as attempting to first estimate and then remove the overlapping T wave component within the F wave duration. Appealing again to the knowledge that F waves have a regular form, this problem can be written as:

$$\mathbf{x} = \mathbf{s} + \mathbf{H}\mathbf{b} + \mathbf{w}$$

with $\mathbf{s}$ and $\mathbf{Hb}$ a single-cycle F wave from a single lead and the T wave spline within the duration of a single F wave, modeled by a basis $\mathbf{H}$ with weights $\mathbf{b}$. These elements are then considered embedded in noise $\mathbf{w}$. Note that this is essentially equivalent to (4.8) with the scale factor A equal to 1. In this section, the same considerations are adopted with respect to the choice of model basis and model degree as was made in Section 4.3. As a note, the choice of low-order polynomials (degree 3) does not allow reliable modeling of QRS complex, hence the rejection of waves within QRS complexes.

Estimation of the unknown spline can be done quite easily. The optimization objective J is the least-square error:

$$\min_{\mathbf{b}} J = \|\mathbf{x} - (\mathbf{s} + \mathbf{H}\mathbf{b})\|_2^2 \tag{4.26}$$

The approximation of basis weights $\mathbf{b}$ is performed with respect to the reference se-

quence $\mathbf{s}$. This could be any wave in the set $\mathcal{F}_{\mathrm{p}}$, which indeed fulfill the criterion. However, this will cause a bias, as all estimated T wave splines will attempt to match a single arbitrary wave. Therefore, the arbitrary reference is replaced with the mean F wave $\bar{\mathbf{s}}_p$, calculated from the set $\mathcal{F}_{\mathrm{p}}$. The objective then becomes:

$$\min_{\mathbf{b}} J = \|\mathbf{x} - (\bar{\mathbf{s}}_p + \mathbf{H}\mathbf{b})\|_2^2 \tag{4.27}$$

The optimized parameter is solved by the LS approach, and is given as

$$\hat{\mathbf{b}} = (\mathbf{H}^\intercal \mathbf{H})^{-1}\mathbf{H}^\intercal(\mathbf{x} - \bar{\mathbf{s}}_p)$$

4.5.2 Results and Discussions Figure 4.16 illustrates the method applied on Lead X of one AFL recording presenting 3:1 AV block ratio. For each heart beat, two F waves are overlapped under T waves. However, by applying T wave overlap removal, the waves can be seen to match the reference well (e.g. the wave at second 3.5). The method can be seen to perform in a regular case (panel (a)), as well as challenging cases (panel (b)). However, in some situations, the method fails (e.g. panel (b), seconds 45 and 46). The reason for failing could be due to insufficient basis complexity, or non-unicity of a spline solution (which has been highlighted in Section 4.3).

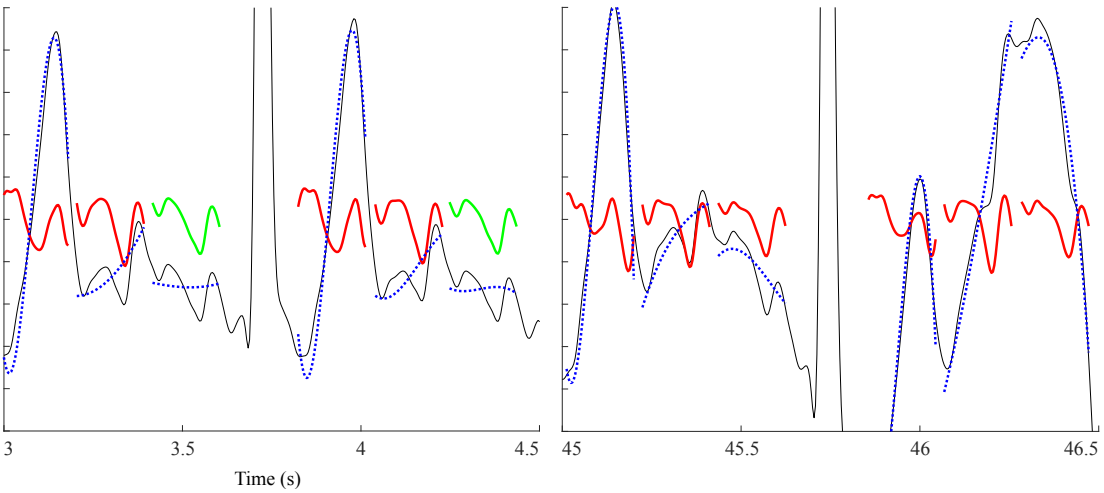

(a) (b)

Figure 4.16: Visualization of the T wave spline estimate (dotted blue lines). Panel (a) shows a regular case with minimal baseline wander. Panel (b) shows a challenging situation where a large wander is observed. Lead X VCG is shown (thin black line), as well as the recovered F waves (wave in green: from $\mathcal{F}_{\mathrm{p}}$, in red: from $\mathcal{F}_{\mathrm{o}}$).

To better view the effect on all 3 VCG leads, Figure 4.17 shows the mean F loops of set $\mathcal{F}_{\mathrm{p}}$ (green), $\mathcal{F}_{\mathrm{o}}$ (magenta) and $\mathcal{F}_{\mathrm{o}}^{\mathrm{t}}$ (red). It can be seen that after removal of T wave splines, the resulting mean resembles the reference loop $\bar{\mathbf{s}}_p$ much better that the

uncorrected loop.

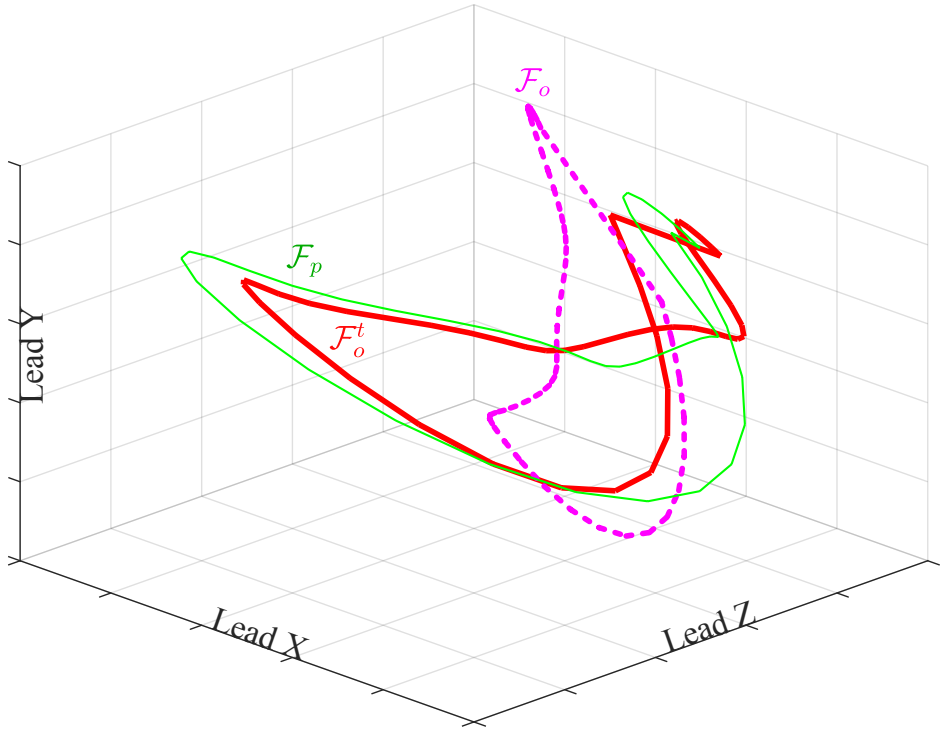

Figure 4.17: Effect of correction on overlapped F waves of one recording. Loops displayed here are averaged loops for each set. Broken-lined magenta loop refers to set $\mathcal{F}_{\mathrm{o}}$, bold red loop to set $\mathcal{F}_{\mathrm{o}}^{\mathrm{t}}$. The thin green loop to set $\mathcal{F}_{\mathrm{p}}$.

There exists an edge effect attributed to the use of the polynomial basis, as mentioned earlier (the Runge's phenomenon [59]). This is due to the equidistancing of time samples, which has the effect of exaggerating the polynomial estimate at the edges of the observation window. To attenuate this effect, all F waves were truncated at the onset and end by 5 ms at each side. Corrected waves are grouped in a set $\mathcal{F}_{\mathrm{o}}^{\mathrm{t}}$.

To quantify the effect of this procedure on loop morphology, the parameter D described in (4.25), as well as an additional parameter C:

$$C = \frac{1}{N} \sum_{n=0}^{N-1} \frac{\mathbf{X}(n)\mathbf{S}(n)^{\intercal}}{\|\mathbf{X}(n)\|_2 \|\mathbf{S}(n)\|_2} \tag{4.28}$$

were calculated for all recordings. $\mathbf{X}(n)$ refers to the n-th row of $\mathbf{X} = [\mathbf{x}_X\ \mathbf{x}_Y\ \mathbf{x}_Z]$. These two parameters capture the similarity of the loops to one another, with C capturing the global similarity between loops, and D quantifying the differences due to local oscillating patterns. Remark that $C = 1$ and $D = 0$ indicates perfect match. Before calculation of these parameters, the loops are zero-centered and each lead was normalized by the square-root of their energy. Figure 4.18 shows a box-and-whisker comparison of the two parameters when calculated using sets $\mathcal{F}_{\mathrm{o}}^{\mathrm{t}}$ and $\mathcal{F}_{\mathrm{p}}$ (marked as F_1) and sets $\mathcal{F}_{\mathrm{o}}$ and $\mathcal{F}_{\mathrm{p}}$ (marked as F_2), for all recordings. Table 4.2 resumes the group statistics of the quantitative indices. All loops are shown to achieve higher resemblance to the reference waves after correction. This is reflected by the high C and low D values after correction. This suggests, on the other hand, the adequacy of a basis of degree 3.

Table 4.2: Group Statistics of Comparison F_1 and F_2.

	C	D
F_1	0.95 ± 0.08	0.30 ± 0.20
F_2	0.48 ± 0.24	1.08 ± 0.31

Values expressed as median ± mean absolute deviation

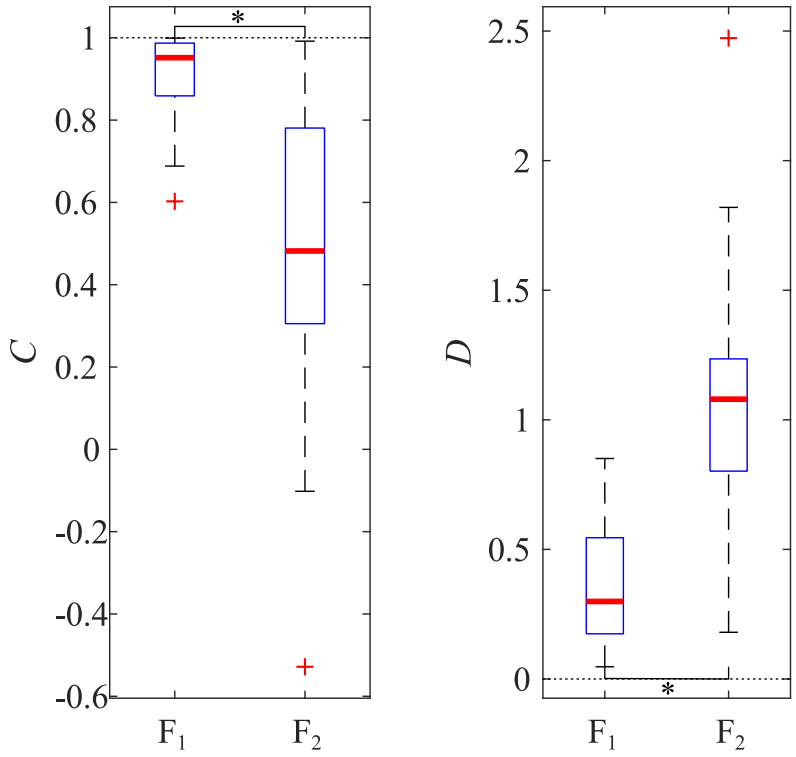

Figure 4.18: Box-and-whisker comparison of mean loop similarity quantities. The horizontal dashed line represents the target value, where loop similarity is maximized. Quantities C and D are described in the text. F_1 and F_2 represent the comparisons between the mean loop of set $\mathcal{F}_o^t$ and set $\mathcal{F}_p$, and the mean loop of set $\mathcal{F}_o$ and set $\mathcal{F}_p$ respectively. The asterisk indicates significant difference ($p < 0.01$, Mann-Whitney U test).

4.6 Inverse Dower Transform Optimization

The correspondence of lead systems was reviewed in Section 2.3, where the notion of image space was discussed and how linear matrix transforms such as the Inverse Dower Transform provide the means to change between different lead systems. This is possible provided that the image space coordinates are known, and that the electrode placements are exactly at the same location as the sample points of the image space.

In a real torso, there are many organs and anatomical structures with varying conductivity, hence the volume conductor is heterogeneous. The heterogeneity affects the shape of the image surface greatly and causes the transform coefficients to have errors. Furthermore, electrodes are never placed at the location specified by the image surface, which will cause deviations in the lead vectors. The stringent assumptions made has the effect of propagating the error of model inaccuracy into the transform.

It has been discussed in previous studies that the IDT is not optimal for use with atrial signals, and that custom transforms derived from P waves perform better [78, 79]. The team of Guillem et al. proposed the PLSV transform as an alternative to the IDT. The transform was derived from an average of individual transforms that map averaged ECG P waves onto simultaneously recorded averaged VCG P waves, for 124 patients from the Physikalisch-Technische Bundesanstalt ECG database (`ptbdb` [3, 4]). However, the transform does not aim to improve localization of circuits, but instead to better replicate real VCG. An even better representation of the orthogonal XYZ activation can be obtained from other electrode arrangements [80]. However, these are uncommon arrangements and are not used in a clinical setting.

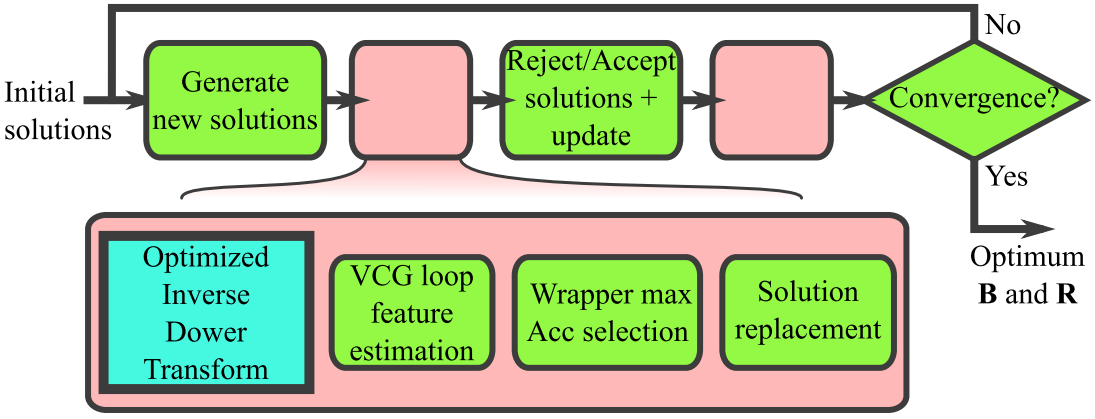

Figure 4.19: Schematic of the optimization procedure for finding optimal **B** and **R**. The thick blue box corresponds to the novel approach employed in this section.

Thankfully, the effects of heterogeneity as well as electrode misplacement can be formulated in a mathematical context. This allows the use of common estimation-

optimization techniques for finding the optimized transform coefficients. In addition, the optimization goal can be based on localization accuracy, which is a more direct endpoint than e.g. similarity to real VCG. However, it is expected that the goal has non-ideal properties, since classifier accuracy depends greatly on the class-conditional distribution of the data given the considered features as well as the optimization coefficients, and the relation between these elements are not known. Figure 4.19 resumes the whole optimization process.

4.6.1 Optimization Setup The IDT describes a linear transform of a reduced set of leads from the 12-lead ECG to the VCG via the following relation:

$$\mathbf{Y} = \mathbf{X}\mathbf{T}^{\intercal} \tag{4.29}$$

$\mathbf{T}$ is the 3×8 IDT matrix described in (2.2), $\mathbf{X}$ and $\mathbf{Y}$ are the $N\times8$ and $N\times3$ 8-lead ECG and VCG respectively. The 8 leads of the ECG used to obtain the VCG are arranged as $[\mathrm{V}_1\ \mathrm{V}_2\ \mathrm{V}_3\ \mathrm{V}_4\ \mathrm{V}_5\ \mathrm{V}_6\ \mathrm{I}\ \mathrm{II}]$.

The quality of the source field potential measures depends on the conductance of the surrounding volume. The simplest assumption to be made on the volume conductor is that it is homogeneously conductive and constant. This is however not true in practice since in a real thorax, each of its constituents (organs, vessels, membranes, etc.) have different conductivities. Furthermore, their values are not constant and vary in time, in direction and from patient to patient. This translates to different conductivity in the direction of each lead vector of any ECG system, hence they have different gain or attenuation factors.

Ideally, ECG electrodes should be placed at the same locations originally indicated. However, this is an impossible feat as physical human anatomy is never the same, hence electrode misplacement is bound to occur. In addition, this is a common procedural problem and can be intentional (e.g. in female torso, to avoid the breast) or unintentional (e.g. operator error, skin sag, etc.). This translates to a shift in lead vector direction, and thus different rotations of the lead vectors.

Both these effects change the VCG such that $\mathbf{Y} \rightarrow \check{\mathbf{Y}} = \mathbf{YQA}$, $\mathbf{A} = \mathrm{diag}(a_X,\ a_Y,\ a_Z)$ being a diagonal matrix of gain (or attenuation), and $\mathbf{Q} \in \mathbb{R}^{3\times3}$ a rotation matrix, satisfying the property $\mathbf{Q}^{\intercal}\mathbf{Q} = \mathbf{I}$. We thus have:

$$\mathbf{YAQ} = \mathbf{X}\mathbf{T}^{\intercal} \tag{4.30}$$

To optimize the IDT, these errors should be compensated as follows:

$$\mathbf{Y} = \mathbf{X}\mathbf{T}^{\intercal}\mathbf{Q}^{\intercal}\mathbf{A}^{-1} \tag{4.31}$$

In practice, estimation of $\text{diag}(b_X,\ b_Y,\ b_Z) = \mathbf{B} = \mathbf{A}^{-1}$ is performed instead. As for $\mathbf{Q}$, $\mathbf{R} = \mathbf{Q}^{\intercal}$ is estimated instead. The matrix can be decomposed into individual 3D rotation matrices $\mathbf{R}_X,\ \mathbf{R}_Y,\ \mathbf{R}_Z$ for each of the 3 axis of the VCG leads, with each matrix computable from angles $\phi_X,\ \phi_Y,\ \phi_Z$ respectively, and $\mathbf{R} = \mathbf{R}_X\mathbf{R}_Y\mathbf{R}_Z$. Note that this is reminiscent of the respiratory motion correction setup in Section 4.4, except that the scale parameter is now considered to be different on each VCG lead.

Ideally, all 24 coefficients of the IDT need to be modified individually. However, this constitutes a model with an outstanding number of parameters, and estimation complexity increases easily with such a large number. The model proposed here only has 6 parameters: 4 times simpler than that, and captures most of the errors observable on the acquisition of the VCG.

It has been argued that the Dower transform represents ventricular activation better than atrial activation, due to the placement of the source dipole origin close to the ventricular origin in Frank's torso model [78]. Since the atrium and ventricle are electrically separate, save for the para-Hisian junction, the cardiac dipole origin is expected to also be different. This would be modeled as a additional translation parameter. It was chosen not to include this into the problem, and instead assume that cardiac dipole remains fixed.

4.6.2 Optimization Goal Properties In an ideal estimation setting, both $\mathbf{X}$ and $\mathbf{Y}$ are required in order to arrive at a closed form solution of the parameters, as had been done in [78]. However, in a synthesis context, no information about $\mathbf{Y}$ is available. In addition, the interest here is not in a better representation of the VCG, but of optimizing the discriminant performance of the classifier.

The goal of the parameter estimation: maximize the classifier accuracy, is different than that of conventional approaches. This requires us to define the goal in the scope of optimization, to be able to decide which method is suitable for use. Furthermore, conventional techniques do not take into account the nature of data distributions given a certain feature set: an item particularly associated with machine learning. The scheme presented here constitutes an original approach that combines elements of optimization and machine learning.

The optimization problem is defined as:

$$\max J = \text{Acc} = \frac{\text{TP} + \text{TN}}{\text{TP} + \text{FN} + \text{FP} + \text{TN}}$$

with each term in the fraction referring to the error classes, defined in Chapter 5.

It is difficult to capture the effects of the parameters using this formulation since no relation is made explicit with respect to the model parameters. Therefore, a different formulation is proposed.

4.6.2.1 Reformulation of the Goal Note that the denominator is constant for a given set of M data points. The numerator is essentially the number of elements in the set union $\{G_{\text{predicted}} = G_{\text{true}}\} = \{G_{\text{predicted}} = \text{Right}|G_{\text{true}} = \text{Right}\} \cup \{G_{\text{predicted}} = \text{Left}|G_{\text{true}} = \text{Left}\}$, with each subset containing data points whose predicted labels $G_{\text{predicted}}$ are similar to the true labels G_{true}, for all available classes. Suppose $\mathbf{g}$ an M-vector of 0 or 1 whose elements represent the incorrect or correct prediction of the class label for each data point, we can then write the optimization problem as:

$$\max \text{Acc} = \frac{1}{M}\|\mathbf{g}\|_0 \tag{4.32}$$

Each entry g_m of $\mathbf{g}$ is determined by the classifier through some evaluation of the conditional probability $\mathbb{P}\{G_m|X, \mathbf{B}, \mathbf{R}, \mathcal{E}\}$ that includes not only the optimization parameters, but also the subset of features $\mathcal{E}$ obtained from a full set of considered features $\mathcal{X}$.

The final form amounts to:

$$\max_{\mathbf{B},\,\mathbf{R},\,\mathcal{E}} \text{Acc} = \frac{1}{M}\|\mathbf{g}(X, \mathbf{B}, \mathbf{R}, \mathcal{E})\|_0 \tag{4.33}$$

It can be shown that the L_0-pseudonorm is multimodal in the considered application. First, for any vectors $\mathbf{u}$ and $\mathbf{v}$, the scaled Minkowski inequality is given as

$$\begin{aligned}\|\lambda\mathbf{u} + (1-\lambda)\mathbf{v}\|_0 &= \max(\|\mathbf{u}\|_0,\ \|\mathbf{v}\|_0,\ \|\mathbf{u}\|_0 + \|\mathbf{v}\|_0) \\ &\leq \\ &\|\lambda\mathbf{u}\|_0 + \|(1-\lambda)\mathbf{v}\|_0 = \|\mathbf{u}\|_0 + \|\mathbf{v}\|_0\end{aligned}$$

and shows that the pseudonorm is convex, with $\lambda \in]0; 1[$. Consider now the equation of (4.33). When optimization is achieved, $\hat{\mathbf{R}}^*$ is the optimized rotation. The three rotation angles $\hat{\phi}_X^*$, $\hat{\phi}_Y^*$, $\hat{\phi}_Z^*$ can be $\pm 180°$ ambiguous. Furthermore, rotation is a length-preserving transform, hence the data distribution does not change, and guarantees the

same L_0 length with any combination of $\pm 180^\circ$ ambiguity. This means that the absolute minimum exists in at least 2^3 locations. This completes the proof of multimodality. In practice, the objective is multimodal since the class distribution is mostly represented by limited sample sizes. Along with distribution overlap, a change in parameter will likely cause local maxima to appear.

The goal also does not have a smooth form. For proof, consider any vector $\mathbf{w} = [w_1 \ \cdots \ w_k \ \cdots \ w_K]$ with non-zero entries. $\|\mathbf{w}\|_0 = K$ for any $w_k \neq 0$. But for $w_k = 0$, we have $\|\mathbf{w}\|_0 = K - 1$, thus there is a non-continuous transition. This proves the non-smoothness of the goal.

4.6.2.2 Illustration of Goal Properties Figure 4.20 demonstrates the non-convexity and non-smoothness of the goal using a hypothetical classification case. Two classes are considered (red and green). Two variables representing two features are used, to illustrate inter-feature interaction. The variables are sampled from a mixture of two standard Gaussian random variables X and Y, according to the following setup:

$$\begin{aligned}
\text{Variable } 1^{(\text{red})} &= \sigma_1 X + \sigma_2 Y + \mu^{(\text{red})} && = \text{Variable } 2^{(\text{red})} \\
\text{Variable } 1^{(\text{green})} &= \sigma_2 X + \sigma_1 Y + \mu^{(\text{green})} && = \text{Variable } 2^{(\text{green})} \\
\mu^{(\text{red})} &= -0.5 \\
\mu^{(\text{green})} &= 0.5 \\
\sigma_1 &= \sqrt{0.5} \\
\sigma_2 &= -\sqrt{0.05}
\end{aligned}$$

For each class, 30000 points were sampled. Distribution of individual variables are shown in the left and bottom figures of Figure 4.20, panel (a). The two variables are covariant, as shown in the top right figure. In particular, they are placed such that the classifier boundary runs exactly through the origin (0,0) at a 135° angle (thick black line); a discriminant vector can be placed at the origin, and the best vector is $[\frac{1}{\sqrt{2}} \ \frac{1}{\sqrt{2}}]^\intercal$ (angled at 45°), perpendicular to the classifier boundary (black arrow).

Classification is performed according to two setups: the first setup uses only a single variable. A point is classed as 'green' when the variable is larger than a threshold $\gamma = 0$, or 'red' otherwise. In the second setup, both variables are used. A discriminant vector of unit length is placed at the origin, and rotated from an angle of -45° (blue downward pointing vector) until 135° (red upward-pointing vector). At each rotation, the observations are projected onto the discriminant vector. Positive-valued projections are classed as 'green', and 'red' otherwise.

The resulting classification accuracy is shown in panel (b), for each presented case. The blue dotted line represents the the evolution of the accuracy with change in the classification parameter. Asymptotically, the accuracy profile is smooth and convex. The thin orange line results when the same classification step is applied on a subset of 60 samples randomly drawn from the 60000 points. The accuracy profile becomes non-smooth and local minima starts to appear. In addition, the accuracy can be seen to be superior when a multivariate classifier is used, due to the possibility of exploiting the covariant relation between the variables. This is not possible in individual cases. In summary, this toy example shows the properties of the optimization goal (non-smooth, non-convex and feature-dependent).

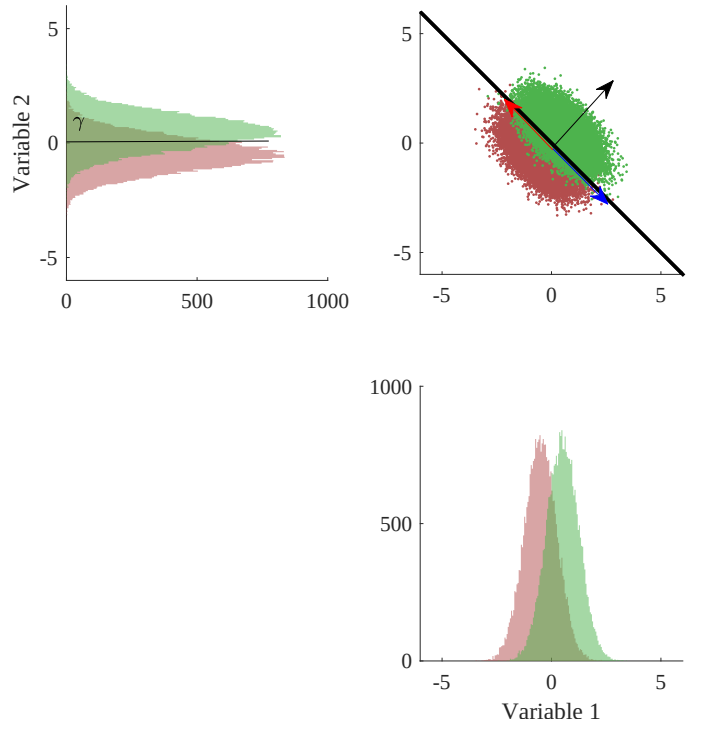

(a)

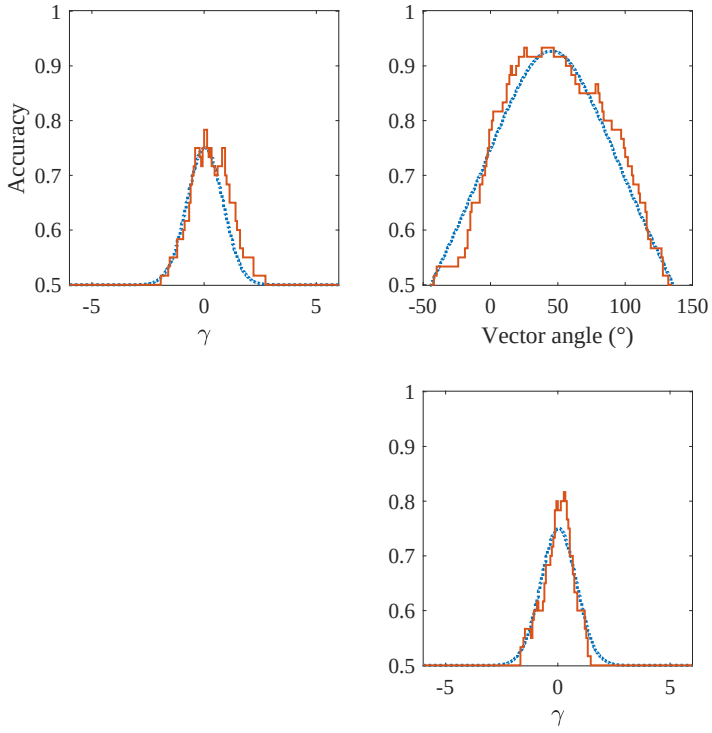

(b)

Figure 4.20: Illustration of the optimization goal property. Panel (a) shows the distribution of two classes according to two variables (individual in left and bottom figures, and multivariate in the top). Panel (b) shows the corresponding classification accuracy based on the distribution of data. Refer to the text for information.

4.6.3 Optimization Scheme Given the nature of the problem, multiple solutions are expected, whilst gradient information is not available due to non-continuity. The optimization method must account for these constraints in order to arrive at a good solution. Such techniques commonly involve sampling *multiple instances* of the parameter space in a single iteration, and using information from the goal evaluation or the instances themselves to decide on the sampling points of the next iteration. They also do not require any information on the gradient, and are termed *derivative-free*.

Many such algorithms have been developed, and are particularly used to solve problems with very complex objectives or with non-ideal goal properties. Among those, are particle swarm optimization (PSO [81]) and genetic algorithm (GA [82]). These two algorithms are inspired by the behavior of natural objects such as animals and cells. They require a number of parameters in order to control the search procedure. PSO requires at least 3 parameters that act as weights on the update of the particle velocity and distances between the best previous individual particle position and the current global optimum. GA uses genetic operators such as genetic crossovers and genetic mutation, which can be translated as a specific combination and variation of parameter values with respect to values of a previous iteration. This is controlled by probabilities that determine the frequency of occurrence of such events.

Although these algorithms respond to our criteria, the effective number of parameters remain an issue, as their tuning is crucial to obtain good functionality. Therefore, other algorithms were considered. One good candidate is cuckoo search (CS [83]). CS was designed by Yang and Deb, and mimics the natural behavior of brood-parasitic cuckoo birds. These birds would lay their eggs in the nest of other bird species. When cuckoo chicks hatch, they evict the eggs of the host species. Upon discovery of this fact, the host mother may either abandon the nest (and the cuckoo chick) or continue to feed the chick (mainly due to confusion or the chick's mimicry of the host species). Once strong enough, the grown-up cuckoo bird continues the cycle.

Translating it into algorithmics, the host nest represents a candidate solution, instantiated randomly in the parameter space. The goal is first evaluated. A cuckoo chick represents a new solution similar to the candidate, that could potentially be better. This new solution is obtained by a Lévy flight: a heavy-tailed random walk that departs from the candidate solution. If better, then the new solution replaces the candidate.

The possibility of abandoning a nest is controlled by a probability parameter p_a. Finally, new nests or solutions are obtained by a biased random walk, which calculates the flight direction based on all the solutions. The algorithm iterates again with the final solutions of iteration $k-1$ used as initial candidates of iteration k, until it satisfies a convergence

criteria. At the end of each iteration, the best value of the goal indicates the best solution.

Due to the use of random walks, the coefficients may assume any value in the real space and produce nonsensical results. A simple bound check is applied after each generation of solution. The scale parameters b are limited to values in the range $[0.001;\ 5]$ and rotation parameters to values in the range $[-179.999;\ 180]^\circ$.

For each evaluation, a set of candidate $\hat{b}_X,\ \hat{b}_Y,\ \hat{b}_Z$ and $\hat{\phi}_X,\ \hat{\phi}_Y,\ \hat{\phi}_Z$ are obtained. For each F wave of each patient, the optimization detailed in (4.31) is applied, loop features are calculated and an exhaustive wrapper evaluation of feature combination up to a length of 5 features is performed. This limits the number of iterations of wrapper evaluation required, and also avoids optimizing on overfitted data. For each feature combination, the accuracy is calculated. The maximum achievable accuracy is taken as the solution's goal value. The linear support vector machine (SVM) classifier is used since it is simple and fast to train.

Fifteen instances we used to simultaneously search the parameter space. The probability p_a is set to 0.25, as was suggested by the authors of CS. No attempt was made to find the best value of p_a or the number of instances. Convergence was set to occur when an accuracy of 1 is achieved or the best goal does not change for 10 iterations. Optimized waveforms are grouped in the set $\mathcal{F}^{\mathrm{d}}$.

4.6.4 Results and Discussions Resulting classifier performances issued from this optimization are not discussed here, but instead in Chapter 6. The set of 6 optimal values $\hat{b}^*_X,\ \hat{b}^*_Y,\ \hat{b}^*_Z$ and $\hat{\phi}^*_X,\ \hat{\phi}^*_Y,\ \hat{\phi}^*_Z$ represent the overall scaling and rotation applied to each XYZ leads of the VCG system. After normalization of the scale values by the largest $\hat{b}$, and addition of $\pm 180^\circ$ to the rotation values, the following values were obtained:

$$\hat{b}^*_X = 0.91,\ \hat{\phi}^*_X = 46.25^\circ$$
$$\hat{b}^*_Y = 1.00,\ \hat{\phi}^*_Y = 23.48^\circ$$
$$\hat{b}^*_Z = 0.57,\ \hat{\phi}^*_Z = 72.79^\circ$$

The transform effects are most present for scaling in lead Z (front-to-back component) and slightly in lead X (right-to-left component). Rotation affects all leads quite strongly, with the largest in lead Z. It is difficult to correlate these results to any physiological interpretation because the transform essentially attempts to enhance separability between classes based on variability. However, later chapters show how this affects classifier

performance positively.

The optimization procedure requires a very long run time due to the use of the exhaustive wrapper evaluation scheme. Parallel processing of each individual candidate solution should, in theory, give shorter run times. Due to the computational cost of this approach, no cross-validation (CV) was performed as well. It is known that CV allows the estimation of these parameters that generalize across unknown datasets.

4.7 Feature Extraction

Once F waves have been obtained and properly corrected of external variability, they can then be characterized in order to obtain quantitative measures as a descriptor to the AFL circuit. In this study, two different kinds of characterization, aiming to capture different properties of AFL, are considered. The first kind is in the form of beat-to-beat VCG loop parameters, extracted from analysis of the VCG loops for several quasi-continuous beats and reflects cycle-to-cycle variability of dipole trajectory map. The second characterization employs recurrence quantification analysis (RQA) in order to obtain recurrence signals reflecting similarity of the atrial dipole trajectory in time. The two approaches can be viewed as complementary, with the first kind preferring a beat-to-beat approach and the second kind preferring a continuous-time approach.

4.7.1 Characterization of AFL VCG Loops Because F waves are quasi-periodic, its representation in VCG resembles a loop. Figure 4.21 illustrates a single loop taken from a recording. This can be viewed as the trajectory of the activation wave of the AFL, and can be subjected to analysis. In particular, the morphological parameters of the loop are of interest, since previous research have highlighted possible variations in these parameters [42, 84]. In order to obtain them, singular value decomposition $\mathbf{X} = \mathbf{U}\mathbf{\Lambda}\mathbf{V}^\intercal$ was applied, with $\mathbf{X} \in \mathbb{R}^{N\times 3}$ an F wave loop, $\mathbf{U}$ and $\mathbf{V}$ the left and right singular vectors, and $\mathbf{\Lambda} = \text{diag}(\lambda_1,\ \lambda_2,\ \cdots,\ \lambda_K)$ the singular values.

VCG loop orientation, given in terms of the azimuth ϕ_{AZ} and elevation ϕ_{EL} was calculated by finding the angle of intersection between the plane spanned by the first two eigenvectors $\mathbf{v}_1$ and $\mathbf{v}_2$ with planes XZ and YZ respectively.

$$\phi_{AZ} = \text{sgn}(b_{AZ}) \arccos\left(\frac{a_{AZ}}{\sqrt{a_{AZ}^2 + b_{AZ}^2}}\right) \tag{4.34}$$

$$\phi_{EL} = \text{sgn}(b_{EL}) \arccos\left(\frac{a_{EL}}{\sqrt{a_{EL}^2 + b_{EL}^2}}\right) \tag{4.35}$$

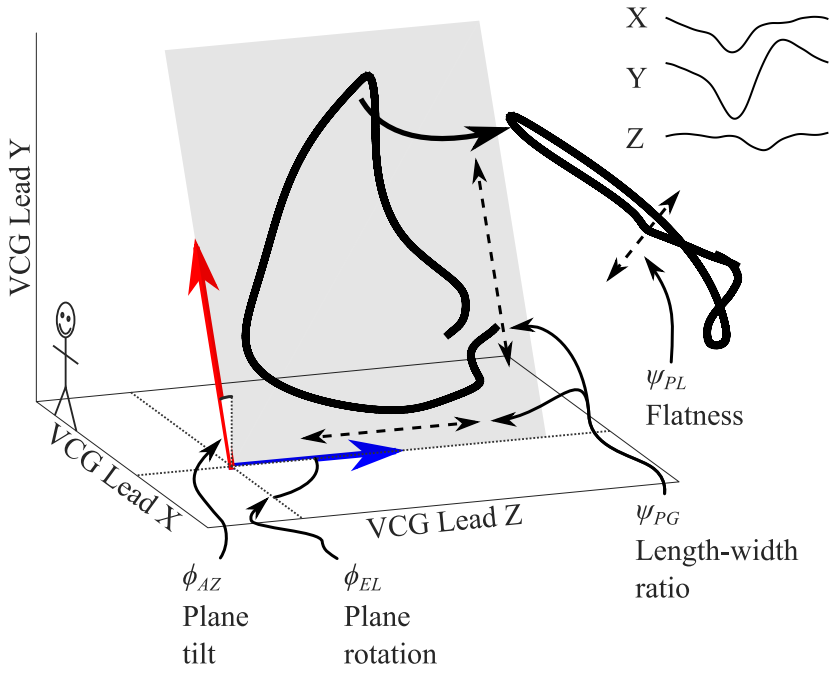

Figure 4.21: Illustration of VCG loop parameters. The red upward-pointing arrow is $\mathbf{v}_1$, and the blue right-pointing arrow is $\mathbf{v}_2$. Individual channel VCGs are shown on the top right.

$$a_{AZ} = v_{2z} - v_{1z}\frac{v_{2y}}{v_{2y}},\ b_{AZ} = v_{2x} - v_{1x}\frac{v_{2y}}{v_{2y}}$$
$$a_{EL} = v_{2z} - v_{1z}\frac{v_{2x}}{v_{2x}},\ b_{EL} = v_{2y} - v_{1y}\frac{v_{2x}}{v_{2x}}$$

The expressions can be found by solving the plane intersection problem $c\mathbf{v}_1 + d\mathbf{v}_2 = \alpha\overrightarrow{u} + \beta\overrightarrow{v}$, where the bases $\overrightarrow{u}$ and $\overrightarrow{v}$ indicate the orthogonal Cartesian unit vectors relevant to the context. The use of the sign function ensures that the bearings are correct with respect to the fixed 3D orientation considered by Frank [2]. An azimuth angle of 90° corresponds to a rotation of the XY plane towards the left (i.e. turning left), and in the opposite direction for an angle of −90°. An elevation angle of 90° corresponds to a tilt of the XY plane to the back, and in the opposite direction for an angle of −90°.

The expressions are different from (3.3) and (3.4) in that $\mathbf{v}_3$ was not used. Here, it is preferable to use eigenvectors associated with the two largest eigenvalues to avoid using eigenvectors associated with a possibly zero-valued eigenvalue. One may like to consider when the loop is perfectly flat. Furthermore, the bearing here was accounted for, and allows the vector to naturally span the whole range of angle values.

VCG loop geometry, given in terms of planarity ψ_{PL} and plane geometry (the shape of

the loop) ψ_{PG} was calculated using the eigenvalues λ, as was done in [85]:

$$\psi_{PL} = 1 - \frac{\lambda_3}{\sum_{i=1}^{3} \lambda_i} \tag{4.36}$$

$$\psi_{PG} = \frac{\lambda_2}{\lambda_1} \tag{4.37}$$

A planarity value of 1 corresponds to a perfectly flat loop, whereas a value of 0 corresponds to a loop that occupies the totality of the 3D space. A plane geometry value of 1 corresponds to a perfectly circular loop, whereas a value of 0 corresponds to a line in 3D space. Contrary to the parameters describing orientation, these two parameters here are not affected by the sign ambiguity as the singular values are always positive.

Each point in the loop was spatially equidistanced before the 4 parameters were calculated across the whole dataset. The distancing, performed using a spline estimation of the loop, ensures that the SVD is not biased by the densely clustered parts of the waves, which are usually the parts that do not fluctuate rapidly.

4.7.1.1 Removing Artificial Variability from ϕ Parameters Singular vectors have been shown to be associated with sign ambiguity, and was shown in Section 4.4 to cause non-physiological parameter value estimates. Here, similar effects lead to orientation parameter values ϕ that are ambiguous by $\pm 180°$. The beat-to-beat series thus contain artificial variability that is not related to AFL, but to the sign ambiguity of the singular vectors. This artificial variability must be filtered out to ensure that the calculation of statistical moments are not biased.

To remove this variability, a simple procedure was employed:

1. Consider Φ the original beat-to-beat series of VCG orientation values (ϕ_{AZ} or ϕ_{EL}), and an empty set $\tilde{\Phi}$
2. Select the first value $\phi_0 \in \Phi$, and insert it into $\tilde{\Phi}$
3. Insert $\phi_k,\ k > 0$ into set $\tilde{\Phi}$ as either ϕ_k or $\phi_k \pm 180°$, whichever minimizes the variance of $\tilde{\Phi}$
4. Increment k and repeat 3. until all values are evaluated

given a beat-to-beat series of VCG orientation values ,

At the end, the set $\tilde{\Phi}$ has a variance much lower than that of Φ. The problem described above is an NP-hard problem, and is the subject of combinatorial optimization. The proposed procedure may not necessarily find the optimal minimum, but from observation, the reduced variance is sufficiently removed such that it no longer becomes a prominent source of variability.

According to the output of the procedure above, the two measures Mean(ϕ_{AZ}) and Mean(ϕ_{EL}) may present inter-recording ambiguity, since the series may be centered around Mean(ϕ) or Mean(ϕ) ± 180. If not removed, these measures will cause artificially increased separation. Therefore, the same correction procedure was applied to the 56 values of each of the two measures. Note that higher-order statistics do not need this correction as they are not affected, and neither do Mean(ψ_{PL}) and Mean(ψ_{PG}).

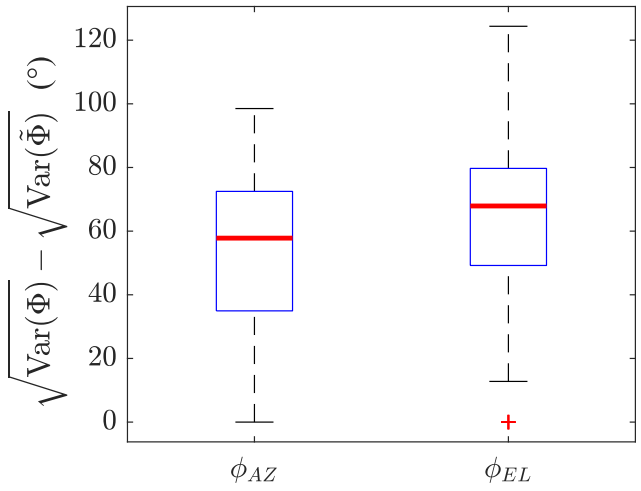

Figure 4.22: Box-and-whiskers plot of the difference in root variance of orientation parameter sets before and after sign ambiguity correction.

To assess the effect of correcting sign ambiguity on the variability of parameter values, the difference between the square-root of set variances (i.e. $\sqrt{\mathrm{Var}(\Phi)}$) before and after correction for parameters ϕ_{AZ} and ϕ_{EL} was analyzed on all recordings. It is expected that the variance is larger before correction is applied, thus the difference should be positive. As shown in Figure 4.22 by the box-and-whisker plot, the differences are all indeed positive. Several records had differences that were zero-valued (7 records for ϕ_{AZ}, 3 records for ϕ_{EL}, not shown in the figure), indicating that the original series did not initially contain variability of sign ambiguity. The median values of non-zero differences are 60.46 ± 17.20 for ϕ_{AZ} and 68.54 ± 17.79 for ϕ_{EL} (both values significant with $p < 0.01$, Wilcoxon signed rank test). This illustrates that sign ambiguity can indeed introduce significant variability into the series.

The result of this step is the obtention of several beat-to-beat series of VCG loop parameter values, clean of any source of artificial variability, and reflecting the beat-

to-beat changes of the AFL circuit. Variability can be measured from this series using several statistical measures. The 4 following measures were used: 1) the mean, 2) the variance, 3) the skewness and 4) the kurtosis. These are essentially the statistical moments of the underlying distribution of parameter values, and characterizes the shape of the distribution. The 4 measures were calculated for each of the 4 parameters ϕ_{AZ}, ϕ_{EL}, ψ_{PL} and ψ_{PG}, for all 56 recordings. In total, there were $4 \times 4 = 16$ measures available. Table 4.3 summarizes the group statistics of each feature for the set $\mathcal{F}_{\text{p}}$.

Table 4.3: Group Statistics for VCG Loop Features (set $\mathcal{F}_{\text{p}}$)

	Feature	Right AFL	Left AFL	p-value
ϕ_{AZ}	Mean(ϕ_{AZ})	34.83 ± 64.76	52.34 ± 61.09	0.33
	Var(ϕ_{AZ})	$4.14 \cdot 10^2 \pm 7.28 \cdot 10^2$	$2.01 \cdot 10^2 \pm 4.19 \cdot 10^2$	0.78
	Skewness(ϕ_{AZ})	0.04 ± 0.57	0.34 ± 0.97	0.06
	Kurtosis(ϕ_{AZ})	3.03 ± 2.24	2.90 ± 4.46	0.37
ϕ_{EL}	Mean(ϕ_{EL})	22.85 ± 90.08	43.12 ± 85.21	0.79
	Var(ϕ_{EL})	$8.64 \cdot 10^2 \pm 1.15 \cdot 10^3$	$4.89 \cdot 10^2 \pm 1.35 \cdot 10^3$	0.45
	Skewness(ϕ_{EL})	-0.55 ± 1.05	-0.32 ± 1.14	0.50
	Kurtosis(ϕ_{EL})	3.19 ± 3.65	3.34 ± 5.00	0.84
ψ_{PL}	Mean(ψ_{PL})	$9.19 \cdot 10^{-1} \pm 2.50 \cdot 10^{-2}$	$9.16 \cdot 10^{-1} \pm 2.22 \cdot 10^{-2}$	0.50
	Var(ψ_{PL})	$4.86 \cdot 10^{-4} \pm 3.82 \cdot 10^{-4}$	$5.55 \cdot 10^{-4} \pm 5.08 \cdot 10^{-4}$	1.00
	Skewness(ψ_{PL})	-0.48 ± 0.45	-0.14 ± 0.55	$< \mathbf{0.05}$
	Kurtosis(ψ_{PL})	2.86 ± 1.08	2.91 ± 1.37	0.92
ψ_{PG}	Mean(ψ_{PG})	0.36 ± 0.09	0.42 ± 0.15	$< \mathbf{0.05}$
	Var(ψ_{PG})	$6.61 \cdot 10^{-3} \pm 7.38 \cdot 10^{-3}$	$7.69 \cdot 10^{-3} \pm 4.79 \cdot 10^{-3}$	0.86
	Skewness(ψ_{PG})	0.78 ± 0.72	0.14 ± 0.64	$< \mathbf{0.01}$
	Kurtosis(ψ_{PG})	4.07 ± 2.29	2.89 ± 1.27	0.13

Values expressed as median ± mean absolute deviation

4.7.1.2 Effect of T Wave Correction on VCG Loop Parameters It has been shown that by correcting overlapped waves, it is possible to have F waves that resemble pure waves (i.e. waves in the set $\mathcal{F}_{\text{p}}$). However, it is not known the effects of such a correction on the VCG loop parameters. Therefore, analysis of the loop parameters should be performed first. For each recording, the average loops of each of the set $\mathcal{F}_{\text{p}}$, $\mathcal{F}_{\text{o}}$ and $\mathcal{F}_{\text{o}}^{\text{t}}$ were calculated. Each loop was then downsampled to 100 Hz to keep only the pertinent information regarding AFL. This is a similar approach to the one in [41], and does not remove pertinent information from the wave related to the morphology. VCG loop parameters were then calculated.

Performance quantification was done by evaluating the distance error with respect to

the parameters of the wave from $\mathcal{F}_{\text{p}}$:

$$\epsilon_{\theta,a,b} = |\theta_a - \theta_p| - |\theta_b - \theta_p|$$

where θ indicates a loop parameter, and a and b the two sets in comparison. This measure quantifies the difference of distance between the values of a and b from a true reference, which here is the values of the set of pure waves. The comparison is made with a = o, the set of overlapped uncorrected waves, and b = ot the set of overlapped corrected waves. It is expected that the errors be positive and large, indicating that the values after correction is closer to the true reference.

With orientation parameters, there is a risk of sign ambiguity when calculating the errors. Therefore when calculating the distance error of orientation parameters, the expression is modified to the following:

$$\epsilon_{\theta,a,b} = \min\left(\left|\theta_a - \theta_p\right|, \left|\theta_a (\text{mod sgn}(-\theta_a)\pi) - \theta_p\right|\right) - \tag{4.38}$$

$$\min\left(\left|\theta_b - \theta_p\right|, \left|\theta_b (\text{mod sgn}(-\theta_b)\pi) - \theta_p\right|\right) \tag{4.39}$$

Table 4.4 resumes this analysis on all four parameters. It can be seen that the correction affects orientation parameters most. There is net positivity in all parameters, showing that the corrected loops approach the parameter values of the pure waves. This result can be supplemented by how similar the loops are, shown in Section 4.5.

Table 4.4: Distance errors ϵ

θ	$\epsilon_{\text{o,ot}}$	p-value
ϕ_{AZ}	28.22 ± 31.22	$<$ **0.01**
ϕ_{EL}	26.78 ± 46.44	$<$ **0.01**
ψ_{PL}	$22.60{\cdot}10^{-3}$ ± $35.00{\cdot}10^{-3}$	$<$ **0.01**
ψ_{PG}	0.15 ± 0.13	$<$ **0.01**

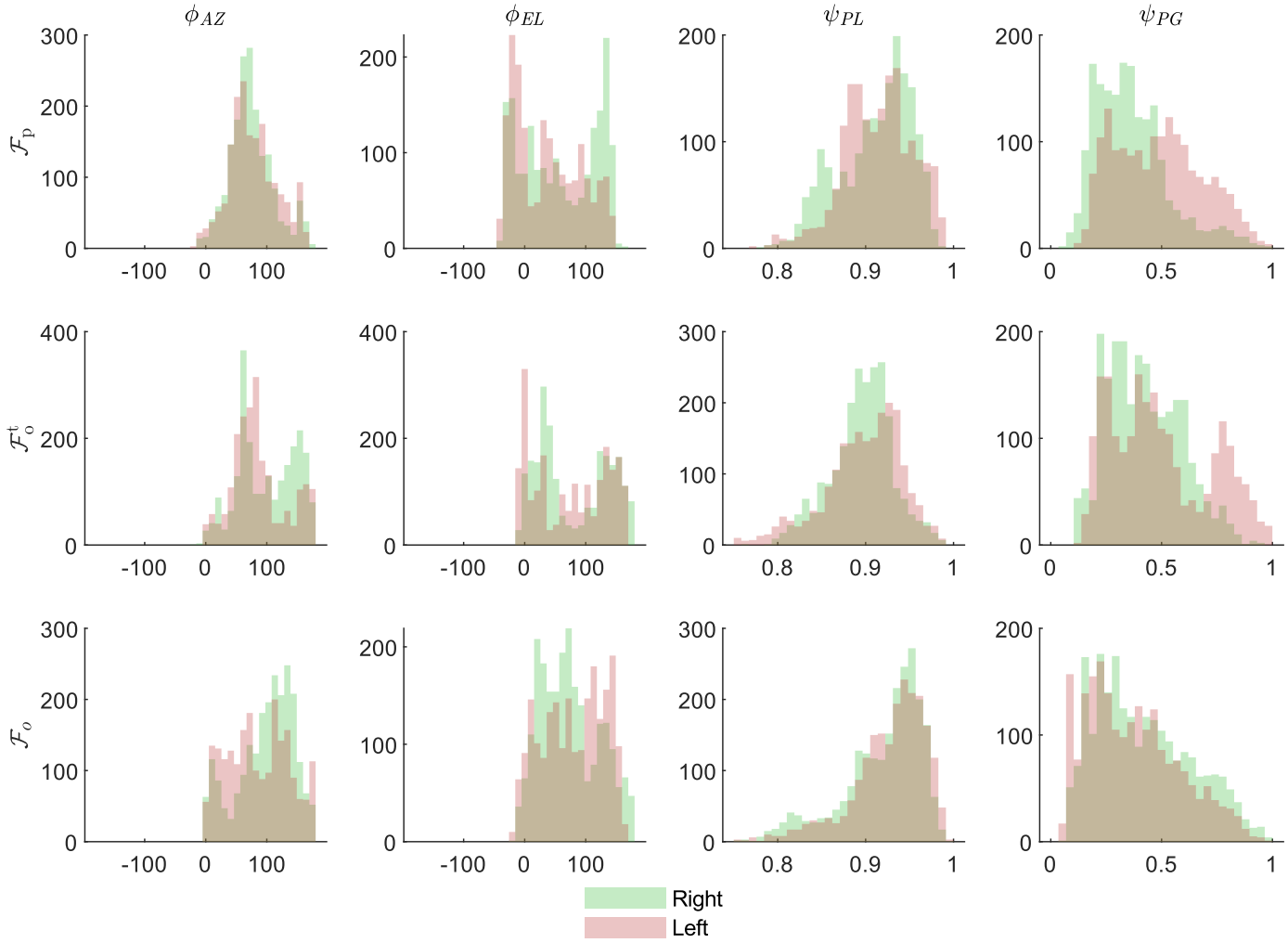

Figure 4.23: Histogram of the distribution of loop parameters for different sets. Top row: $\mathcal{F}_{\mathrm{p}}$. Middle row: $\mathcal{F}_{\mathrm{o}}^{\mathrm{t}}$. Bottom row: $\mathcal{F}_{\mathrm{o}}$.

In Figure 4.23, one can observe the variability profile, given by the histogram of the values of all 4 loop parameters from all 56 recordings. It can be seen that the variability of the set $\mathcal{F}_{\text{o}}$ (bottom panels) differs largely from that of $\mathcal{F}_{\text{p}}$ (top panels). However, upon correction of the T wave component, the profile of $\mathcal{F}_{\text{o}}^{\text{t}}$ (middle panel) seems to resemble that of $\mathcal{F}_{\text{p}}$ more.

4.7.2 Characterization of AFL Using Recurrence Plot The quasi-periodicity of AA during arrhythmia has been shown above to produce circular dipole trajectories. When considering a certain dipole position or state, it may be possible that after one complete cycle, the dipole returns to the same state, or one that is close to it. This recurrent behavior may indicate information about the stability of the circuit. It is expected for stable circuits to return to a state more frequently, and for unstable circuits to never return to a previous state. Moreover, the timings between a cycle of the state vectors may also contain information about the periodicity of propagation.

In this approach, recurrence quantification analysis (RQA) is performed. Details on RQA has been presented in Section 3.3, with the quantifying function $D(i, j)$ detailed in (3.9). Sample URPs can be seen in Figure 4.24 (middle panels) calculated from a 5-second sample of two different VCG signals presenting AFL (top panel). Repetitive patterns can be seen in several subregions of the URP. However, it is clear that the original VCG signal (top panel, dotted black line) has a wandering trend that was not effectively removed, and as a result its URP (middle panel, right) presents bias. This can be seen in the region where $i \in [2.0; 3.0]$ and $j \in [2.0; 3.0]$. As the delay j increases, more portion of the region has recurrence values that are close to 0 (green coloration on the URP). In addition, the strong periodicity of the heart beat due to ventricular complexes (QRST waves) introduce recurrent patterns that are unrelated to AFL.

To obtain a proper signal for RQA, it is preferred to obtain the continuous recording of only atrial activity. However, it has been mentioned that this is difficult to do in AFL. Therefore, a different approach is employed in order to obtain atrial activity recording. Segmented VCG F waves from sets $\mathcal{F}_{\text{p}}$ and $\mathcal{F}_{\text{o}}^{\text{t}}$ of a recording were zeros-meaned (by removing the mean value of the signal in each lead) and placed, at their corresponding time instants $\hat{n}_0$ (previously obtained using the GLRT), into a new signal originally composed of zeros. The result is a restitched signal composed of only atrial activity. An example of this is illustrated in Figure 4.24 (top panel, blue line). Note the straight lines during QRS complexes indicating zeroes.

Using the restitched VCG, the URP in Figure 4.24 (middle panel, left) better represents

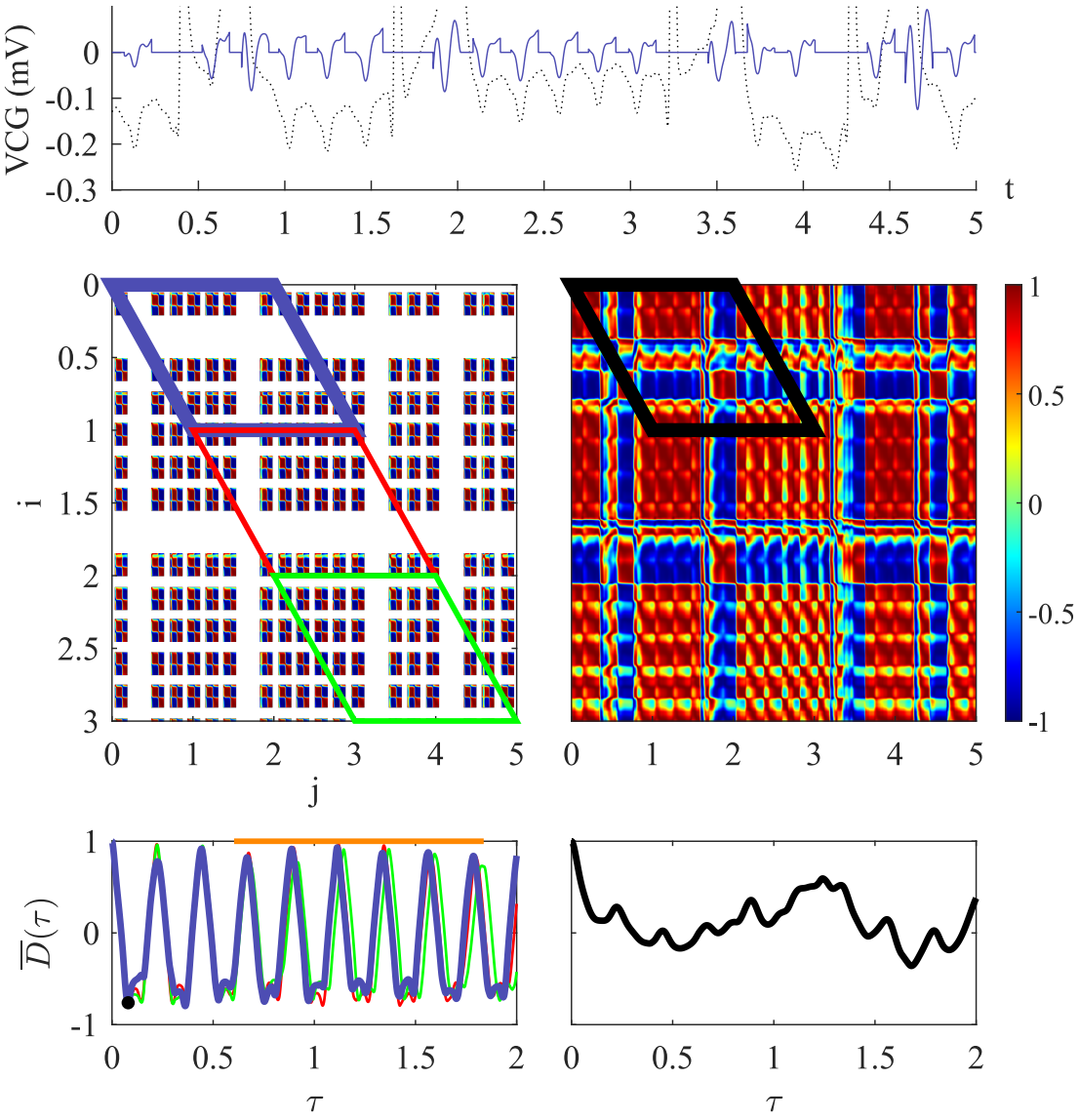

Figure 4.24: Illustration of RQA. Top: post-filtered VCG (black dotted line) and restitched VCG (blue line). Middle: example of URPs $D(i, j)$ for restitched VCG (left) and original ECG (right). The colorbar (right) indicates URP values; white regions correspond to undefined values (NaNs). Bottom: example of recurrence signals $\overline{D}_s(\tau)$ from the corresponding URP segments (colored boxes). Refer to text for details.

the recurrence information of AFL. However, due to the existence of zero-values within the signal, the calculation of recurrence becomes undefined, hence the URP contains large portions of undefined values. In implementation, these undefined values are instantiated as not-a-numbers (NaNs).

4.7.2.1 Calculation of Recurrence Signal The URP can be used as-is to retrieve recurrence features [86–89]. However, it is common to observe non-stationary behaviors in these plots, inherited from the signal. Therefore, quantification must be performed

with care in order to properly capture information without risking bias in the analysis. One method is to process the URP in short segments rather than in whole in order to achieve stationarity, but at the expense of increase in estimation variance.

A segment starts at the main diagonal, and progresses along the diagonal up to a length I. The segment width spans from the main diagonal towards the edge of the plot to the right (i.e. increasing j) for up to a width J for each row of the diagonal. On the other hand, note that the delay variable can be introduced by $\tau = j - i \Leftrightarrow j = i + \tau$. A segment of index k can be described by the equation:

$$D_k(i, \tau) = D(i, i + \tau),\ i \in [(k-1)I; kI[\tag{4.40}$$

A highlight of segments can be found in Figure 4.24 (middle panel). The choice of segment length and width I and J determines the properties of the segment, and should be considered as parameters. However, it can be reasoned in the context of AFL that stationarity can be guaranteed for long periods of time due to the regularity of F wave manifestation. For this research, I is set to 2000 samples (1 second at $f_s = 2000$ Hz), and J to 4000 samples (2 seconds at $f_s = 2000$ Hz). Note that $\tau \in [0; J-1]$. The value of J assures that a large amount of AFL cycles can be captured in the segment.

A recurrence signal can be defined as the average of a segment along i:

$$\overline{D}_k(\tau) = \frac{1}{I} \sum_{i=(k-1)I}^{kI} D_k(i, \tau) \tag{4.41}$$

An example of this signal is shown in Figure 4.24 (bottom panels). It is clear that AFL has a quasi-periodic recurrent behaviour, as shown by the high and repetitive peaks. Furthermore, this is better represented using the restitched signal compared to the original signal, whose recurrence signal presents a very large undulating trend with low recurrence values that mask the peaks related to AFL.

To quantify recurrent behavior, two parameters were considered (Figure 4.25). The first parameter S_1 relates to the range of variation in AA propagation. This is given by the peak-to-peak amplitude of the recurrence signal, taken from one maximum to the next minimum. It is hypothesized that the two AFL localizations will have different ranges in recurrence of spatial propagation. The second parameter S_2 relates to the periodicity of propagation, and is essentially an estimate to the AFL cycle length. This is calculated by the peak-to-peak interval of the available maxima. The two parameters are calculated for all available points in the signal, hence making a series of values.

Calculation of these parameters can be done for each segment. However, the existence

of long periods of undefined values can be troublesome, as recurrence signals present discontinuities due to these values. In order to combat this problem, the signals were aggregated by calculating their median value:

$$\tilde{D}(\tau) = \text{median}_{k=1}^{K} \overline{D}_k(\tau) \tag{4.42}$$

where K is the number of segments available. The use of the median is preferred over the mean for its robustness. The result is a single continuous recurrence signal. In some recordings, the function $\tilde{D}$ was unfortunately still discontinuous due to undefined regions that were too long. These patients were discarded (4 right AFL, 3 left AFL).

From the two parameters, several features can be calculated, that aim to capture the cycle-to-cycle variability in AFL: the 1) mean, 2) variance, 3) skewness, and 4) kurtosis of the two series S_1 and S_2. As mentioned before, the features are in fact statistical moments, and characterize the properties of the series distribution. In total, there are $2 \times 4 = 8$ features considered. A summary statistic of these features can be found in Table 4.5.

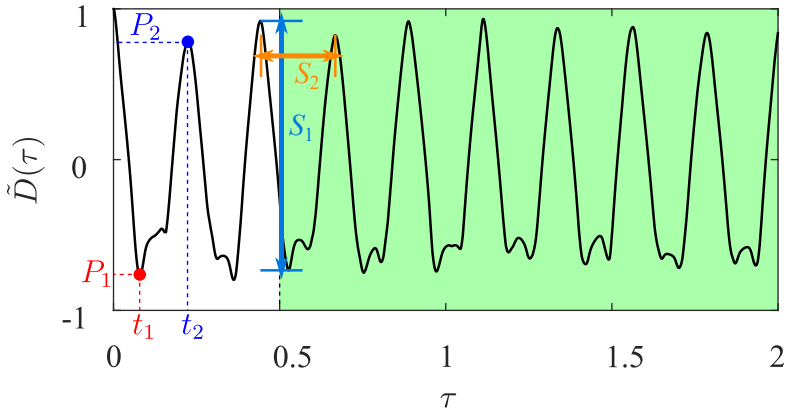

Figure 4.25: Illustration of recurrence features obtained from a recurrence signal.

Table 4.5: Group Statistics for RQA Features

	Feature	Right AFL	Left AFL	p-value
S_1	Mean(S_1)	1.47 ± 0.16	1.48 ± 0.17	0.88
	Var(S_1)	$1.24 \cdot 10^{-2} \pm 1.31 \cdot 10^{-2}$	$1.20 \cdot 10^{-2} \pm 1.48 \cdot 10^{-2}$	0.65
	Skewness(S_1)	0.80 ± 0.61	0.58 ± 0.45	0.58
	Kurtosis(S_1)	2.84 ± 0.93	2.64 ± 0.82	0.64
S_2	Mean(S_2)	0.23 ± 0.04	0.20 ± 0.06	$< \mathbf{0.01}$
	Var(S_2)	$4.78 \cdot 10^{-5} \pm 2.51 \cdot 10^{-3}$	$1.25 \cdot 10^{-5} \pm 1.68 \cdot 10^{-4}$	0.08
	Skewness(S_2)	$9.75 \cdot 10^{-14} \pm 5.51 \cdot 10^{-1}$	$7.20 \cdot 10^{-3} \pm 4.03 \cdot 10^{-1}$	0.90
	Kurtosis(S_2)	2.27 ± 0.49	2.11 ± 0.43	0.65

4.7.2.2 Analysis of AFL Spatial Variability In this short section, a supplementary analysis is performed to study AFL spatial variability. A similar study on AF using BSPM (184 leads) has been done recently [49], and showed some interesting properties on the pathology. AF was discovered to be a spatially variable process with stationary temporal properties. This was confirmed by analyzing the relation between short-term and long-term recurrence, and short-term and long-term AA subspace.

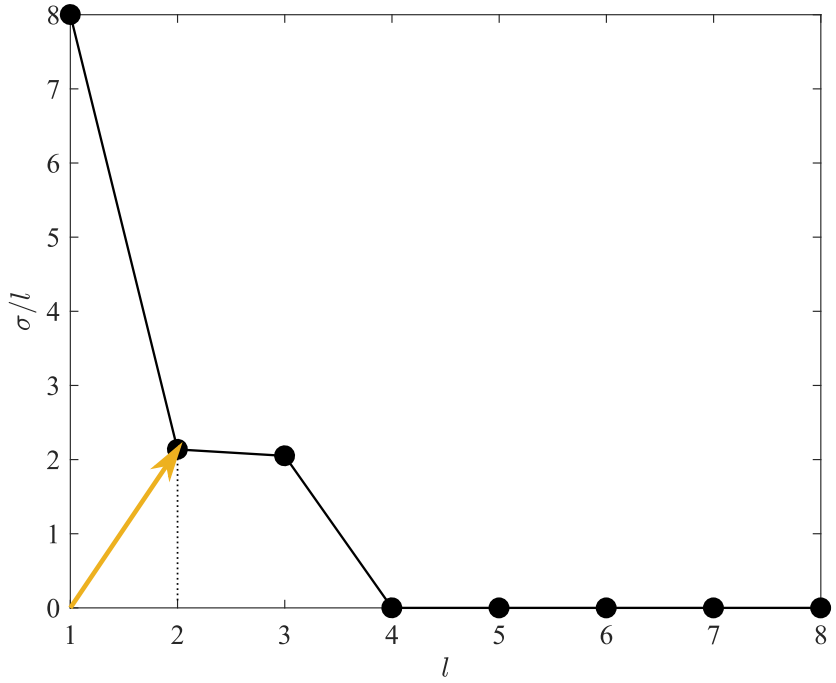

Figure 4.26: Determination of AA subspace. The orange vector corresponds to the vector with the shortest length, beginning at (1,0) and touching the normalized spectrum. The value of the abscissa at the touch point is taken as the measure of AA subspace.

Short-term recurrence is given as the mean of the absolute value of the first negative peak $|P_1|$ over all recurrence signals $\overline{D}_k$ (see Figure 4.24, bottom left panel, black dot). Long-term recurrence is given as the mean of the mean of the absolute value of the later portion of the recurrence signal Mean($\left|\overline{D}_k(\tau)\right|$) with $0.59 \leq \tau \leq 1.76$ (duration of orange line in Figure 4.24).

AA subspace is determined by performing SVD on the AA, then plotting the singular values in order, dividing each by the number of leads, and determining the point closest to the point (1,0) (see Figure 4.26). The value of the l axis gives the subspace value. Short-term subspace (Ss) calculates this metric on individual AA cycles and averaging them, whilst long-term subspace (Sl) calculates this on the complete signal (VA removed prior to calculation).

The results found for AF showed that Ss and Sl for AF was different, with Ss being significantly lower than Sl. Subspaces were also shown to be negatively correlated with

Mean($|P_1|$) and Mean($\left|\overline{D}_k\right|$). This means that AF exhibits large spatial variability, with the AA propagation patterns varying greatly over time, and that this translates to lower recurrent behavior.

For AFL, a modified approach was adopted. Because the URP has many undefined values, some recurrence signal $\overline{D}$ have discontinuities at the points of interest. Therefore, the short and long term recurrence were quantified on $\tilde{D}$ instead (see Figure 4.25, green area). To determine the AA subspace, the ensemble of VCG loops were retransformed back to 8-leads ECG via the Dower transform. Short-term subspace was calculated on single AFL cycles and then averaged, whilst long-term subspace on concatenation of all AFL waves for a single record (i.e. joining the waves from end to end).

For AFL, the difference between Ss and Sl showed that short and long term subspace did not vary much, although significant (median $8.8 \cdot 10^{-3}$, $p < 0.05$, Wilcoxon signed rank test). Mann-Whitney U test on Ss and Sl returned the null hypothesis at a non-significant p-value. This shows that AFL is a stable spatial process. This is supported in physiology by the existence of a unique circuit, as opposed to in AF, where multiple circuits cause chaotic phase breaking. Hence the propagation pattern is expected to be much more stable.

Neither short-term nor long-term recurrence was shown to be linked with AFL subspace (correlation values near zero). This is most probably due to the stability of spatial properties, hence it is difficult to achieve any significant variation. In addition, the median subspace value was close to 3 for both Ss and Sl. This suggests that AFL is not only spatially stable, but a majority of this spatial information is contained within a small subset of leads.

A different analysis was conducted on the values of the first negative peak (equal to short-term recurrence) and the second positive peak P_2 (see Figure 4.25, red and blue dots respectively) as well as their times of occurrence t_1 and t_2. These markers can be regarded as quantifying recurrence within a single AFL cycle. In AF, it was found that $|P_1|$ and P_2 were positively correlated with Mean($\left|\overline{D}_k\right|$). This shows that long-term recurrent behavior can be predicted from short-term behaviors (lower short-term recurrence = lower long-term recurrence). In AFL, this was found to be the same with both $|P_1|$ (Spearman $\rho = 0.76$, $p < 0.01$) and P_2 (Spearman $\rho = 0.48$, $p < 0.01$).

In AF, $|P_1|$ and P_2 were negatively correlated with t_1 and t_2 respectively. In AFL, no significant results were obtained when the same is performed. It could be that because AFL has a stable spatial property, this variation is not very defined. However it is observed that t_1 and t_2 were correlated (Spearman $\rho = 0.66$, $p < 0.01$) and they were different for right and left AFL. Table 4.6 resumes this difference. It is interesting

to see that this is the same conclusion with Table 4.5, and it can be reached with the analysis of a single recurrence cycle. On the other hand, it suggests the difference in AFL propagation dynamics, with left AFL seemingly completing cycles much faster than right AFL.

Table 4.6: Statistics of t_1 and t_2

	Right AFL	Left AFL	p-value
t_1	95.0 ± 20.3 ms	80.0 ± 21.2 ms	$\mathbf{< 0.01}$
t_2	231.5 ± 50.8 ms	196.5 ± 59.6 ms	$\mathbf{< 0.01}$

4.8 Dataset

The dataset of this research consists of essentially two types of item: 1) 12-lead ECG recordings of 1 minute in length, and 2) post-operative ablation procedure reports. The ECG recordings constitute the main item for processing, whereas the reports help to determine circuit location. The relatively long recording length ensures that enough F waves can be obtained, even in challenging conditions such as 3:1 or even 2:1 blocks. The reports act as the gold standard for data labeling, given that it reflects the exact location of the circuit.

The patient group in this study consists of 60 patients admitted into the Centre Hospitalier Princesse Grace, Monaco, for ablation of AFL during the period starting from January until December 2017. Some statistics regarding the group can be found in Table 4.7.

Table 4.7: Summary of Patient Information

	Right AFL	Left AFL	p-value	
Age (yrs)	71.39 ± 10.34	70.31 ± 9.55	NS	Values
Weight (kg)	89.03 ± 27.89	87.92 ± 32.73	NS	
Height (cm)	164.00 ± 34.07	163.20 ± 26.49	NS	
Body Mass Index ($kg{\cdot}m^{-2}$)*	26.60 ± 2.63	26.63 ± 4.43	NS	
Number of recordings	31	25	-	

expressed as mean ± standard deviation, except for *, expressed instead as median ± median absolute deviation; NS: not statistically significant

ECG recordings were taken during the ablation procedure. Each patient was placed on the operating table in a supine position. 9 electrodes were placed on the body surface for acquisition of the 12-lead ECG using the Labsystem Pro recording system (Boston Scientific, USA). The acquisition happens at a sampling frequency of f_s = 2000 Hz and analog-to-digital conversion has a resolution of 16 bits.

During the ablation operation, mapping maneuvers allowed the determination of the right or left circuit localization. Ablation was performed and at the end of each procedure, regardless of success, a report was given, detailing the conditions of the patient prior and after the operation, maneuvers performed and in particular, the description of the circuit, encompassing the actual physical pathway, the direction of rotation and the estimated isthmus location.

In total, 62 recordings of AFL were obtained. After refining the selection by removing recordings that were too difficult to use (atrial activity amplitude too low, block ratio too low), 56 recordings remain: 31 recordings associated with right AFL (of which 24

are typical AFL) and 25 associated with left AFL. 21 of the circuits in the right AFL are typical CCW AFL, and 3 of the circuits are typical CW AFL.

4.9 Conclusion

In this chapter, the methodology for extracting variability features from AFL was presented. Section 4.2 discussed filter settings required to remove external variability from the ECG related to observation noise and physiologic motion. Novel methods for F wave detection using GLRT was presented in Section 4.3 and showed great performance in detecting F waves (Acc = 0.93, AUC = 0.97).

Next, external sources of variability were removed. An original method for removal of respiratory motion was presented in Section 4.4 with an improvement in respiratory parameter estimation to produce physiologically-correct parameter values. In Section 4.5, a method for T wave overlap correction is presented that allows reliable recovery of overlapped F waves (mean similarity after correction $0.95/1.00$, compared to non-overlapped waves).

Section 4.6 presented an original method for optimizing the Inverse Dower Transform that accounts for distortion factors observed when recording the ECG.

Finally, characterization of AFL was detailed Section 4.7, where two approaches allowed the extraction of variability features that can be used for localization. The first approach, based on VCG loops, was shown to contain artificial variability related to the sign ambiguity of singular vectors. A procedure was introduced to correct this problem and thus remove this artificial variability.

Chapter 5

Application of Supervised Learning for Localization and Analysis of Atrial Flutter

5.1 Introduction

In the previous chapter, features were proposed that capture the variability contained within AFL manifestation on the ECG. These features are assumed to take different values according to the localization of AFL. Through application of supervised learning techniques, it should be possible to obtain a practical classifier for right-or-left AFL localization. Practicality implies, in part, the identification of the model and its hyperparameters, as well as measures of its generalized performance (i.e. performance on unknown datasets).

This chapter is dedicated to explaining the supervised learning techniques used for separating AFL circuit localization, as well as its application on the dataset prepared from the processing pipeline of Chapter 4. Much of the material and jargon here derive from the machine learning domain. A notable reference was prepared by Hastie et al. [90]. Section 5.2 introduces briefly the problem of supervised linear classification, performance generalization and selection of relevant features. Details on two original learning recipes for performance generalization and feature selection are presented, useful for identifying the best classifier model. Section 5.3 details the results of classification when applied on the dataset issued from the beat-to-beat approach, and Section 5.4 details the results of classification for the recurrence quantification approach.

The notation in this chapter is slightly different, with lower cases x denoting a deterministic scalar, but also a vector or matrix, according to context. When x is a vector, it is a column vector whose size will be defined in the text. Uppercase letters X are random scalars, vectors or matrices depending on the context.

5.2 Supervised Learning Methods for Classification

In this research, focus is given to supervised learning methods, since the dataset includes labels (right or left) of each recording. Also, linear techniques have been utilized for classification of data. The main reason for preferring this approach is 1) due to the small

size of the dataset ($N = 56$) that does not favor more advanced methods, which typically require hundreds of data samples, and 2) it is preferred in this research to investigate the difference between right and left AFL without incurring risk of method-related issues such as overfitting.

5.2.1 Linear Classification Linear classifiers attempt to model the relation between its input variables and outputs as a linear function. Given an input data x belonging to a class k, the aim is to perform a linear fit f_k on the data such that $f_k = b_{k0} + x^\intercal b_k > 0$, whose value is different to that of another data z belonging to class l and having fit parameters $[b_{l0}\ b_l{}^\intercal]^\intercal$. The most important thing to note is that the class boundary satisfying $(b_{k0} - b_{l0}) + (x - z)^\intercal (b_k - b_l) = 0$ is linear, and hence resembles a hyperplane. When considering two classes, the input space is divided into two half-spaces, each mapping onto different decisions. *Domination* occurs when one of the two fits change sign; the one with a positive sign sets the label of the data. This is a classic approach of *linear classification*, and the fit function is known as a *discriminant function*. In this work, the focus is to classify right or left localization, hence only two classes are available, and so in theory, only one such function is necessary.

There are several ways of finding such a discriminant function. One way is by the evaluation of the *logarithm of the odds ratio*. This approach relies heavily on the class-conditional densities, as there is explicit involvement of the probabilities. Example of classifiers based on this approach are the *linear discriminant analysis* (LDA) and *logistic regression* (LOG) classifiers. Alternatively, the linear separation boundary can be found by an optimization approach that tries to fit a linear *separating hyperplane* boundary between the two class densities. A popular example of this type of classifier is the *support vector machine* (SVM) classifier.

5.2.2 Generalization of Classification Performance Classifiers rely on data in order to approximate the class boundary. The more data there is, the better the approximation (i.e. the lower the estimation variance); an ideal case would be infinite data, hence the class boundary to be exactly known, and it is often termed the *optimal Bayes boundary*. However in practice, there is never infinite data: more often than not, there is lack of data due to e.g. rarity of target events (rarity of diseases), or difficulty of data extraction (e.g. high financial or temporal cost) and this is quite common in fields related to biomedical engineering. Hence, the boundary can only be estimated from typically small amounts of available data, usually termed *training samples* $\mathcal{Y}_{\text{train}} = \{(x_i, g_i), \cdots, (x_M, g_M)\}$, where x represents an observed data with associated label g. It is expected that this boundary is not optimal compared to the Bayes boundary.

When unknown samples are presented to the classifier, it may either correctly or wrongly classify it. The goal in generalization will be to infer the error the model will make on these unknown data when trained with a limited set of data. In doing so, what is achieved is the assessment of the generalized classifier performance. Methods of measuring generalized performance are split into two: analytic approaches such as the information criteria (Akaike, Bayesian) and minimum description length, and *sample reuse methods* such as cross-validation and bootstraps. In this research, the focus will be on cross-validation methods.

Cross-validation (CV) essentially attempts to measure the average prediction error made by a classifier when trying to predict a target class, given an input. This is achieved by performing multiple fits to several subsets $\mathcal{Y}$ of the training data, equally split into K number of *folds*. At each iteration, one fold is left out for testing (i.e. used as $\mathcal{Y}_{\text{test}}$, and the remaining folds are used as training examples $\mathcal{Y}_{\text{train}}$. The rationale behind this is that each fold should be composed of a set of points different than the other folds, hence it is possible to assume each fold as containing independent draws from the same class-conditional distribution. The training and test folds would then have the same distribution, but independent samples. Traditionally, the average of the errors of all folds is taken as a measure of generalized performance.

The number of iterations depends on the number of folds. On one hand, retraining of the classifier is easy when there are limited data points (i.e. K is large, hence less data per fold), but on the other hand the CV iterations grow as well. In general, it is preferred to train with as much data as possible. K is usually set to around 5 to 10. However, this is good when the total number of training examples are large (above 100 for example). When there are under 100 training examples, the proposed value of K does not guarantee enough data for training. In these cases, the K is maximized by setting it to M, the number of available examples. Each fold collapses into one single example. The training set is of size $M - 1$ and the test set is a single example. This is commonly known as *leave-one-out cross validation* (LOOCV). The tradeoff here is a high variance in estimating the prediction error, in exchange for better training conditions.

5.2.3 Modified LOOCV for Threshold Selection LOOCV allows us to also tune some parameters of the model. Because most of the items in this research deal with performing two-class decision like detection in Section 4.3 and classification, one particular parameter that will be tuned is the threshold of decision γ. One 'drawback' with traditional LOOCV is that the method does not allow us to choose the most performing γ for a given dataset. For each fold, a different threshold will be achieved

due to different training examples. It is tentative to take the average threshold or the average model parameters, but there is no guarantee of good performance.

Instead, the LOOCV recipe can be modified. This original modification utilizes the class probabilistic information within the distribution of points after fitting is done to determine the most probable class label for the test sample. The algorithm is described below, and summarized in Algorithm 2.

Let $\mathcal{Y}^i_{\text{test}}$ be the i-th test fold, and $\mathcal{Y}^i_{\text{train}}$ its associated training examples. The model is first fitted to $\mathcal{Y}^i_{\text{train}}$ to obtain the fitting parameters $[\hat{b}_0\ \hat{b}^\intercal]^\intercal$. A threshold γ is selected from a set $\mathbf{\Gamma}$. Then the following quantities are calculated:

$$P^{\text{T}}_{>\gamma} = \mathbb{P}\{G = \text{T}|(\hat{b}_0 + \hat{b}^\intercal x) > \gamma\} \tag{5.1}$$

$$P^{\text{T}}_{<\gamma} = \mathbb{P}\{G = \text{T}|(\hat{b}_0 + \hat{b}^\intercal x) < \gamma\} \tag{5.2}$$

$$P^{\text{F}}_{>\gamma} = \mathbb{P}\{G = \text{F}|(\hat{b}_0 + \hat{b}^\intercal x) > \gamma\} \tag{5.3}$$

$$P^{\text{F}}_{<\gamma} = \mathbb{P}\{G = \text{F}|(\hat{b}_0 + \hat{b}^\intercal x) < \gamma\} \tag{5.4}$$

These are essentially the conditional probabilities of the classes of fitted points with respect to the threshold.

Validation is then performed by predicting the test label $\hat{g}^{(i)}$ through comparison of two probabilities ($P^{\text{T}}_{>\gamma}$ vs. $P^{\text{F}}_{>\gamma}$ or $P^{\text{T}}_{<\gamma}$ vs. $P^{\text{F}}_{<\gamma}$) depending on the location of $\hat{b}_0 + \hat{b}^\intercal x^{(i)}_{\text{test}}$ with regards to γ, and deciding the class based on which probability is larger. The predicted label $\hat{g}^{(i)}$ is tested against $g^{(i)}_{\text{test}}$: if matching, then a counter C^{T}_{+} or C^{T}_{-} is incremented based on the class of g_{test}. If not matching, then the counter C^{F}_{+} or C^{F}_{-} is incremented based on $(\hat{b}_0 + \hat{b}^\intercal x_{\text{test}})$ being higher or lower than γ. These counters start initially at 0.

The process is repeated by iterating on a different fold. At the end of the CV procedure, the counters indicate the total counts of true positives, true negatives, false positives and false negatives respectively for γ. This can performed for all values of $\gamma \in \mathbf{\Gamma}$.

Standard performance metrics such as sensitivity, specificity and accuracy can be calculated as follows:

$$\text{Se}_{\text{CV}} = \frac{\text{C}^{\text{T}}_{+}}{\text{C}^{\text{T}}_{+} + \text{C}^{\text{F}}_{-}} \tag{5.5}$$

$$\text{Sp}_{\text{CV}} = \frac{\text{C}^{\text{T}}_{-}}{\text{C}^{\text{T}}_{-} + \text{C}^{\text{F}}_{+}} \tag{5.6}$$

$$\text{Acc}_{\text{CV}} = \frac{\text{C}^{\text{T}}_{+} + \text{C}^{\text{T}}_{-}}{\text{C}^{\text{T}}_{+} + \text{C}^{\text{F}}_{-} + \text{C}^{\text{F}}_{+} + \text{C}^{\text{T}}_{-}} \tag{5.7}$$

and a pseudo-receiver-operating characteristic (pseudo-ROC) curve can be derived, allowing us to calculate the area under the pseudo-ROC curve. All metrics are valued between 0 and 1. The threshold that maximizes the Youden statistic $\mathrm{J_{CV}}(\gamma) = \mathrm{Se_{CV}}(\gamma) + \mathrm{Sp_{CV}}(\gamma) - 1$ is deemed the optimal threshold γ_{opt}. Note that the three performance quantities $\mathrm{Se_{CV}}$, $\mathrm{Sp_{CV}}$ and $\mathrm{Acc_{CV}}$ are different than the three quantities described previously: here, they are issued from a cross-validation approach.

The key difference in this approach is to be able to obtain a single optimal threshold for the ensemble of folds. This is contrasted to the standard CV approach, where there would be K optimal thresholds: one for each fold. It is not directly immediate which one of these K thresholds would be optimal for the ensemble. In addition, the Youden statistic can be replaced by any other metric that is convenient to selecting the threshold.

Data: Set of examples $\mathcal{Y} = \{(x_1,\ g_1),\ \cdots,\ (x_M,\ g_M)\}$

Define threshold values $\mathbf{\Gamma} = \{\gamma_1 \cdots \gamma_K\}$

foreach $\gamma_k \in \mathbf{\Gamma}$ **do**
- Set counters $\mathrm{C_+^T}$, $\mathrm{C_-^T}$, $\mathrm{C_+^F}$, $\mathrm{C_-^F} = 0$
- **for** $i \leftarrow 1$ **to** M **do**
  - Set $\mathcal{Y}_{\mathrm{test}}^{(i)} = \{(x_i,\ g_i)\}$ and the remaining into $\mathcal{Y}_{\mathrm{train}}^{(i)}$
  - Use $\mathcal{Y}_{\mathrm{train}}^{(i)}$ to calculate $[\hat{b}_0\ \hat{b}^\intercal]^\intercal$ and class conditional probabilities (5.1)-(5.4)
  - **if** $(\hat{b}_0 + \hat{b}^\intercal x_{test}^{(i)}) > \gamma$ **then** $\hat{g}^{(i)} = \mathrm{T}$
  - **else** $\hat{g}^{(i)} = \mathrm{F}$
  - **if** $\hat{g}^{(i)} = g_{test}^{(i)}$ **then**
    - **if** $(\hat{b}_0 + \hat{b}^\intercal x_{test}^{(i)}) > \gamma$ **then**
      - increment $\mathrm{C_+^T}$
    - **else**
      - increment $\mathrm{C_-^T}$
  - **else**
    - **if** $(\hat{b}_0 + \hat{b}^\intercal x_{test}^{(i)}) > \gamma$ **then**
      - increment $\mathrm{C_+^F}$
    - **else**
      - increment $\mathrm{C_-^F}$
- **end**

end

Algorithm 2: Modified leave-one-out cross-validation

5.2.4 Selecting Features A common issue in obtaining a practical classifier is the *selection of a set of input variables or features* that should be used. This problem is well-known in the machine learning community, and often referred to as *feature selection*. The rationale for this, as opposed to using only one of any available features (or all together), can be justified by two remarks.

In Section 4.6, a toy classification example has been presented. The general remark then was that using two features may present some dependence that can be leveraged by classifiers to achieve higher performance. Secondly, increasing model complexity has the effect of forcing the classifier to overfit to the training samples. Ideally, this will drive the training error to zero, but any extra unknown samples will typically be wrongly classified because of the overestimated boundary. This is usually exacerbated in setups with very small sample sizes: at a certain input-space complexity (e.g. a high-dimensional space) but with small amounts of data points, adding more complexity to the input space causes classifier performance to drop (the Hughes phenomenon [91,92]).

Reducing model complexity avoids overfitting, but it is assumed that the classes must be separable with the low-complexity boundary, but this is not always guaranteed. There is a tradeoff between avoiding overfitting (high *variance*) and avoiding false assumption of a low-complexity boundary (high *bias*). Domingos provided a formulation for this tradeoff as [93]:

$$\begin{aligned}\mathbb{E}[L(g,G(x))] =& \text{Noise}(g,G^*(x)) \\ &+\text{Bias}(G^*(x),\mathbb{E}[G(x)]) \\ &+\text{Variance}(\mathbb{E}[G(x)],G(x))\end{aligned} \tag{5.8}$$

where L is a loss function, g is the true label, $G(x)$ is the class label estimator and $G^*(x)$ the class label with the highest probability, given x as an input. The exact terms are not developed in further detail. The term Noise is an irreducible error unrelated to the model, but instead to the training samples. Bias refers to the error made by the optimum prediction compared to the expected prediction, and Variance relates to the error between the expected prediction and the predicting function evaluated over a set of training dataset (which could be the K cross-validation folds, for example).

Highly complex models reduce Bias due to the high precision of $G(x)$ in predicting $G^*(x)$, but incur large Variance because for each fold, the model overfits the training data and thus $G^*(x)$ will be very different from the predictions issued from each fold. The inverse happens when model complexity is reduced. Therefore, a compromise should be achieved between high- and low-complexity models. In this research, complexity

is measured by the *number of features* used. At some number of features, the bias-variance tradeoff will cause the performance to have an inflection point, which will indicate the best number of features.

In selecting features, the ones that are most *relevant* should be selected. A discussion on this aspect can be found in [94,95]. Relevance of a feature $\xi_i \in \mathcal{X}$ is defined in [94] as:

$$\mathbb{P}\{G = k|X = x, \mathcal{X}\} \neq \mathbb{P}\{G = k|X = x, \mathcal{X} \setminus \xi_i\} \tag{5.9}$$

where the notation $\mathcal{X} \setminus \xi_i$ means the feature ξ_i is removed from the set $\mathcal{X}$. This means relevant features affect the class conditional probability. The optimal feature subset $\mathcal{E}^* \subseteq \mathcal{X}$ would then maximize that probability (and implicitly, the classifier performance).

Three common approaches are found in the literature for this purpose: 1) the *wrapper* approach that utilizes the classifier as a part of the selection process, 2) the *filter* approach that screens features for relevance using some kind of covariance index (e.g. correlation, covariance, information-theoretic measures [96,97]), and 3) the *embedded* approach where the selection process is built into the learning process (e.g. weights, penalty or regularization terms, such as in group lasso).

Filters are simple and quick since they are usually based on analytically computable criteria. However, they do not take into account the classifier and its inherent complexity or strategy in learning. Embedded approaches are trickier since the constraints have to be included inside the classifier algorithm, and this typically requires an additional tuning parameter to be used as a learning rate or weight. Here, the wrapper approach is preferred, as it does not explicitly require tuning parameters, and integrates the classifier algorithm into the selection workflow.

The wrapper approach was detailed by Kohavi and John [94]. It consists of using the classifier inside the selection process to produce a performance index which guides the selection. This is done according to Figure 5.1. The learning algorithm is considered as a black box, and communicates with the wrapper process by receiving the training data and feature subsets, and outputting predictions on the training data. This makes the wrapper adaptable to any learning algorithms.

The process attempts to select the optimal subset by performing a selection heuristics. Then the subset of features are passed to the classifier, which performs a fit and produces a certain performance index. This is evaluated and used to guide the selection heuristics. This can be done until a certain convergence criterion or exhaustively (i.e. evaluate all possible combinations). The output of the procedure is $\mathcal{E}^*$, which can then be tested

on a separate test dataset. The reason for a selection heuristics is because in some

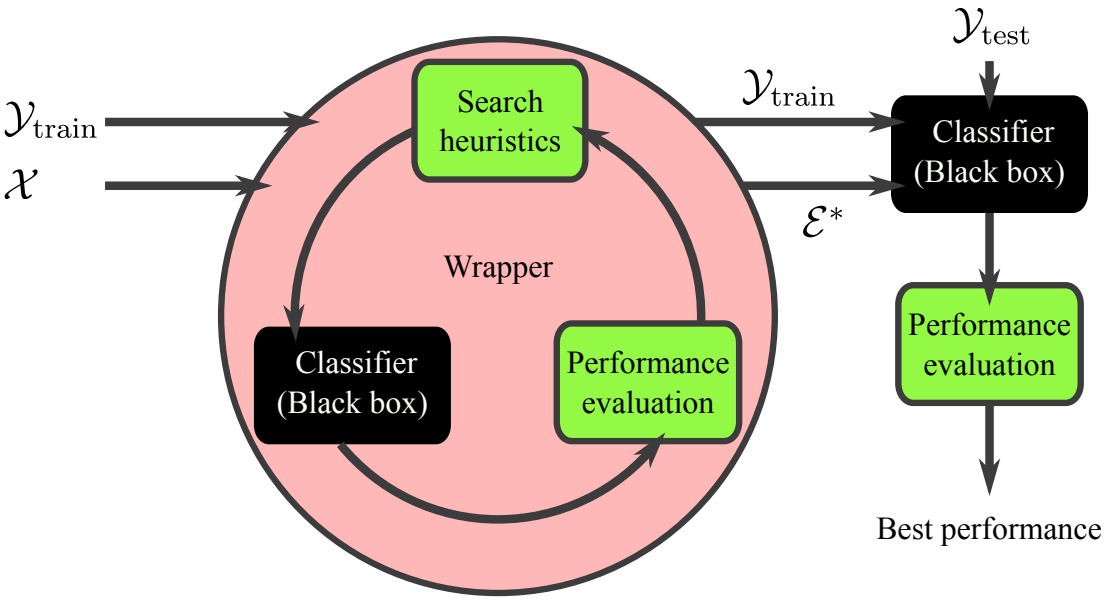

Figure 5.1: Illustration of the wrapper approach.

cases, the full set of features may be large and the search space scales exponentially. For I features, the total number of possible combinations is $2^I - 1$. This is not good for problems with even as little as 20 features. A common strategy is to start with all features included, and progressively eliminate features that do not satisfy a criterion (e.g. large reduction in performance). However, for low-dimensional problems, a search heuristics would probably perform comparably to an exhaustive approach.

5.2.5 Feature Scoring for Quantification of Relevance The output of the wrapper procedure should return the best feature subset. Although it is the goal that is sought after, it is also interesting to determine which feature presents the most relevance. This could help to understand how the classifier recruits features as model complexity increases, and in a more clinical viewpoint, what differentiates the two AFL localization.

The wrapper approach in itself does not return this information, hence an original strategy is adopted to extract this information. Note that (5.9) details a criteria for quantifying relevance. Interpreting it slightly differently, a relevant feature should be retained if it affects the class-conditional probability. Adding to this, it is preferred that the relevant features also contribute to a higher classification performance. Thus, relevant features in this sense should be seen as the features that are retained in the series of combinations giving the maximum performance as more (less relevant) features are added.

Therefore, the following recipe is adopted, summarized by Algorithm 3.

Data: Set of features $\mathcal{X} = \{\xi_1\ \xi_2\ \cdots\ \xi_I\}$

Set all score counters $s_i,\ i \in [1; I]$ to 0
foreach $l \in [1; L]$ **do**
  Set $\mathcal{E} = \varnothing$
  Perform a wrapper evaluation of all possible feature combinations of length l and calculate their performance metric S
  Determine the features participating in the best combinations of length l, and store them in $\mathcal{E}$
  foreach $\xi_i \in \mathcal{E}$ **do**
    Increment s_i
  end
end
foreach $i \in [1; I]$ **do**
  $\tilde{s}_i = \dfrac{s_i}{I}$
end

Algorithm 3: Feature scoring algorithm

Relevant features, by this procedure, should be present at every maximum performance combination, and attain a score $\tilde{s}_i \simeq 1$, whilst irrelevant features will have low scores (close to 0). Note that the wrapper evaluation is exhaustive, hence the number of features will then be important as it determines the computational cost. In this research, the number of features remain manageable (< 20), thus an exhaustive evaluation is permitted.

5.3 Localization of AFL Using VCG Loop Variability

As seen in Section 4.7, the F waves can be described as VCG loops, whose orientation and geometry may be quantified from singular values and vectors. These quantities capture the morphological information within the F wave. Employing the previous methodology detailed in Chapter 4, this variability can be extracted.

In this section, results of the application of the supervised learning methods from Section 5.2 is presented. Different setups are considered to analyze the effect of different parts of the processing chain on the performance of classification. Note that the evaluation of set $\mathcal{F}_{\mathrm{p}}^{\mathrm{r}}$ is not discussed in this chapter, but in Chapter 6 instead.

5.3.1 Localization Using Uncorrected Loops In a first try, it is interesting to see if localization can be performed using only waves without any processing (i.e. only waves after filtering). Only the sets $\mathcal{F}_{\mathrm{p}}$ (set of pure, non-overlapped F waves) and $\mathcal{F}_{\mathrm{o}}$ (set of T wave-overlapped F waves) are considered in this section. This is reasonable as the traditional way of visual inspection does not require any additional processing other than what is done by the acquisition device. Furthermore, it gives a baseline of comparison to the various processing stages that come later.

The 16 VCG loop variability features calculated from Section 4.7 were used as inputs to the three linear classifiers LDA, LOG and SVM. Figure 5.2 shows the plot of the accuracy against the number of features in a combination. A rather good starting accuracy can be seen with 1 feature. The mean performance is shown to increase as more features are added, suggesting that combination of some features add information to the separability between right and left AFL. At around 7 features, the maximum envelope (top dashed lines) becomes stable. The maximum accuracy, obtained from set $\mathcal{F}_{\mathrm{p}}$ for all three classifier is (Acc = 0.86, (Se, Sp) = (0.90, 0.84)) for LDA, (Acc = 0.93, (Se, Sp) = (1.00, 0.87)) for LOG and (Acc = 0.91, (Se, Sp) = (0.94, 0.88)) for SVM.

Using overlapped waves without any correction is expected to give worse performance compared to using pure waves, since the T wave variability was not removed. This is confirmed in Figure 5.2, with $\mathcal{F}_{\mathrm{o}}$ accuracy values much lower than pure ones. However, it is quite remarkable that the maximum accuracy for LOG and SVM is reasonable, given the condition of the wave set.

From Figure 5.3, which illustrates the sensitivity and specificity at the combinations of maximum accuracy, it can be seen that the classifiers have different learning strategies on the dataset. LDA and SVM seem to start with a high sensitivity, and adding features increase specificity. LOG has the opposite happening, starting with high specificity, and trading it off with sensitivity. For this classifier, it can be seen that sensitivity and specificity on the set $\mathcal{F}_{\mathrm{o}}$ has a remarkably large variation.

The results of feature scoring can be seen in Table 5.1 for set $\mathcal{F}_{\mathrm{p}}$ and Table 5.2 for set $\mathcal{F}_{\mathrm{o}}$, where the performance metric is taken as the maximum accuracy. Several relevant features can be identified, indicated arbitrarily by a score > 0.80. The high scores indicate a constant involvement of such features in the discrimination process, and may help explain the factors which allow for discrimination between right and left AFL. For the set of pure waves, it can be seen that Skewness(ψ_{PL}) is the most relevant across all three classifiers. Indeed, this feature was shown to be significantly different for right and left AFL (see Section 4.7). Additionally, some of the other features like Mean(ψ_{PG}) are also significantly different with respect to right and left AFL, and belong to the

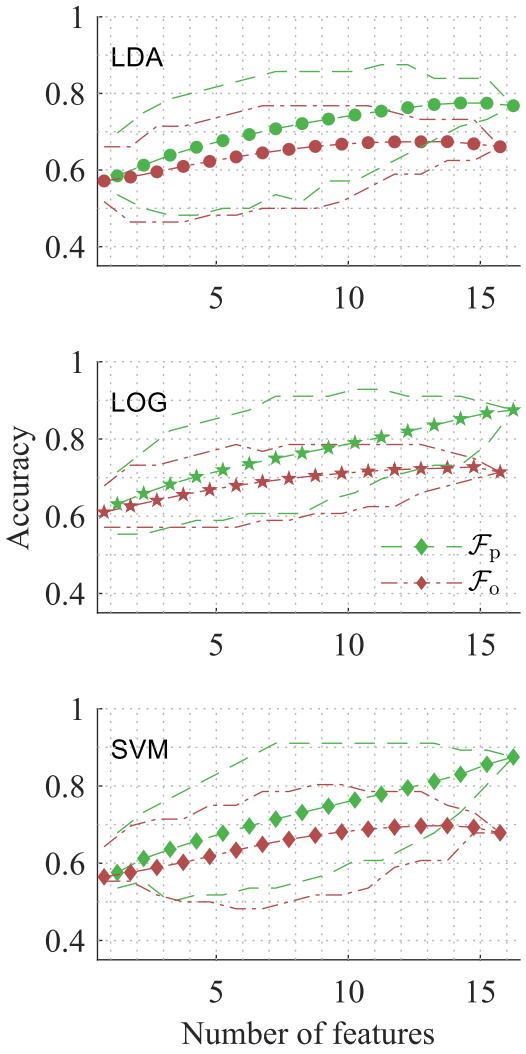

Figure 5.2: Accuracy of classifiers on the VCG loop variability dataset. Broken lines indicate the range of accuracy (max,min) of the respective set. Middle line with markers indicates the mean accuracy.

class of relevant features. It is also notable that the relevant features of $\mathcal{F}_p$ are related to the loop geometry parameters.

For overlapped waves, the set of relevant features are more diverse, and relate more to the loop orientation parameters. Var(ϕ_{EL}) is shown to be the most relevant for LDA and LOG, and three features share the same score for SVM. Care should be taken when interpreting the difference in relevant features between the two sets of waves, since $\mathcal{F}_o$ contains variability that is yet to be removed.

5.3.1.1 Comparison to Alternative Methods To establish a baseline comparison, the dataset was tested using two alternative methods. The first method is the one detailed by Kahn et al., which produces an index R_{XY} described in (3.2). The second

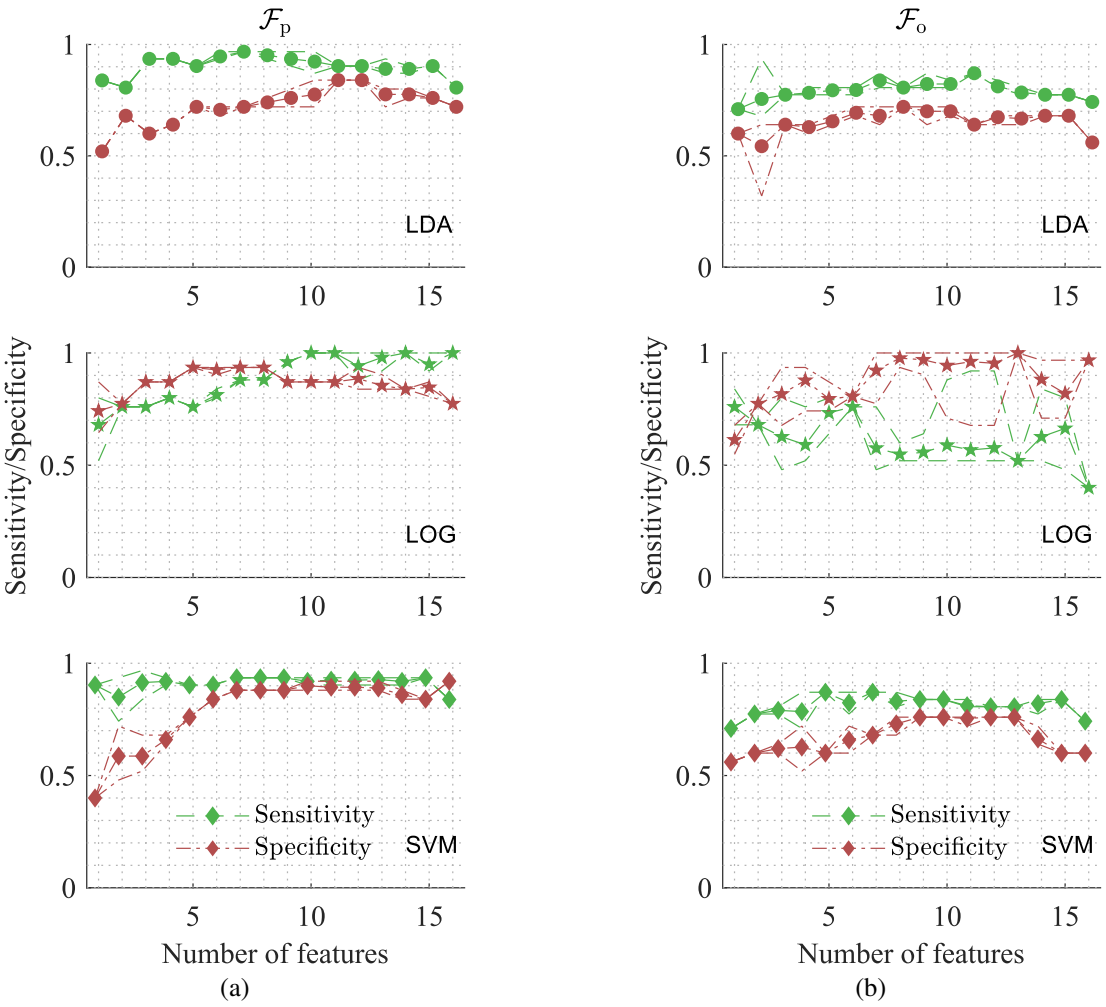

Figure 5.3: Sensitivity and specificity of the classifiers on the dataset at the combinations of maximum accuracy for sets (a) $\mathcal{F}_p$ and (b) $\mathcal{F}_o$ respectively. Broken lines indicate the range (max,min) of values. Middle line with markers indicates the mean performance value.

method consists of classing the mean F wave of set $\mathcal{F}_p$ using the polarity Pol(·) of leads II, III, aV_F and V_1, which emulates a standard clinical diagnostic performed by cardiologists. Polarity is determined by the sign of the largest peak (either positive or negative peak), after zero-centering the wave. A polarity of 0 is assigned if the peak to peak height is lower than 5 µV. Additionally, the values of min and max of each wave were also considered, to emulate a more graded input as opposed to the polarity (which is discrete).

Table 5.3 resumes the comparison between alternative methods. It it seen that VCG loop features perform better than all of them for 1 single feature. The same is observed for 2 features. For 4 features, the accuracy becomes comparable for all methods. Note that the VCG loop feature for the 4-combination is optimal for the LOG classifier. For

Table 5.1: Feature Score $\tilde{s}$ for VCG Loop Features (set $\mathcal{F}_{\text{p}}$)

Feature	LDA	LOG	SVM
Mean(ϕ_{AZ})	0.38	0.38	0.50
Var(ϕ_{AZ})	0.75	0.50	0.56
Skewness(ϕ_{AZ})	0.69	0.56	0.63
Kurtosis(ϕ_{AZ})	0.38	0.31	0.56
Mean(ϕ_{EL})	0.38	0.44	0.63
Var(ϕ_{EL})	0.75	0.69	0.75
Skewness(ϕ_{EL})	0.56	0.75	0.50
Kurtosis(ϕ_{EL})	0.69	0.50	0.69
Mean(ψ_{PL})	0.50	0.50	*0.81*
Var(ψ_{PL})	0.69	0.31	0.69
Skewness(ψ_{PL})	**0.94**	**1.00**	**0.94**
Kurtosis(ψ_{PL})	*0.88*	*0.88*	*0.88*
Mean(ψ_{PG})	0.75	*0.94*	**0.94**
Var(ψ_{PG})	0.56	0.50	0.19
Skewness(ψ_{PG})	*0.81*	0.63	0.50
Kurtosis(ψ_{PG})	0.50	0.56	0.56

Table 5.2: Feature Score $\tilde{s}$ for VCG Loop Features (set $\mathcal{F}_{\text{o}}$)

Feature	LDA	LOG	SVM
Mean(ϕ_{AZ})	0.69	0.69	0.63
Var(ϕ_{AZ})	0.69	0.69	0.69
Skewness(ϕ_{AZ})	0.56	0.69	**0.88**
Kurtosis(ϕ_{AZ})	*0.81*	*0.81*	**0.88**
Mean(ϕ_{EL})	0.69	0.75	0.50
Var(ϕ_{EL})	**0.94**	**0.94**	0.69
Skewness(ϕ_{EL})	0.44	0.63	0.63
Kurtosis(ϕ_{EL})	0.56	0.56	0.69
Mean(ψ_{PL})	0.69	0.69	0.69
Var(ψ_{PL})	0.25	0.38	0.50
Skewness(ψ_{PL})	0.38	0.44	0.44
Kurtosis(ψ_{PL})	0.50	0.38	0.50
Mean(ψ_{PG})	*0.81*	*0.81*	**0.88**
Var(ψ_{PG})	0.56	0.50	0.38
Skewness(ψ_{PG})	0.50	0.63	0.50
Kurtosis(ψ_{PG})	0.56	0.56	0.56

LDA and SVM, other combinations gave better performance (0.80 for both). Despite the similar performance, one conclusion to be made here is that the beat-to-beat analysis was able to capture similar discriminant information compared to raw ECG analysis. However, it is seen to perform better overall.

Table 5.3: Comparison of Accuracy using Alternative Methods

Feature	LDA	LOG	SVM
Pol(V_1)	0.55	0.55	0.55
Max(V_1)	0.55	0.55	0.55
Min(V_1)	0.50	0.50	0.55
R_{XY}	0.55	0.63	0.63
Skewness(ψ_{PL})	0.70	0.71	0.57
[Max(V_1) Min(V_1)]	0.52	0.54	0.55
[Skewness(ψ_{PL}) Mean(ψ_{PG})]	0.68	0.77	0.66
[Pol(V_1) Pol(II) Pol(III) Pol(aV_F)]	0.68	0.68	0.68
[Max(V_1) Min(II) Min(III) Min(aV_F)]	0.84	0.82	0.82
[Min(V_1) Max(II) Max(III) Max(aV_F)]	0.61	0.63	0.61
[Mean(ϕ_{EL}) Skewness(ψ_{PL}) Kurtosis(ψ_{PL}) Mean(ψ_{PG})]	0.73	0.84	0.79

5.3.1.2 Performance Gain of Beat-to-Beat Methodology One particular uniqueness of the approach is to consider higher-order statistics in the calculation of parameter variability. This was hypothesized to capture the fine difference between right and left AFL, and not just e.g. a mean of the parameter series. To investigate this matter, the classification accuracy was considered when only the parameter Mean(·) was used, compared to using other parameters excluding Mean(·). This is shown in Figure 5.4, where the maximum accuracy is plotted in both cases. As can be seen, using higher-order statistics allowed the capture of the discriminant variability. Using the mean only allowed a limited capture of this variability. For the set $\mathcal{F}_o$, using the means helped achieve better classification in SVM. Again, this may probably be due to the additional variability that was not corrected.

Nevertheless, this does not mean that the means should be discarded. It was shown that some of these measures are significantly different according to localization. However, what should be done is to consider them together with higher-order measures.

Another uniqueness of this methodology is to analyze the waves individually as compared to the average of all waves. It is expected that averaging the waves will diminish the discriminatory variability. To test this, the four loop parameters were calculated for an averaged and downsampled F wave (f_s = 100Hz) for each recording. The same exhaustive wrapper evaluation was performed. The maximum accuracy is shown in Figure 5.5. The grey dot represents the maximum accuracy of the beat-to-beat methodology for the considered sets. Again, this is shown to be superior to the performance obtained using only the mean of the waves. For the set $\mathcal{F}_o$, averaging the waves did not allow better classification.

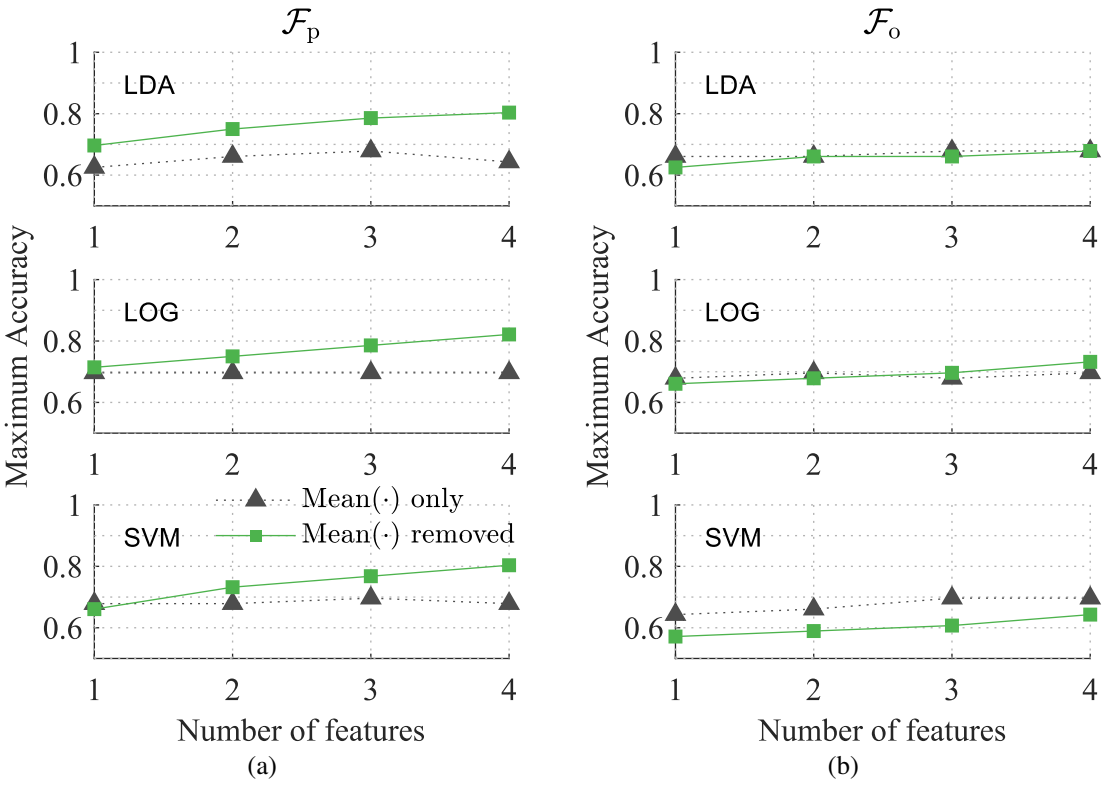

Figure 5.4: Comparison of using only Mean(·) and not using Mean(·) and the resulting maximum classifier accuracy for sets (a) $\mathcal{F}_p$ and (b) $\mathcal{F}_o$ respectively.

Figure 4.23 shows the distribution of the loop parameters for all waves in the respective sets, and divided by localization. It can be seen that the profile of variability is complex, but there are particular traits that are remarkable, such as the form of distribution for ψ_{PL} and ψ_{PG} for set $\mathcal{F}_p$. This could be an explanation as to why it was possible to localize AFL using the beat-to-beat approach. In addition, note that the mean of several parameters are very similar for both right and left AFL. This serves to show as well that only using the mean will not guarantee good separability.

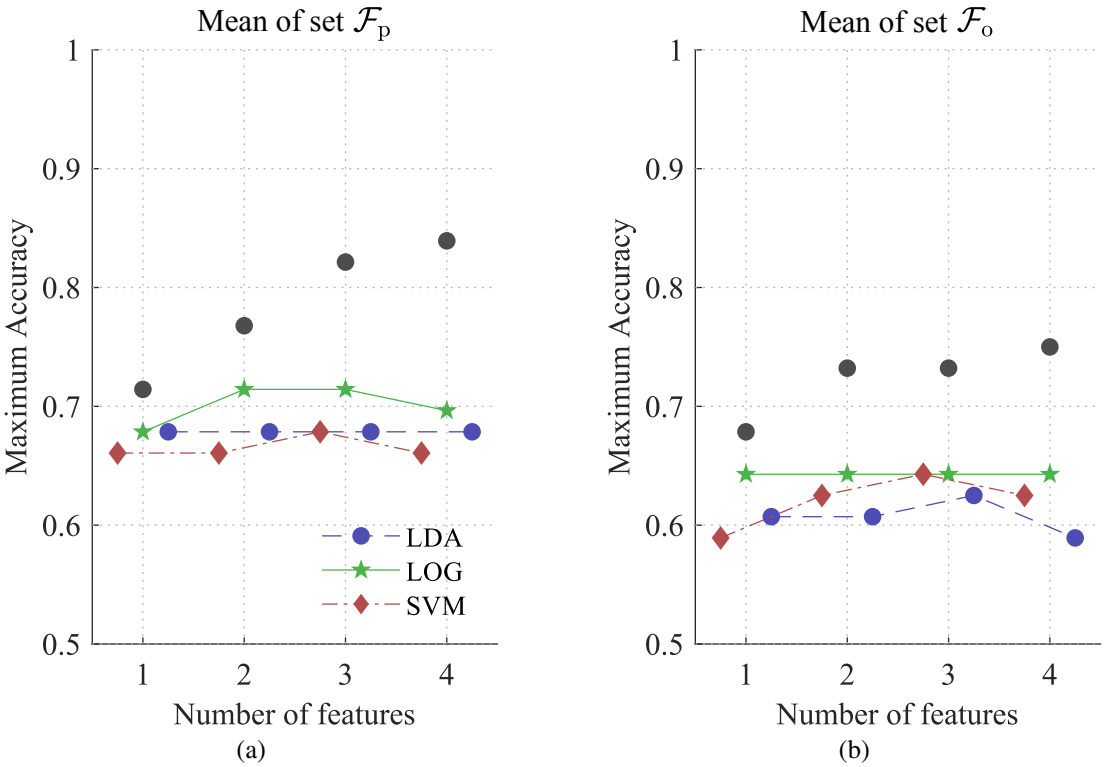

Figure 5.5: Comparison of using averaged waves and using beat-to-beat parameter series and the resulting maximum classifier accuracy for sets (a) $\mathcal{F}_p$ and (b) $\mathcal{F}_o$ respectively. Grey dots on top indicate the maximum accuracy of the respective set when using a beat-to-beat approach and the LOG classifier.

5.3.2 Effect of T Wave Correction It has been shown in Section 4.7 that the correction of T waves allowed the mean loops from set $\mathcal{F}_{\mathrm{o}}^{\mathrm{t}}$ to achieve good loop similarity to those of set $\mathcal{F}_{\mathrm{p}}$, as well as comparable variability profiles. Here, the dataset $\mathcal{F}_{\mathrm{o}}^{\mathrm{t}}$ is used to classify right or left localization.

The resulting classifier performance is shown in Figure 5.6. As evidenced, correcting the wave allowed increase of classifier performance in all classifiers. The max envelope can be seen to achieve higher values in LDA and LOG and the early portions of SVM. Overall, LDA and LOG had an increase of 3% in max accuracy (LDA Acc = 0.80, $(\mathrm{Se}, \mathrm{Sp}) = (0.90, 0.68)$; LOG Acc = 0.82, $(\mathrm{Se}, \mathrm{Sp}) = (0.90, 0.68)$). The mean accuracy is improved in general, getting better with more features. Observation of the sensitivity and specificity in Figure 5.7 shows that the correction reduces the variation of these two performance measure. It can now clearly be seen that the algorithms have very different strategies in classifying right and left AFL.

However, when respiratory motion is applied before T wave correction (referring to the set $\mathcal{F}_{\mathrm{o}}^{\mathrm{rt}}$), this causes a decrease in classifier performance (seen in panel (b)). It could be that respiratory motion was already corrected in a way by the T wave spline, hence additional processing actually deteriorates the discriminatory variability. Note that this only applies to the set of overlapped waves.

Is was shown in Figure 4.23 that the overlap-corrected F waves have distributions that approach those of the pure waves. It has been seen that pure waves gave the best performance so far, therefore by approaching the same variability as that of pure waves, this could lead to the increase in performance of classification.

Table 5.4 shows the feature score for the set $\mathcal{F}_{\mathrm{o}}^{\mathrm{t}}$. Comparing with the scores before correction, it can be seen that several features are still relevant, in addition to new previously irrelevant features. Again, most of these features relate to the orientation of the loop. It can be hypothesized that because the T wave component affects the loop orientation the most, these features might previously be masked.

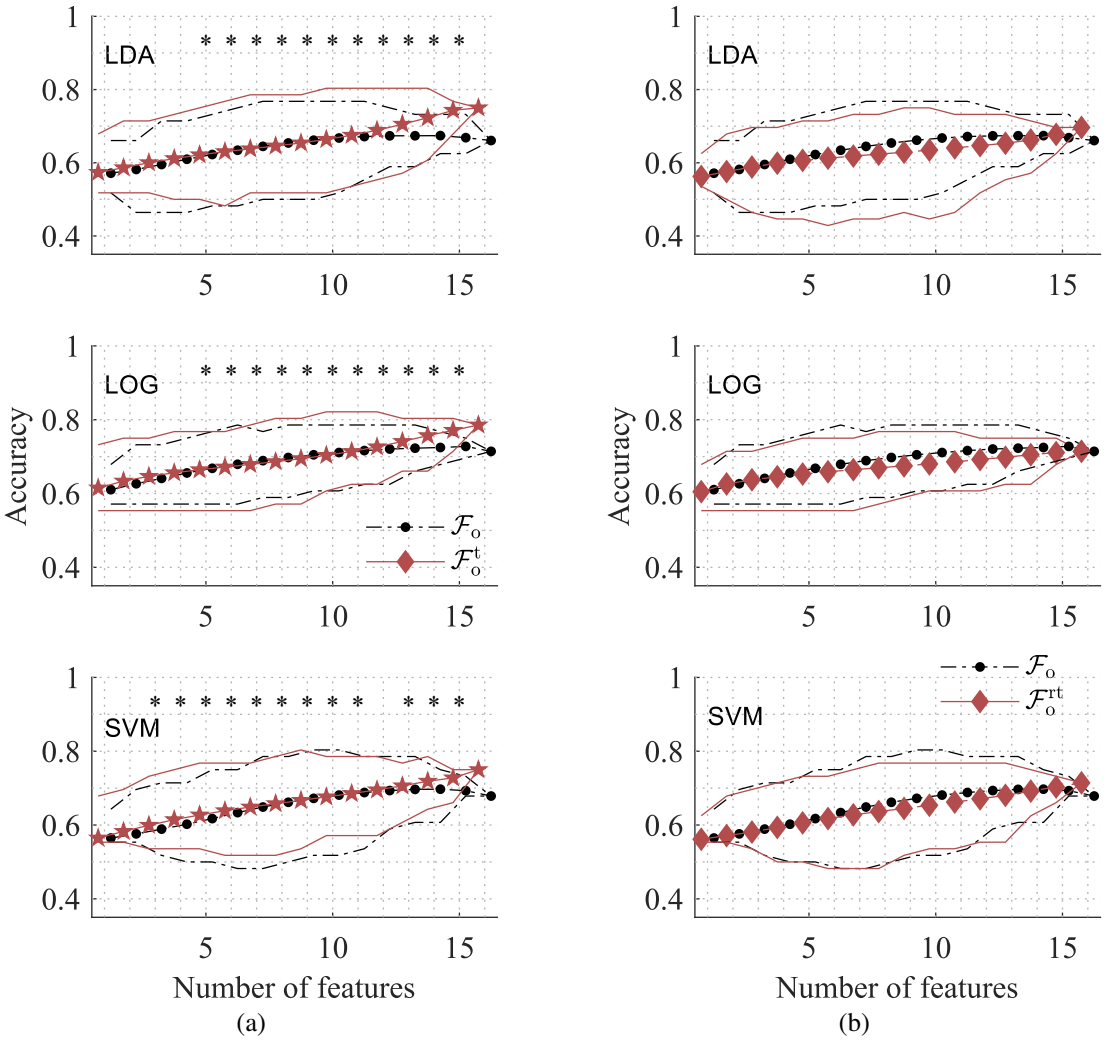

Figure 5.6: Classifier performance using overlapped-corrected waves for sets (a) $\mathcal{F}_o^t$ and (b) $\mathcal{F}_o^{rt}$ respectively. Red lines indicate the range of accuracy (max,min) of the respective set. Middle line with markers indicates the mean accuracy. Baseline performance is shown in black. The stars in panel (a) show significant change in accuracy for the given combination length ($p < 0.05$, Wilcoxon signed rank test).

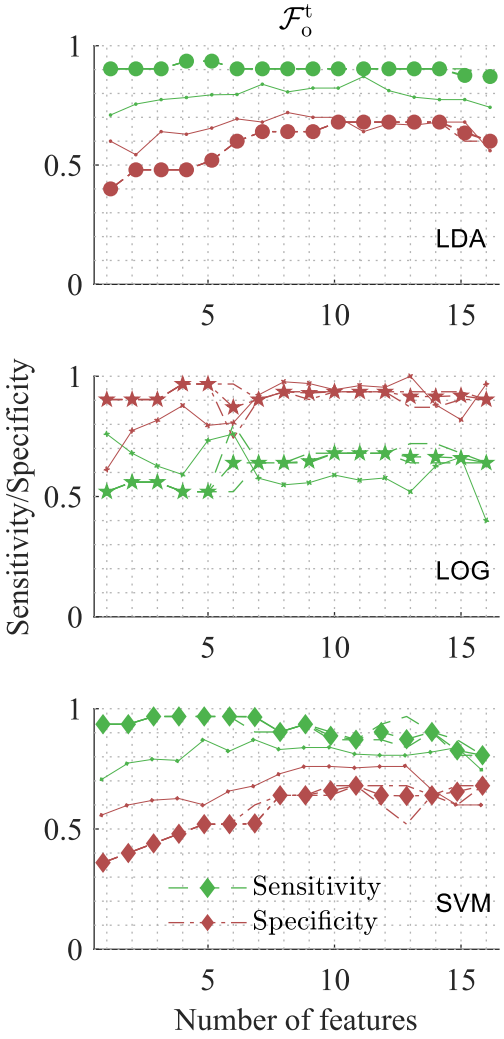

Figure 5.7: Sensitivity and specificity of the set $\mathcal{F}_o^t$ at the combinations of maximum accuracy. Broken lines indicate the range of performance (max,min). Middle line with markers indicates the mean accuracy. The thin lines represent the mean sensitivity and specificity of the uncorrected set $\mathcal{F}_o$.

Table 5.4: Feature Score $\tilde{s}$ for VCG Loop Features (set $\mathcal{F}_{\mathrm{o}}^{\mathrm{t}}$)

Feature	LDA	LOG	SVM
Mean(ϕ_{AZ})	0.69	**1.00**	0.63
Var(ϕ_{AZ})	0.69	0.75	0.69
Skewness(ϕ_{AZ})	0.56	*0.88*	**0.88**
Kurtosis(ϕ_{AZ})	*0.81*	0.50	**0.88**
Mean(ϕ_{EL})	0.69	0.56	0.50
Var(ϕ_{EL})	**0.94**	*0.88*	0.69
Skewness(ϕ_{EL})	0.44	*0.94*	0.63
Kurtosis(ϕ_{EL})	0.56	*0.88*	0.69
Mean(ψ_{PL})	0.69	0.50	0.69
Var(ψ_{PL})	0.25	*0.88*	0.50
Skewness(ψ_{PL})	0.38	0.63	0.44
Kurtosis(ψ_{PL})	0.50	0.69	0.50
Mean(ψ_{PG})	*0.81*	0.63	**0.88**
Var(ψ_{PG})	0.56	0.44	0.38
Skewness(ψ_{PG})	0.50	0.44	0.50
Kurtosis(ψ_{PG})	0.56	0.75	0.56

5.3.3 Effect of Transform Optimization It has been argued previously that the Inverse Dower Transform is non-optimized due to the simplistic assumption it made on the nature of the volume conductor. By modeling the heterogeneity and integrating it into the transformation, as well as pursuing model parameter estimation with accuracy maximization as the goal, it is possible to optimize the transform to achieve better performance.

The classifier accuracy of the SVM classifier, used to perform the estimation, is shown in Figure 5.8. Note that the optimization was done up to a combination length of 5 only. An improvement can be seen within this range, with the final optimum value of the iteration evaluating to 0.82. For longer combination lengths, the classifier seems to be relatively similar in performance prior to correction. However, the mean performance is consistently increasing. The result illustrates the validity of the approach.

When used with the LOG classifier however, an improvement can be remarked. The maximum classifier value goes up to 0.93 at length 10. This corresponds to a sensitivity/specificity pair of $(\mathrm{Se}, \mathrm{Sp}) = (0.88, 0.97)$. From the previous result, this is an improvement of 2% (Acc = 0.91, $(\mathrm{Se}, \mathrm{Sp}) = (0.92, 0.90)$). Similar trend happens with the LDA classifier, with 3% increase in maximum accuracy (Acc = 0.89, $(\mathrm{Se}, \mathrm{Sp}) = (0.97, 0.80)$). This supplements the validity of the approach.

When applied to the set $\mathcal{F}_{\mathrm{p}}$, the performance is not much greater for the LOG and SVM classifiers compared to before. The maximum classifier performance drops, but the mean performance is generally stable. However, the LDA classifier achieved a maximum accuracy of 0.91 ($(\mathrm{Se}, \mathrm{Sp}) = (0.97, 0.84)$, 5% improvement). This behavior could be due to the fact that the model parameters estimated by the procedure relied on SVM's efficiency at finding a good separation. The way that SVM derives its boundary–which has a similar trait to LOG's boundary–on the transformed dataset might not be optimal for the two classifier, as compared to LDA. Analysis of the sensitivity and specificity, shown in Figure 5.9 illustrates that in LDA classifier, there is increased specificity using both sets, whilst sensitivity remains comparable. For LOG, the effect of the transform optimizes specificity, but degrades sensitivity in both sets.

Table 5.5 and Table 5.6 shows the relevant features for sets $\mathcal{F}_{\mathrm{p}}^{\mathrm{rd}}$ and $\mathcal{F}_{\mathrm{p}}^{\mathrm{d}}$ respectively. Note that the postfix $^{\mathrm{d}}$ indicates application of optimized IDT (e.g. $\mathcal{F}_{\mathrm{p}}^{\mathrm{rd}}$ is the set $\mathcal{F}_{\mathrm{p}}^{\mathrm{r}}$ with VCG representation calculated using optimized IDT). Interestingly for $\mathcal{F}_{\mathrm{p}}^{\mathrm{d}}$, the transform allowed other features to become relevant as well, whilst still retaining previously relevant features. Also of note, is the possibility to access features related to orientation parameters (e.g. $\mathrm{Var}(\phi_{EL})$). Set $\mathcal{F}_{\mathrm{p}}^{\mathrm{rd}}$ did not retain most of the previously relevant features of set $\mathcal{F}_{\mathrm{p}}$. It is possible that the effect of respiratory motion correction

caused this.

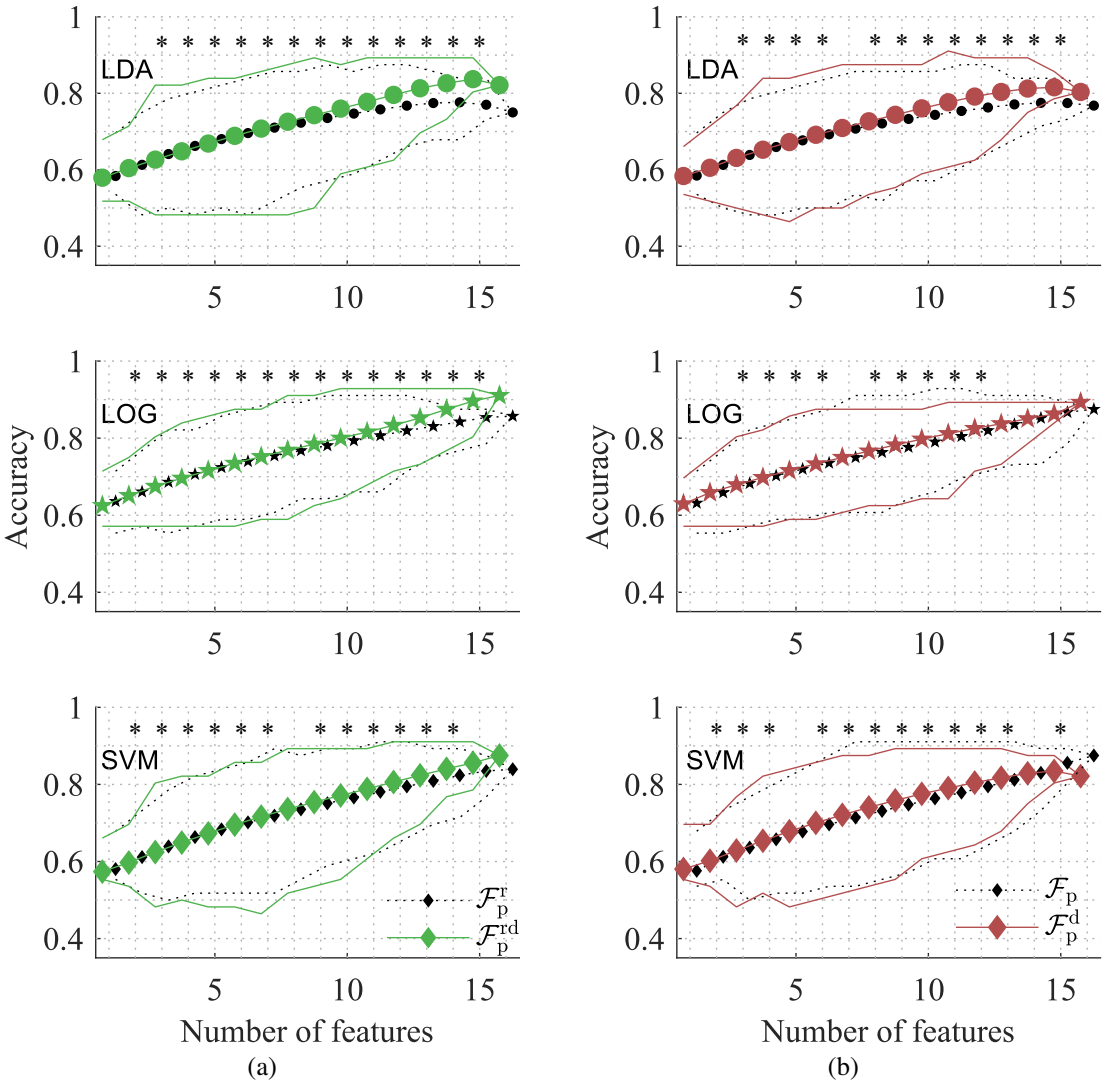

Figure 5.8: Comparison of classifier performance after application of optimized Inverse Dower Transform to the sets (a) $\mathcal{F}_{\mathrm{p}}^{\mathrm{rd}}$ and (b) $\mathcal{F}_{\mathrm{p}}^{\mathrm{d}}$ respectively. Full lines indicate the range of accuracy (max,min) of the respective set. Middle line with markers indicates the mean accuracy. Baseline performance is shown in black. The stars on top of each figure show significant change in accuracy for the given combination length ($p < 0.05$, Wilcoxon signed rank test).

Application of the optimized transform on the set of overlapped-corrected waves gave an even larger boost in performance, as can be seen in Figure 5.10. The highest increase was seen in the LDA and LOG classifier (13% increase in maximum accuracy) for the set $\mathcal{F}_{\mathrm{o}}^{\mathrm{t}}$. Across all classifiers for set $\mathcal{F}_{\mathrm{o}}^{\mathrm{rt}}$, the increase was 9%. This shows that the corrective effects of the optimized IDT was able to uncover more variability for the set of overlapped waves. The highest performance was obtained by LOG (Acc = 0.91, (Se, Sp) = (0.88, 0.94) for the set $\mathcal{F}_{\mathrm{o}}^{\mathrm{td}}$; Acc = 0.89, (Se, Sp) = (0.84, 0.94) for the

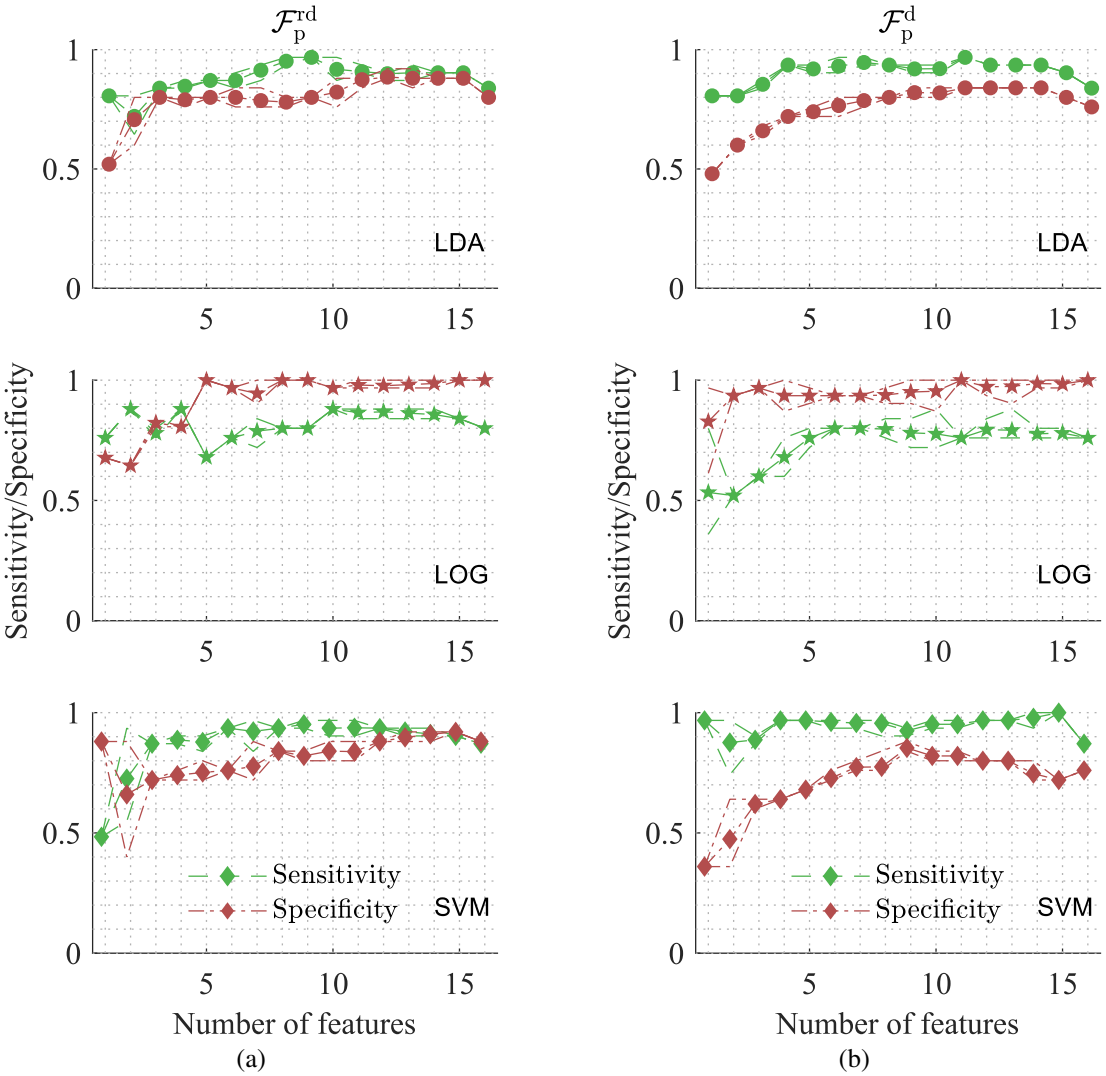

Figure 5.9: Sensitivity and specificity at the combinations of maximum accuracy of the sets (a) $\mathcal{F}_p^{rd}$ and (b) $\mathcal{F}_p^{d}$ respectively. Broken lines indicate the range of performance (max,min). Middle line with markers indicates the mean performance.

set $\mathcal{F}_o^{rtd}$). Inspection of the sensitivity and specificity (Figure 5.11) showed that the performance approaches that of the set of pure waves. Feature scores in Table 5.7 and Table 5.8 shows that the correction allows access to more features that are associated with the pure sets.

Alternatives to the IDT are available. Because these transforms target the atrial activity specifically, it is suggestive that their use may produce results that are better than our method. To investigate this matter, classifier performance results using the PLSV transform of Guillem et al. were also obtained [78]. The processing scheme is similar to Chapter 5, except that the IDT is replaced by the PLSV transform, and no optimization was carried out.

Table 5.5: Feature Score $\tilde{s}$ for VCG Loop Features (set $\mathcal{F}_{\mathrm{p}}^{\mathrm{rd}}$)

Feature	LDA	LOG	SVM
Mean(ϕ_{AZ})	0.63	0.44	0.75
Var(ϕ_{AZ})	0.63	0.56	0.75
Skewness(ϕ_{AZ})	0.69	0.75	0.63
Kurtosis(ϕ_{AZ})	0.69	0.63	0.63
Mean(ϕ_{EL})	0.56	0.50	0.63
Var(ϕ_{EL})	*0.94*	**0.94**	**1.00**
Skewness(ϕ_{EL})	0.31	0.44	0.44
Kurtosis(ϕ_{EL})	0.69	0.69	0.69
Mean(ψ_{PL})	0.69	0.56	0.56
Var(ψ_{PL})	0.69	0.75	0.75
Skewness(ψ_{PL})	0.69	0.75	0.75
Kurtosis(ψ_{PL})	*0.81*	0.63	*0.81*
Mean(ψ_{PG})	0.56	0.50	0.56
Var(ψ_{PG})	0.69	0.56	0.56
Skewness(ψ_{PG})	**1.00**	0.63	*0.88*
Kurtosis(ψ_{PG})	*0.81*	*0.88*	*0.81*

Table 5.6: Feature Score $\tilde{s}$ for VCG Loop Features (set $\mathcal{F}_{\mathrm{p}}^{\mathrm{d}}$)

Feature	LDA	LOG	SVM
Mean(ϕ_{AZ})	0.69	0.75	0.63
Var(ϕ_{AZ})	0.75	0.63	0.50
Skewness(ϕ_{AZ})	0.75	0.75	0.38
Kurtosis(ϕ_{AZ})	0.38	0.69	0.50
Mean(ϕ_{EL})	0.56	0.50	0.50
Var(ϕ_{EL})	*0.88*	*0.88*	*0.88*
Skewness(ϕ_{EL})	0.63	0.56	0.56
Kurtosis(ϕ_{EL})	0.44	0.50	0.63
Mean(ψ_{PL})	0.69	0.75	0.63
Var(ψ_{PL})	*0.88*	**0.94**	**1.00**
Skewness(ψ_{PL})	**0.94**	**0.94**	*0.94*
Kurtosis(ψ_{PL})	0.50	0.56	0.56
Mean(ψ_{PG})	*0.88*	*0.88*	0.81
Var(ψ_{PG})	0.75	0.75	0.69
Skewness(ψ_{PG})	0.63	0.69	0.56
Kurtosis(ψ_{PG})	0.75	0.75	0.63

Classifier performance is shown in Figure 5.12(a) and Figure 5.12(b) for the set $\mathcal{F}_{\mathrm{p}}^{\mathrm{r}}$ and $\mathcal{F}_{\mathrm{o}}^{\mathrm{t}}$ respectively. As can be seen, performance of the PLSV transform is low and does not match the optimized IDT. Compared to the optimization applied here, there is a difference of 7−9% in maximum accuracy. This shows that the IDT is still useful in the context of localization using beat-to-beat approach, and that its optimization results in

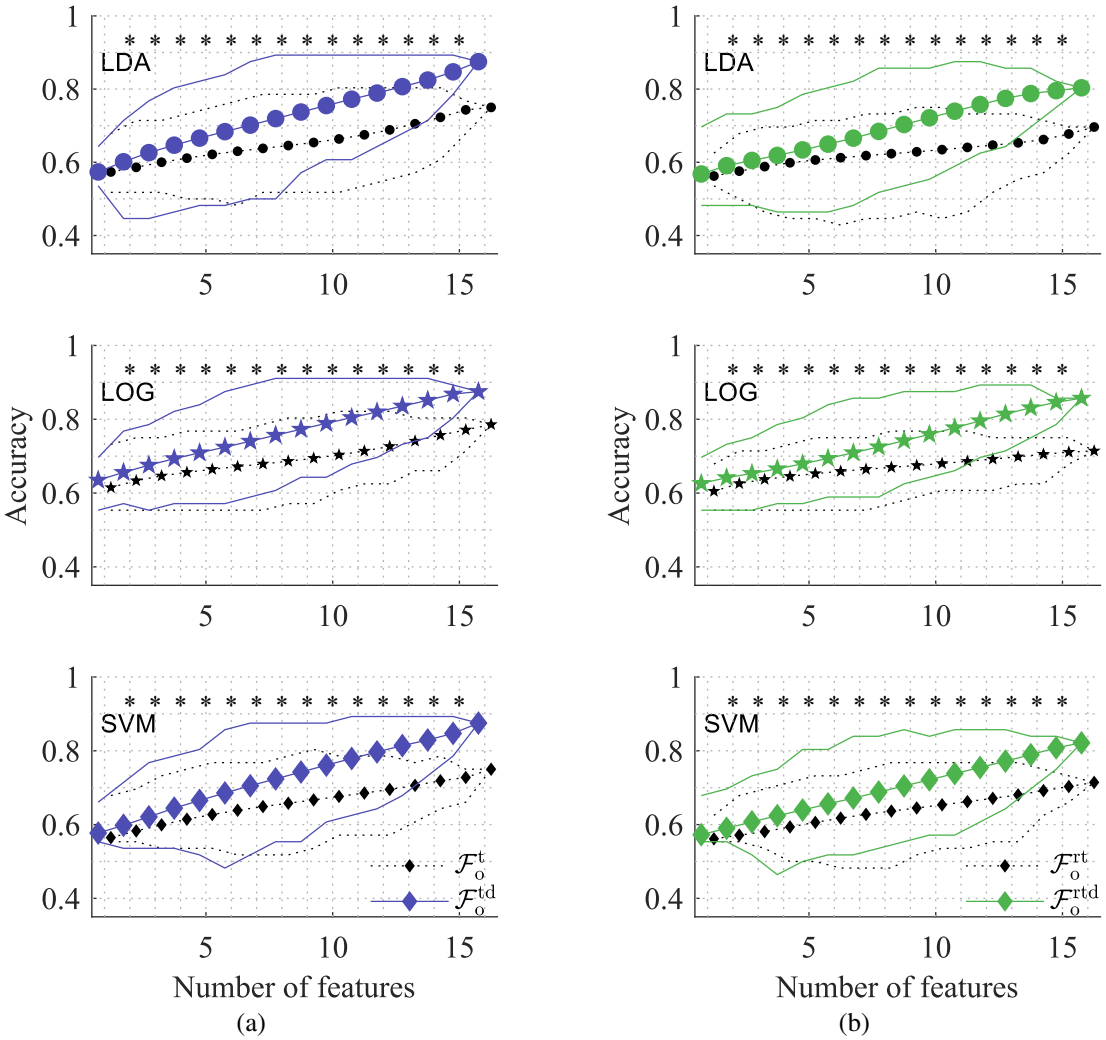

Figure 5.10: Comparison of classifier performance after application of optimized Inverse Dower Transform to the sets (a) $\mathcal{F}_{\mathrm{o}}^{\mathrm{td}}$ and (b) $\mathcal{F}_{\mathrm{o}}^{\mathrm{rtd}}$ respectively. Full lines indicate the range of accuracy (max,min) of the respective set. Middle line with markers indicates the mean accuracy. Baseline performance is shown in black. The stars on top of each figure show significant change in accuracy for the given combination length ($p < 0.05$, Wilcoxon signed rank test).

increased performance as opposed to using alternative transforms. Granted, this also shows that the transform applied does not guarantee similarity to the orthogonal dipolar activation of the heart, which is what PLSV aims to do.

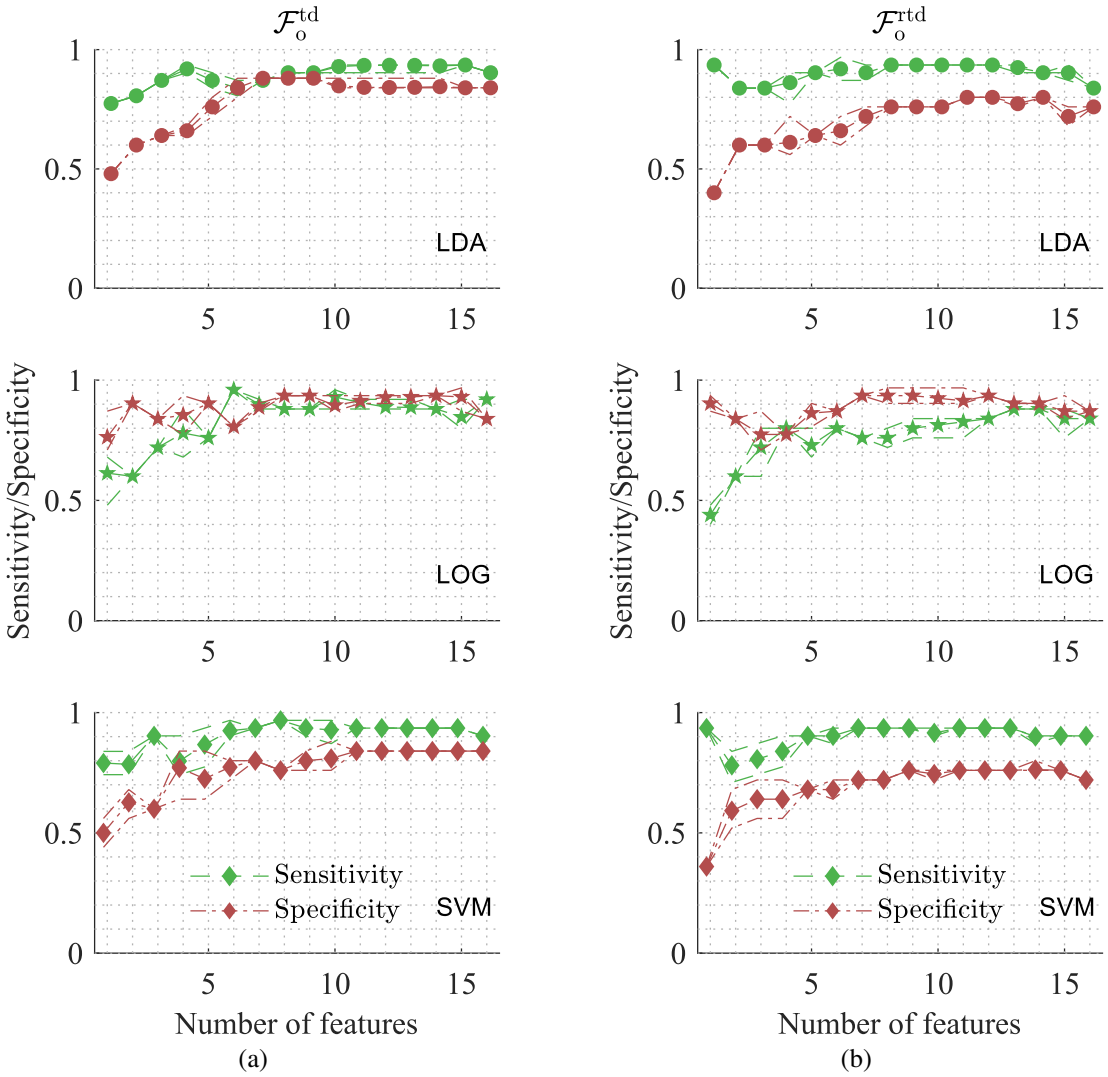

Figure 5.11: Sensitivity and specificity at the combinations of maximum accuracy of the sets (a) $\mathcal{F}_o^{td}$ and (b) $\mathcal{F}_o^{rtd}$ respectively. Broken lines indicate the range of performance (max,min). Middle line with markers indicates the mean performance.

Table 5.7: Feature Score $\tilde{s}$ for VCG Loop Features (set $\mathcal{F}_{\text{o}}^{\text{td}}$)

Feature	LDA	LOG	SVM
Mean(ϕ_{AZ})	0.63	0.56	0.75
Var(ϕ_{AZ})	0.50	0.44	0.63
Skewness(ϕ_{AZ})	0.50	0.38	0.63
Kurtosis(ϕ_{AZ})	0.63	0.63	**1.00**
Mean(ϕ_{EL})	0.69	0.63	*0.88*
Var(ϕ_{EL})	*0.81*	**0.81**	*0.88*
Skewness(ϕ_{EL})	*0.81*	**0.81**	0.75
Kurtosis(ϕ_{EL})	*0.81*	**0.81**	0.69
Mean(ψ_{PL})	0.50	0.44	0.63
Var(ψ_{PL})	0.63	0.63	0.44
Skewness(ψ_{PL})	*0.81*	**0.81**	0.75
Kurtosis(ψ_{PL})	0.69	0.50	0.69
Mean(ψ_{PG})	0.63	0.69	*0.88*
Var(ψ_{PG})	0.56	0.63	0.63
Skewness(ψ_{PG})	**0.88**	0.69	0.69
Kurtosis(ψ_{PG})	0.56	0.50	0.69

Table 5.8: Feature Score $\tilde{s}$ for VCG Loop Features (set $\mathcal{F}_{\text{o}}^{\text{rtd}}$)

Feature	LDA	LOG	SVM
Mean(ϕ_{AZ})	0.50	0.56	0.69
Var(ϕ_{AZ})	0.63	0.50	0.38
Skewness(ϕ_{AZ})	0.50	0.56	0.38
Kurtosis(ϕ_{AZ})	**1.00**	**1.00**	**1.00**
Mean(ϕ_{EL})	*0.81*	*0.81*	*0.94*
Var(ϕ_{EL})	0.50	*0.81*	0.63
Skewness(ϕ_{EL})	*0.81*	*0.81*	*0.88*
Kurtosis(ϕ_{EL})	0.56	0.44	0.69
Mean(ψ_{PL})	0.44	0.25	0.56
Var(ψ_{PL})	0.38	0.50	0.38
Skewness(ψ_{PL})	0.63	0.69	0.44
Kurtosis(ψ_{PL})	0.38	0.69	0.50
Mean(ψ_{PG})	0.56	0.44	0.56
Var(ψ_{PG})	*0.88*	0.69	0.75
Skewness(ψ_{PG})	*0.81*	0.69	*0.88*
Kurtosis(ψ_{PG})	0.56	*0.88*	*0.81*

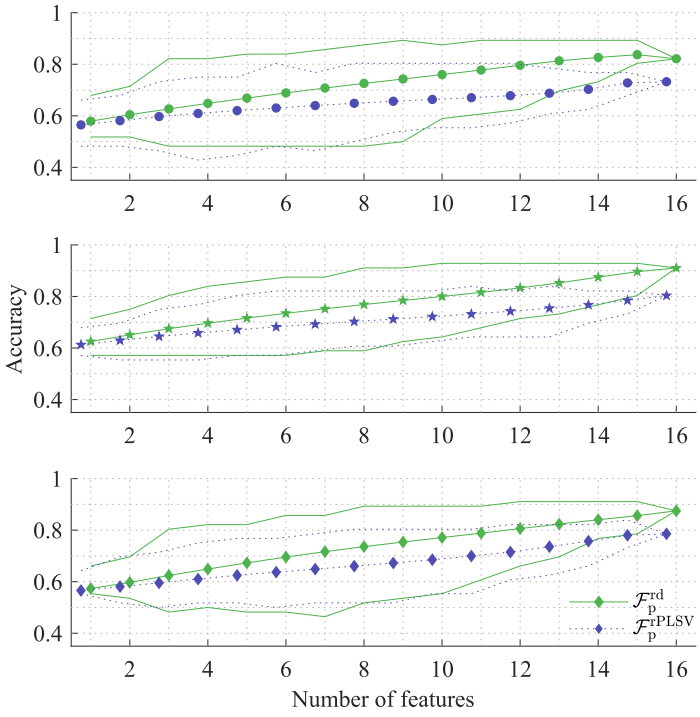

(a)

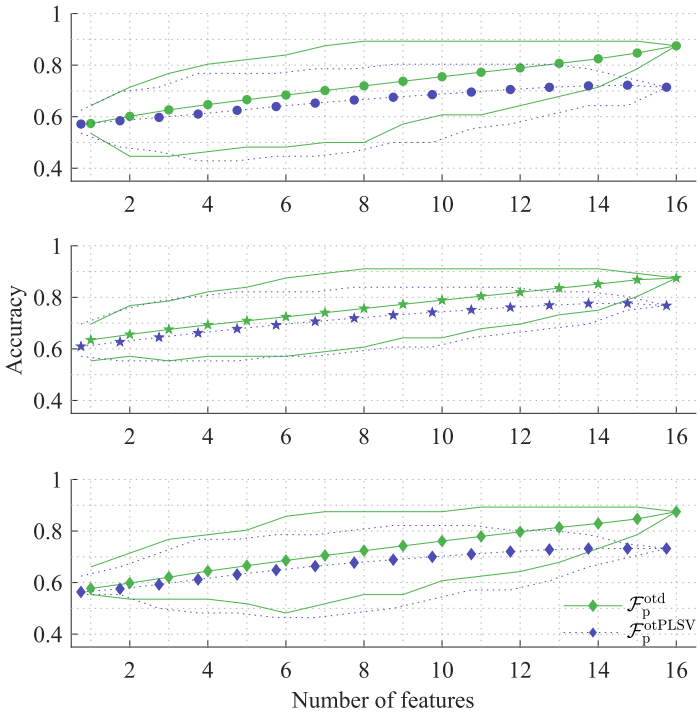

(b)

Figure 5.12: Comparison of classifier performance using optimized IDT and PLSV transform for sets (a) $\mathcal{F}_p^r$ and (b) $\mathcal{F}_o^t$. Full lines indicate the range of accuracy (max,min) of the respective set. Middle line with markers indicates the mean accuracy.

5.3.4 Combination of Wave Sets $\{\mathcal{F}_{\mathbf{p}} + \mathcal{F}_{\mathbf{o}}^{\mathbf{t}}\}$ So far, wave sets have been considered separately. It has been shown that they achieve good classification performance all by themselves. The next step naturally would be to combine wave sets together. This is sensible, because it has been shown that through proper processing of overlapped waves, they become similar to pure waves. Furthermore, it could be hypothesized that increasing the number of waves would result in better estimates of loop variability. Another reason for this would be to render the methodology useful in cases where AFL presents the challenging 2:1 block ratio or irregular heartbeat. In these cases, one is left with many overlapped waves compared to pure ones.

Several combinations are considered, out of the total possible combinations of sets. The selection of sets are based on first of all, the rationale in processing. For example, it does not make sense to combine uncorrected overlapped waves with optimized pure waves. Also, waves should generally be corrected for external variability. Second, the combination includes sets that exhibited good performance in the previous section. The combined sets are:

$\mathcal{A})$ $\mathcal{F}_{\mathrm{p}} + \mathcal{F}_{\mathrm{o}}^{\mathrm{t}}$

$\mathcal{B})$ $\mathcal{F}_{\mathrm{p}}^{\mathrm{r}} + \mathcal{F}_{\mathrm{o}}^{\mathrm{t}}$

$\mathcal{C})$ $\mathcal{F}_{\mathrm{p}}^{\mathrm{r}} + \mathcal{F}_{\mathrm{o}}^{\mathrm{rt}}$

$\mathcal{D})$ $\mathcal{F}_{\mathrm{p}}^{\mathrm{rd}} + \mathcal{F}_{\mathrm{o}}^{\mathrm{rtd}}$

Other combinations were not considered.

For each elementary set in the combination, the indicated processing is applied first. Then, the waves are grouped together before calculating the loop parameters and features. Figure 5.13 shows the overall performance of the classifier on the four sets above. In general, the performance does not increase significantly. All four mean accuracies were below that of the set $\mathcal{F}_{\mathrm{p}}$, currently the set with the best accuracy.

It can be seen that the combination $\mathcal{A}$ has the best performance of the whole group, in mean and max accuracy in general (maximum Acc = 0.84, $(\mathrm{Se}, \mathrm{Sp}) = (0.76, 0.94)$). As more correction steps are added, the performance of the combination deteriorates. Applying the optimized IDT can be seen to increase the performance slightly in SVM, but the general observation would be that the respiratory motion correction tends to deteriorate the performance. It would be suggestive to conclude that respiratory motion was the cause of separability, and removing it deteriorates the classifier performance, however it must be mentioned that the risk in combining wave sets is that they may have

different variability profiles which may itself deteriorate classification performance. Thus, this observation does not go against the conclusions of Chapter 6.

Table 5.9 provides the feature score for set $\{\mathcal{F}_{\mathrm{p}} + \mathcal{F}_{\mathrm{o}}^{\mathrm{t}}\}$. It can be seen that previously relevant features present in set $\mathcal{F}_{\mathrm{p}}$ have lower scores. However, those of set $\mathcal{F}_{\mathrm{o}}^{\mathrm{t}}$ are more present here. Mean(ψ_{PG}) seems to be the common relevant feature in both sets, and is retained here. The effect of this on classifier performance can be seen in Figure 5.14, where the maximum and mean performance lies between those of the individual sets that constitute the combination. Since most of the relevant features belong to the set $\mathcal{F}_{\mathrm{o}}^{\mathrm{t}}$ (which has a lower overall performance than $\mathcal{F}_{\mathrm{p}}$), it is suggestive that this is what caused the drop in performance. This shows that there is indeed risk in combining wave sets, where the risk is losing relevance of several features. But at the same time, common relevant features may be preserved.

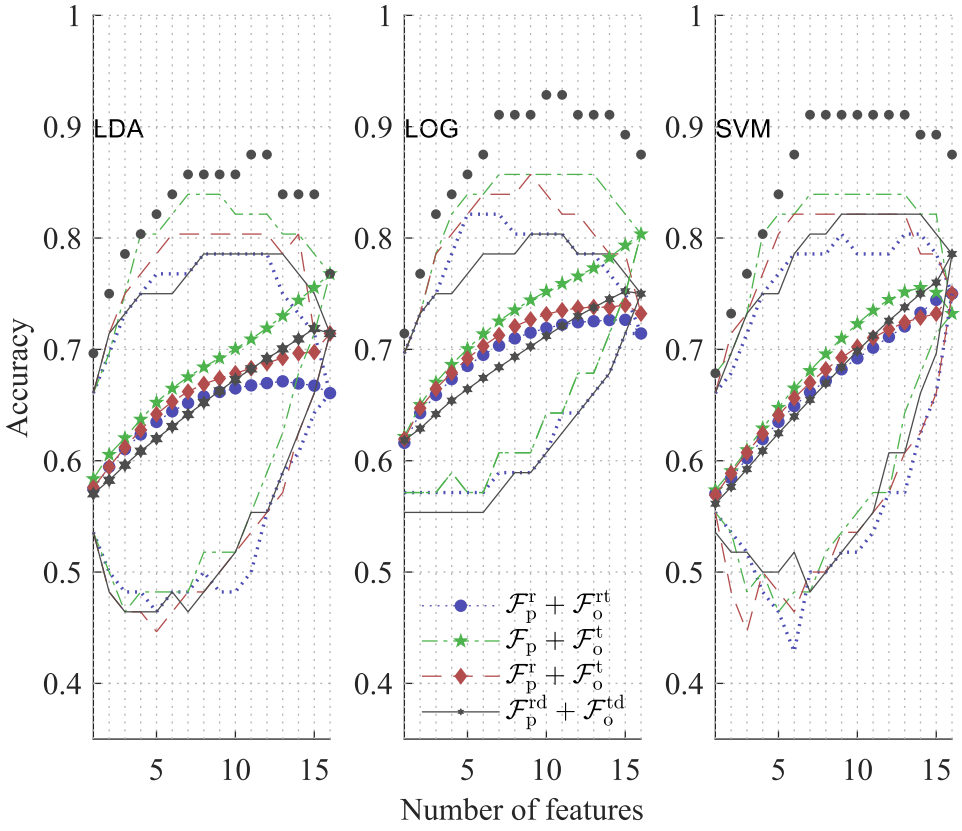

Figure 5.13: Comparison of classifier performance of combinations of sets. Lines without markers indicate the range of accuracy (max,min). Lines with markers indicate the mean accuracy. The grey diamonds at the top represent the max accuracy of the set $\mathcal{F}_{\mathrm{p}}$.

Table 5.9: Feature Scores for VCG Loop Features (set $\{\mathcal{F}_p + \mathcal{F}_o^t\}$)

Feature	LDA	LOG	SVM
Mean(ϕ_{AZ})	0.50	0.75	0.63
Var(ϕ_{AZ})	0.56	0.75	0.69
Skewness(ϕ_{AZ})	0.56	0.69	0.63
Kurtosis(ϕ_{AZ})	0.63	0.56	0.69
Mean(ϕ_{EL})	0.38	0.56	0.69
Var(ϕ_{EL})	**0.94**	0.50	**0.94**
Skewness(ϕ_{EL})	0.63	0.63	0.50
Kurtosis(ϕ_{EL})	**0.94**	**0.94**	*0.88*
Mean(ψ_{PL})	0.63	0.44	0.75
Var(ψ_{PL})	0.50	0.69	0.69
Skewness(ψ_{PL})	0.50	0.56	0.63
Kurtosis(ψ_{PL})	*0.81*	0.69	*0.81*
Mean(ψ_{PG})	0.75	*0.81*	*0.88*
Var(ψ_{PG})	0.63	0.69	0.63
Skewness(ψ_{PG})	0.63	0.44	0.44
Kurtosis(ψ_{PG})	*0.88*	*0.88*	*0.88*

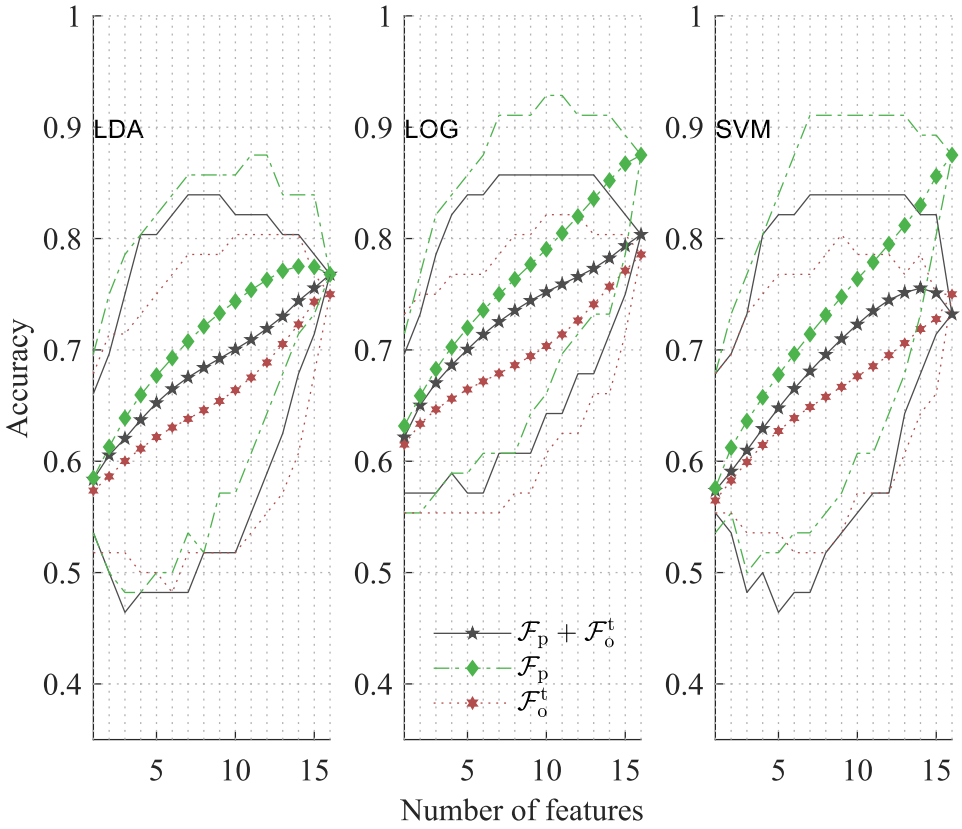

Figure 5.14: Classifier performance of the best combination of set $\{\mathcal{F}_p + \mathcal{F}_o^t\}$, compared to the individual sets $\{\mathcal{F}_p\}$ and $\{\mathcal{F}_o^t\}$. Lines without markers indicate the range of accuracy (max,min). Lines with markers indicate the mean accuracy.

5.3.5 Cross-validation of Selected Sets The previous sections covered the classification problem without any validation of the given results. It is important that the classifiers be validated in order to obtain their generalized performance. In doing so, the best feature set and parameters may be obtained, that allows finally obtention of a practical classifier.

It has been discussed in Section 5.2 that CV is a computationally expensive procedure. Therefore, a validation plan has to be considered. It is known that the generalized performance tends to be lower than the training performance. Therefore, it is reasonable to tune model parameters to known, best performing values. In this research, the model parameter considered is the set of features. The goal of this section would then be to determine the best feature set $\mathcal{E}^*$ as well as its fitting parameters and decision threshold γ_{opt}.

Modified LOOCV was performed as described in Section 5.2. The considered feature combinations were taken as those which gave the best performance at each combination length for the considered set and classifier. This is reasonable as taking combinations with non-optimum performance would lead to even worse generalization performance. At each fold, the classifier is trained using $\mathcal{Y}_{\text{train}}$. The threshold is defined as the percentiles of the fitted outputs $b_0 + b^\intercal x_{\text{train}}$, and varies from 0th to 100th percentile. Before calculating this, all outputs are subtracted by the minimum and normalized by the difference between the maximum and minimum fit value. This ensures that the outputs are bound between 0 and 1, to avoid ambiguous interpretation of the percentile.

It is acknowledged that different classifiers produce different performance as well as fitting criteria. Therefore, to make the selection process more objective, the classifier and set with the largest Acc_{CV} will be selected as the optimal classifier. Should there be any classifier ties in max accuracy value in the same or across several sets, the one with the lower count of features is selected.

Figure 5.16, Figure 5.17, Figure 5.18 and Figure 5.19 summarizes the result of LOOCV. The expected behavior of cross-validation can be observed, and exhibiting a rise and fall behavior with respect to the number of features. Depending on the dataset and classifier, the optimum point is seen to fluctuate in position. For most sets, and especially those of the pure waves, the generalization performance is relatively high, an approaches the value 0.8 at the optimum point. This suggests that the considered features are generalizable.

For the overlapped wave sets, this is not true. The maximum points do not approach close to 0.8. This suggests that even though their performance in training is remarkably high, it may be artificial.

Selection of the best generalized performance was performed, and it was found that the set $\mathcal{F}_{\text{p}}$ has the highest performance using SVM with a max generalized accuracy of 0.88 ($(\text{Se}_{\text{CV}}, \text{Sp}_{\text{CV}}) = (0.90, 0.84)$, AUC = 0.85) for a combination length of 6 features, which are

$$[\text{Var}(\phi_{EL}) \ \text{Kurtosis}(\phi_{EL})$$
$$\text{Mean}(\psi_{PL}) \ \text{Skewness}(\psi_{PL}) \ \text{Kurtosis}(\psi_{PL}) \ \text{Mean}(\psi_{PG})]$$

The pseudo-ROC curve is shown in Figure 5.15.

Note that two features in the combination present significant difference between classes (see Table 4.3). This shows that the feature selection process returns features that have a significance in terms of separability, and not just random features. In addition, some of the features that do not present significant separation are shown to be relevant in other sets. It could mean that the significant features help leverage the separability that is not possible considering only itself.

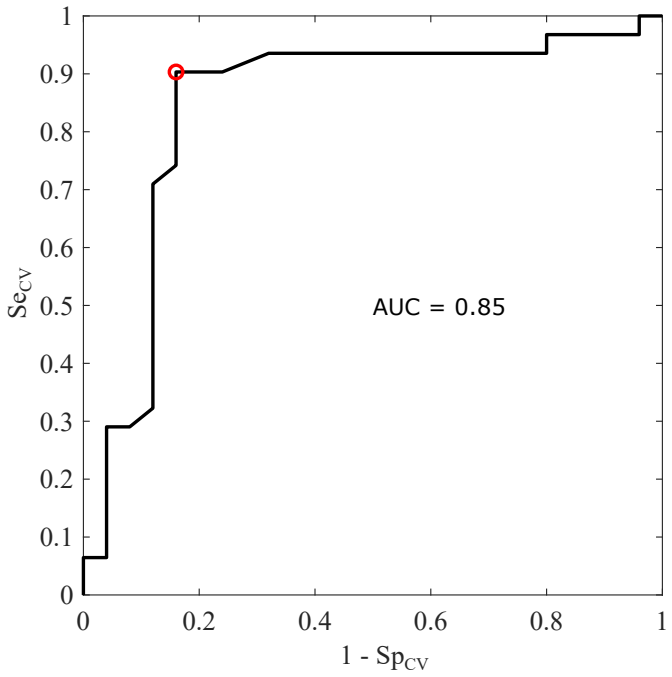

Figure 5.15: Pseudo-ROC curve of the best feature subset. The red circle indicates the optimal point.

From the CV procedure, there are at least $M = 56$ fit parameters available. Unfortunately, there is no simple way to determine which model is the most suitable, since the randomness in parameter values are related to the samples available for the learning process. With such a low sample count, it is not possible to infer a good model, despite there being techniques to estimate these parameter fits from sample reuse [90]. It is hoped that by supplying more data, the generalized fit parameter can be obtained.

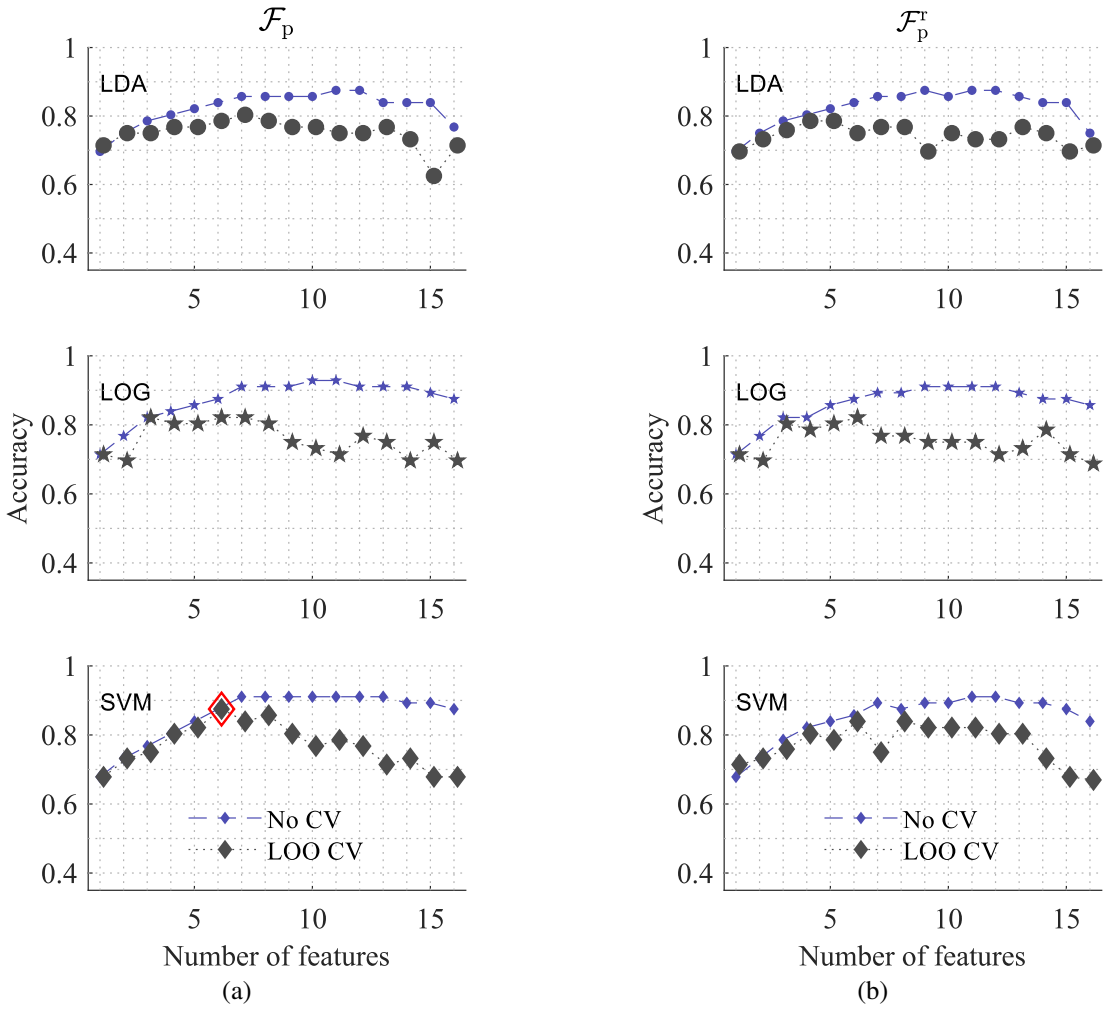

Figure 5.16: Modified LOOCV performance of classifier on sets (a) $\mathcal{F}_{\mathrm{p}}$ and (b) $\mathcal{F}_{\mathrm{p}}^{\mathrm{r}}$ respectively. Large grey markers indicate the maximum $\mathrm{Acc}_{\mathrm{CV}}$. As a baseline, the maximum accuracy of each set and classifier is shown in small blue markers. The red diamond marks the location of highest generalized accuracy across all considered sets and classifiers.

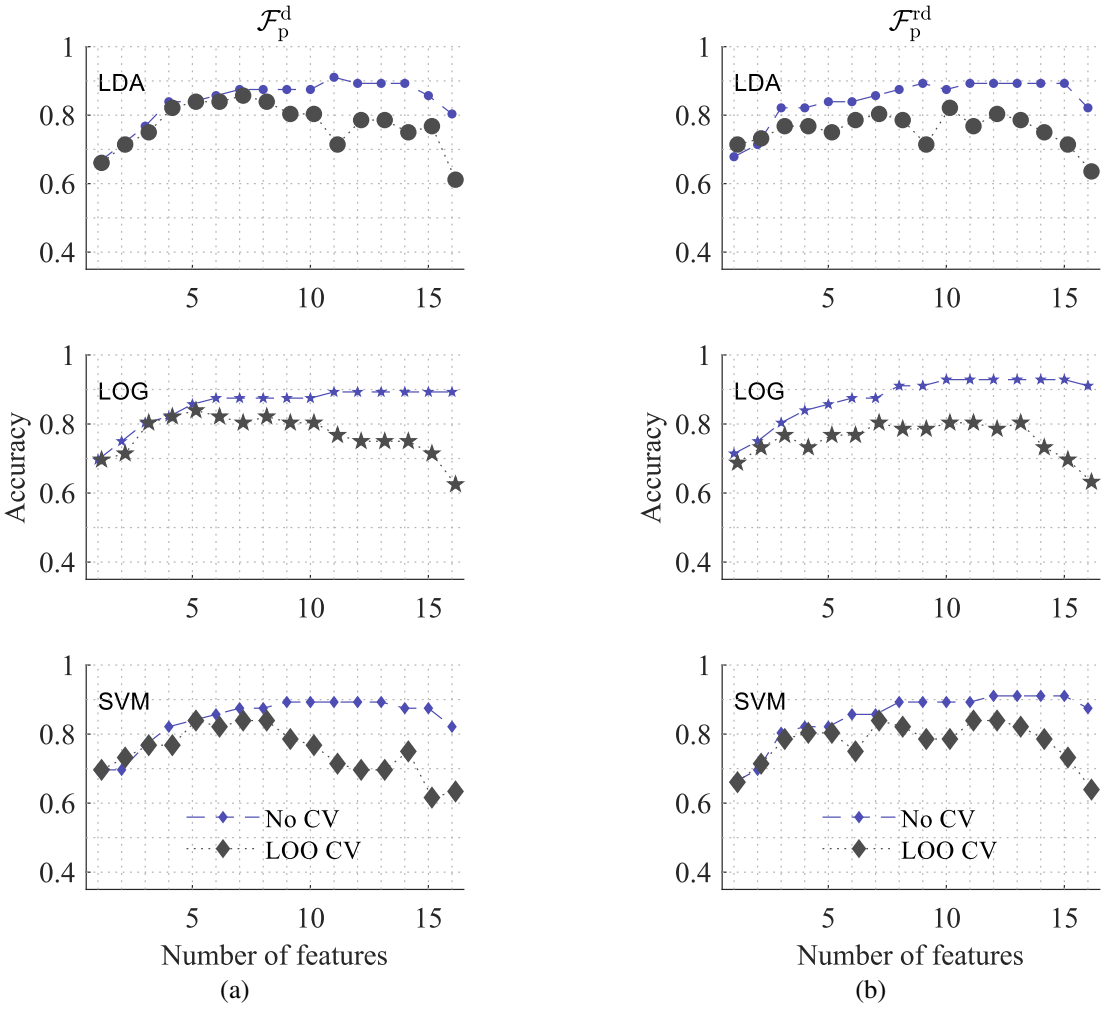

Figure 5.17: Modified LOOCV performance of classifier on sets (a) $\mathcal{F}_{\mathrm{p}}^{\mathrm{d}}$ and (b) $\mathcal{F}_{\mathrm{p}}^{\mathrm{rd}}$ respectively. Large grey markers indicate the maximum $\mathrm{Acc}_{\mathrm{CV}}$. As a baseline, the maximum accuracy of each set and classifier is shown in small blue markers.

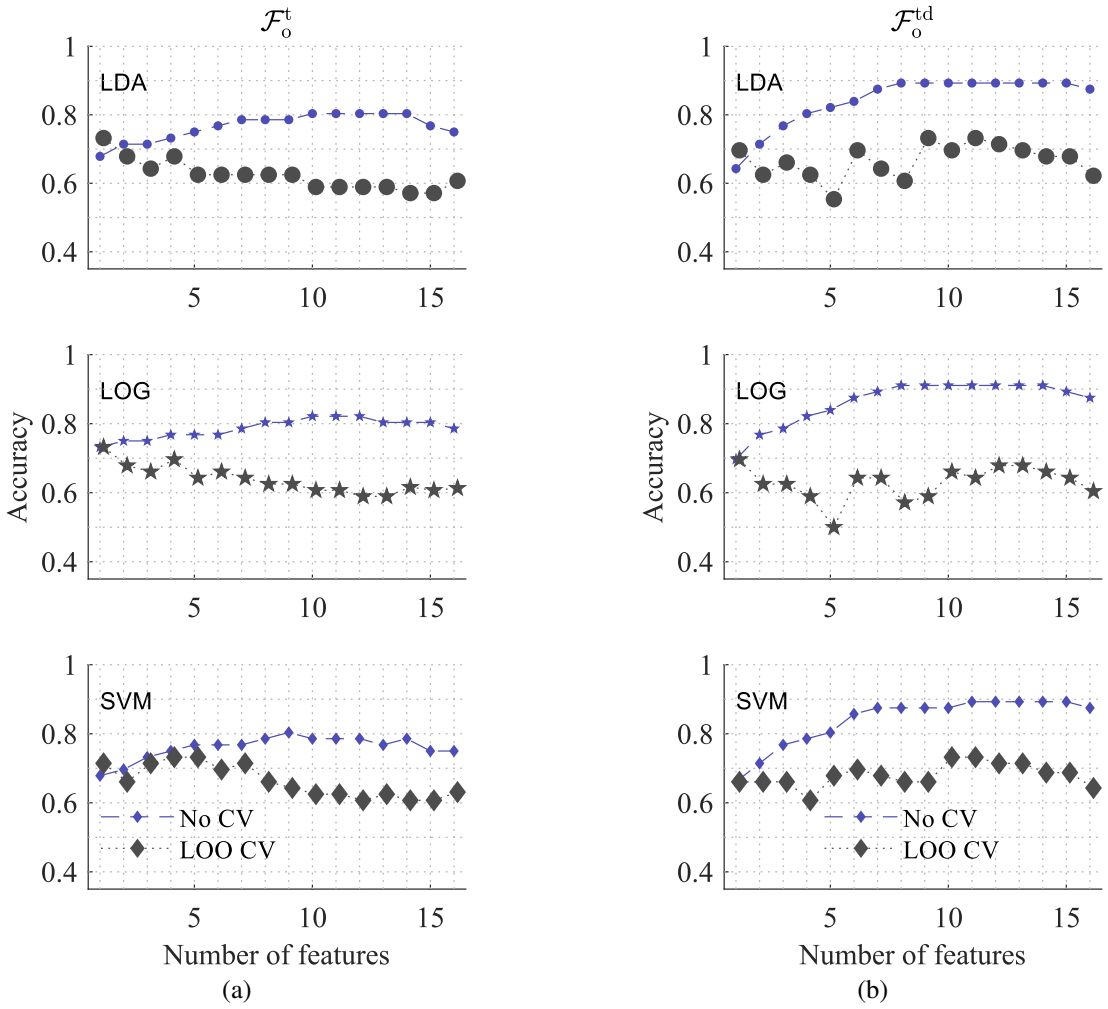

Figure 5.18: Modified LOOCV performance of classifier on sets (a) $\mathcal{F}_o^t$ and (b) $\mathcal{F}_o^{td}$ respectively. Large grey markers indicate the maximum Acc_{CV}. As a baseline, the maximum accuracy of each set and classifier is shown in small blue markers.

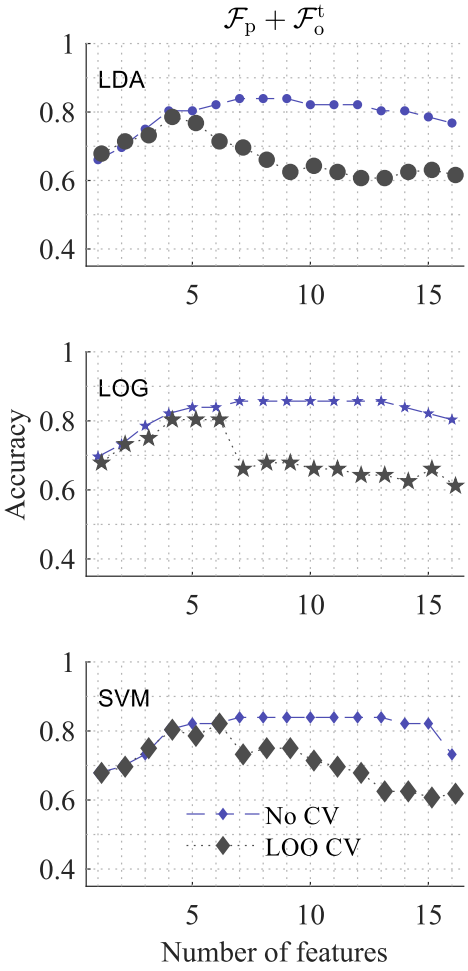

Figure 5.19: Modified LOOCV performance of classifier on the set $\{\mathcal{F}_\mathrm{p} + \mathcal{F}_\mathrm{o}^\mathrm{t}\}$. Large grey markers indicate the maximum Acc_CV. As a baseline, the maximum accuracy of each set and classifier is shown in small blue markers.

5.4 Localization of AFL Using Recurrence Quantification Analysis

In the previous section, beat-to-beat VCG loop variability has been analyzed. This was shown to extract some relevant information concerning the variability of the AFL circuit that manifests from cycle to cycle. Using linear classifiers, it was possible to obtain a good localization accuracy. Now, departing from the beat-to-beat view and considering a more time-continuous approach, this section aims to analyze the performance of spatiotemporal indices obtained from RQA.

The rationale in this approach was mentioned earlier. The quasi-periodicity of AFL may contain some information regarding the variability of AFL, but this was not evaluated by the beat-to-beat approach. The RQA methodology presented in Section 4.7 was able to access this information. Therefore in this chapter, the same supervised learning methods employed in the previous section are applied to the set of features obtained from RQA to evaluate the potential of these features in separating right and left AFL.

The result of classification is shown in Figure 5.20, where the mean accuracy is drawn as a line, and the upward- and downward-pointing arrows are the max and min value at each combination length. As can be seen, recurrence quantification gave features that are discriminative with respect to AFL localization. Good performance can be achieved, with the best achieved by the LOG classifier at 4 features. At this point, Acc = 0.84, (Se, Sp) = (0.68, 0.93) for LOG. This was obtained using linear classifiers and with a small amount of features, suggesting that overfitting was avoided. The LOG classifier has the consistent highest mean accuracy, compared to SVM and LDA. The 4 features used were [Skewness(S_1), Kurtosis(S_1), Mean(S_2), Var(S_2)].

Table 5.10: Feature Score $\tilde{s}$ for RQA Parameters

Feature	LDA	LOG	SVM
Mean(S_1)	0.75	0.63	0.23
Var(S_1)	0.75	0.50	0.63
Skewness(S_1)	0.63	0.50	0.38
Kurtosis(S_1)	*0.88*	*0.88*	*0.88*
Mean(S_2)	**1.0**	**1.0**	**1.0**
Var(S_2)	0.63	0.50	0.63
Skewness(S_2)	0.25	0.13	0.75
Kurtosis(S_2)	0.75	0.50	0.50

Further analysis of the relevant features was performed by scoring each feature. Table 5.10 shows the feature scores for each classifier. The highest participation was found to be of Mean(S_2). As was already shown in Section 4.7, right and left AFL is different

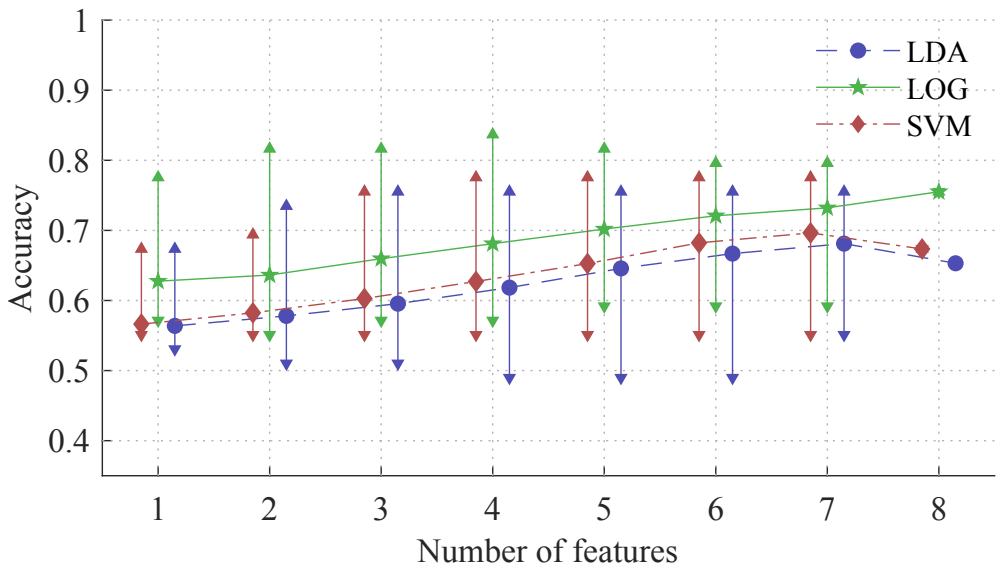

Figure 5.20: Performance of RQA features for AFL localization. Top and bottom triangles represent the range of accuracy (max Δ, min ∇). Middle lines represent the mean accuracy.

regarding their pseudo-period. This was leveraged by the classifiers to obtain better separation of the two localizations. The next most relevant feature is Kurtosis(S_1), evidenced by the second-highest score among the other features. Correlation between the two features did not give any significant result (Spearman $\rho = -0.19$, $p = 0.19$). This suggests that the relevant feature allowed access to additional separability, despite the features not being significantly related.

The features presented here aim to capture information in terms of spatial and temporal variability: it is expected that the features related to spatial variability would present some significant difference in regards to AFL localization. However, this was not the case. It can be argued then that regardless of the localization, AFL spatial variability is similar, but temporal variability is different.

Modified LOOCV is applied to the dataset, considering only the best feature subset at each combination length. Figure 5.21 shows the result of the procedure. Indeed, the best performance was achieved using only two features by the SVM classifier ($\text{Acc}_{\text{CV}} = 0.78$, $(\text{Se}_{\text{CV}}, \text{Sp}_{\text{CV}}) = (0.89, 0.64)$, AUC curve = 0.74). Additional variables seem to give good performance on the whole, but not in generalization. The best feature set in this case is $\mathcal{E}^* = [\text{Kurtosis}(S_1)\ \text{Mean}(S_2)]$. The pseudo-ROC curve can be seen in Figure 5.22. Note that the comparison is between modified LOOCV performance and max performance without CV (and not training performance).

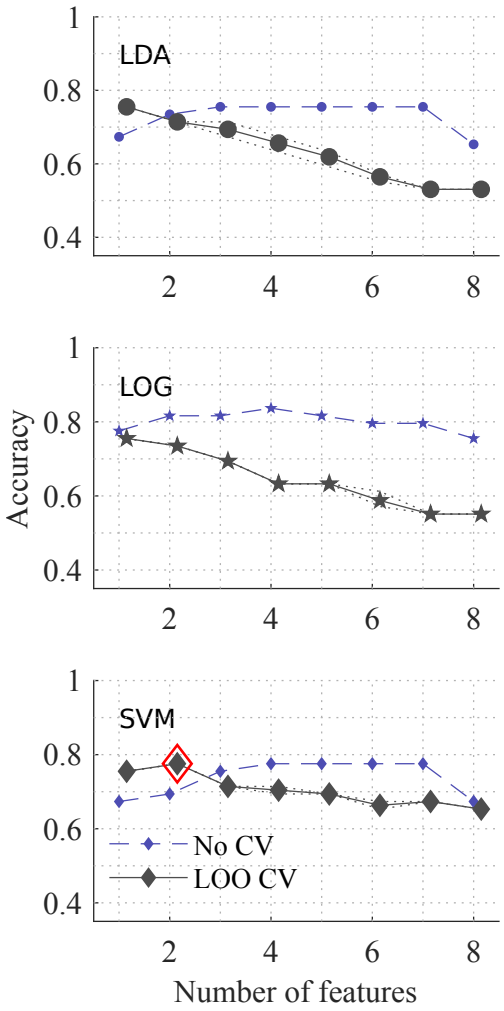

Figure 5.21: Modified LOOCV performance on the best feature sets at each combination length. Dotted lines indicate the range of variation of Acc (max,min). The middle line with markers indicates the mean accuracy. As a baseline, the maximum accuracy without CV is given in dashed blue lines. The red diamond indicates the best modified LOOCV accuracy across all classifiers.

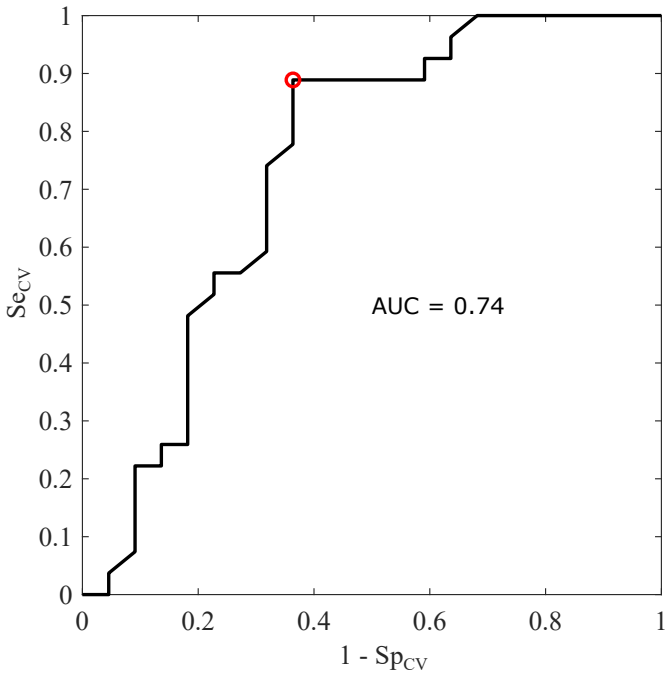

Figure 5.22: Pseudo-ROC curve for the fit using the best feature combination. The red circle indicates the optimal point.

5.5 Conclusion

In this chapter, presentation of the supervised learning methods was given, encompassing supervised linear classification, cross-validation and feature selection. These methods were then applied to the different dataset of F waves issued from the processing stage detailed in Chapter 4 to assess the performance of right-or-left localization.

The result of analysis from this chapter showed that it was possible to localize AFL using variability features issued from a beat-to-beat methodology. Localization performance is deemed satisfactory, with baseline performance reaching up to Acc = 0.91 and $(\mathrm{Se}, \mathrm{Sp}) = (0.94, 0.88)$ using the SVM classifier. Modified cross-validation gave a generalized performance of $\mathrm{Acc}_{\mathrm{CV}} = 0.88$ and $(\mathrm{Se}_{\mathrm{CV}}, \mathrm{Sp}_{\mathrm{CV}}) = (0.90, 0.84)$ using the SVM classifier, which remains satisfactory. Feature selection showed that the features presenting significant difference regarding right or left AFL contributed the most in the localization, and these features are not only first-order measures (e.g. Mean), but higher-order measures.

Application of learning methods on the dataset issued from RQA initially gave a good performance, with Acc = 0.84 and $(\mathrm{Se}, \mathrm{Sp}) = (0.68, 0.93)$, but performance dropped in generalization, with $\mathrm{Acc}_{\mathrm{CV}} = 0.78$ and $(\mathrm{Se}_{\mathrm{CV}}, \mathrm{Sp}_{\mathrm{CV}}) = (0.89, 0.64)$.

Chapter 6

Validation of Respiratory Motion as a Source of Discriminatory Variability

6.1 Introduction

It has been shown in the previous chapter that variability in the VCG loop parameters can be exploited to determine a right or left AFL circuit localization. This shows that employing the methodology presented in Chapter 4 allows extraction of the crucial variability information related to AFL localization. Among the items in the methodology was the removal of respiratory motion from the F loops. It has been discussed in earlier chapters the effect of respiration on the ECG. Using the method of Section 4.4, this was removed from F waves.

Recalling some key elements from Section 2.3, surface potential measures are subject to distortion related to the electrical conductivity of the thorax as well as the location of the electrode with respect to the cardiac dipole origin. It is known that due to the tilting of the heart towards the left, the right atrium is closer to the body surface. The left atrium, on the other hand, is located deeper inside the thoracic cage. This should in theory amount to different signal quality as the surrounding conductivity is different in the two localizations.

Coupled with respiratory motion, this should translate into different variability between localization. This induces a hypothesis that atrium position within the thorax and respiratory motion both interplay to contribute to the variability on the surface ECG. It may have been the reason for the good performance of set $\mathcal{F}_{\mathrm{p}}$, which is the set of loops without any correction. This is a valid reasoning from a clinical standpoint, since by clinical definitions, AFL is regarded as having a stable activation (compared to AF), thus regardless of localization, AFL should not exhibit much difference in variability.

In this section, this original hypothesis is tested using an original methodology described in Section 6.2. Analysis of changes in variability is made to highlight the eventual effects of respiratory motion removal, and compared to changes in classifier performance. Section 6.3 then presents the result of this analysis.

6.2 Validation of Respiratory Motion as Discriminatory Variability

The correction of respiratory motion will necessarily affect several parameters of the VCG loop. On one hand, the rotation of the loops due to **R** will change the orientation parameters. On the other hand, scaling and rotation corrections should not affect the geometry parameters, since the loop morphology does not undergo any change. Since each F waves were corrected by a different value, changes in the variability of the beat-to-beat series are expected, which will necessarily affect the classifier performance. This change in performance, as well as the change in variability values are useful in determining if the variability observed from the recordings are related to AFL or to the respiratory motion.

The initial hypothesis $\mathcal{H}_0 =$ C_1 AND C_2 is that *respiratory motion introduces variability that allows us to discriminate between right and left AFL*. Should this be true, then by removing the variability related to respiratory motion, it is expected C_1: a significant drop in classifier performance coupled with C_2: a significant decrease in variability, with different amounts in right and left AFL. If not, then the classifier performance should remain relatively stable; the increase or decrease in variability will indicate the addition or removal of variability.

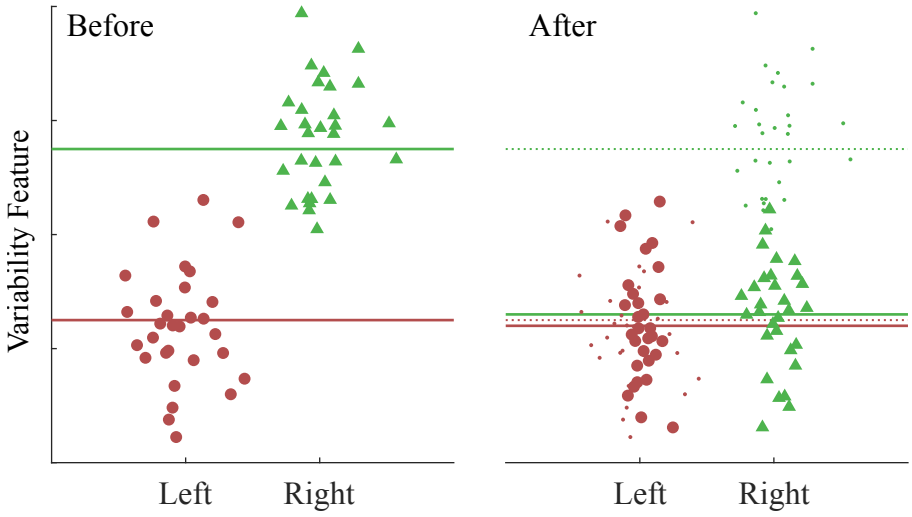

Figure 6.1: Hypothetical scenario of respiratory motion correction effect on VCG loop parameter variability. Lines (full and dotted) indicate the mean of the distribution of points.

Figure 6.1 illustrates the picture when conditions C_1 and C_2 are fulfilled. Two hypothetical point clouds are shown, belonging to two different classes. Both are originally separable, with some overlap. Once correction is applied, the two clouds move, in a different manner for both localization, validating condition C_2. The clouds become

more overlapped, hence condition C_1 is validated as well due to reduced accuracy.

The convergence of point cloud is a result of the parameter series becoming more similar to each other. In theory, this would translate to equal statistical measures (e.g. mean, variance, etc.), thus a first approach would be to evaluate the change in all variability features.

Discriminatory variability is not related to only a single feature, but to a set of different combinations of features. This is a reasonable argument, since it has been shown that in some cases, two or more features may reveal more separability than a single feature alone. However, composite variability index resulting from the combination of several features may be difficult to interpret in terms of change. Therefore, this is done instead through analysis of the classification accuracy.

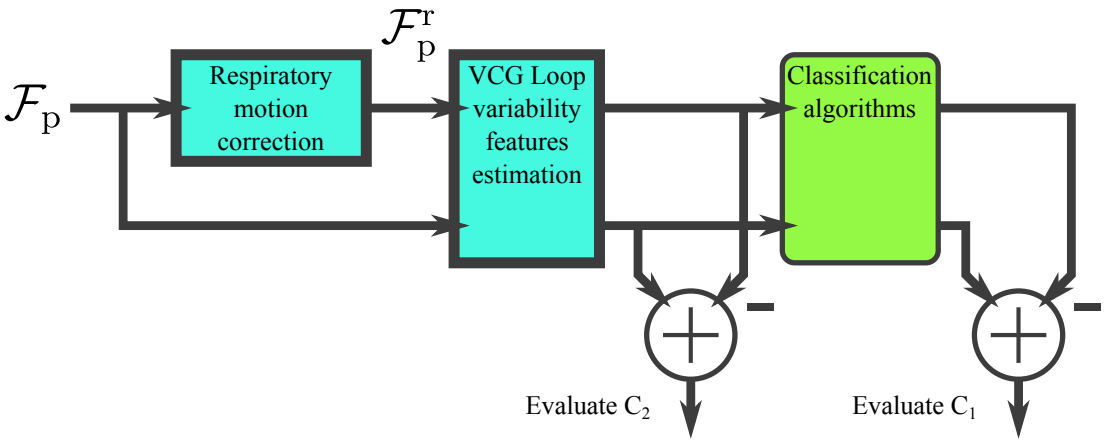

Figure 6.2: Illustration of the approach for the validation of respiratory motion as discriminatory variability.

Figure 6.2 summarizes the approach of this chapter. The matter is investigated by analyzing the difference between the variability before and after correction, on all beat-to-beat parameter series. Additionally, the change in classification performance was also analyzed.

6.3 Results & Discussion

A comparison of classifier performance is shown in Figure 6.3. As can be seen, there is insignificant change in the mean performance, as well as its hull. Towards larger combination lengths, the performance decreases slightly, but not by a significant amount. The maximum reduction in performance (not visible on the figure) corresponds to 10 misclassified recordings using LDA, but only happened in two combinations, out of the $2^{16} - 1$ possible ones available. The mean change in accuracy before and after

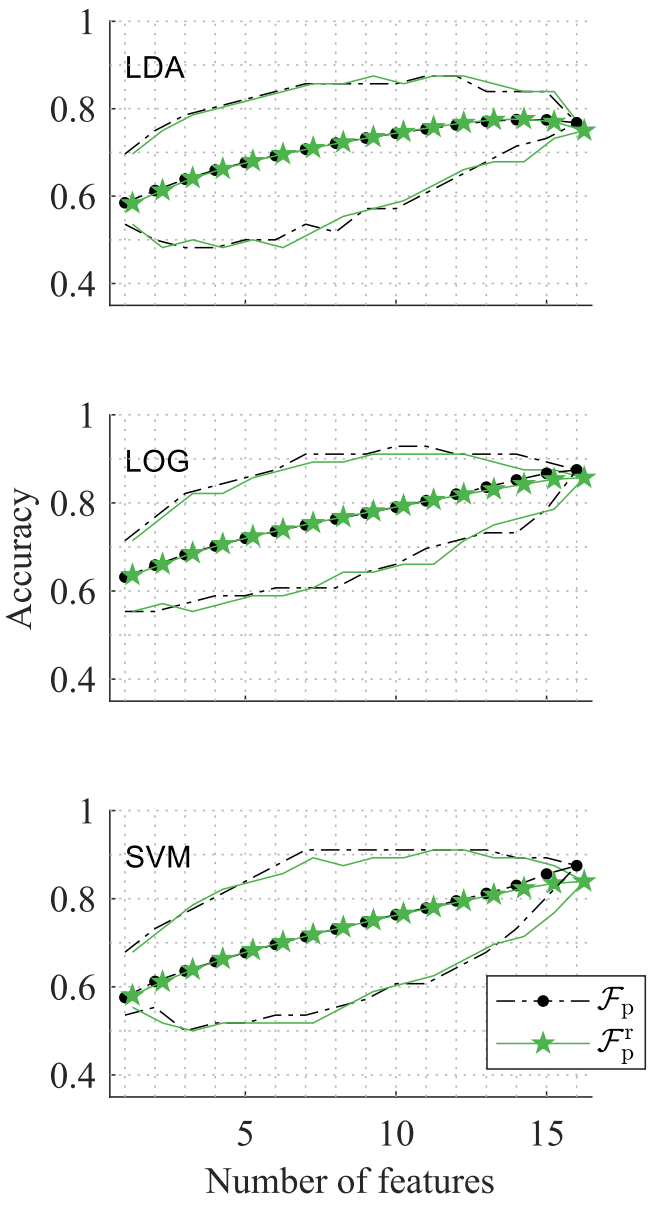

Figure 6.3: Classifier performance on waves from set $\mathcal{F}_p$ and $\mathcal{F}_p^r$, defined by the classifier accuracy. Top and bottom lines represent the maximum and minimum accuracy, whereas the middle line represents the mean.

correction across all possible combinations was $-2.80 \cdot 10^{-3}$ for LDA, and $-3.70 \cdot 10^{-3}$ for LOG and SVM, which actually suggests an increase in performance, instead of a decrease (i.e. performance before was smaller than after). However, the small value suggests very minimal improvement. With these observations, condition C_1 is negated.

The change of parameter variability, quantified by calculating the difference of features before and after respiratory motion correction is shown in Table 6.1. The prefix Δ indicates the difference of values. Note that loop geometry features are not displayed, since they are not affected by the rotation and scaling performed by respiratory motion

correction. Their median levels and deviation values are observed to be ≈ 0, as was expected.

As for orientation parameters, it can be seen that most of the median levels are small negative values. Compared to standard values that the orientation parameters assume, this change is relatively small ($< 1\%$). This indicates an insignificant change in variability content. Only two differences were reported as significant, however their relative value in regards to those of their respective feature is negligible. Also worthy of note, the changes are mostly similar for right and left AFL, illustrated by median levels that are relatively similar for the two localization. This suggests that the correction affects loops from both localization in a similar manner.

Table 6.1: Statistics of Differences of Variability Features ($\mathcal{F}_{\mathrm{p}}$ vs. $\mathcal{F}_{\mathrm{p}}^{\mathrm{r}}$)

Feature	Right AFL	Left AFL	p-value
$\Delta\mathrm{Mean}(\phi_{AZ})$	0.24 ± 1.23	-0.20 ± 1.08	0.61
$\Delta\mathrm{Var}(\phi_{AZ})$	-2.59 ± 13.78	-1.57 ± 8.20	0.80
$\Delta\mathrm{Skewness}(\phi_{AZ})$	-0.02 ± 0.05	$\mathbf{-0.05 \pm 0.09}$	0.19
$\Delta\mathrm{Kurtosis}(\phi_{AZ})$	0.01 ± 0.14	0.02 ± 0.12	0.61
$\Delta\mathrm{Mean}(\phi_{EL})$	-0.30 ± 2.52	-0.15 ± 2.28	0.99
$\Delta\mathrm{Var}(\phi_{EL})$	$\mathbf{-17.85 \pm 85.21}$	1.97 ± 134.14	0.26
$\Delta\mathrm{Skewness}(\phi_{EL})$	0.00 ± 0.14	0.00 ± 0.17	0.78
$\Delta\mathrm{Kurtosis}(\phi_{EL})$	0.04 ± 0.37	0.02 ± 0.30	0.79

Values expressed as median ± mean absolute deviation
Bold text indicates $p < 0.05$ using Wilcoxon signed rank test

The initial hypothesis supposes a significant decrease in classifier performance (C_1) and also variability (C_2). It has been shown however that classifier performance did not drop significantly after applying respiratory motion correction onto the VCG F loops (i.e. $\overline{\mathrm{C}}_1$), suggesting that the variability of the observations are still able to provide discriminatory information for right and left AFL. In addition, there is no significant change of variability in either localization (i.e. $\overline{\mathrm{C}}_2$). This leads to a conclusion that $\mathcal{H}_0$ is not true: respiratory motion does not explain the variability that is observed from the VCG loop parameters. The more likely conclusion is that the variability that allows discrimination of right and left AFL might originate from the pathology itself.

One possible explanation for the rather small effect of respiratory motion on the ECG would be that these recordings were taken during ablation operations, where the patients are supine and relaxed (sometimes even unconscious). The breathing pattern would be expected to be more gentle, as opposed to in a conscious state. This has already been suggested in Section 4.4, where the morphological changes are essentially zero. In several cases of research, exaggeration of breathing (heavy inspiration or expiration) was

able to induce significant but arguably small changes in ECG morphology [17,77]. This is not the case during operation, therefore wave morphology should remain relatively constant.

The conclusion is, unfortunately, not mutually exclusive of other effects that may not be compensated, such as the actual thorax inhomogeneity. However, this is difficult to correct, as such parameter may not be estimable. To further study this idea, a setup using BSPM may give more insight into the inhomogeneity by enriching spatial resolution. Also of interest, would be the study of actual circuit variability using EGM.

6.4 Conclusion

In this chapter, validation of respiratory motion as a discriminatory source of variability was tested using an original methodology of analyzing the difference in change of variability and classifier performance. It was shown that respiratory motion is not the source of variability that allowed right-or-left localization, and this is supported by the small, non-significant changes of variability parameters respiratory motion correction (relative change of values $< 1\%$) as well as the small, non-significant changes in classifier performance before and after respiratory motion correction ($< -2.80 \cdot 10^{-3}$), suggesting increase in performance). The conclusion of this analysis further reinforces the fact that the variability that separates right and left AFL originates not from respiratory motion, but from the pathology itself.

Chapter 7

Conclusion & Future Works

7.1 Introduction

The work presented here shows that it is possible to discriminate AFL localization by applying advanced signal processing techniques and analyzing higher-order statistical properties of the VCG F loop parameters. This work belongs to a category of novel techniques that rely on more than just the standard metrics widely used in order to localize AFL. Along the way, there were several necessary yet important works that have been done.

7.2 Summary of Important Elements

7.2.1 Novel Methodologies for AFL Localization A novel right or left AFL localization methodology was developed. The scheme exploits the variability contained in beat-to-beat series of vectorcardiographic F loop parameters, using the assumption that the localization of the circuit produces different amount of variability. This was shown to have sound clinical reasoning. Using several measures of variability, it is possible to reliably extract this difference and use it to determine right and left atrium localization. This is suggestive of the truth behind the initial hypothesis in Chapter 4. Furthermore, a reasonably high performance occurs at a relatively low combination length, avoiding possible overfitting issues which can be related to large combination lengths.

Even though the good performance was obtained via combination of several variability indices, feature selection was addressed in hopes that the results from that exercise allows some explanation to the good performance of the classifier. It was shown that the optimal set of features contained several significant features that present good separability. This provides a proof of the validity of the separation, and shows that it is not due to overfitting of the classifier with irrelevant features.

In addition, recurrence quantification analysis showed that AFL is a spatially stable process. This is different than AF, which has a variable spatial process. A reason for this was mentioned: that because AFL is a single-circuit pathology, the spatial organization is expected to be higher. In addition, there is a significant difference in AFL cycle length in right and left AFL. This allowed a good classification of right or

left AFL.

Some future directions for this work can be discerned. In our study, the F waves were taken at fixed length, under the supposition that the activity duration does not vary much from beat to beat. This assumption neglects the information contained in the wave duration, which may provide some information on the propagation pattern of the circuit inside the atrium. Indeed, the right atrium presents a specific set of stable blocks, compared to the left atrium, which presents more functional blocks. We can expect right AFL to be more consistent in the timing variability than left AFL.

A recently published paper showed that applying machine learning onto the ECG without further transformations, it was possible to discriminate right and left AFL with a rather high cross-validated performance [98]. This opens the way to exploring the ECG–as simple as it sounds–for features that may not be obtained by direct reasoning. This falls under the category of deep learning, and should surely benefit the problem at hand.

7.2.2 Validation of Respiratory Motion Variability Effects An original hypothesis regarding the source of variability in AFL was proposed. In short, respiratory motion causes remarkable change in the ECG due to body movement and physiological changes inside the thorax. In addition to that, the right atrium being closer to the heart than the left atrium, it could be suggested that above-mentioned changes affect right and left AFL observations differently. The motion in and of itself is a prominent source of variability, that is remarked in the literature and in the clinic. This constitutes a confounding variability source that could be the reason for the good localization performance.

It was shown however, through the use of original respiratory motion correction strategy, that this is not true. The main proofs brought forth in this research is that the content of variability is not significantly changed, as well as the classification accuracy, which is used as a surrogate measure of separability. This exercise constitutes an original way of approaching the problems dealt with in biomedical engineering, as guided by the clinic. In turn, it allows original ideas to be developed, as well as new methods.

Between the heart and the surface electrodes are layers of organs, bones and tissues. This without doubt causes certain effects that produce some variability. Unfortunately, it is difficult to obtain any adequate information regarding these effects in order to correct them. A larger issue that is difficult to resolve is the physical location of the right and left atrium with respect to the torso surface. The right atrium is much closer to the surface than the left atrium. It could be suggested that the variability may be

due to the distance of the right and left atrium with respect to the surface. This being a factor that cannot be corrected on the surface ECG, the issue of whether variability in the AFL is caused by the physical location requires the study of electrical recordings from inside the heart to characterize the 'true' variability of AFL.

Alternatively, it could be that the variability is an artifact of the loop parameter estimation. It is not possible, however, to analyze this as no true information on respiratory motion exists from the recordings. A simulation study consisting of artificially generated respiratory motion and baseline wandering affecting F waves may be useful in determining whether the quantities estimated from the surface ECG using the proposed loop parameters correspond to parameters of the simulated noise.

7.2.3 F Wave Detection Using GLRT The detection of F waves by means of GLRT presents a novelty in atrial signal detection and segmentation. Coupled with the signal models utilized, it was shown that taking into account of the T wave overlaps and heavy-tailed noises allowed a much better detection accuracy than with only a Gaussian assumption without accounting for T wave overlap. This has not been seen in the literature, to the author's knowledge, and certainly presents a prospective line of work to be continued.

Several leads for future works in this direction include:

1. Leveraging quasi-periodicity of AFL waves to increase detection performance. This may require either working in frequency space, or utilizing the periodicity from the outputs of the already available detector

2. Improvement in overlapping spline estimation. This could be done by considering other bases than polynomials. In particular, B-spline and piecewise cubic Hermite interpolants may provide an interesting alternative [59]. Another strategy would be to increase polynomial degree, but perform a constrained estimation, in particular on the possible range of values of A (the template amplitude). An interesting estimator has been proposed, that allows a somewhat closed-form expression for inequality-constrained LS with problems of degenerate rank [99]

7.2.4 Degeneracy in Respiratory Motion Parameter Estimation It has been found that the spurious respiratory motion angle estimates were due to some form of degeneracy in the data, such that the rotation of loops become a reflection. Although in theory, this is an impossibility, the observation proves different. Solving this problem is important for future works that rely on serial analysis of ECG-derived respiratory

motion parameters. Before the undertaking of this work, these issues have been highlighted [71, 100], but no solution was proposed.

A methodology for correcting this effect has been proposed in this work, and shows that it is possible to correctly estimate respiratory motion angles. Although here, it serves as a tool to remove variability from F wave, the methodology is general to any application that requires it. In addition, it can be seen that the complexity required to perform this correction is not overly large.

7.2.5 Optimization with Non-Ideal Goals A unique methodology was explored to optimize the IDT, that allowed improvement of classification accuracy. This is a more direct endpoint to the problem of this work, but there is no direct relationship to the optimization goal. The presented methodology illustrates that optimization may be extended to problem goals like this. However, it can be seen that this is a non-trivial task and in the case of this work, it presents a computationally expensive method.

7.2.6 Machine Learning Methodologies Machine learning techniques is an important part of this work since it makes up the basis for inducing a practical classifier for AFL localization. Practicality implies knowing several crucial parameters of the classifier setup as well as the techniques necessary to control learning. In this research, there is a need to know not only the generalized performance, but the threshold at which best classification can be obtained. The technique of modified LOOCV presented in this work constitutes an original approach to obtaining both items together.

Feature selection is also another issue that must be addressed in order to derive a practical classifier. Feature interactions can be difficult to determine, but through the use of a learning algorithm, it is possible to uncover them. This is the key advantage of the wrapper approach, despite being an expensive one. Furthermore, inspection of the best feature combinations allowed the uncovering of how relevant features interact with other features.

The main theme under this section is explainable learning. For future works, it would be interesting to use non-linear classifiers, or even neural network with some kind of regularization.

7.3 Publications Issued From This Work

1. M. H. Kamarul Azman, O. Meste, K. Kadir, and D. G. Latcu, "Estimation and Removal of T Wave Component in Atrial Flutter ECG to Aid Non-Invasive Localization of Ectopic Source," in Computing in Cardiology, Rennes, France, 2017, vol. 44.

2. P. Bonizzi, S. Zeemering, J. Karel, M. H. Azman, T.A.R. Lankveld, U. Schotten, H. Crijns, R. Peeters, O. Meste, "Noninvasive Characterisation of Short-and Long-Term Recurrence of Atrial Signals During Persistent Atrial Fibrillation," in Computing in Cardiology, Rennes, France, 2017, vol. 44.

3. M. H. Azman, O. Meste, K. Kadir, and D. G. Latcu, "Localizing Atrial Flutter Circuit using Variability in the Vectorcardiographic Loop Parameters," presented at the Computing in Cardiology, Maastricht, Netherlands, 2018, vol. 45.

4. M. H. Azman, O. Meste, and K. Kadir, "Detecting Flutter Waves in the Electrocardiogram Using Generalized Likelihood Ratio Test," presented at the Computing in Cardiology, Maastricht, Netherlands, 2018, vol. 45.

5. M. H. Azman, O. Meste, D. G. Latcu, and K. Kadir, "Non-Invasive Localization of Atrial Flutter Circuit using Recurrence Quantification Analysis and Machine Learning," presented at the Computing in C ardiology, Singapore, Singapore, 2019, vol. 46.

6. M. H. Azman, O. Meste, D. G. Latcu, and K. Kadir, "Improving Flutter Localization Performance by Optimizing the Inverse Dower Transform," presented at the Computing in Cardiology, Singapore, Singapore, 2019, vol. 46.

7. O. Meste, H. K. Azman, and D. G. Latcu, "Machine learning approach and waves synchronization improvement for the localization of Atrial Flutter circuit based on the 12-leads ECG," presented at the Computing in Cardiology, Singapore, Singapore, 2019, vol. 46.

Bibliography

[1] J. Malmivuo and R. Plonsey, *Bioelectromagnetism*. Oxford University Press, 1995.

[2] E. Frank, "An accurate, clinically practical system for spatial vectorcardiography," *Circulation*, vol. 13, no. 5, pp. 737–749, May 1956.

[3] R. Bousseljot, D. Kreiseler, and A. Schnabel, "Nutzung der EKG-signaldatenbank CARDIODAT der PTB über das internet," *Biomedizinische Technik / Biomedical Engineering $V 40*, no. s1, pp. 317–318, 1995.

[4] A. L. Goldberger, L. A. Amaral, L. Glass, J. M. Hausdorff, P. C. Ivanov, R. G. Mark, J. E. Mietus, G. B. Moody, C. K. Peng, and H. E. Stanley, "PhysioBank, PhysioToolkit, and PhysioNet: components of a new research resource for complex physiologic signals." *Circulation*, vol. 101, no. 23, pp. E215–220, Jun. 2000.

[5] L. Lilly, *Pathophysiology of Heart Disease*. Lippincott Williams & Wilkins, 2011.

[6] H. C. Burger and J. B. van Milaan, "Heart-vector and leads; geometrical representation." *British Heart Journal*, vol. 10, no. 4, pp. 229–233, Oct. 1948.

[7] "Standardisation of Precordial Leads: Joint Recommendations of the Cardiac Society of Great Britain and Ireland and the American Heart Association," *The Lancet*, vol. 231, no. 5969, pp. 221 – 222, 1938.

[8] F. N. Wilson, C. E. Kossmann, G. E. Burch, E. Goldberger, A. Graybiel, H. H. Hecht, F. D. Johnston, E. Lepeschkin, and G. B. Myers, "Recommendations for Standardization of Electrocardiographic and Vectorcardiographic Leads," *Circulation*, vol. 10, no. 4, pp. 564–573, 1954.

[9] F. N. Wilson, A. G. Macleod, and P. S. Barker, "The potential variations produced by the heart beat at the apices of Einthoven's triangle," *American Heart Journal*, vol. 7, no. 2, pp. 207 – 211, 1931.

[10] W. Einthoven, "Weiteres über das Elektrokardiogramm," *Archiv für die gesamte Physiologie des Menschen und der Tiere*, vol. 122, no. 12, pp. 517–584, May 1908.

[11] H. Mann, "A Method Of Analyzing the Electrocardiogram," *JAMA Internal Medicine*, vol. 25, no. 3, pp. 283–294, 1920.

[12] W. Hollman and H. Hollman, "Neue electrocardiographische untersuchungsmethode," *Z. Kreislaufforsch*, vol. 29, pp. 546–558, 1939.

[13] E. Frank, "The image surface of a homogeneous torso," *American Heart Journal*, vol. 47, no. 5, pp. 757–768, May 1954.

[14] G. Dower, H. B. Machado, and J. A. Osborne, "On deriving the electrocardiogram from vectoradiographic leads," *Clinical Cardiology*, vol. 3, no. 2, pp. 87–95, Apr 1980.

[15] L. Edenbrandt and O. Pahlm, "Vectorcardiogram synthesized from a 12-lead ecg: Superiority of the inverse dower matrix," *Journal of Electrocardiology*, vol. 21, no. 4, pp. 361 – 367, 1988.

[16] A. Karpov and I. Tsofin, "Electrical conductivity of lungs and respiratory volumes in functional and diagnostic testing. Preliminary results." accessible at mobecomm.com.

[17] M. C. Saki, Y. Z. Ider, B. Ozin, and A. Oto, "Respiration affects on P wave alignment and averaging," in *1992 14th Annual International Conference of the IEEE Engineering in Medicine and Biology Society*, vol. 2, Oct. 1992, pp. 553–554.

[18] I. Ruttkay-Nedecký, "Respiratory changes of instantaneous spatial cardiac vectors," in *Proceedings of the 11th International Symposium on Vectorcardiography*, New York, 1970, pp. 115–8.

[19] "Disease burden and mortality estimates: Cause-specific mortality, 2000-2016." [Online]. Available: http://www.who.int/healthinfo/global_burden_disease/estimates/en/

[20] S. S. Chugh, R. Havmoeller, K. Narayanan, D. Singh, M. Rienstra, E. J. Benjamin, R. F. Gillum, Y.-H. Kim, J. H. McAnulty, Z.-J. Zheng, M. H. Forouzanfar, M. Naghavi, G. A. Mensah, M. Ezzati, and C. J. Murray, "Worldwide Epidemiology of Atrial Fibrillation: A Global Burden of Disease 2010 Study," *Circulation*, vol. 129, no. 8, pp. 837–847, Feb. 2014.

[21] "Atrial Fibrillation Fact Sheet: Data & Statistics," Nov. 2018. [Online]. Available: https://www.cdc.gov/dhdsp/data_statistics/fact_sheets/fs_atrial_fibrillation.htm

[22] J. Granada, W. Uribe, P. H. Chyou, K. Maassen, R. Vierkant, P. N. Smith, J. Hayes, E. Eaker, and H. Vidaillet, "Incidence and predictors of atrial flutter in the general population," *Journal of the American College of Cardiology*, vol. 36, no. 7, pp. 2242–2246, Dec. 2000.

[23] J. H. King, C. L.-H. Huang, and J. A. Fraser, "Determinants of myocardial conduction velocity: implications for arrhythmogenesis," *Frontiers in Physiology*, vol. 4, 2013.

[24] S.-S. Bun, D. G. Latcu, F. Marchlinski, and N. Saoudi, "Atrial flutter: more than just one of a kind," *European Heart Journal*, vol. 36, no. 35, pp. 2356–2363, Sep. 2015.

[25] A. Bochoeyer, "Surface Electrocardiographic Characteristics of Right and Left Atrial Flutter," *Circulation*, vol. 108, pp. 60–66, 2003.

[26] F. García Cosío, A. Pastor, A. Núñez, A. P. Magalhaes, and P. Awamleh, "Atrial flutter: an update," *Rev. española Cardiol.*, vol. 59, no. 8, pp. 816–831, 2006.

[27] C. Pedrinazzi, O. Durin, G. Mascioli, A. Curnis, R. Raddino, G. Inama, and L. Dei Cas, "Atrial flutter: from ecg to electroanatomical 3d mapping," *Heart International*, vol. 2, no. 3-4, Dec. 2006.

[28] Y. Yuniadi, C.-t. Tai, K.-t. Lee, B.-h. Huang, Y.-j. Lin, S. Higa, T.-y. Liu, and J.-l. Huang, "Heart Rhythm Disorders A New Electrocardiographic Algorithm to Differentiate Upper Loop Re-Entry From Reverse Typical Atrial Flutter," *J. Am. Coll. Cardiol.*, vol. 46, no. 3, pp. 524–528, 2005.

[29] P. Jais, D. C. Shah, M. Haissaguerre, M. Hocini, J. T. Peng, A. Takahashi, S. Garrigue, P. Le Metayer, and J. Clementy, "Mapping and ablation of left atrial flutters," *Circulation*, vol. 101, no. 25, pp. 2928–2934, Jun. 2000.

[30] P. M. Kistler, K. C. Roberts-thomson, H. M. Haqqani, S. P. Fynn, S. Singarayar, J. K. Vohra, J. B. Morton, P. B. Sparks, and J. M. Kalman, "P-Wave Morphology in Focal Atrial Tachycardia Development of an Algorithm to Predict the Anatomic Site of Origin," *J. Am. Coll. Cardiol.*, vol. 48, no. 5, pp. 0–7, 2006.

[31] M. C. Wijffels, C. J. Kirchhof, R. Dorland, and M. A. Allessie, "Atrial Fibrillation Begets Atrial Fibrillation," *Circulation*, vol. 92, no. 7, pp. 1954–1968, Oct. 1995.

[32] G. Lee, P. Sanders, and J. M. Kalman, "Catheter ablation of atrial arrhythmias: state of the art," *The Lancet*, vol. 380, no. 9852, pp. 1509–1519, 2012.

[33] E.-S. Jin and P. J. Wang, "Cryoballoon Ablation for Atrial Fibrillation: a Comprehensive Review and Practice Guide," *Korean Circulation Journal*, vol. 48, no. 2, pp. 114–123, Jan. 2018.

[34] G. Barbato, V. Carinci, C. Tomasi, V. Frassineti, M. Margheri, and G. D. Pasquale, "Is electrocardiography a reliable tool for identifying patients with isthmus-dependent atrial flutter ?" *Europace*, pp. 1071–1076, 2009.

[35] B. P. Knight, G. F. Michaud, S. A. Strickberger, and F. Morady, "Electrocardiographic differentiation of atrial flutter from atrial fibrillation by physicians," *Journal of Electrocardiology*, vol. 32, no. 4, pp. 315–319, Oct. 1999.

[36] C. Medi and J. M. Kalman, "Prediction of the atrial flutter circuit location from the surface electrocardiogram," *Europace*, pp. 786–796, 2008.

[37] T. Irie, Y. Kaneko, T. Nakajima, A. Saito, M. Ota, T. Kato, T. Iijima, M. Tamura, H. Kobayashi, T. Ito, M. Manita, and M. Kurabayashi, "Typical atrial flutter with atypical flutter wave morphology due to abnormal interatrial conduction," *Cardiol. J.*, vol. 18, no. 4, pp. 450–453, 2011.

[38] D. E. Krummen, M. Patel, H. Nguyen, G. Ho, D. S. Kazi, P. Clopton, M. C. Holland, S. L. Greenberg, G. K. Feld, M. N. Faddis, and S. M. Narayan, "Accurate ECG Diagnosis of Atrial Tachyarrhythmias Using Quantitative Analysis: A Prospective Diagnostic and Cost-Effectiveness Study," *Journal of Cardiovascular Electrophysiology*, vol. 21, no. 11, pp. 1251–1259, Nov. 2010.

[39] A. Kahn, D. Krummen, G. Feld, and S. Narayan, "Localizing circuits of atrial macro-reentry using ecg planes of coherent atrial activation," *Heart Rhythm*, vol. 4, no. 4, pp. 445–451, Apr 2007.

[40] S. M. Narayan, G. K. Feld, A. Hassankhani, and V. Bhargava, "Quantifying intracardiac organization of atrial arrhythmias using temporospatial phase of the electrocardiogram," *J. Cardiovasc. Electrophysiol.*, vol. 14, no. 9, pp. 971–981, 2003.

[41] J. Ng, A. Sahakian, W. Fisher, and S. Swiryn, "Atrial flutter vector loops derived from the surface ecg: Does the plane of the loop correspond anatomically to the macroreentrant circuit?" *Journal of Electrocardiology*, vol. 36, pp. 181–186, Dec 2003.

[42] U. Richter, M. Stridh, A. Bollmann, D. Husser, and L. Sörnmo, "Spatial characteristics of atrial fibrillation electrocardiograms," *Journal of Electrocardiology*, vol. 41, no. 2, pp. 165–172, Mar–Apr 2008.

[43] F. Castells, O. Meste, A. Quesada, M. Guillem, A. Climent, and J. Millet, "Characterization of typical and atypical atrial flutter loops from the vectorcardiogram," in *2011 Annual International Conference of the IEEE Engineering in Medicine and Biology Society*, 2011, pp. 4976–4979.

[44] T. Kao, Y. Y. Su, H. W. Tso, Y. C. Lin, S. A. Chen, and C. T. Tai, "Nonlinear analysis of human atrial flutter and fibrillation using the surface electrocardiogram," in *Computers in Cardiology*, vol. 31, 2004, pp. 441–444.

[45] F. Takens, "Detecting strange attractors in turbulence," in *Dynamical Systems and Turbulence, Warwick 1980*, D. Rand and L.-S. Young, Eds. Berlin, Heidelberg: Springer Berlin Heidelberg, 1981, pp. 366–381.

[46] O. Meste, S. Zeemering, T. Lankveld, U. Schotten, H. Crijns, R. Peeters, and P. Bonizzi, "Noninvasive recurrence quantification analysis predicts atrial fibrillation recurrence in persistent patients undergoing electrical cardioversion," in *Computing in Cardiology*, vol. 43, 2016, pp. 677–680.

[47] J.-P. Eckmann, S. O. Kamphorst, and D. Ruelle, "Recurrence plots of dynamical systems," *Europhysics Letters (EPL)*, vol. 4, no. 9, pp. 973–977, Nov. 1987.

[48] J. S. Iwanski and E. Bradley, "Recurrence plots of experimental data: To embed or not to embed?" *Chaos (Woodbury, N.Y.)*, vol. 8, no. 4, pp. 861–871, Dec. 1998.

[49] P. Bonizzi, S. Zeemering, J. Karel, M. H. Azman, T. Lankveld, U. Schotten, H. Crijns, R. Peeters, and O. Meste, "Noninvasive characterisation of short-and long-term recurrence of atrial signals during persistent atrial fibrillation," in *Computing in Cardiology*, vol. 44, 2017.

[50] F. Ouyang, S. Ernst, T. Vogtmann, M. Goya, M. Volkmer, A. Schaumann, D. Bänsch, M. Antz, and K.-H. Kuck, "Characterization of reentrant circuits in

left atrial macroreentrant tachycardia: Critical isthmus block can prevent atrial tachycardia recurrence," *Circulation*, vol. 105, no. 16, pp. 1934–1942, Apr. 2002.

[51] J. J. Rieta, F. Castells, C. Sanchez, V. Zarzoso, and J. Millet, "Atrial activity extraction for atrial fibrillation analysis using blind source separation," *IEEE Transactions on Biomedical Engineering*, vol. 51, no. 7, pp. 1176–1186, Jul. 2004.

[52] R. Llinares and J. Igual, "Exploiting periodicity to extract the atrial activity in atrial arrhythmias," *EURASIP Journal on Advances in Signal Processing*, vol. 2011, no. 1, Dec. 2011.

[53] J. Slocum, E. Byrom, L. McCarthy, A. Sahakian, and S. Swiryn, "Computer detection of atrioventricular dissociation from surface electrocardiograms during wide QRS complex tachycardias." *Circulation*, vol. 72, no. 5, pp. 1028–1036, Nov. 1985.

[54] O. Meste and N. Serfaty, "QRST cancellation using bayesian estimation for the auricular fibrillation analysis," in *2005 IEEE Engineering in Medicine and Biology 27th Annual Conference*. Shanghai, China: IEEE, 2005, pp. 7083–7086.

[55] R. Sassi, V. D. A. Corino, and L. T. Mainardi, "Analysis of Surface Atrial Signals: Time Series with Missing Data?" *Annals of Biomedical Engineering*, vol. 37, no. 10, pp. 2082–2092, Oct. 2009.

[56] V. Jacquemet, B. Dubé, R. Nadeau, A. R. LeBlanc, M. Sturmer, G. Becker, T. Kus, and A. Vinet, "Extraction and analysis of T waves in electrocardiograms during atrial flutter," *IEEE Trans. Biomed. Eng.*, vol. 58, no. 4, pp. 1104–1112, 2011.

[57] S. Kay, *Fundamentals of Statistical Signal Processing: Detection theory*, ser. Prentice Hall Signal Processing Series. Prentice-Hall PTR, 1998.

[58] E. K. Roonizi and R. Sassi, "A Signal Decomposition Approach to Morphological Modeling of P wave," in *Computing in Cardiology*, vol. 41, Cambridge, 2014, pp. 341–344.

[59] D. Kahaner, C. B. Moler, S. Nash, and G. E. Forsythe, *Numerical methods and software*. Prentice Hall, 1989.

[60] J. Martinez and S. Olmos, "A robust T wave alternans detector based on the GLRT for Laplacian noise distribution," in *Computers in Cardiology*, 2002, pp. 677–680.

[61] S. Kotz, T. Kozubowski, and P. Krzysztof, *The Laplace Distribution and Generalizations*. Birkhäuser, 2001.

[62] S. Kay, *Fundamentals of Statistical Signal Processing: Estimation Theory*, ser. Prentice Hall Signal Processing Series. Prentice-Hall PTR, 1993.

[63] B. Bidabad, "L1 Norm Based Computational Algorithms," 2005, accessible at bidabad.com.

[64] R. Farebrother, *L_1-Norm and L_∞-Norm Estimation*, ser. SpringerBriefs in Statistics. Springer-Verlag, 2013.

[65] R. R. Singleton, "A method for minimizing the sum of absolute values of deviations," *The Annals of Mathematical Statistics*, vol. 11, no. 3, pp. 301–310, 09 1940.

[66] G. O. Wesolowsky, "A new descent algorithm for the least absolute value regression problem," *Communications in Statistics - Simulation and Computation*, vol. 10, no. 5, pp. 479–491, 1981.

[67] Y. Li and G. R. Arce, "A Maximum Likelihood Approach to Least Absolute Deviation Regression," *EURASIP Journal on Advances in Signal Processing*, vol. 2004, no. 12, Dec. 2004.

[68] I. Barrodale and F. D. K. Roberts, "An Improved Algorithm for Discrete l1 Linear Approximation," *SIAM Journal on Numerical Analysis*, vol. 10, no. 5, pp. 839–848, 1973.

[69] G. Moody, R. Mark, A. Zoccola, and S. Mantero, "Derivation of respiratory signals from multi-lead ecgs," in *Computers in cardiology*, vol. 12, 1985, pp. 113–116.

[70] F. Pinciroli, R. Rossi, and L. Vergani, "Detection of electrical axis variation for the extraction of respiratory information," in *Computers in Cardiology*, vol. 12, 1985, pp. 499–502.

[71] L. Sörnmo, "Vectorcardiographic loop alignment and morphologic beat-to-beat variability," *IEEE Transactions on Biomedical Engineering*, vol. 45, no. 12, pp. 1401–1413, Dec 1998.

[72] P. H. Schönemann, "A generalized solution of the orthogonal procrustes problem," *Psychometrika*, vol. 31, no. 1, pp. 1–10, Mar. 1966.

[73] B. K. Horn, "Closed-form solution of absolute orientation using unit quaternions," *Josa a*, vol. 4, no. 4, pp. 629–642, 1987.

[74] K. S. Arun, T. Huang, and S. Blostein, "Least-squares fitting of two 3-d point sets," *IEEE Transactions on Pattern Analysis and Machine Intelligence*, vol. PAMI-9, no. 5, pp. 698–700, Sep 1987.

[75] S. Umeyama, "Least-squares estimation of transformation parameters between two point patterns," *IEEE Transactions on Pattern Analysis and Machine Intelligence*, vol. 13, no. 4, pp. 376–380, Apr 1991.

[76] J. Pan and W. J. Tompkins, "A Real-Time QRS Detection Algorithm," *IEEE Transactions on Biomedical Engineering*, vol. BME-32, no. 3, pp. 230–236, Mar. 1985.

[77] H. Riekkinen and P. Rautaharju, "Body position, electrode level, and respiration effects on the Frank lead electrocardiogram," *Circulation*, vol. 53, no. 1, pp. 40–45, Jan. 1976.

[78] M. S. Guillem, A. Sahakian, and S. Swiryn, "Derivation of orthogonal leads from the 12-lead ECG. accuracy of a single transform for the derivation of atrial and ventricular waves," in *Computing in Cardiology*, vol. 33, Sep. 2006, pp. 249–252.

[79] M. S. Guillem, A. M. Climent, A. Bollmann, D. Husser, J. Millet, and F. Castells, "Limitations of dower's inverse transform for the study of atrial loops during atrial fibrillation: limitations of dower's inverse transform for AF," *Pacing and Clinical Electrophysiology*, vol. 32, no. 8, pp. 972–980, Aug. 2009.

[80] A. van Oosterom, Z. Ihara, V. Jacquemet, and R. Hoekema, "Vectorcardiographic lead systems for the characterization of atrial fibrillation," *Journal of Electrocardiology*, vol. 40, no. 4, pp. 343.e1–343.e11, Jul. 2007.

[81] J. Kennedy and R. Eberhart, "Particle swarm optimization," in *Proceedings of ICNN'95 - International Conference on Neural Networks*, vol. 4, Nov. 1995, pp. 1942–1948 vol.4.

[82] J. H. Holland, "Genetic Algorithms and Adaptation," in *Adaptive Control of Ill-Defined Systems*, O. G. Selfridge, E. L. Rissland, and M. A. Arbib, Eds. Boston, MA: Springer US, 1984, pp. 317–333.

[83] X.-S. Yang and Suash Deb, "Cuckoo search via lévy flights," in *2009 World Congress on Nature & Biologically Inspired Computing (NaBIC)*. IEEE, 2009, pp. 210–214.

[84] J. Ng, A. Sahakian, W. Fisher, and S. Swiryn, "Surface ecg vector characteristics of organized and disorganized atrial activity during atrial fibrillation," *Journal of Electrocardiology*, vol. 37, pp. 91–97, Oct 2004.

[85] U. Richter, "Spatial characterization and estimation of intracardiac propagation patterns during atrial fibrillation," Ph.D. dissertation, Department of Electrical and Information Technology, 2010.

[86] J. P. Zbilut and C. L. Webber, "Embeddings and delays as derived from quantification of recurrence plots," *Physics Letters A*, vol. 171, no. 3, pp. 199 – 203, 1992.

[87] C. L. J. Webber and J. P. Zbilut, "Dynamical assessment of physiological systems and states using recurrence plot strategies." *Journal of applied physiology (Bethesda, Md. : 1985)*, vol. 76, no. 2, pp. 965–973, Feb. 1994.

[88] L. L. Trulla, A. Giuliani, J. P. Zbilut, and C. L. Webber, "Recurrence quantification analysis of the logistic equation with transients," *Physics Letters A*, vol. 223, no. 4, pp. 255 – 260, 1996.

[89] N. Marwan, N. Wessel, U. Meyerfeldt, A. Schirdewan, and J. Kurths, "Recurrence-plot-based measures of complexity and their application to heart-rate-variability data." *Physical review. E, Statistical, nonlinear, and soft matter physics*, vol. 66, no. 2 Pt 2, p. 026702, Aug. 2002.

[90] T. Hastie, R. Tibshirani, and J. Friedman, *The Elements of Statistical Learning: Data Mining, Inference, and Prediction*, 2nd ed. Springer, 2008.

[91] G. Hughes, "On the mean accuracy of statistical pattern recognizers," *IEEE Transactions on Information Theory*, vol. 14, no. 1, pp. 55–63, Jan. 1968.

[92] G. V. Trunk, "A Problem of Dimensionality: A Simple Example," *IEEE Transactions on Pattern Analysis and Machine Intelligence*, vol. PAMI-1, no. 3, pp. 306–307, Jul. 1979.

[93] P. Domingos, "A unified bias-variance decomposition and its applications," in *In Proc. 17th International Conf. on Machine Learning*. Morgan Kaufmann, 2000, pp. 231–238.

[94] R. Kohavi and G. H. John, "Wrappers for feature subset selection," *Artificial Intelligence*, vol. 97, no. 1-2, pp. 273–324, Dec. 1997.

[95] I. Guyon and A. Elisseeff, "An Introduction to Variable and Feature Selection," *Journal of Machine Learning Research*, vol. 3, pp. 1157–1182, Mar. 2003.

[96] D. Koller and M. Sahami, "Hierarchically classifying documents using very few words," Stanford InfoLab, Tech. Rep., 1997.

[97] L. Yu and H. Liu, "Efficient Feature Selection via Analysis of Relevance and Redundancy," *Journal of Machine Learning Research*, vol. 5, pp. 1205–1224, 2004.

[98] O. Meste, H. K. Azman, and D. G. Latcu, "Machine learning approach and waves synchronization improvement for the localization of Atrial Flutter circuit based on the 12-leads ECG," in *Computing in Cardiology*, vol. 46, Singapore, 2019.

[99] H. Werner and C. Yapar, "On inequality constrained generalized least squares selections in the general possibly singular Gauss-Markov model: A projector theoretical approach," *Linear Algebra and its Applications*, vol. 237-238, pp. 359–393, Apr. 1996.

[100] M. Sunemark, L. Edenbrandt, H. Holst, and L. Sörnmo, "Serial VCG/ECG Analysis Using Neural Networks," *Computers and Biomedical Research*, vol. 31, no. 1, pp. 59–69, Feb. 1998.

APPENDICES

Appendix A

Derivation of Detector Expressions

Here, a series of partial workouts of detector expressions are given. The strategy in developing the detectors come from observations on the mathematical expression of the likelihood-ratio test.

To begin, let $L(\mathbf{x}, \boldsymbol{\theta})$ be a function that performs an operation on $\mathbf{x}$ with parameters $\boldsymbol{\theta}$, and $f(\cdot)$ and $g(\cdot)$ arbitrary functions. Let α be a constant. Under sample independence, it is possible to write the PDF in both Gaussian normal and Laplace case as:

$$p(\mathbf{x}; \boldsymbol{\theta}) = \alpha f(\sigma_w^2)^N \exp\big(-g(\sigma_w^2) L(\mathbf{x}, \boldsymbol{\theta})\big) = \prod_{n=0}^{N-1} p(x[n]; \boldsymbol{\theta})$$

where the quantities are left undefined for the time being. Note that this is not similar to the Neyman-Fisher factorization. The Neyman-Pearson theorem states that:

$$T(\mathbf{x}) = \frac{p(\mathbf{x}; \mathcal{H}_1, \boldsymbol{\theta}_1)}{p(\mathbf{x}; \mathcal{H}_0, \boldsymbol{\theta}_0)} \underset{\mathcal{H}_0}{\overset{\mathcal{H}_1}{\gtrless}} \gamma$$

It is now convenient to proceed. The likelihood ratio test is written as

$$\begin{aligned} T(\mathbf{x}) &= \frac{p(\mathbf{x}; \mathcal{H}_1, \boldsymbol{\theta}_1)}{p(\mathbf{x}; \mathcal{H}_0, \boldsymbol{\theta}_0)} \\ &= \frac{\alpha f(\sigma_{w1}^2)^N \exp\big(-g(\sigma_{w1}^2) L(\mathbf{x}, \boldsymbol{\theta}_1)\big)}{\alpha f(\sigma_{w0}^2)^N \exp\big(-g(\sigma_{w0}^2) L(\mathbf{x}, \boldsymbol{\theta}_0)\big)} \\ &= \left(\frac{f(\sigma_{w1}^2)}{f(\sigma_{w0}^2)}\right)^N \frac{\exp\big(-g(\sigma_{w1}^2) L(\mathbf{x}, \boldsymbol{\theta}_1)\big)}{\exp\big(-g(\sigma_{w0}^2) L(\mathbf{x}, \boldsymbol{\theta}_0)\big)} \end{aligned} \tag{A.1}$$

Applying a logarithm to $T(\mathbf{x})$, the expression becomes:

$$\ln T(\mathbf{x}) = N\big(\ln f(\sigma_{w1}^2) - \ln f(\sigma_{w0}^2)\big) + \big(g(\sigma_{w0}^2) L(\mathbf{x}, \boldsymbol{\theta}_0) - g(\sigma_{w1}^2) L(\mathbf{x}, \boldsymbol{\theta}_1)\big) \tag{A.2}$$

Consider now when σ_w^2 is known and equal ($\sigma_{w1}^2 = \sigma_{w0}^2 = \sigma_w^2$). The terms $\ln(f(\cdot))$ cancel out and $g(\sigma_w^2)$ can be factored. Note that logarithm is a monotone transform, therefore it does not affect the range of the likelihood ratio and thus is permissible. Normalizing by $g(\sigma_w^2)$, the expression becomes:

$$T'(\mathbf{x}) = g(\sigma_w^2)^{-1} \ln T(\mathbf{x}) = L(\mathbf{x}, \boldsymbol{\theta}_0) - L(\mathbf{x}, \boldsymbol{\theta}_1) \tag{A.3}$$

Note that the quantities on both sides are assumed to be known. If this is the case, then this would be the end of the development. If not, then estimation can be performed due to independence of the parameters under each hypothesis.

The function L can be defined as

$$L(\mathbf{x}, \boldsymbol{\theta}) = \begin{cases} \sum_{n=0}^{N-1} (x[n] - \mathbf{H}(n)\boldsymbol{\theta})^2 & \text{under } \mathcal{N} \\ \sum_{n=0}^{N-1} |x[n] - \mathbf{H}(n)\boldsymbol{\theta}| & \text{under Laplace} \end{cases} \tag{A.4}$$

with (n) denoting the n-th row. For the case under Gaussian normal, the estimator has been shown to be the LS estimator. Under Laplace, the estimator is the LAD estimator, solved computationally.

If the variances were not known, then estimation of the parameter must be performed. To do this, the derivative can be taken at (A.2) with respect to the variance in question. Illustrating for σ_{w1}^2:

$$\frac{\partial \ln T(\mathbf{x})}{\partial \sigma_{w1}^2} = N \frac{\partial \ln f(\sigma_{w1}^2)}{\partial \sigma_{w1}^2} - \frac{\partial g(\sigma_{w1}^2)}{\partial \sigma_{w1}^2} L(\mathbf{x}, \boldsymbol{\theta}_1)$$

Here, the functions f and g has to be defined to obtain an analytical expression. Let

$$f(x) = \frac{1}{(2x)^{\frac{1}{2}}} \tag{A.5}$$

$$g(x) = \begin{cases} \frac{1}{2x} & \text{under } \mathcal{N} \\ \frac{2}{(2x)^{\frac{1}{2}}} & \text{under Laplace} \end{cases} \tag{A.6}$$

Continuing with the LS estimation

$$\begin{aligned} \frac{\partial \ln T(\mathbf{x})}{\partial \sigma_{w1}^2} &= -\frac{N}{2}\frac{1}{\sigma_{w1}^2} + \frac{1}{2(\sigma_{w1}^2)^{-2}} L(\mathbf{x}, \boldsymbol{\theta}_1) = 0 \\ &\Leftrightarrow \frac{1}{(\sigma_{w1}^2)^{-2}} L(\mathbf{x}, \boldsymbol{\theta}_1) = \frac{N}{\sigma_{w1}^2} \\ &\Rightarrow \hat{\sigma_{w1}^2} = \frac{1}{N} L(\mathbf{x}, \boldsymbol{\theta}_1) = \frac{1}{N} \sum_{n=0}^{N-1} (x[n] - \mathbf{H}(n)\boldsymbol{\theta})^2 \end{aligned} \tag{A.7}$$

Under Laplacian noise, the estimation is, for σ_{w1}^2

$$\begin{aligned}\frac{\partial \ln T(\mathbf{x})}{\partial \sigma_{w1}^2} &= -\frac{N}{2}\frac{1}{\sigma_{w1}^2} + \frac{2}{(2\sigma_{w1}^2)^{\frac{3}{2}}}L(\mathbf{x},\boldsymbol{\theta}_1) = 0 \\ \Leftrightarrow &\frac{2}{(2\sigma_{w1}^2)^{\frac{3}{2}}}L(\mathbf{x},\boldsymbol{\theta}_1) = \frac{N}{2}\frac{1}{\sigma_{w1}^2} \\ \Rightarrow &\hat{\sigma_{w1}^2} = \frac{2}{N^2}\Big(L(\mathbf{x},\boldsymbol{\theta}_1)\Big)^2 = \frac{2}{N^2}\left(\sum_{n=0}^{N-1}|x[n]-\mathbf{H}(n)\boldsymbol{\theta}|\right)^2 \end{aligned} \tag{A.8}$$

Note that in both cases of noise distribution, the estimator of σ_w^2 under both hypotheses will maximize the likelihood function in (A.1). This can be shown by substituting the estimated parameter values into the equation. The likelihood ratio then simplifies to

$$T(\mathbf{x}) = \left(\frac{\hat{\sigma_{w0}^2}}{\hat{\sigma_{w1}^2}}\right)^{\frac{N}{2}} > \gamma$$

or equivalently

$$T''(\mathbf{x}) = (T(\mathbf{x}))^{\frac{2}{N}} = \frac{\hat{\sigma_{w0}^2}}{\hat{\sigma_{w1}^2}} > \gamma^{\frac{2}{N}} \tag{A.9}$$

Both (A.3) and (A.9) are usable to obtain all detector expressions, except for T_9, to which the reader should be referred below.

Extending to a multilead setup, it is assumed that all leads are independent of each other. Hence, the multilead likelihood ratio should be used

$$T(\mathbf{x}) = \prod_{m=1}^{M}\frac{p(\mathbf{x}_m;\mathcal{H}_1,\boldsymbol{\theta}_1)}{p(\mathbf{x}_m;\mathcal{H}_0,\boldsymbol{\theta}_0)} \underset{\mathcal{H}_0}{\overset{\mathcal{H}_1}{\gtrless}} \gamma$$

However, note that by applying the logarithm on the multilead likelihood ratio, the individual ratios of each lead become separated

$$\ln T(\mathbf{x}) = \ln\left(\prod_{m=1}^{M}\frac{p(\mathbf{x}_m;\mathcal{H}_1,\boldsymbol{\theta}_1)}{p(\mathbf{x}_m;\mathcal{H}_0,\boldsymbol{\theta}_0)}\right) = \sum_{m=1}^{M}\ln\left(\frac{p(\mathbf{x}_m;\mathcal{H}_1,\boldsymbol{\theta}_1)}{p(\mathbf{x}_m;\mathcal{H}_0,\boldsymbol{\theta}_0)}\right)$$

Since the detector expression remains fixed for all lead, this shows that multilead detectors derived from the log-likelihood (A.3) is essentially a sum of the detector output of each lead.

On the other hand, each likelihood ratio can be decomposed to the form in (A.1). If the

detectors assume unknown variance, then it has been shown that this results in (A.9). When performed on all leads, this essentially reduces the multilead likelihood ratio to a product of the term in (A.9) over all lead, or essentially a product of the output of the test of all leads.

Derivation of Locally Optimum Detector

For the case where A and σ_w^2 are not estimated, the detector under Laplacian noise was shown to be (4.15). This would be as far as the calculation may go. However, in this work, a slightly different detector has been used, which is asymptotically optimal (see [57]).

First, note that the log-likelihood $\ln p_{\mathcal{H}_1}(\mathbf{x} - A\mathbf{s})/p_{\mathcal{H}_0}(\mathbf{x})$ can be seen as a function of A. Assuming sample independence, perform a first-order Taylor approximation about $A = 0$ on the log-likelihood for a single sample

$$\ln \frac{p_{\mathcal{H}_1}(x - As[n])}{p_{\mathcal{H}_0}(x)} \simeq$$

$$\ln \frac{p_{\mathcal{H}_1}(x - As[n])}{p_{\mathcal{H}_0(x)}}\bigg|_{A=0} + \frac{\dfrac{dp(x - As[n])}{d(x - As[n])}}{p(x - As[n])}\bigg|_{A=0} ((x - As[n]) - (x - As[n])|_{A=0}) =$$

$$- \frac{\dfrac{dp(x)}{d(x)}}{p(x)} s[n]A \tag{A.10}$$

with $p(x[n])$ the PDF of a single sample. Then, we have, for the Laplacian case:

$$\begin{aligned} \frac{dp(x)}{dx} &= \frac{d}{dx}\Big(\frac{1}{\sqrt{2\sigma_w^2}} e^{-\sqrt{\frac{2}{\sigma_w^2}}|x|}\Big) \\ &= -\frac{1}{\sqrt{2\sigma_w^2}}\Big(\sqrt{\frac{2}{\sigma_w^2}}\operatorname{sgn} x\Big) e^{-\sqrt{\frac{2}{\sigma_w^2}}|x|} \end{aligned}$$

where $\operatorname{sgn} x$ indicates the sign of x. Note that the derivative is taken despite its non-existence at $x = 0$. But this will never happen in practice except for when $x = s$. Implementation-wise, this is handled by giving it a positive sign. Replacing this result back in (A.10), we obtain the following expression:

$$\begin{aligned} T(\mathbf{x}) &= \sum_{n=0}^{N-1} -\frac{\dfrac{dp(x[n])}{dx[n]}}{p(x[n])} s[n] \\ &= \sum_{n=0}^{N-1} \sqrt{\frac{2}{\sigma_w^2}} \operatorname{sgn} x[n] s[n] > \gamma \\ \sqrt{\frac{\sigma_w^2}{2}} T(\mathbf{x}) = T'(\mathbf{x}) &= \sum_{n=0}^{N-1} \operatorname{sgn} x[n] s[n] > \gamma' = \sqrt{\frac{\sigma_w^2}{2}}\gamma \end{aligned} \tag{A.11}$$

This particular detector is known as the locally optimum detector [57] and shares practically the same form as the replica-correlator, except for the non-linear sign operator that clips $x[n]$ according to its sign.

Appendix B

Proof of Relation between Weighted Averaging and SVD

In this section, a short proof of the relation between SVD and weighted averaging is given. The objective is:

$$\min_{\mathbf{s},\mathbf{a}} I = \|\mathbf{Z} - \mathbf{s}\mathbf{a}^\intercal\|_F = \operatorname{tr}(\mathbf{Z}^\intercal\mathbf{Z}) + \operatorname{tr}(\mathbf{a}\mathbf{s}^\intercal\mathbf{s}\mathbf{a}^\intercal) - 2\operatorname{tr}(\mathbf{Z}^\intercal\mathbf{s}\mathbf{a}^\intercal)$$

with $\mathbf{Z} = [\mathbf{z}_1 \ \cdots \ \mathbf{z}_K]$ a set of observations, and $\mathbf{s}$ and $\mathbf{a}$ the representative waveform and the relative weight fitting $\mathbf{s}$ to each $\mathbf{z}_k$. LS estimation was given in Section 4.4, which is $\hat{\mathbf{a}} = \mathbf{Z}^\intercal\mathbf{s}/\mathbf{s}^\intercal\mathbf{s}$ and $\hat{\mathbf{s}} = \mathbf{Z}\mathbf{a}/\mathbf{a}^\intercal\mathbf{a}$. Note that $\hat{\mathbf{s}}$ is essentially a weighted average of each observation $\mathbf{z}_k$ by $a_k/\sum a_k^2$. However, there exists a problem of non-unicity since for any solution $\hat{\mathbf{s}}$ and $\hat{\mathbf{a}}$, $\hat{\mathbf{s}}\hat{\mathbf{a}}^\intercal = \alpha\hat{\mathbf{s}}\hat{\mathbf{a}}^\intercal/\alpha = (\alpha\hat{\mathbf{s}})(\hat{\mathbf{a}}^\intercal/\alpha) = \check{\mathbf{s}}\check{\mathbf{a}}^\intercal$, therefore it is also required that $\hat{\mathbf{a}}^\intercal\hat{\mathbf{a}} = 1$.

A solution of type $\mathbf{s} = \mathbf{Z}\mathbf{m},\ \mathbf{m}^\intercal\mathbf{m} = 1$ is compliant to the LS estimator, and is imposed. The selection of $\mathbf{m}$ seems arbitrary for the moment, therefore it is also imposed that:

$$\hat{\mathbf{m}} = \arg\max_{\mathbf{m}} \mathbf{s}^\intercal\mathbf{s} = \mathbf{m}^\intercal\mathbf{Z}^\intercal\mathbf{Z}\mathbf{m} = \mathbf{m}^\intercal\mathbf{C}_Z\mathbf{m}$$

with $\mathbf{C}_Z$ the covariance matrix of $\mathbf{Z}$. This implies that $\mathbf{m}$ should weigh each observation accordingly such that the resulting vector has maximum energy. To solve this, a criterion J is defined such that:

$$J = \mathbf{m}^\intercal\mathbf{C}_Z\mathbf{m} - \lambda(\mathbf{m}^\intercal\mathbf{m} - 1)$$

Differentiating J with respect to $\mathbf{m}$ and setting it to zero produces $\mathbf{C}_Z\mathbf{m} = \lambda\mathbf{m}$. This is reminiscent to the eigendecomposition setup, and indeed J can be maximized if $\mathbf{m}$ is taken as the eigenvector $\mathbf{v}$ associated with the largest eigenvalue of $\mathbf{C}_Z$.

Imposing $\mathbf{s} = \mathbf{Z}\mathbf{m}$ and replacing this in I, the second and third terms become:

$$\operatorname{tr}(\mathbf{a}\mathbf{m}^\intercal\mathbf{Z}^\intercal\mathbf{Z}\mathbf{m}\mathbf{a}^\intercal) - 2\operatorname{tr}(\mathbf{Z}^\intercal\mathbf{Z}\mathbf{m}\mathbf{a}^\intercal) = \operatorname{tr}(\mathbf{a}\mathbf{m}^\intercal\mathbf{C}_Z\mathbf{m}\mathbf{a}^\intercal) - 2\operatorname{tr}(\mathbf{C}_Z\mathbf{m}\mathbf{a}^\intercal)$$

Note that the first term of I is constant and positive, thus it is only necessary to minimize the terms above. Derivating the criterion by $\mathbf{a}$ results in $2\mathbf{m}^\intercal\mathbf{C}_Z\mathbf{m} - 2\mathbf{C}_Z\mathbf{m}$. Setting this to zero, the expression becomes $\mathbf{m}^\intercal\mathbf{C}_Z\mathbf{m}\mathbf{a} = \mathbf{C}_Z\mathbf{m}$. Setting $\mathbf{m}$ to $\mathbf{v}$, the largest eigenvector of $\mathbf{C}_Z$, the expression then becomes $\mathbf{v}^\intercal\lambda\mathbf{v}\mathbf{a} = \lambda\mathbf{v}$, and thus $\mathbf{a} = \mathbf{v}$. This solution was shown to be compliant to the LS estimator of $\mathbf{s}$, and also maximizes its

energy.